Advancing Mid-IR Lasers

by

Andrew Malouf

Thesis submitted for the degree of
Doctor of Philosophy
November 2019

School of Physical Sciences
The University of Adelaide
Adelaide, South Australia, 5005

Contents

Abstract

The mid-IR spectral region is important in a wide range of applications. Many molecules have unique characteristic absorption features in this region due to strong vibrational transitions. Mid-IR lasers, tuned to these absorption lines, are an excellent source for detecting trace gases such as air pollutants for environmental monitoring, biomarkers in exhaled human breath for medical diagnosis, and trace explosives for security. Furthermore, the mid-IR region includes two atmospheric transmission windows, 3 µm – 5 µm and 8 µm – 13 µm, which overlap with the strong absorption lines of many molecules. These transmission windows may be exploited with differential absorption lidar technology to remotely detect atmospheric gases. New and exciting applications for mid-IR lasers will open up as mid-IR lasers become more powerful, stable, tunable, and ultrafast.

This thesis details three approaches to advancing mid-IR lasers and their uses. Firstly, a feasibility study is presented that assesses the detectability of diesel exhaust emissions in the atmosphere using differential absorption lidar from an airborne platform. This technology could be developed to identify and monitor major sources of air pollution at any location accessible by an aircraft. The study shows that carbon monoxide is a suitable target gas in the 2.3 µm wavelength band, while nitrogen dioxide and formaldehyde are suitable targets in the 3.5 µm band.

Secondly, a numerical model is presented that simulates the physical processes in 3.5 µm dual-wavelength pumped fibre lasers. The model, validated against three experiments reported in literature, provides time domain analysis of ionic energy state populations, predicts laser performance, and has become a valuable tool for the optimisation of fibre laser design. The model was adapted to study Q-switching behaviour of these lasers with high temporal resolution.

Finally, this thesis presents a detailed characterisation of graphene under high intensity radiation to understand its suitability for passively mode-locking mid-IR lasers. Intensity dependent transmission measurements were performed on trilayer graphene in the 1.55 µm – 3.50 µm spectral region using a 100 fs laser source and the z-scan technique. The measured saturation intensities were combined with others reported in literature to find that saturation intensity depends on the third power of photon energy in the femtosecond regime while longer pulses show a square root dependence. Furthermore, multilayer graphene is shown to exhibit two-photon absorption as well as saturable absorption when subjected to high intensity radiation. Two-photon absorption limits the effective modulation depth and can be detrimental to mode-locking mid-IR lasers. This explains why lasers beyond the 3 µm wavelength band have not been mode-locked using multilayer graphene.

Declaration

I certify that this work contains no material which has been accepted for the award of any other degree or diploma in my name, in any university or other tertiary institution and, to the best of my knowledge and belief, contains no material previously published or written by another person, except where due reference has been made in the text. In addition, I certify that no part of this work will, in the future, be used in a submission in my name, for any other degree or diploma in any university or other tertiary institution without the prior approval of the University of Adelaide and where applicable, any partner institution responsible for the joint-award of this degree.

I acknowledge that copyright of published works contained within this thesis resides with the copyright holder(s) of those works.

I also give permission for the digital version of my thesis to be made available on the web, via the University's digital research repository, the Library Search and also through web search engines, unless permission has been granted by the University to restrict access for a period of time.

I acknowledge the support I have received for my research through the provision of an Australian Government Research Training Program Scholarship.

Andrew Malouf
1st November, 2019

Acknowledgements

Many people have participated in this work in some way, often from behind the scenes.

Firstly, this work would not have been possible without the experience, knowledge, and guidance of my supervisors Prof. David J. Ottaway and Dr. Ori Henderson-Sapir. I extend my sincere gratitude to each of you for your continual support during candidature and your constructive reviews during the write-up of this thesis. Most of all, I thank you for your patience.

To the other co-authors of the publications presented in this work – Prof. Shinji Yamashita, Dr. S. Y. Set, and Dr. Martin Gorjan – your contributions were invaluable from the very early stages of those works. I thank you for your insightful suggestions and enthusiasm.

Special thanks to Patrick Tapping for his support in the laser lab. Your kind assistance and cooperation are greatly appreciated. I am also grateful to Tak Kee for the provision of the femtosecond laser facilities.

I have had the pleasure of working amongst numerous people who have assisted in some way, such as providing equipment, sharing ideas, reviewing written works, giving encouragement, or just listening. They include, but are not limited to, Roger Clay, Elizaveta Klantsataya, Richard White, Miftar Ganija, Robert Chivell, Chris Perrella, Leszek Swierkowski, Geoff Williams, Peter Apoefis, Ashley Slattery, Jason Gascooke, Christopher Gibson, Ramona Rogers, Kathryn McDonnell, Albert Kong, Nathaniel Bawden, and 'roommate' Joshua Pease.

My deepest gratitude extends to my close family members and friends who, despite being affected by my commitment to this candidature, have provided enduring support and encouragement along the way. I am forever grateful to Carolyn Forrest and Paul Gordon for having more faith in me than I had. I am especially grateful to Andrew Frydrych for his support and commitment to the family business.

Finally, I am most grateful to my dear wife and pillar of support, Margerette, for eternal understanding, patience, and sustenance.

Publications

This thesis includes the following publications that encapsulate some of the research performed during candidature:

1. A. Malouf, O. Henderson-Sapir, M. Gorjan, D. J. Ottaway. Numerical modeling of 3.5 µm dual-wavelength pumped erbium-doped mid-infrared fiber lasers. *IEEE Journal of Quantum Electronics*, 52(11):1–2, Nov 2016.

2. A. Malouf, O. Henderson-Sapir, S. Set, S. Yamashita, D. J. Ottaway. Two-photon absorption and saturable absorption of mid-IR in graphene. *Applied Physics Letters*, 114(9):091111, 2019.

In addition, contributions have been made to the following publication:

O. Henderson-Sapir, A. Malouf, N. Bawden, J. Munch, S. D. Jackson, D. J. Ottaway. Recent advances in 3.5 µm erbium-doped mid-infrared fiber lasers. *IEEE Journal of Selected Topics in Quantum Electronics*, 23(3):6–14, May 2017.

and conference proceedings:

A. Malouf, O. Henderson-Sapir, M. Gorjan, D. J. Ottaway. Modelling and optimisation of a dual-wavelength pumped 3.5 µm fibre laser at the watt level. In *Photonics and Fiber Technology 2016 (ACOFT, BGPP, NP)*, page ATh4C.4. Optical Society of America, 2016.

O. Henderson-Sapir, S. D. Jackson, A. Malouf, M. Gorjan, J. Munch, D. J. Ottaway. Erbium-doped mid-infrared fiber lasers. In *2016 Conference on Lasers and Electro-Optics (CLEO)*, page STh1O.1. Optical Society of America, 2016.

O. Henderson-Sapir, A. Malouf, N. Bawden, E. Klantsataya, J. Munch, M. R. Majewski, S. D. Jackson, H. Matsukuma, S. Tokita, S. Y. Set, S. Yamashita, D. J. Ottaway. Erbium-doped mid-infrared fiber lasers. In *Laser Technology for Defense and Security XV*, volume 10981. SPIE, 2019.

Figures

Tables

Abbreviations

2D	Two-dimensional
2PA	Two-photon absorption
AOM	Acousto-optic modulator
BP	Band pass
CaF_2	Calcium fluoride
CO	Carbon monoxide
CP	Conventional pumping
CPU	Central processor unit
CVD	Chemical vapour deposition
CW	Continuous-wave
DIAL	Differential absorption lidar
Dy	Dysprosium
DFG	Difference frequency generation
DWP	Dual-wavelength pumping
Er	Erbium
IR	Infrared
EOM	Electro-optic modulator
ESA	Excited state absorption
FLAPP	Fibre Laser Atomic and Photonic Populations
FoV	Field of view
FTIR	Fourier transform IR
GPU	Graphical processor unit
GSA	Ground state absorption
H_2CO	Formaldehyde
HITRAN	High-resolution transmission molecular absorption database
Ho	Holmium
Lidar	Light detection and ranging
LP	Long pass
MARPOL	The International Convention for the Prevention of Pollution from Ships
MP	Multi-phonon
ND	Neutral density
NEP	Noise equivalent power
NIST	National Institute of Standards and Technology
NO	Nitric oxide
NO_2	Nitrogen dioxide

OD	Optical density
OPA	Optical parametric amplifier
P_1, P_2	Pump 1, Pump 2
PMMA	Polymethyl methacrylate
ppb	parts-per-billion
ppm	parts-per-million
ppt	parts-per-trillion
Ref.	Reference
RK4	Rung-Kutta (fourth order)
SA	Saturable absorption
SESAM	Semiconductor saturable absorber mirror
Sig.	Signal
SNR	Signal-to-noise ratio
SO_2	Sulfur dioxide
TLG	Trilayer graphene
TLS	Tunable laser source
Tm	Thulium
ULSDF	Ultra-low sulfur diesel fuel
UV	Ultraviolet
Yb	Ytterbium
ZBLAN	ZrF_4-BaF_2-LaF_3-AlF_3-NaF

Symbols

a	Lattice constant (real space)
$\mathbf{a}_1, \mathbf{a}_2$	Primitive translation vectors (real space)
A_{atm}	Atmospheric absorption
A_{t}	Area of DIAL telescope receiver
A_{S}	Area on Earth surface defined by telescope field of view
$\mathbf{b}_1, \mathbf{b}_2$	Primitive translation vectors (reciprocal space)
c	Speed of light in vacuum
C_{tg}	Concentration of target gas [ppm]
C_{tgv}	Concentration of target gas [m^{-3}]
Δf_{D}	Bandwidth of detector
E	Energy
E_0	Onsite energy of π electron
E_{ph}	Photon energy
E_{s}	Energy of sent pulse
f	Focal length
F_{s}	Saturation fluence
F_{dam}	Damage threshold fluence
h	Planck's constant
I	Intensity
I_{s}	Saturation intensity
I_{dam}	Damage threshold intensity
$\mathbf{k}$	Wave vector (k_x, k_y) in reciprocal space
k_{B}	Boltzmann constant
l	Length, altitude
$\mathbf{K}$	Reciprocal lattice vectors
K, K'	Vertices of the first Brillouin zone (k-space)
M^2	Beam propagation parameter
P_{avg}	Average power
P_{peak}	Peak power
P_{r}	Power of return pulse
P_{s}	Power of sent pulse
$\mathbf{r}$	Position vector (x, y) in real space
r_{t}	Radius of telescope receiver
$\mathbf{R}$	Real lattice vectors
S	Spectral line intensity

S_{D}	Noise equivalent power of detector
S_{L}	Sensitivity of lidar
T	Transmission
T_{rel}	Relative transmission
T_{sub}	Transmission through the substrate
T_l	Transmission of pulse over path length l
T_{K}	Temperature
w	Spot size of beam (radius)
w_0	Spot size of beam at waist (radius)
z	Position along z-axis
z_0	Position of beam waist along z-axis
α	Absorption coefficient
α_0	Modulation depth parameter
α_{ns}	Non-saturable absorption coefficient
β	Two-photon absorption coefficient
γ	Overlap integral for nearest neighbour hopping
θ_{t}	Telescope field of view
λ	Wavelength
λ_{on}	Wavelength of online pulse
λ_{off}	Wavelength of offline pulse
$\Delta\lambda_{\mathrm{F}}$	Bandwidth of spectral filter
ν	Frequency
ρ	Surface reflectance
σ	Cross section
τ	Lifetime
τ_{p}	Pulse duration

Chapter 1
Introduction

The first laser was demonstrated in 1960.[1] A ruby crystal, with parallel silver-coated end faces, was irradiated by a high power flash lamp resulting in the amplification of visible light at a wavelength of 694.3 nm (deep red). Since then, laser technology has become ubiquitous in modern society, with applications in manufacturing, communication, spectroscopy, remote sensing, metrology, surgery, defence, entertainment, and more.

Mid-infrared (mid-IR) laser sources have attracted enormous interest in recent years as new developments emerge. The mid-IR spectral region contains strong absorption lines of gas-phase molecules, as well as several transparent windows of the atmosphere, that offer significant opportunities for trace gas sensing. The last decade has seen exciting progress in mid-IR fibre lasers, semiconductor lasers, frequency combs, and supercontinuum generation. Continued progress will realise sensing technologies ranging from portable breath analysis for medical diagnosis to remote sensing of multiple trace gases in the atmosphere for air pollution monitoring. However, translating the more matured technology of near-IR lasers into the mid-IR domain has been challenging and the brightness of mid-IR laser sources continue to lag behind their near-IR counterparts.

This research was motivated by the need for bright, ultrafast mid-IR laser sources in applications such as trace gas sensing. This thesis presents three approaches toward advancing mid-IR lasers, which are summarised as follows:

i. Feasibility study for the detection of diesel exhaust gases in the atmosphere using differential absorption lidar (DIAL) technology from an airborne platform for broad-area environmental monitoring (Chapter 2);

ii. Modelling of fibre lasers, both in the temporal and spatial domains, for analysis and optimisation of laser performance (Chapter 3);

iii. Theoretical and experimental study of graphene and its response to mid-IR radiation for potential use in mode-locking mid-IR lasers (Chapters 4, 5, and 6).

This Chapter presents an overview of the current landscape of mid-IR lasers. Section 1.1 introduces the mid-IR spectral region and how this electromagnetic radiation interacts with molecules. Section 1.2 discusses some current and potential applications of mid-IR lasers to highlight their importance. In Section 1.3, the common types of mid-IR lasers and their characteristics are introduced, while broadband laser sources are discussed in Section 1.4. Q-switching and mode-locking principles are introduced in Section 1.5. Finally, the scope of this thesis is outlined in Section 1.6.

1.1 Mid-IR spectral region

The boundaries of the mid-IR spectral band are not consistent in literature since the applications that relate to this spectral region are diverse. The international standard ISO 20473:2007 defines the near-IR, mid-IR, and far-IR spectral bands as 0.78 µm – 3.0 µm, 3 µm – 50 µm, and 50 µm – 1 mm respectively.[2] However, the spectral region 2 µm – 20 µm, for example, has also been used to describe the mid-IR since a large number of molecules undergo strong characteristic vibrations in this domain.[3,4] Much of the work presented in this thesis relates to the 1.5 µm – 4 µm spectral region with particular emphasis on the 3.5 µm band.

The absorption spectrum of any molecule is determined by all allowed transitions between pairs of energy levels. The quantised energy levels are superpositions of electronic, vibrational, and rotational states of the molecule. Electronic, vibrational, and rotational transitions typically occur within the ultraviolet-visible, infrared, and microwave spectral bands respectively.[5] A particular bonded pair of atoms has a characteristic vibrational frequency. For example, if a carbon-hydrogen bond (C–H bond) exists in any molecule, the bond will have a characteristic vibrational frequency (wavenumber) in the range 2850 cm^{-1} – 3300 cm^{-1} (wavelength range 3.0 µm – 3.5 µm).[6]

The mid-IR spectral band contains the fundamental vibrational absorption lines of many molecules while overtone vibrational transitions occur in the higher energy near-IR band. Transitions in both vibrational and rotational states, often abbreviated as ro-vibrational transitions, add fine structure to mid-IR absorption spectra since rotational transitions require much lower energies than vibrational transitions.[7] Since mid-IR absorption spectra contain characteristic features that uniquely identify a molecular species, spectral regions within the mid-IR band (such as 2 µm – 20 µm) may be referred to as the mid-IR molecular "fingerprint" region.[4,8]

Figure 1.1 illustrates the absorption lines of various molecules, commonly consid-

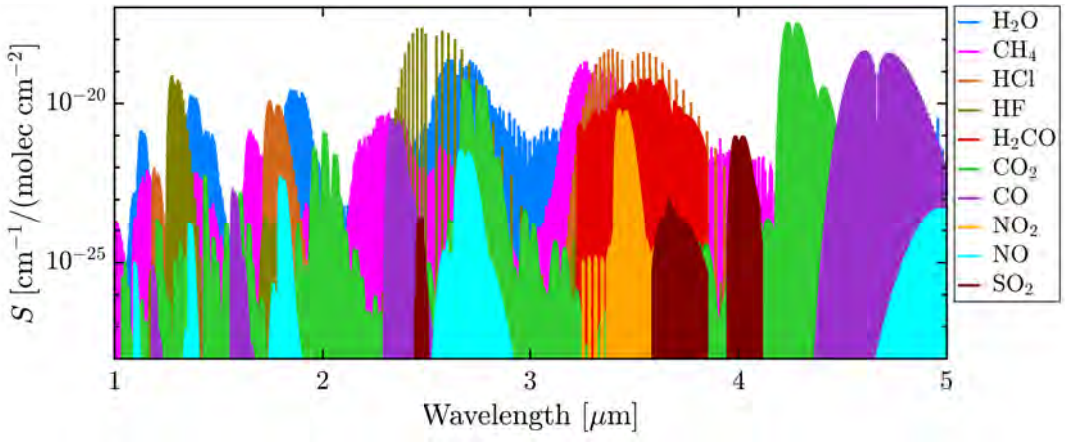

Figure 1.1: Spectral line intensities of various gases in the 1.0 µm – 5.0 µm spectral region. The data was sourced from the HITRAN2016 database.[9] The units for spectral line intensity S may be thought of as wavenumbers per unit column density. Higher peaks indicate stronger absorption.

ered either greenhouse gases or air pollutants, in the 1.0 µm – 5.0 µm spectral region. The highest absorption peak within a complete mid-IR spectrum is associated with the fundamental excitation (from the ground to the first excited state).[5] Less intense overtone bands are observed at shorter wavelengths due to excitations from the ground state to higher excited states. The photon energies of these overtones are approximate integer multiples of the fundamental photon energy.[5]

1.2 Mid-IR laser applications

This Section provides an overview of several mid-IR laser applications to highlight their importance. The applications (current and potential) discussed are broadly categorised into the following three areas: (i) remote sensing; (ii) medical; and (iii) defence.

1.2.1 Remote sensing

The intense absorption bands of many trace gases in the atmosphere fall within the spectral region between 2.5 µm and 14 µm.[9,10] The mid-IR band contains several important windows in which the Earth's atmosphere is relatively transparent, including the 3 µm – 5 µm and 8 µm – 13 µm spectral regions. The absorption features of the atmosphere show the relatively transparent and opaque spectral regions (illustrated in Figure 2.5). The transparent windows may be exploited for applications such as mapping of the Earth surface or detecting pollutant and greenhouse gases in the atmosphere for environmental monitoring.

Lidar (light detection and ranging), commonly used for surveying, is one of the most promising instruments for studying the atmosphere and monitoring pollution.[10] Lidars are designed to illuminate a target with laser light and then measure the backscatter return. Most lidars consist of three basic modules: transmitting, receiving, and control systems. The transmitter consists of a laser source and optics to control the spot size, divergence angle, and direction of the emitted beam. The receiver consists of a telescope, spectral filter, and a photodetector. The control system controls laser emission, digitises the signal, and processes the data.[10]

Differential absorption lidar (DIAL), first proposed by Schotland[11] in 1974, is an effective technique used to measure the concentrations of trace gases in the atmosphere with sensitivities in the parts-per-billion (ppb) regime.[10,12] This technique emits pairs of co-aligned laser pulses that are separated by a short time interval. One pulse (online) is tuned to the absorption line of the target gas while the other pulse (offline) is slightly off tune and not absorbed by the target gas. The concentration of the target gas is then determined by the *differential* absorption of the pulse pairs.

One advantage of DIAL technology for atmospheric sensing is that the transmitter and receiver are co-located and thus can operate from a mobile platform. However, the laser power emitted must be high enough to be backscattered and detected. Peak power is optimised at a particular wavelength for maximum absorption by the target gas and therefore maximum detectability. In this way, DIAL systems are optimised for detectability of a *single* target gas.

Chapter 2 presents a feasibility study for the potential detection of diesel exhaust gases in the atmosphere using DIAL technology in the mid-IR domain.

1.2.2 Medical

Water, the main component of tissue, is characterised by strong absorption in the 3 µm and 6 µm wavelength bands which may be exploited for minimally invasive, high-precision laser surgery.[13,14] Ultrafast mid-IR laser pulses can be used effectively to ablate selective tissue, with minimal collateral damage to surrounding areas, for medical applications such as laser scalpel,[15] coagulation,[14] nanobiopsy,[16] biological tissue mapping,[17] and early detection of skin cancer.[18]

Figure 1.2 illustrates the effectiveness of a laser scalpel for ablating selective tissue with minimal damage to surrounding areas (illustration adapted from Ref. 15). The Er:YAG laser source (Picosecond IR Laser) emits picosecond pulses, in the strongly absorbed 3 µm wavelength band, to eject tissue faster than energy can diffuse to the surrounding areas. The resulting incision has a narrow damage zone when compared with incisions made by a mechanical scalpel or conventional medical laser that emits

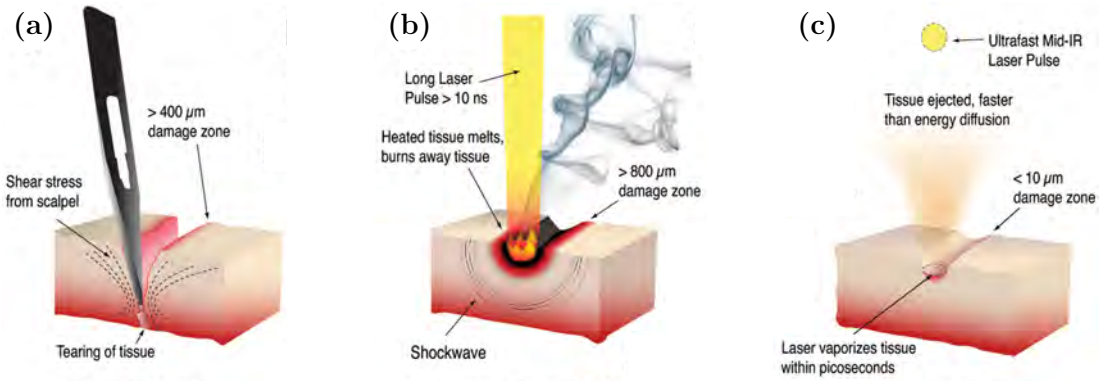

Figure 1.2: Illustration of cutting tissue using mechanical and laser scalpels.[15] **(a)** The mechanical scalpel cuts with shear forces that exceed the elastic limit of tissue and can cause damage up to 400 µm away from the incision borders. **(b)** The conventional medical laser cuts by depositing heat until the tissue melts or burns away causing damage up to 800 µm away from the ablation edge. **(c)** The Picosecond IR Laser (Er:YAG) emits short pulses of radiation in the 3 µm wavelength band that are absorbed by water within the tissue. The tissue is ejected faster than energy can be dissipated to surrounding areas causing minimal damage outside the ablation zone. This illustration was adapted from Ref. 15.

longer (nanosecond) pulses.[15]

Protein, as well as water, absorbs mid-IR radiation in the 5.9 µm – 6.6 µm wavelength band. When minimising collateral damage is the only concern, optimal wavelengths are 6.45 µm for brain surgery, 6.0 µm for corneal stroma, and the 6.0 µm – 6.45 µm range for skin.[14]

Breath analysis has become a highly desirable, non-invasive procedure for clinical diagnosis.[19] Exhaled breath contains more than 1,000 trace volatile organic compounds (VOCs) in concentrations that range between the ppt to ppm levels. In addition, the concentrations of nitric oxide (NO), dihydrogen (H_2), ammonia (NH_3), and carbon monoxide (CO) in exhaled breath can reflect a potential disease or recent exposure to a drug or environmental pollutant.[20] For example, detection of ammonia in human breath has the potential to probe processes involving the kidneys, liver, and bacterial infection,[21] while acetone is a biomarker for diabetes.[22] The presence and concentrations of these biomarkers constitute a distinctive "breathprint" that could potentially be analysed for early disease detection and general health diagnosis.[23] Highly-sensitive mid-IR gas sensing devices, sufficiently compact for outpatient clinics, would enable fast, cost effective, point-of-care medical services to patients.

1.2.3 Defence

The mid-IR spectral region between 2 µm and 5 µm is of interest to Defence for defeating missiles in a Directed Infrared Countermeasure (DIRCM) system.[24] Mid-IR lasers can be used to jam and/or damage IR guided missiles to defeat these threats, although the pulse energy required for damage is considerably higher than the energy required for jamming.[25] Due to the need for tunability and a lack of solid-state laser materials with suitable transitions in the mid-IR spectral region, nonlinear frequency down conversion devices, such as optical parametric oscillators (OPOs) containing zinc germanium phosphide (ZGP), have been the sources of choice for countermeasure systems.[24–26]

Standoff detection of trace amounts of explosive materials has attracted interest in counterterrorism for the protection of life and property.[27,28] Current methods of detection rely on close-range techniques, such as mass spectrometry of swabs and K9 units. Various explosive materials show distinct absorption bands between 5 µm and 11 µm.[28] Consequently, mid-IR backscatter techniques have the potential to detect explosives from standoff distances whilst meeting criteria for eye safety and stealth.

1.3 Types of mid-IR lasers

The direct generation of mid-IR laser radiation has been achieved with quantum cascade and interband cascade lasers, vibronic solid state lasers (transition metal-doped zinc chalcogenides), and fibre lasers. This Section presents an overview of these laser classes.

The great challenge in solid-state lasers for mid-IR operation is finding materials with low phonon energies. Solid state lasers which emit wavelengths longer than about 2.5 µm are often quenched by non-radiative processes caused by high energy phonons (crystal lattice vibrations). When the energy gap between two adjacent energy manifolds is less than five times the maximum phonon energy, non-radiative transitions quench the upper manifold.[29] Hence, to develop an efficient mid-IR laser with a wavelength longer than ~ 2.5 µm, a low phonon energy host material (such as fluoride and chalcogenide glasses or various laser quality crystals) is required.[29,30]

Nonlinear techniques have also generated mid-IR radiation by shifting high brightness near-IR sources into the mid-IR. Such techniques include optical parametric oscillators and amplifiers, difference frequency generation, and Raman shifting.[31]

1.3.1 Quantum and interband cascade lasers

The landscape of mid-IR sources has changed since the mid 1990s with the development of the quantum cascade laser (QCL).[32] This semiconductor injection laser operates on intersubband transitions between conduction band states in periodic structures of alternating quantum wells and barriers.[8,33] Once a photon is emitted from one period of the structure, following an intersubband electronic transition, it can tunnel into the next period and cause the emission of another photon. The continuation of this process gives rise to a *cascade* of photons. QCLs have good design flexibility with an achievable wavelength range of $\sim 3\,\mu m - 25\,\mu m$.[33] However, the peak power of QCLs is often limited by low wall plug efficiency and short upper state lifetimes (picoseconds) owing to fast non-radiative phonon decay between subbands that limit energy storage capability. Furthermore, a significant amount of heat needs to be dissipated from the active region of QCLs for CW operation at room temperature.[31,33–37]

Interband cascade lasers (ICL) combine the cascading scheme of a QCL with the relatively longer (nanoseconds) upper-level electron-hole recombination lifetime of a conventional diode laser.[34,38] Although ICLs require low drive power when compared with QCLs, their performance for applications that demand high peak power is still limited by upper state lifetimes (nanoseconds).[31,38,39] ICLs are suitable for laser spectroscopy applications in the $3\,\mu m - 6\,\mu m$ spectral region which do not require high output power but do need to be hand-portable and/or battery operated.[38]

1.3.2 Vibronic solid state lasers

Vibronic laser gain media, such as transition metal-doped zinc chalcogenides, are characterised by strong interactions between lattice vibrations and electronic states (*vibronic* interactions) which give rise to strong homogeneous broadening and large gain bandwidth. This class of media is suitable for broad wavelength tuning and generation of ultrashort pulses. However, the power scaling of these lasers may be limited (to $\sim 20\,W$) by quenching from multi-phonon emission.[37]

Transition metal-doped zinc chalcogenides were introduced in the late 1990s as a new class of gain media for mid-IR lasers.[40] Zinc chalcogenide hosts (such as ZnS and ZnSe) are effective gain media for mid-IR lasers since they feature low intrinsic phonon energies, broad IR transparency, and high thermal conductivity.[41] Divalent transition metals (such as Cr^{2+} and Fe^{2+}) feature high cross sections, broad emission and absorption bands, and the absence of excited state absorption.[42]

Cr^{2+}:ZnS and Cr^{2+}:ZnSe lasers operate with close to 100 % quantum efficiency at room temperature and are tunable over the $1.9\,\mu m - 3.4\,\mu m$ spectral range.[41,42] They

are conveniently pumped by erbium and thulium fibre lasers with $>60\,\%$ pump conversion efficiency. Meanwhile, Fe^{2+}:ZnS and Fe^{2+}:ZnSe lasers are tunable over the $3.4\,\mu m - 5.2\,\mu m$ spectral range, although they do require cooling in the CW regime.[42] Single-crystal, highly-doped chalcogenides are difficult to grow with high quality while highly doped polycrystalline materials are an effective and scalable alternative.[42]

1.3.3 Fibre lasers

Fibre lasers provide high efficiency and high output power with good thermal dissipation and excellent beam quality. An all-fibre design does not require the sensitive alignment of free-space optics, making them suitable for compact, robust systems that require low maintenance. Furthermore, the waveguide property of fibres gives rise to high overlap of pump and laser modes along the full length of the gain medium.

Since the first demonstration of a glass fibre laser in 1964,[43,44] the fabrication of glass fibres have advanced tremendously. Silicates and exotic glasses (such as fluorozirconates and chalcogenides) are doped with rare earth ions (such as Tm^{3+}, Er^{3+}, Ho^{3+}, and Dy^{3+}) and drawn into fibres to form near- and mid-IR laser gain media. Silica glasses have low loss, high strength, and are suitable for the $1.0\,\mu m - 2.2\,\mu m$ spectral region. The high phonon energy of silicates, however, attenuates radiation wavelengths longer than $2.2\,\mu m$ and these hosts, therefore, are not suitable for the mid-IR domain.[37]

Fluorozirconate glasses such as ZBLAN (ZrF_4-BaF_2-LaF_3-AlF_3-NaF) have low phonon energy, high mid-IR transparency, and high allowable doping levels (up to $10\,mol\,\%$).[45] Although ZBLAN glasses are more complicated to produce than silica glasses, they receive much attention due to broad transparency (from the UV to the mid-IR) and low insertion loss. The potential implications of these features, in areas such as medical, telecommunications, and military, have led to recent experiments in manufacturing high-quality ZBLAN fibre in a zero-gravity environment on board the International Space Station (ISS).[46,47]

The performance of IR fibre lasers are summarised in Figure 1.3 (reproduced from Refs. 37 and 63). The average output powers of various lasers reported in literature are plotted as a function of emission wavelength. The trend line was added for a guide to the eye only and shows a general decline in laser output power with emission wavelength. The main reason for this trend is that the laser transitions for longer wavelengths are located high above the ground state. Therefore, the quantum defect (the difference between pump and laser photon energies) generally increases with laser emission wavelength.[37,63] Furthermore, excited states located below the laser transition levels often have long lifetimes and therefore trap ions (causing *bottlenecking*), delaying their return to the ground state. Bottlenecking affects the pump cycle by depleting the

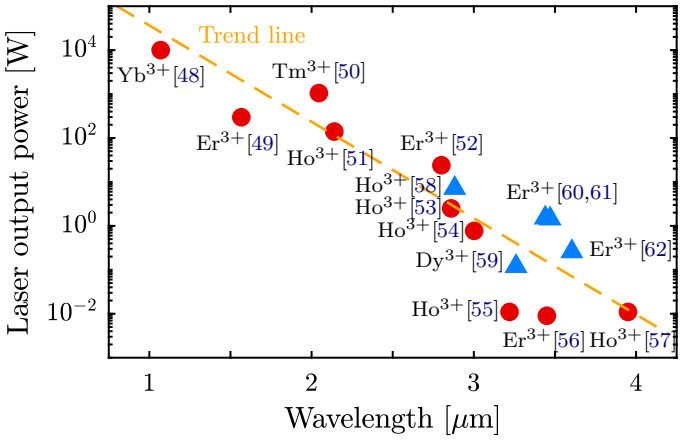

Figure 1.3: Laser output power from published demonstrations of infrared fibre lasers as a function of the emission wavelength. The reduction in output power with increasing emission wavelength is caused primarily by the growing quantum defect. The 3.9 µm emission demonstration required cryogenic cooling.[57] This illustration was adapted from previously reported reviews by Jackson[37] (2012, red circles) and Henderson-Sapir et al.[63] (2017, blue triangles).

ground state and consequently reducing pump absorption.[63]

Dual-wavelength pumping (DWP) was developed for 3.5 µm Er^{3+}-doped ZBLAN fibre lasers to overcome limitations caused by bottlenecking and improve the efficiency of these lasers.[62] Two pump sources, each operating at different wavelengths, are used to excite ions to the upper laser level. The first pump excites ions to a long-lived excited state while the second pump excites ions from that state to the upper laser level. This approach improves laser efficiency, when compared with conventional single-wavelength pumping,[64] by effectively converting a long-lived excited state from a "bottleneck" state to a "virtual ground" state. This demonstration of DWP became an important step forward in the development of 3.5 µm fibre lasers and motivated much of the work presented in this thesis.[60–63,65–67]

In Chapter 3, the processes and performances of DWP 3.5 µm Er^{3+}-doped ZBLAN fibre lasers are studied and modelled, in both the temporal and spatial domains, to advance these systems further.

1.4 Broadband laser sources

Broadband spectroscopy is an invaluable tool for measuring multiple gas-phase species simultaneously in applications such as breath analysis and atmospheric gas sensing. However, there are significant challenges involved with the development of broadband mid-IR sources and detection techniques to provide the necessary resolution and sen-

sitivity.[19] This Section discusses broadband mid-IR laser sources for gas sensing.

1.4.1 Frequency combs

Laser frequency combs are coherent light sources that emit a broad spectrum of discrete, evenly spaced narrow lines. Frequency combs have matured in the visible and near-IR domains, largely motivated by applications in frequency metrology and precision spectroscopy. The generation of mid-IR frequency combs has gained much attention for applications in spectroscopy and gas sensing.[3]

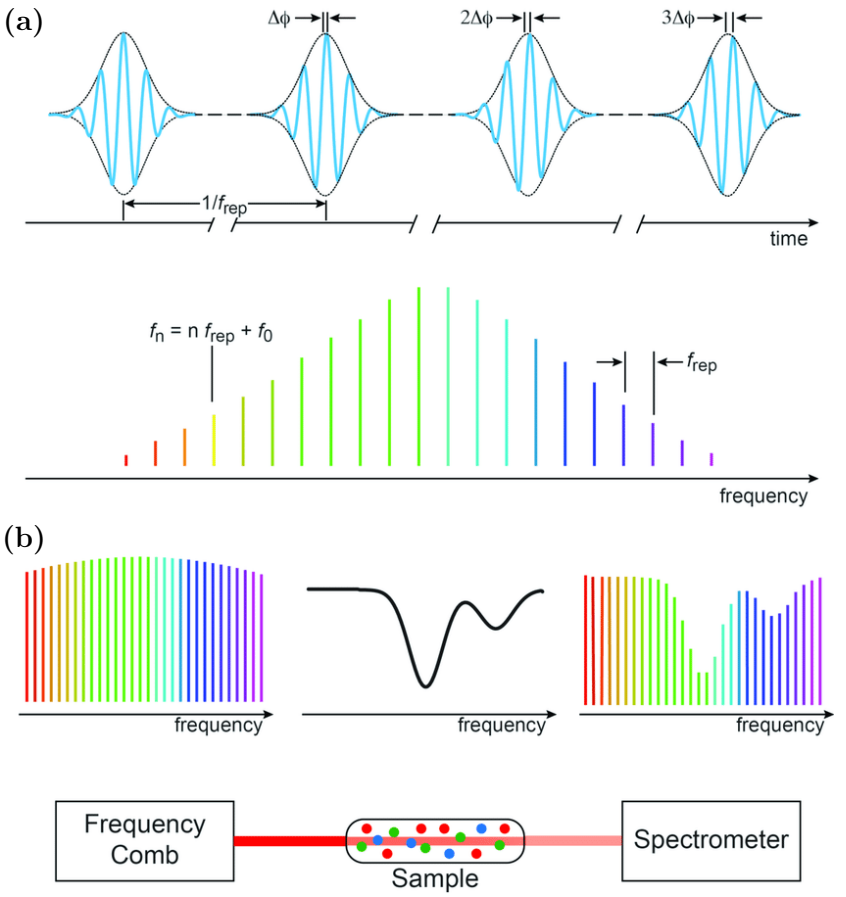

Figure 1.4: Frequency comb principles.[4] **(a)** Time domain (top) and frequency domain (bottom) representations of a pulse train at the output of a mode-locked laser. The spectrum is a *comb* of narrow lines separated by the pulse repetition frequency f_{rep}. The phase shift $\Delta\phi$ of the carrier wave relative to the envelope of the pulses arises due to dispersion inside the laser cavity and induces a translation $f_0 = f_{\mathrm{rep}}\Delta\phi/2\pi$ of all the lines in the spectrum from their harmonic frequencies nf_{rep}. **(b)** A gas sample is interrogated by a broadband frequency comb. The absorption by the gas produces a transmission spectrum formed by discretely spaced lines. This illustration was adapted from Ref. 4.

The fundamental principles of a frequency comb are illustrated in Figure 1.4 (illus-

tration adapted from Ref. 4). The regular pulse train of a mode-locked femtosecond laser can produce a comb spectrum of millions of laser modes with precisely controlled equidistant spacing f_{rep} determined by the inverse of the cavity round-trip time of the laser pulse.[3,31] The carrier-envelope offset (CEO) phase shift per round trip, $\Delta\phi$, arises due to dispersion inside the laser cavity. The rate at which the peak of the carrier frequency 'slips' from the peak of the pulse envelope is the CEO frequency f_0. Stabilisation of the CEO phase is required to overcome random fluctuations, synthesise an optical frequency from a microwave frequency standard, and improve conversion efficiency of nonlinear optical processes by optimising the peak strength and reproducibility of the electric field from pulse to pulse.[68] Recent demonstrations of mode-locked mid-IR fibre lasers[69–71] open new possibilities for compact mid-IR fibre laser combs in the near future.

Mode-locking techniques are introduced in Section 1.5.2, while graphene mode-locked mid-IR lasers are discussed in Section 4.6. The growing demand for mode-locked mid-IR lasers for frequency comb generation motivated the study of graphene presented in Chapters 4, 5, and 6 for mode-locking mid-IR lasers.

1.4.2 Supercontinuum

Mid-IR supercontinuuum generation can be achieved by nonlinear processes when launching ultrashort, high intensity pulses into soft glass fibres (such as fluoride and chalcogenide fibres).[72] Some of these broadband sources can span more than 10 µm of the molecular fingerprint region, covering entire transmission windows of the atmosphere.[73,74] The most common pump sources for mid-IR supercontinua to date have been free-space systems based on parametric conversion.[75] However, recent demonstrations toward all-fibre designs show potential for robust mid-IR supercontinuum sources for field-deployable instruments in the future.[75–78]

1.4.3 Tunable fibre lasers

Broadly tunable mid-IR laser emission was demonstrated in 2016 using a dual-wavelength pumped Er^{3+}-doped ZBLAN fibre laser.[61] The laser emission had a tuning range of 450 nm (the widest tuning range of any rare earth doped laser demonstrated at the time) centred at 3.5 µm. An output power of 1.45 W was achieved at a wavelength of 3.47 µm. The tunability was performed by using the zero order of a diffraction grating as the output coupler.[61]

Wavelength-swept lasers have matured in the near-IR, largely driven by optical coherence tomography (a technique commonly used for medical imaging).[79] These tunable

laser sources are *swept* rapidly and periodically over a broad spectral range, incrementing the radiation wavelength multiple times within each *sweep*. However, extending this concept to the mid-IR is complicated by limited availability of appropriate gain media.[80] The first mid-IR wavelength-swept laser was demonstrated in 2019 using a Dy^{3+}-doped ZBLAN fibre gain medium pumped by a 2.8 µm Er^{3+}-doped ZBLAN fibre pump source.[80] Wavelength-swept tunability from 2.89 µm to 3.25 µm was performed electronically using an acousto-optic tunable filter and output powers exceeding 100 mW were achieved. This progress creates new opportunities for real-time gas sensing using compact mid-IR fibre laser sources.

1.5 Short pulse generation

This Section introduces Q-switching and mode-locking principles which are techniques used to emit short laser pulses.

1.5.1 Q-switching

Q-switching is a technique that generates a laser pulse by switching the quality factor (Q factor) of a laser resonator. Quality factor Q is defined as the ratio of the energy stored in the cavity to the energy loss per cycle.[81] To achieve a laser pulse, the laser is held in a low Q state that prevents lasing while a large population is established in the upper laser level. The cavity Q is then switched to a high Q state, meaning lasing conditions are well above threshold. A pulse rapidly develops, extracting the energy stored in the gain medium. Pulse durations achieved by Q-switching are typically in the nanosecond regime (refer to modelled Q-switched pulses presented in Figures 3.20 and 3.22).

Q-switching may be achieved (i) *actively* with an acousto-optic modulator (AOM), electro-optic modulator (EOM), or liquid crystal modulator (LCM); or (ii) *passively* with a saturable absorber such as a semiconductor saturable absorber mirrors (SESAM) or graphene. The concept of saturable absorption in graphene is explained in Section 4.5.1 while experimental observations of saturable absorption in graphene are presented in Chapters 5 and 6.

Q-switched fibre lasers in the 3.5 µm wavelength band have been demonstrated recently. A passively Q-switched 3.46 µm DWP Er^{3+}-doped ZBLAN fibre laser was recently achieved by focussing the laser beam onto a gold mirror coated with black phosphorous flakes.[82] A pulse energy of 1.8 µJ and pulse width of 2.05 µs was achieved at 66.3 kHz repetition rate. The black phosphorus saturable absorber was also used to demonstrate passive mode-locking at 3.49 µm. An actively Q-switched 3.47 µm DWP

Er^{3+}-doped ZBLAN fibre laser was recently achieved by implementation of an AOM.[67] A pulse energy of 7.8 µJ and pulse width of 538 ns was achieved at 15 kHz repetition rate. The Q-switching behaviour of this laser is modelled and studied in Section 3.5.

Dual-wavelength Q-switched fibre lasers have also been demonstrated for DIAL applications that require synchronous emission of online and offline pulses (as described in Sections 1.2.1 and 2.2). Dual-wavelength Q-switching in the 1550 nm wavelength band has been achieved using both active[83] and passive[84] Q-switching techniques. Sharma et al.[83] achieved 10 µJ pulse energy and 5 µs pulse duration at 20 kHz repetition rate while Wang et al.[84] achieved 70 nJ pulse energy and 8 µs pulse duration at 22 kHz repetition rate using graphene as a saturable absorber.

Chapter 2 presents a DIAL feasibility study for the remote detection of diesel exhaust gases in the atmosphere. The study shows that there are several gases that could potentially be targeted in the 2 µm – 4 µm wavelength band using DIAL technology. The majority of the work presented in this thesis is relevant for advancing dual-wavelength Q-switched fibre lasers into the mid-IR domain.

1.5.2 Mode-locking

Mode-locking is a technique that produces a periodic train of ultrafast (typically picosecond to femtosecond) laser pulses. This technique phase-locks the longitudinal modes of the laser, either actively (e.g. with an AOM or EOM) or passively (with a saturable absorber such as a SESAM or graphene), to generate a pulse train. Passive mode-locking can also be achieved using *artificial* saturable absorber techniques such as Kerr lensing and nonlinear polarisation rotation. The pulse width is inversely related to the bandwidth of the laser emission.[81]

Passive mode-locking can achieve pulses as short as a few femtoseconds while active mode-locking typically produces longer ($\sim$ 100 ps) pulses.[85] The CW and low intensity pulse components are more heavily attenuated by the saturable absorber than the high intensity pulse components which saturate the absorber. Therefore, short pulse generation is favoured while CW radiation is suppressed.[85,86]

Graphene has been used extensively as a saturable absorber to passively mode-lock near-IR lasers.[70,87–95] Compared to traditional SESAMs and single-walled carbon nanotubes, graphene has an extremely broad wavelength response, a high modulation depth, and low saturation intensity.[87] Graphene mode-locked lasers are discussed further in Section 4.6.

Graphene has unique properties which, when combined with the growing demand for ultrafast mid-IR lasers, motivated the research presented in Chapters 4, 5, and 6. These Chapters present a theoretical and experimental study of graphene to assess its

potential as a mode-locking element for mid-IR lasers.

1.6 Scope of this thesis

This thesis is structured as follows:

Chapter 2 presents a feasibility study for the potential use of DIAL technology to measure the concentrations of diesel exhaust gases in the atmosphere from an airborne platform. The development of DIAL technology to detect these gases would enable remote identification of major exhaust emitters, over almost any region of interest, for air pollution monitoring and control. This study investigates the strong absorption lines of these gases which are accessible within the transparent windows of the atmosphere. Exhaust plumes are also studied to investigate the detectability of gases emitted by a single point source. The lidar sensitivity is estimated for the most detectable target gases and compared with background concentrations in the atmosphere. This technology could be developed to identify and monitor major sources of air pollution at any location accessible by an aircraft. This research shows that there is a potential to detect at least three exhaust constituents using DIAL technology. These gases are carbon monoxide (CO) in the 2.3 µm wavelength band, and nitrogen dioxide (NO_2) and formaldehyde (H_2CO) in the 3.5 µm wavelength band.

In Chapter 3, a numerical model is presented that simulates the physical processes in 3.5 µm dual-wavelength pumped fibre lasers. The published article "Numerical modeling of 3.5 µm dual-wavelength pumped erbium-doped mid-infrared fiber lasers" is presented within Chapter 3. The model, validated against three experiments reported in literature, provides time-domain analysis of ionic energy state populations, predicts laser performance, and has become a valuable tool for the optimisation of fibre laser design. The model was also adapted to study Q-switching behaviour of these lasers with high temporal resolution.

Chapters 4, 5, and 6, present a theoretical and experimental study of graphene to assess its suitability as a passive mode-locking element for mid-IR lasers. Chapter 4 introduces the properties of graphene that motivated the study of this unique 2D material. Chapter 5 presents details of the experiment performed to measure the response of graphene to high intensity radiation. Intensity dependent transmission measurements were performed on trilayer graphene in the spectral region between 1.55 µm and 3.5 µm using a 100 fs laser source and the z-scan technique.

The results of the intensity dependent transmission measurements are presented in Chapter 6 and show that multilayer graphene exhibits two-photon absorption as well as saturable absorption when subjected to high intensity radiation. Two-photon

absorption limits the effective modulation depth of the saturable absorber which can be detrimental to mode-locking mid-IR ultrafast lasers. The published article "Two-photon absorption and saturable absorption of mid-IR in graphene" is presented within Chapter 6. The saturation intensities, measured at six wavelengths, are compared with other reported measurements and are found to fall into two regimes of pulse duration. Two empirical relationships between saturation intensity and photon energy are proposed – one for each pulse duration regime.

Finally, the conclusions of this work and possible future directions are presented in Chapter 7.

Chapter 2
DIAL for Diesel Exhaust Detection

This Chapter presents a feasibility study for the use of differential absorption lidar (DIAL) technology to detect diesel exhaust gases remotely from an airborne platform. Diesel engine exhaust is a known carcinogen.[96] The development of DIAL technology to detect these gases would enable remote identification of major exhaust emitters, over almost any region of interest, for air pollution monitoring and control. Spectral absorption of diesel exhaust constituents are modelled to investigate the potential use of DIAL to detect these gases. This research shows that there is a potential to detect at least three exhaust constituents using DIAL technology. These gases are carbon monoxide (CO) in the 2.3 µm wavelength band, and nitrogen dioxide (NO_2) and formaldehyde (H_2CO) in the 3.5 µm wavelength band.

2.1 Background

Diesel engines have extensive usage compared to petrol engines due to their high energy efficiency, durability, and reliability as well as low operating cost. Diesel engines power most commercial transport vehicles such as trucks, buses, trains, and ships as well as off-road industrial vehicles such as excavation machinery and mining equipment. However, diesel engines are considered to be one of the largest contributors to environmental pollution caused by exhaust emissions.[97]

The primary pollutants from internal combustion engines are nitrogen oxides (NO_x), carbon monoxide (CO), sulfur oxides (SO_x), volatile organic compounds (VOC), and particulate matter (PM). Carbon dioxide (CO_2), a greenhouse gas widely attributed to cause anthropogenic global warming, is one of the major exhaust constituents of internal combustion engines. Most of the NO_x is emitted as nitric oxide (NO) which is gradually converted to nitrogen dioxide (NO_2) by reactions with ozone (O_3) in the atmosphere. The SO_x content in exhaust is determined by the sulfur content in the fuel. VOCs include formaldehyde (H_2CO) and benzene (C_6H_6).

The release rate of each pollutant can be estimated from *emission factors* such as those reported by the United States Environmental Protection Agency and the Australian Government Department of Environment and Energy.[98,99] An emission factor relates the quantity (such as mass) of a pollutant released to the atmosphere with an activity (such as distance travelled by a vehicle or the energy output from an engine) associated with its release. Emission factors are often averaged over available data and therefore represent long-term emission averages. However, emission load estimates can vary widely between engines designed for different uses, such as garden equipment and commercial marine, due to variations in fuel content, engine combustion efficiency, and control measures.[100]

Vehicle manufacturers have tried for decades to reduce pollutant emissions to meet increasingly stringent emission standards. Their research has focussed on engine modifications, electronic controlled fuel injection systems, and fuel improvement.[97] However, these measures have not been completely successful, and vehicles are equipped with aftertreatment (post combustion) emission control systems to meet the actual emissions standards. Studies for emission control systems have focussed on reduction of NO_x emissions because NO_x content in diesel exhaust has the highest percentage among the pollutant emissions.[97]

The sulfur content in diesel fuel varies around the globe as global standards shift toward low (<500 ppm) and ultra-low (<15 ppm) sulfur diesel fuels. The global status of sulfur levels in diesel fuels as at August 2008 and March 2017 were reported by the United Nations Environment Programme (UNEP) and are shown in Appendix A, Figures A.18 and A.19. A comparison of the two figures shows a general global trend to reduce sulfur content in diesel fuel to prevent harmful effects of SO_2.

Shipping contributes to coastal emissions that are subsequently transported over land. Maritime transport is one of the leading sources of air pollution in ports and coastal cities.[101–103] This mainly results from the berthing (hotelling), manoeuvring, and cruising operative modes of vessels while at port.[104,105] The power usage depends on the operating mode. Cruise ships particularly stand out as air pollutants in ports because of their large demands for electrical power.[103,106]

Global NO_x and SO_x emissions from all shipping represent about 15 % and 13 % of global NO_x and SO_x from anthropogenic sources respectively.[107,108] The International Convention for the Prevention of Pollution from Ships (MARPOL) is the main international convention for addressing pollution sourced from ships. MARPOL Annex VI limits the main air pollutants contained in ship exhaust, including NO_x, SO_x, and particulate matter. It also introduces emission control areas to reduce emissions of those air pollutants further in designated sea areas. From 1 January 2020, for example, the

allowed concentration of sulfur in marine fuel used outside emission control areas will drop from 3.5 % to 0.5 % (m/m).

Enforcement of MARPOL regulations on fuel content are limited by the ability to detect violations. A study by the International Transport Forum (ITF) and the Organisation for Economic Co-operation and Development (OECD) noted that 'bunker fuel delivery notes are notoriously subject to irregularities and fraud' and stressed the limitations of sampling in the ports with respect to potential violations which may have taken place before the vessel entered the port.[109] Ships that navigate both inside and outside emission control areas may carry different types of fuel, making it difficult for port officers to detect potential violations. Ocean going vessels, for example, primarily use a low quality fuel (residual oil) that has a relatively high sulfur content.[105]

The International Agency for Research on Cancer (France) has classified diesel engine exhaust as a Group 1 carcinogen – "carcinogenic to humans".[96] The concentration of exhaust in the air will vary within any geographic area depending on the number and types of diesel engines and the atmospheric patterns of dispersal. Certain occupational populations (such as transportation workers, garage workers, and heavy-equipment operators) can be exposed to much higher levels of diesel exhaust than the general population.[110] In Australia, diesel engine exhaust is the second most common carcinogenic agent that workers are exposed to, preceded only by solar ultraviolet radiation.[111] The occupational groups exposed included farmers, heavy vehicle drivers, miners, and metal workers.

Diesel exhaust plumes contain constituents that are potentially detectable by an airborne DIAL system from hundreds of metres away. DIAL remotely measures the concentration of target gases using a tuned laser source and detection system. Previously demonstrated applications include the remote sensing of methane (CH_4)[112,113] and carbon dioxide (CO_2).[114] A DIAL system that is broadly tunable can potentially detect two or three molecular species of interest.[115] A critical component of a DIAL system is the laser emitter. Whilst the lasers required are not readily available, they could become available within 3 to 5 years using expertise that currently exist. One group at The University of Adelaide, for example, has been developing Q-switched lasers for the remote detection of methane gas using DIAL technology. The proprietary techniques that were developed for detecting methane could be easily transferable to the 3.5 µm band using existing technology.

2.2 Introduction

DIAL is a fast and effective technique used to measure concentrations of gases in the atmosphere with the potential to detect diesel exhaust gases. DIAL is a form of lidar (light detection and ranging) in which pairs of pulses, separated by a short time interval, are emitted. The wavelength of one of the pulse pair is tuned to a gas absorption line and the second pulse is close in wavelength but not absorbed by the gas. The role of this second path is to calibrate the non-gas induced losses of the laser path. This allows the path length integrated concentration of the target gas to be determined.

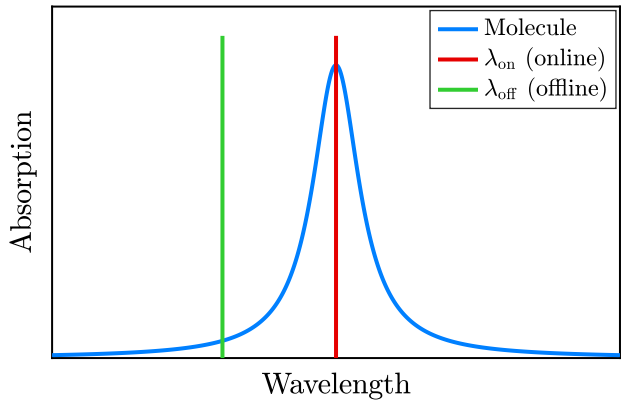

Figure 2.1: Wavelengths of DIAL pulses relative to the molecular absorption line of a target gas.

The DIAL technique relies on a minimum of two laser wavelengths, λ_{on} (online) and λ_{off} (offline). Figure 2.1 illustrates the wavelengths of online and offline pulses relative to a molecular absorption line of a target gas. Wavelength λ_{on} is tuned to an absorption line of the molecular species of interest, while λ_{off} lies just off this line.[116] The laser source emits pairs of pulses, one at each wavelength, through the atmosphere. The online and offline pulses are separated by a short time interval (typically between 1 µs and 5 ms) so that their propagation paths are closely matched. The pulses scatter from atmospheric constituents or a topographical scatterer and a small fraction of the pulse energies are backscattered toward a detector co-located with the laser source.

The online and offline pulses are spectrally separated by a small wavelength difference (< 1 nm). Therefore, the cross sections for aerosol scattering are nearly identical for each pulse. However, the online pulse is strongly absorbed by the gas of interest whereas the offline pulse is not. Therefore, the difference in power of the return signals is due to absorption of the target gas. The two laser wavelengths must be carefully chosen to prevent interference from other atmospheric molecule absorption lines, minimise

temperature dependence, and optimise optical depth.[12]

In the case of airborne DIAL, the laser source and detection system are mounted on an aircraft. The airborne DIAL technique can measure large areas efficiently with high spatial (horizontal) resolution. A considerable improvement in sensitivity can be achieved if the DIAL technique is used in conjunction with a topographical scatterer (such as the ocean surface used throughout this analysis). However, this gain in sensitivity is achieved at the expense of range resolution.[116] Therefore, the difference in power of pulse pairs that are reflected from the Earth surface can only measure the concentration *integrated* over the path length. The strength of the lidar signal is proportional to

$$\int_0^L C_{\text{species}}\sigma_{\text{species}}\mathrm{d}l \approx \bar{C}_{\text{species}}\sigma_{\text{species}}L \tag{2.1}$$

where C_{species} is the spatially dependent molecular concentration ($\text{molec}\,\text{m}^{-3}$), σ_{species} is the absorption cross section, $\bar{C}_{\text{species}}$ is the spatially averaged concentration, and L is the measurement path length. Both $\bar{C}_{\text{species}}$ and L can be evaluated with a knowledge of the emission rate and the plume propagation rate. Lidar sensitivity is defined by the minimum detectable concentration length.

The performance of a lidar in detecting a chemical species may be characterised by several properties, including the following:

i. Laser wavelength: The online laser radiation needs to be absorbed by the target molecule while the offline radiation must have a much lower absorption. The radiation at both wavelengths must have high transmission through the atmosphere. The offline scattering and absorption properties must be as close as possible to those of the online if the target molecule were removed.

ii. Sensitivity: The minimum detectable concentration length defines the lidar sensitivity. That is, the minimum concentration that is detectable over a distance of 1 m. For example, 1 ppm m.

iii. Range: The maximum distance from the source and receiver to the target that produces a detection.

iv. Surveillance speed: The speed at which an area defined by the Earth surface is surveyed. The surveillance speed is determined by the pulse repetition rate, speed of the aircraft, and the area covered by the flight path. For example, $100\,\text{km}^2\,\text{hr}^{-1}$.

The aim of this work was to assess the detectability of diesel exhaust gas emissions using DIAL technology. A feasibility study is performed that assesses the potential use of DIAL to detect these trace gases remotely from an airborne platform so that large areas may be scanned and mapped quickly. A complete feasibility study would be

complicated due to numerous possible target gases, topographical scatterers, ambient atmospheres, and types of air pollution sources that can be classified as point, line, or area sources. This work assesses a DIAL application in which the laser emitter and receiver are mounted on an airborne platform and the return signal is scattered by an ocean surface. The choice of an ocean surface is a conservative approach, since the reflectance of an ocean surface is lower than most other surface scatterers and, therefore, the laser power reflected from an ocean surface back toward the detector is likely to be lower than the power reflected from urban and regional topographical scatterers.[117] This research has potential applications in monitoring air pollution over large areas (such as coastal regions and shipping ports) and detecting violations of diesel fuel regulations from point sources (such as ocean going vessels and cruise ships).

The approach taken to assess the detectability of diesel exhaust throughout this Chapter may be summarised as follows:

i. Determine the emission rates of exhaust constituents from a diesel engine;

ii. Estimate the concentration of exhaust constituents in the background atmosphere and downwind from an emitting source;

iii. Perform spectral analysis of diesel exhaust molecules and identify absorption features within transmission windows of the background atmosphere;

iv. Model the propagation of DIAL pulses emitted from an airborne platform;

v. Estimate SNR over a broad spectral region for the possible detection of multiple gases;

vi. Model the absorption of the most detectable gases;

vii. Estimate the lidar sensitivities for detection of four target gases and compare with the background concentrations of those gases;

This preliminary analysis of diesel exhaust identified several constituents that had a combination of emission rate and absorption cross section that was high enough for detection using light emitted within the transmission windows of the atmosphere. Two of these gases, NO_2 and H_2CO, have strong absorption lines in the 3.5 µm wavelength band where the atmosphere is highly transparent. Other potential targets include carbon monoxide (CO), propylene (C_3H_6), and sulfur dioxide (SO_2) in the wavelength bands 2.33 µm, 3.39 µm, and 3.98 µm respectively.

This Chapter compares the flow rates of exhaust constituents emitted from a diesel engine against the atmospheric background concentrations of those gases in Section 2.3. A plume study is presented for the estimation of exhaust gas concentrations downwind from a point source. In Section 2.4, the absorption lines of diesel exhaust molecules,

which were available from the HITRAN2016 database,[9] are presented. The absorption lines which are accessible within transparent spectral regions of the atmosphere are identified. The propagation of a laser pulse emitted from an airborne platform is modelled in Section 2.5. The pulse is backscattered from an ocean surface and enters a telescope receiver that is co-located with the laser emitter. In Section 2.6, expressions for the target gas concentration, estimated from the returned pair of DIAL pulses that enter the telescope receiver, are presented, followed by an expression for the DIAL sensitivity. An SNR assessment for a single pulse is presented in Section 2.7 to determine the spectral region with the highest SNR. The gases which are characterised by strong absorption lines within spectral regions that have high SNR and high transparency in the background atmosphere are assessed in Section 2.8. The lidar sensitivity is calculated for the most detectable gases and compared with background concentrations and regulation guidelines in Section 2.9. Finally, conclusions are presented in Section 2.10.

2.3 Concentrations of exhaust constituents

In this Section, the flow rates of exhaust constituents emitted from a single diesel engine are estimated using reported emission factors. Then the downwind concentration of each constituent is estimated by assuming a Gaussian air pollution dispersion.

2.3.1 Flow rates

The "Compilation of Air Pollutant Emissions Factors" report provided by the United States Environmental Protection Agency[98] lists diesel exhaust constituents and their emission factors. The information provided in the report was used to estimate the flow rates of each air exhaust constituent for large stationary diesel engines. The flow rates of exhaust constituents emitted from an engine operating at a power load of 1000 kW were calculated from the listed emission factors. This 1000 kW power load is low when compared with 97,020 kW of engine power (total of six medium-speed engines) installed on Ocean-class cruise ships.[118] The results, however, are presented in such a way that they can be readily scaled to any diesel engine, or multiple thereof, once the gas emission rates are known. The emission factor of NO_x was provided by the United States Environmental Protection Agency[98] for the cases of controlled and uncontrolled engines. A NO_x controlled engine and ultra low sulfur diesel fuel (ULSDF) were assumed throughout the following analysis.

The mass flow rates $F_{\mathrm{m}i}$ of each constituent i are given by

$$F_{\mathrm{m}i}\left(\mathrm{g\,s^{-1}}\right) = X_i\left(\mathrm{g\,J^{-1}}\right) P_{\mathrm{E}}\left(\mathrm{W}\right) \tag{2.2}$$

where X_i are the emission factors and P_{E} is the engine power load. The molecular flow rates F_i of each constituent i, in units of molecules per second ($\mathrm{molec\,s^{-1}}$), are given by

$$F_i\left(\mathrm{molec\,s^{-1}}\right) = \frac{F_{\mathrm{m}i}\left(\mathrm{g\,s^{-1}}\right) N_{\mathrm{A}}\left(\mathrm{mol^{-1}}\right)}{M_i\left(\mathrm{g\,mol^{-1}}\right)} \tag{2.3}$$

where N_{A} is the Avogadro constant (number of molecules per mole) and M_i are molecular weights sourced from the online database PubChem.

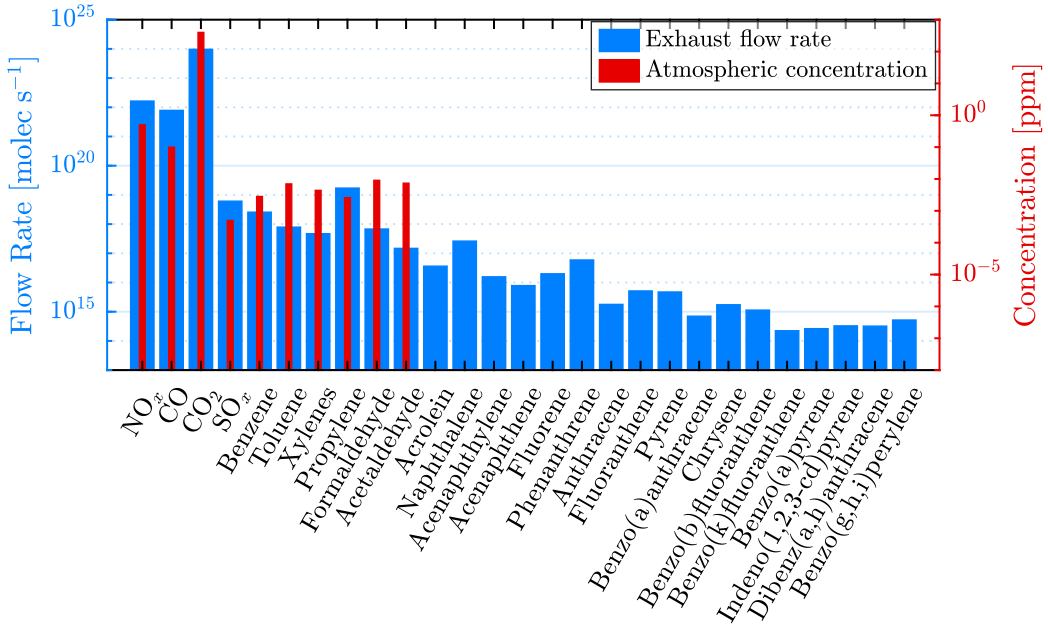

Figure 2.2: Flow rates of diesel exhaust molecules upon release into the atmosphere (left axis) compared with background concentrations (right axis). Flow rates were calculated for an engine load of 1000 kW from emission factors provided by Ref. 98. Atmospheric concentrations were estimated for a typical urban environment from Ref. 119.

The calculated flow rates F_i of air exhaust constituents are illustrated in Figure 2.2. The total exhaust flow rate was assumed to be $2.0\,\mathrm{kg\,s^{-1}}$, estimated from specifications for the Wärtsilä 20 range of diesel engines for an engine load of 1000 kW. The flow rates are compared with background concentrations in a typical urban atmosphere.[119] Note that background concentrations of NO_x vary widely between remote marine ($0.02-0.04$ ppb) and urban ($10-1000$ ppb) atmospheres. A NO_x background

concentration of 500 ppb was assumed for this analysis. The breakdown of NO_x (NO and NO_2) emissions are discussed in Section 2.8.2 and Appendix A.3.1. In regard to SO_x, both the background concentration and fuel content can vary considerably. Background SO_2 levels range from 20 ppt in a remote marine atmosphere to >1 ppb in continental air. A SO_2 background concentration of 500 ppt and a fuel concentration of 15 ppm (ULSDF) were assumed for this analysis. Note that MARPOL Annex VI restrictions on sulfur content in marine diesel fuel, effective from 1 January 2020, allow 0.5 % (m/m) sulfur content outside emission control areas, which is more than 300 times higher than the sulfur content in ULSDF.

Further plume modelling is required to predict how the discharged exhaust concentration changes in time and space due to temperature, wind, buoyancy, dispersion, and diffusion.

2.3.2 Plume dispersion

Once exhaust is emitted into the air, it will begin to disperse and be transported with the prevailing wind. Dispersion of a gas plume subjected to wind can be visualised using the Gaussian dispersion model illustrated in Figure 2.3. The gas concentration in the plane that is transverse to the plume centreline is assumed to have a Gaussian profile.

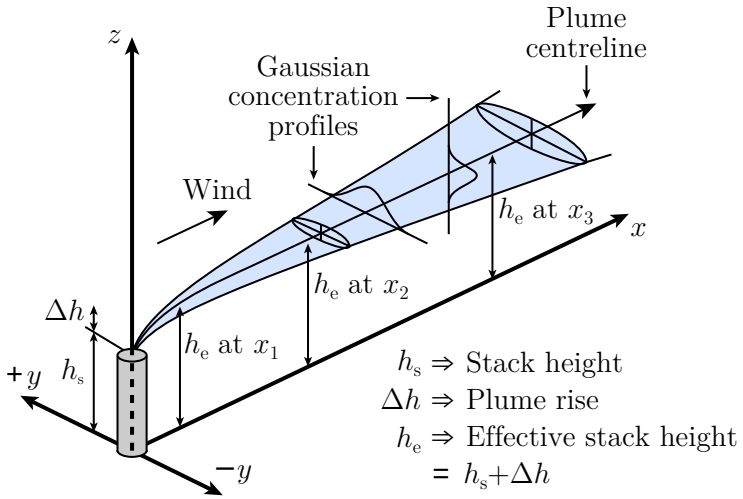

Figure 2.3: Gaussian air pollution dispersion model. The plume, emitted from an exhaust stack, is buoyant since it is warmer and less dense than the ambient air. The concentrations of air pollutants are assumed to have a Gaussian distribution. This illustration was adapted from Ref. 120.

The factors which affect the dispersion of a plume include the following:

i. Stability of the atmosphere, i.e., temperature of the Earth surface relative to the

air above it;

ii. Relative buoyancy of the emitted exhaust constituents;

iii. Wind velocity and turbulence of the flow;

iv. Velocity of the emitting source.

The dispersion of an exhaust plume downwind from the source can be estimated for various levels of atmospheric stability, classified by Pasquill [121]. The standard deviations of dispersion as a function of distance from the source were reported by Hanna et al. [122]. At 1 km downwind, the standard deviations in the horizontal extent vary between 33 m in a stable atmosphere and 200 m in a very unstable atmosphere. In the vertical extent, standard deviations vary between 13 m and 500 m for the same atmospheric conditions respectively. The large range of values in the vertical extent is not significant for vertically downward pointing lidar, since this lidar measures the plume concentration multiplied by the plume height. The concentrations of exhaust gases used in this analysis were calculated for the case of a slightly unstable atmosphere at a distance 1 km downwind from the source. The horizontal and vertical standard deviations were 100 m and 60 m respectively.

2.3.3 Plume concentrations

The concentrations C_i of each exhaust constituent i are estimated for an exhaust plume 1 km downwind from the source. The ideal gas law $N = \frac{P_{\text{atm}}V}{k_{\text{B}}T_{\text{K}}}$ is used to estimate the total number of molecules N in a volume V defined by the cross sectional area A_{p} of the plume and an average ocean wind speed $\bar{u}$ over a time period of 1 s. Then the molecular fraction of constituent i is the molecular flow rate F_i divided by the total number of molecules N in a plume volume extended over 1 s. Multiplying by 10^6 gives a concentration C_i in units of ppm.

$$C_i = \frac{F_i}{N}10^6 = \frac{F_i}{A_{\text{p}}\bar{u}}\frac{k_{\text{B}}T_{\text{K}}}{P_{\text{atm}}}10^6 \tag{2.4}$$

The quantities used to calculate the plume concentrations C_i of exhaust constituents i for any given flow rate F_i were approximated as follows:

i. Cross sectional plume area $A_{\text{p}} = 100{\times}60 = 6000\,\text{m}^2$ 1 km downwind; [122]

ii. Average ocean wind speed $\bar{u} = 6.64\,\text{m}\,\text{s}^{-1}$ (12.9 kn); [123]

iii. Boltzmann constant $k_{\text{B}} = 1.38{\times}10^{-23}\,\text{m}^2\,\text{kg}\,\text{s}^{-2}\,\text{K}^{-1}$;

iv. Temperature $T_{\text{K}} = 288\,\text{K}$;

v. Atmospheric pressure $P_{\text{atm}} = 101,325\,\text{Pa}$ (standard atmosphere).

2.4 Spectral analysis

In this Section, the absorption spectra of various diesel exhaust gases are presented. The spectral regions that contain strong absorption lines and are accessible within transparent windows of the atmosphere are identified. The highest absorption peak within any given spectrum is associated with the fundamental excitation (from the ground to the first excited state).[5] In some cases, less intense overtone bands are observed at shorter wavelengths due to excitations from the ground state to the higher excited states. The photon energies of these overtones are approximate integer multiples of the fundamental photon energy. The spectral response of commercially available detectors is also discussed.

2.4.1 Molecular species

The spectral line intensities S of various molecules that exist in diesel exhaust are illustrated in Figure 2.4. The data was sourced and adapted from the HITRAN2016 database.[9] The molecules included in this illustration are the only diesel exhaust molecules listed in the HITRAN2016 database.

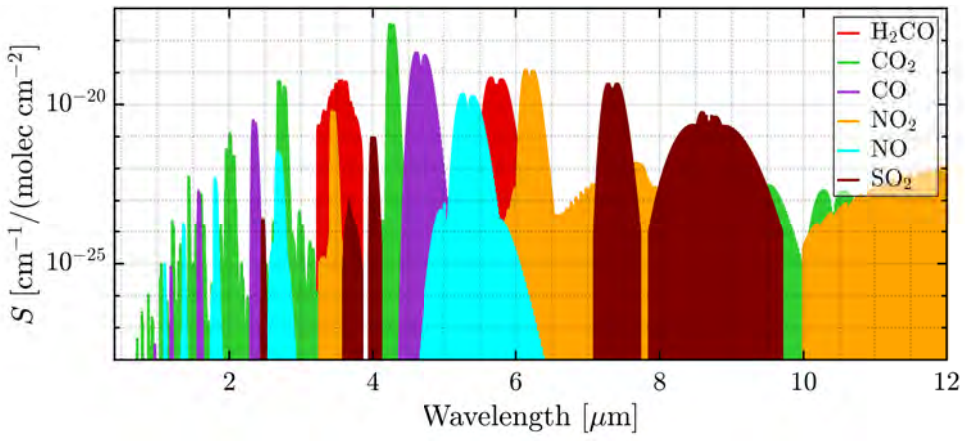

Figure 2.4: Spectral line intensities S of various diesel exhaust molecules. The data was sourced from the HITRAN2016 database.[9] The units for line intensity may be thought of as wavenumbers per unit column density. Higher peaks indicate stronger absorption.

Spectral line intensities S are defined in units of $\text{cm}^{-1}/\,(\text{molec}\,\text{cm}^{-2})$ for single molecules, per unit volume, at a temperature of 296 K. The units for line intensity may

be thought of as wavenumbers per unit column density. Absorption cross section σ is related to spectral line intensity S by the following formula:[12]

$$\sigma = \frac{S}{\pi} \frac{\gamma_L}{(\tilde{\nu} - \tilde{\nu}_0)^2 + \gamma_L^2} \tag{2.5}$$

where the spectral line shape is assumed to be Lorentzian, γ_L [cm^{-1}] is the Lorentzian half-width at half-maximum, $\tilde{\nu}$ is the wavenumber [cm^{-1}], and $\tilde{\nu}_0$ is the wavenumber at line centre.

Absorption spectra of diesel exhaust constituents were sourced from the National Institute of Standards and Technology (NIST) Chemistry WebBook for all exhaust molecules available. However, the concentrations used to obtain the NIST data are unknown and the absorption spectra are suitable for identification only, not quantification. Therefore, the data were normalised to the highest peak within each spectrum. For some spectra, the highest peak was located at a wavelength greater than 12 µm. The absorption spectra produced from NIST data are presented in Appendix A.1.3.

Some spectral regions of radiation are strongly absorbed by the atmosphere. A lidar must be designed to operate in a wavelength band located within a transmission window of the atmosphere. The molecular species within the troposphere that absorb most of the light within spectral regions of interest are H_2O, CO_2, and CH_4. In order to perform any laser monitoring of the atmosphere, it is necessary to have quantitative information on absorption coefficients in the atmospheric window located close to the wavelength of laser radiation, as well as information on absorption due to nearby spectral lines of atmospheric gases.[124]

The atmospheric absorption A_{atm} of radiation was modelled for a DIAL application and is presented in Figure 2.5. The absorption was modelled using the spectral tool SpectralCalc which sourced spectral data from the HITRAN2016 database. The absorption was modelled for the case when radiation propagates twice through a vertical column of atmosphere as in the case of a laser pulse that is vertically emitted from, and backscattered to, an airborne platform. The model atmosphere selected was US_Standard comprising all isotopologues of H_2O, CO_2, O_3, N_2O, CO, and CH_4. The transmittance was firstly modelled by setting observer height, target height, and Nadir angle (i.e. angle from the vertically downward pointing direction) to 0.5 km, 0 km, and 0 degrees respectively. The transmittance was then squared and subtracted from 1 to predict the atmospheric absorption A_{atm} of a return pulse that propagates over a total path length of 1 km. The model shows the broad spectral regions where the atmosphere is either opaque (high absorption) or transparent (low absorption).

The HITRAN spectral line intensities S of various diesel exhaust molecules is over-

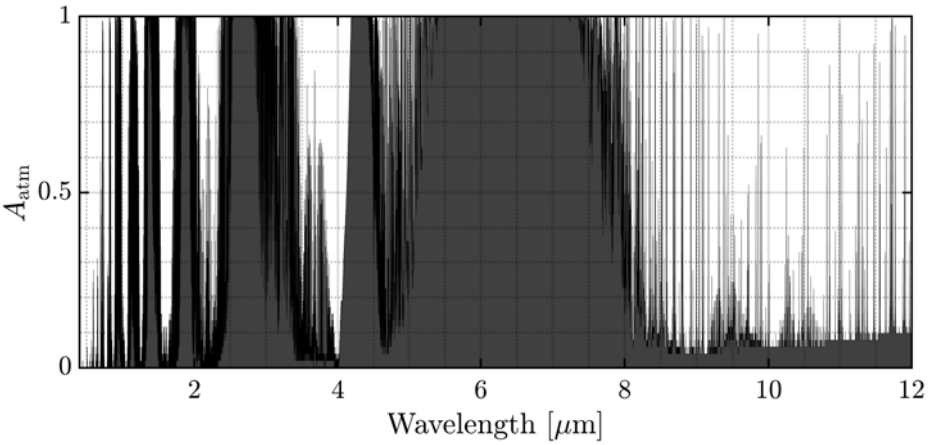

Figure 2.5: Atmospheric absorption A_{atm} modelled using SpectralCalc and the HITRAN2016 database. Absorption is denoted by the black line and the area under the absorption is shaded grey. Areas that appear black represent closely spaced absorption lines. The absorption was modelled for a return pulse from an altitude of 500 m, i.e. a total path length of 1 km.

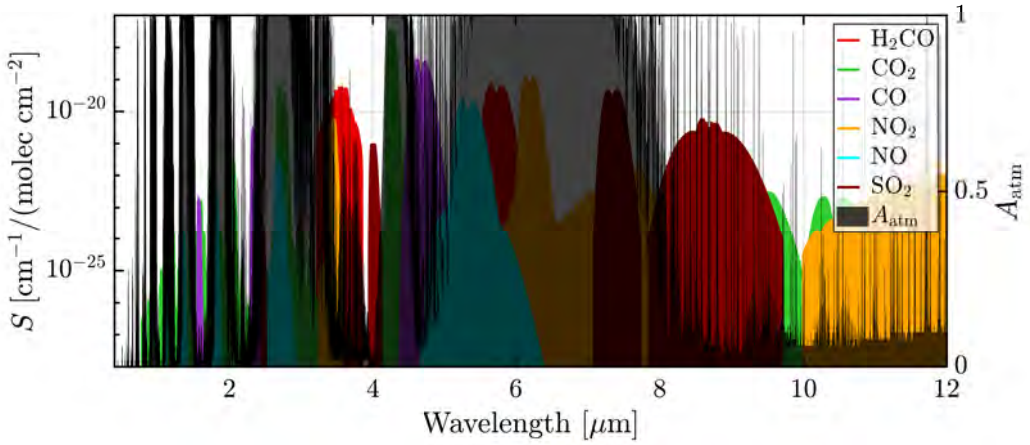

Figure 2.6: The spectral line intensities S of various diesel exhaust molecules (left axis) with atmospheric absorption A_{atm} (right axis) overplotted. The spectral regions where atmospheric absorption is low indicate which spectral lines are accessible within the transparent windows of the atmosphere.

layed with the modelled atmospheric absorption spectrum A_{atm} in Figure 2.6 to broadly illustrate where line intensity peaks coincide with atmospheric windows. These atmospheric windows will be analysed with higher resolution in Section 2.8. The spectral line intensities were obtained from HITRAN2016 data and can be observed more closely in Appendix A.1.1 where the broad spectral region between 1.0 µm and 5.0 µm is divided into eight equal (500 nm) regions with higher resolution. Although the atmosphere is transparent above 8.0 µm, this spectral region is excluded from the higher resolution analysis due to limitations in detector sensitivity at longer wavelengths. The depen-

dence of wavelength on detector sensitivity is explained in Section 2.4.2.

The HITRAN2016 database also contains the absorption cross sections of acetaldehyde and acrolein. The flow rates of acetaldehyde and acrolein exhaust gases are low when compared with the flow rates of the exhaust gases listed in the HITRAN2016 line intensity database. Propylene, however, has a flow rate higher than SO_x and formaldehyde (H_2CO). The absorption cross sections of propylene, acetaldehyde, and acrolein are shown in Figure A.9. The propylene cross sections were provided by Es-Sebbar et al.[125]. These gases have absorption features in the spectral region between 3.2 µm and 3.8 µm where atmospheric transmission windows are present. Figure A.10 shows the absorption cross sections of the three gases in this spectral region with atmospheric absorption overplotted. Propylene may be a promising target gas for diesel exhaust detection using a laser wavelength near 3.39 µm. However, the flow rate of propylene is several orders of magnitude lower than those of NO_x, CO, and CO_2.

The NIST absorbance data is similarly analysed against atmospheric absorption in Figure A.12. The NIST database includes a larger set of exhaust constituents than HITRAN2016 with some limitations. The NIST data has lower resolution and the magnitudes of the absorption peaks are only relative within each spectrum, i.e. not relative from one spectrum to another. The spectral region from 3.20 µm to 3.80 µm contains absorption features of several exhaust constituents within atmospheric windows. Figure 2.2 shows that most of these molecules, with the exception of propylene, have relatively low concentrations in diesel exhaust and are unlikely to be detectable.

2.4.2 Detectivity

The specific detectivity D^* of IR detectors is a measure of the detector spectral response in units of cm $Hz^{1/2}$ W^{-1}. The specific detectivity D^* is derived from the noise equivalent power (NEP) S_D (units W $Hz^{-1/2}$) and active detector area A_D (units cm^2) as follows:

$$D^* = \frac{\sqrt{A_D}}{S_D} \tag{2.6}$$

The spectral responses of Hamamatsu and Vigo IR detectors are shown in Figures A.13 and A.14 respectively. The detectivities relate to the photodiode only, not a complete detector module with an integrated preamplifier. The general decline in detectivity with increasing wavelength means that even strong molecular lines at long wavelengths ($>\sim 6$ µm) can be difficult to detect. Note that some of the Hamamatsu detectors require cooling by liquid nitrogen to operate at −196 °C.

Analysis of the spectral line intensities shown in Figure 2.6 and the detectivity of IR detectors shown in Figures A.13 and A.14 help to narrow down the spectral

regions of interest in selecting potentially detectable exhaust constituents using DIAL. The spectral peaks that occur in the transparent windows between 1 µm and 5 µm are analysed further for three reasons:

i. there are no significant molecular line intensities of exhaust molecules below 1 µm;

ii. the atmosphere is almost opaque between 5 µm and 8 µm;

iii. the spectral response of IR detectors drop by 2 orders of magnitude over the wavelength range between 5 µm and 8 µm;

iv. thermal radiation from the Earth surface is a significant noise source in the spectral region beyond 5 µm, as will be shown in Figure 2.9.

A lidar detector is followed by a data acquisition (DAQ) system that requires as many bits as possible for the best vertical resolution of a detected pulse. Some state of the art DAQs have 16 bit resolution and a maximum sampling rate of 250 MS s^{-1} (AlazarTech ATS9625). The minimum pulse width that can be detected at this sampling rate, with adequate horizontal resolution, is ∼100 ns. This minimum pulse width has a rise time of ∼50 ns. Therefore, a detector is required to have a minimum bandwidth (highest frequency response) of $\sim (2\pi \times 50 \times 10^{-9})^{-1} \sim 3.2$ MHz. Not all detectors depicted in Figures A.13 and A.14 have bandwidths greater than 3.2 MHz.

2.5 Pulse propagation

In this Section, an expression (Equation 2.13) is derived for the power P_r of a return pulse in terms of sent pulse power P_s. The modelled pulse is emitted vertically downward from an airborne platform at altitude l, strikes an ocean surface, and is backscattered toward a telescope receiver that is co-located with the laser emitter. The expression for the return pulse power will be required for estimating the target gas concentration and lidar sensitivity in Section 2.6.

2.5.1 Reflectance from sea water

A lidar may be designed to depend on a return pulse that was scattered from the Earth surface to maximise the energy in the return pulse. The spectral reflectance of sea water at normal angle of incidence is displayed in Figure 2.7.

Lidar backscatter R_S from a surface can be defined as the Fresnel reflectance ρ per unit solid angle Ω in the backscatter direction. That is, $R_S = \frac{\rho}{\Omega}$ and Ω models the pattern of reflected radiation for backscatter. Both ρ and Ω are dependent on angle of incidence θ from Nadir ($\theta = 0$). If the ocean surface could be characterised as a diffuse

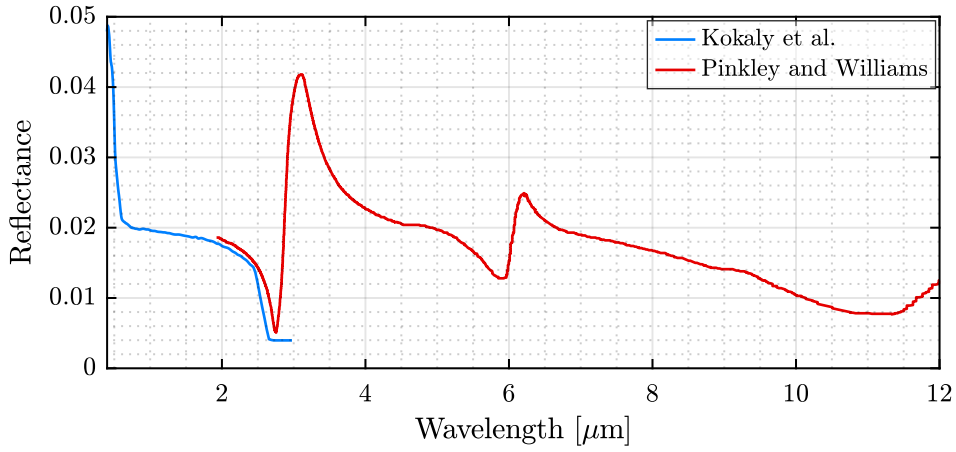

Figure 2.7: Spectral reflectance of sea water at near-normal incidence. The visible to near-IR data and mid-IR data were sourced from Kokaly et al. [126] and Pinkley and Williams [127] respectively.

reflector, the Lambertian model of $\Omega = \frac{\pi}{\cos\theta}$ would give a backscatter of $R_S = \frac{\rho\cos\theta}{\pi}$. [128] At Nadir angle of incidence, the Lambertian backscatter simplifies to $R_S = \frac{\rho}{\pi}$.

While Lambertian reflectance is often the case for terrain targets where multiple scattering occurs, the ocean is more like a distorted mirror surface that gives rise to specular reflections or glints from wave facets that are aligned for backscattering to the laser receiver. Wave slopes aligned perpendicular to the incident beam and included within the incident laser footprint on the ocean appear to the lidar receiver as specular points or glints. [128]

The lidar backscatter R_S from an ocean surface is dependent on angle of incidence θ from Nadir, laser wavelength λ, wind speed u, and atmospheric stability. [129] The expression for lidar backscatter R_S from an ocean surface may be written as [128–130]

$$R_S = \frac{\rho}{\Omega} = \frac{\rho\sec^4(\theta)}{2\pi\langle s^2\rangle}\exp\left(-\frac{\tan^2(\theta)}{\langle s^2\rangle}\right) \tag{2.7}$$

$$= \frac{1}{2}\rho\sec^4(\theta)\,G(\tan\theta) \tag{2.8}$$

where $\langle s^2\rangle$ is the total mean-square slope variance in the ocean surface (includes upwind and crosswind components) and $G(\tan\theta)$ is the normalised 2D Gaussian distribution function for surface slope $(\tan\theta)$ with variance $\langle s^2\rangle/2$.

At Nadir angle $(\theta = 0)$, the lidar backscatter R_S simplifies to

$$R_S = \frac{\rho}{2\pi\langle s^2\rangle} \tag{2.9}$$

The mean-square slope variance $\langle s^2\rangle$ is determined by wind speed u. Winds below

$7\,\mathrm{m\,s^{-1}}$ (13.6 kn) are characteristic of gravity wave influence, while slopes for winds above $7\,\mathrm{m\,s^{-1}}$ are primarily due to capillary waves.[128] Wu[131] proposed the following empirical relations for the two regimes from data collected by Cox and Munk[132]:

$$\left\langle s^2 \right\rangle = \begin{cases} (\ln u_{10} + 1.2) \times 10^{-2}, & u_{10} \leq 7\,\mathrm{m\,s^{-1}}\ (13.6\,\mathrm{kn}) \\ (0.85 \ln u_{10} - 1.45) \times 10^{-1}, & u_{10} > 7\,\mathrm{m\,s^{-1}}\ (13.6\,\mathrm{kn}) \end{cases} \tag{2.10}$$

where wind speed u_{10} was measured at 10 m above the ocean surface in units of $\mathrm{m\,s^{-1}}$. At a global average ocean wind speed $\bar{u}_{10} = 6.64\,\mathrm{m\,s^{-1}}$[123] (12.9 kn), $\langle s^2 \rangle = 0.03$ and backscatter R_S is more than 16 times greater than the Lambertian diffuse model at Nadir angle of incidence. By comparison, an ocean wind speed of $10\,\mathrm{m\,s^{-1}}$ (19.4 kn) results in $\langle s^2 \rangle = 0.05$ and a backscatter R_S that is 10 times greater than the Lambertian diffuse model.

2.5.2 Return pulse

An expression that relates pulse power returned P_r to pulse power sent P_s is presented. Consider a pulse sent from an airborne laser source with power $P_\mathrm{s} = \frac{E_\mathrm{s}}{\tau_\mathrm{p}}$, energy E_s, duration τ_p, wavelength λ, and angle of incidence $\theta = 0$ (Nadir). The pulse propagates vertically downward through the atmosphere over distance l with transmission T_l before striking the ocean surface. The ocean surface has reflectance ρ and scatters the pulse with backscatter R_S. Assuming a global average wind speed $u = 6.64\,\mathrm{m\,s^{-1}}$ (12.9 kn), the backscatter may be approximated by $R_\mathrm{S} = \frac{\rho}{\Omega} \approx 16\frac{\rho}{\pi}\,\mathrm{sr^{-1}}$. Some fraction of the reflected pulse is directed back toward the lidar telescope that has an aperture radius r_t and area $A_\mathrm{t} = \pi r_\mathrm{t}^2$. The solid angle defined by the telescope receiver is $\frac{A_\mathrm{t}}{l^2}$. The reflected pulse propagates through the atmosphere over distance l before entering the telescope receiver. The detection system has an optical efficiency η, assumed to be $\eta = 1$ to simplify the analysis.

$$P_\mathrm{r} = \frac{A_\mathrm{t}}{l^2} R_\mathrm{S} T_l^2 P_\mathrm{s} \tag{2.11}$$

$$\approx 16 \frac{A_\mathrm{t}}{l^2} \frac{\rho}{\pi} T_l^2 P_\mathrm{s} \tag{2.12}$$

$$\approx 16 \left(\frac{r_\mathrm{t}}{l}\right)^2 \rho T_l^2 P_\mathrm{s} \tag{2.13}$$

$$\approx 16 \left(\frac{r_\mathrm{t}}{l}\right)^2 \rho T_l^2 \frac{E_\mathrm{s}}{\tau_\mathrm{p}} \tag{2.14}$$

where T_l^2 is the transmission of a pulse through the atmosphere over a distance $2l$.

The transmission T_l^2 of a return pulse through an atmosphere that is uniform below altitude l may expressed as:[133]

$$T_l^2 = \exp\left[-2\left(\alpha_{\text{tg}} + \alpha_{\text{other}}\right) l\right] \tag{2.15}$$

where α_{tg} is the absorption coefficient for the target gas and α_{other} is the attenuation due to scattering and absorption by other species. The gas will be targeted on a spectral line that is not absorbed by other species, so attenuation $\alpha_{\text{other}} = 0$ is assumed to simplify the analysis. The wavelength dependent absorption coefficient α_{tg} is related to the target gas concentration C_{tgv} (per unit volume) by the wavelength dependent absorption cross section σ as follows:

$$\alpha_{\text{tg}} = \sigma C_{\text{tgv}} \tag{2.16}$$

Then the transmission of the return pulse, emitted at Nadir angle of incidence from altitude l through a uniform atmosphere, is approximated by

$$T_l^2 \approx \exp\left(-2\sigma C_{\text{tgv}} l\right) \tag{2.17}$$

2.6 Target gas concentration

In this Section, expressions are derived for (i) target gas concentration C_{tg} (units ppm, Equation 2.24) measured from pairs of DIAL pulses; and (ii) the minimum detectable concentration length, or lidar sensitivity S_{L} (units ppm m, Equation 2.33), that can be measured from the pulse pair. The lidar sensitivity S_{L} can be estimated from the absorption through a known concentration of gas and the system SNR.

2.6.1 How concentration is measured

The DIAL technique relies on pulse pairs of wavelengths λ_{on} and λ_{off} that are separated by a small interval, as introduced in Section 2.2, to measure the concentration of the target gas. Assuming that the pulse pair are closely separated in time such that they propagate through equal atmospheres and are backscattered equally from the ocean surface, the transmission of each pulse differs due to the different absorption cross sections, σ_{on} and σ_{off}, of the target gas at the online and offline wavelengths respectively. The DIAL measures the *relative* transmission T_{rel} of the online and offline pulses defined as follows:

$$T_{\mathrm{rel}} = \frac{T_{l,\mathrm{on}}^2}{T_{l,\mathrm{off}}^2} = \frac{P_{\mathrm{r,on}}/P_{\mathrm{s,on}}}{P_{\mathrm{r,off}}/P_{\mathrm{s,off}}} = \frac{P_{\mathrm{r,on}}}{P_{\mathrm{r,off}}} \tag{2.18}$$

$$= \exp\left(-2\Delta\sigma C_{\mathrm{tgv}} l\right) \tag{2.19}$$

where the powers of the sent pulses are assumed to be equal such that $P_{\mathrm{s,on}} = P_{\mathrm{s,off}} = P_{\mathrm{s}}$ and $\Delta\sigma = \sigma_{\mathrm{on}} - \sigma_{\mathrm{off}}$ is the differential absorption cross section between online and offline wavelengths.

The target gas concentration C_{tgv} (number per unit volume) is therefore given by

$$C_{\mathrm{tgv}}\,(\mathrm{m}^{-3}) = \frac{-\ln\left(T_{\mathrm{rel}}\right)}{2\Delta\sigma l} = \frac{-\ln\left(P_{\mathrm{r,on}}/P_{\mathrm{r,off}}\right)}{2\Delta\sigma l} \tag{2.20}$$

The target gas concentration C_{tg} in units of ppm can be estimated from C_{tgv} and the total gas concentration $C_{\mathrm{v}} = N/V = P_{\mathrm{atm}}/k_{\mathrm{B}}T_{\mathrm{K}}$ (number per unit volume) by applying the ideal gas law given in Section 2.3.3.

$$C_{\mathrm{tg}}\,(\mathrm{ppm}) = \frac{C_{\mathrm{tgv}}}{C_{\mathrm{v}}} 10^6 \tag{2.21}$$

$$= C_{\mathrm{tgv}} \frac{k_{\mathrm{B}}T_{\mathrm{K}}}{P_{\mathrm{atm}}} 10^6 \tag{2.22}$$

$$= \frac{-\ln\left(T_{\mathrm{rel}}\right)}{2\Delta\sigma l} \frac{k_{\mathrm{B}}T_{\mathrm{K}}}{P_{\mathrm{atm}}} 10^6 \tag{2.23}$$

where k_{B} is the Boltzmann constant, T_{K} is the temperature (units Kelvin), and $P_{\mathrm{atm}} \approx 1\,\mathrm{atm}$ is the atmospheric pressure.

The vertical distribution of the target gas cannot be determined from the return pulses. Therefore, DIAL measures an integrated concentration length $2lC_{\mathrm{tg}}$ that is commonly expressed in units of ppm m.

$$2lC_{\mathrm{tg}}\,(\mathrm{ppm\,m}) = \frac{-\ln\left(T_{\mathrm{rel}}\right)}{\Delta\sigma} \frac{k_{\mathrm{B}}T_{\mathrm{K}}}{P_{\mathrm{atm}}} 10^6 \tag{2.24}$$

2.6.2 Lidar sensitivity

The lidar sensitivity is determined by the minimum detectable concentration of the target gas and, therefore, the minimum detectable change in transmission T_{rel}. Let a small change in target gas concentration be $\Delta C_{\mathrm{tgv}} = C'_{\mathrm{tgv}} - C_{\mathrm{tgv}}$ and the resulting small change in transmission be $\Delta T_{\mathrm{rel}} = T'_{\mathrm{rel}} - T_{\mathrm{rel}}$. Then, from Equation 2.20, the relative

change in concentration is given by

$$\frac{\Delta C_{\mathrm{tgv}}}{C_{\mathrm{tgv}}} = \frac{-\ln\left(T'_{\mathrm{rel}}\right) + \ln\left(T_{\mathrm{rel}}\right)}{-\ln\left(T_{\mathrm{rel}}\right)} \tag{2.25}$$

The relative change in concentration may equally be expressed in units of ppm (C_{tg}) instead of per unit volume (C_{tgv}), such that

$$\begin{aligned}
\Delta C_{\mathrm{tg}} &= \frac{C_{\mathrm{tg}}}{-\ln\left(T_{\mathrm{rel}}\right)} \ln\left(\frac{T_{\mathrm{rel}}}{T'_{\mathrm{rel}}}\right) && (2.26)\\
&= \frac{C_{\mathrm{tg}}}{-\ln\left(T_{\mathrm{rel}}\right)} \ln\left(\frac{T_{\mathrm{rel}}}{T_{\mathrm{rel}} + \Delta T_{\mathrm{rel}}}\right) && (2.27)\\
&= \frac{C_{\mathrm{tg}}}{\ln\left(T_{\mathrm{rel}}\right)} \ln\left(\frac{T_{\mathrm{rel}} + \Delta T_{\mathrm{rel}}}{T_{\mathrm{rel}}}\right) && (2.28)\\
&= \frac{C_{\mathrm{tg}}}{\ln\left(T_{\mathrm{rel}}\right)} \ln\left(1 + \frac{\Delta T_{\mathrm{rel}}}{T_{\mathrm{rel}}}\right) && (2.29)\\
&\approx \frac{C_{\mathrm{tg}}}{\ln\left(T_{\mathrm{rel}}\right)} \frac{\Delta T_{\mathrm{rel}}}{T_{\mathrm{rel}}} && (2.30)
\end{aligned}$$

The minimum detectable change in transmission is equivalent to the noise level while the minimum detectable *relative* change in transmission $\left|\frac{\Delta T_{\mathrm{rel}}}{T_{\mathrm{rel}}}\right|_{\mathrm{min}}$ is the inverse of the SNR for an offline pulse. Therefore, the minimum detectable change in concentration of the target gas $\left|\Delta C_{\mathrm{tg}}\right|_{\mathrm{min}}$ is

$$\begin{aligned}
\left|\Delta C_{\mathrm{tg}}\right|_{\mathrm{min}} &= \frac{C_{\mathrm{tg}}}{-\ln\left(T_{\mathrm{rel}}\right) \times \mathrm{SNR}} && (2.31)\\
&\approx \frac{C_{\mathrm{tg}}}{A_{\mathrm{rel}} \times \mathrm{SNR}} && (2.32)
\end{aligned}$$

where $A_{\mathrm{rel}} = 1 - T_{\mathrm{rel}}$ is the relative absorption of the online and offline pulses.

The lidar sensitivity $S_{\mathrm{L}} = 2l\left|\Delta C_{\mathrm{tg}}\right|_{\mathrm{min}}$ is an estimate of the minimum concentration length detectable in units of ppm m. It can be estimated from the SNR and the absorption A_{2l} over a distance $2l$ through a known low concentration of the target gas. That is,

$$S_{\mathrm{L}} = \frac{2lC_{\mathrm{tg}}}{A_{2l} \times \mathrm{SNR}} \tag{2.33}$$

2.7 Signal to noise analysis

In this Section, the SNR of a single pulse is modelled as a function of wavelength. The expression for return pulse power given in Equation 2.13 is used throughout the assessment. The pulse was assumed to propagate through a transparent atmosphere. The spectral region was confined to 1 µm – 5 µm due to limitations in detectivity described in Section 2.4.2 and Figures A.13 and A.14. Although the SNR does not change significantly with wavelength in the model presented in Figure 2.10, the spectral regions with the highest SNR were determined and the dominant noise components (detector and speckle) were identified. When combined with the spectral analysis of diesel exhaust gases and atmospheric transmission windows, the spectral region 3.4 µm – 4.0 µm is shown to have a combination of (i) relatively high SNR; (ii) high atmospheric transparency; and (iii) strong spectral line intensities for three diesel exhaust gases – NO_2, H_2CO, and SO_2. The modelled SNRs are illustrated in Figure 2.10 while the parameters used in the model are listed in Table 2.1. These SNRs were used for the lidar sensitivity S_L estimates listed in Table 2.2 of Section 2.9.

2.7.1 Noise sources

2.7.1.1 Shot noise

Shot noise in photon counts occur in the regime of low photon numbers. Shot noise follows Poisson statistics and scales as the square root of photons received. Since the standard deviation of shot noise is equal to the square root of the average number of photon events N_{ph}, the SNR due to shot noise, SNR_{Shot}, is given by

$$SNR_{Shot} = \frac{N_{ph}}{\sqrt{N_{ph}}} = \sqrt{N_{ph}} \tag{2.34}$$

From Equations 2.14 and 2.34, the number N_{ph} of return photons, which have wavelength λ and photon energy $E_{ph} = \frac{hc}{\lambda}$, is given by

$$N_{ph} = \frac{P_r \tau_p}{E_{ph}} = \frac{P_r \tau_p \lambda}{hc} \tag{2.35}$$

$$\approx 16 \left(\frac{r_t}{l}\right)^2 \rho T_l^2 \frac{E_s \lambda}{hc} \tag{2.36}$$

$\mathrm{SNR}_{\mathrm{Shot}}$ is the square root of the number of return photons N_{ph}.

$$\mathrm{SNR}_{\mathrm{Shot}} = \sqrt{N_{\mathrm{ph}}} \tag{2.37}$$

$$\approx 4\frac{r_{\mathrm{t}}}{l}\sqrt{\rho T_l^2 \frac{E_{\mathrm{s}}\lambda}{hc}} \tag{2.38}$$

2.7.1.2 Detector noise

The noise-equivalent power (NEP), S_{D}, of a detector is the minimum optical input power required for an output SNR of one in a one hertz output bandwidth. NEP is expressed in units of $\mathrm{W}/\sqrt{\mathrm{Hz}}$. The detector noise power P_{D} is the product of the NEP and square root of detector bandwidth Δf_{D}.

$$P_{\mathrm{D}} = S_{\mathrm{D}}\sqrt{\Delta f_{\mathrm{D}}} \tag{2.39}$$

The SNR due to detector noise $\mathrm{SNR}_{\mathrm{Detector}}$ is the ratio of return power P_{r} to detector noise power P_{D}. From Equations 2.13 and 2.39,

$$\mathrm{SNR}_{\mathrm{Detector}} = \frac{P_{\mathrm{r}}}{P_{\mathrm{D}}} \tag{2.40}$$

$$\approx 16\left(\frac{r_{\mathrm{t}}}{l}\right)^2 \frac{\rho T_l^2}{S_{\mathrm{D}}\sqrt{\Delta f_{\mathrm{D}}}} P_{\mathrm{s}} \tag{2.41}$$

The NEP of a detector and integrated preamplifier with specific detectivity D^* can be calculated from Equation 2.6. The filtered detector bandwidth is assumed to be $\Delta f_{\mathrm{D}} = 5\,\mathrm{MHz}$ throughout this analysis.

2.7.1.3 Speckle noise

The vast majority of surfaces are extremely rough on the scale of an optical wavelength. Under illumination by coherent light from a laser source, the waves reflected from such surfaces consist of contributions made from many independent scattering areas. Propagation of this reflected light to a distant observation point results in the addition of these various scattered components with relative delays that form a complex interference pattern, or a *speckle* pattern.[134] The mean speckle size is proportional to the laser wavelength λ.[135] Speckle noise decreases with increasing number of speckle cells due to averaging.

The SNR of the detected intensity of a single shot DIAL measurement due to rough target speckle is proportional to the square root of the total number of statistically independent speckle nodes in the image plane – a manifestation of negative exponential

statistics of rough target speckle. For a telescope receiver with diameter $2r_\mathrm{t}$ and field of view (FoV) θ_t, the SNR due to speckle, $\mathrm{SNR}_\mathrm{Speckle}$, is approximated by[136]

$$\mathrm{SNR}_\mathrm{Speckle} \approx \sqrt{1 + 4\left(\frac{\theta_\mathrm{t} r_\mathrm{t}}{\lambda}\right)^2} \tag{2.42}$$

2.7.1.4 Solar background

Solar radiation has a spectral power distribution $\mathrm{SPD}_\mathrm{Solar}$ as shown in Figure 2.8. The lidar telescope receives part of the solar radiation reflected from an area A_S on the ocean surface defined by the telescope FoV, distance l from the ocean surface, and viewing angle θ from Nadir. The solar radiation that is reflected from the ocean surface and directed toward the telescope is largely dependent on incident angle of sunlight, viewing angle θ, and weather conditions. To a first approximation, we assume the diffuse Lambertian model of reflectance, removing the dependence on angle of incidence of sunlight. Most of the solar radiation that enters the telescope aperture is blocked by a bandpass filter with a bandwidth $\Delta\lambda_\mathrm{F}$ centred around the laser wavelength. At Nadir viewing angle, the solar power P_Solar that enters the telescope can be estimated by

$$P_\mathrm{Solar} = \mathrm{SPD}_\mathrm{Solar} \times \frac{A_\mathrm{t}}{l^2}\frac{\rho}{\pi} T_l A_\mathrm{S} \Delta\lambda_\mathrm{F} \tag{2.43}$$

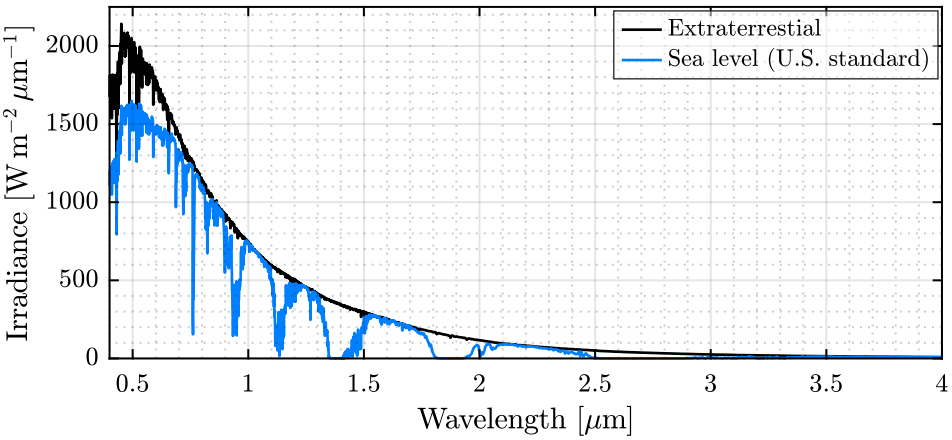

Figure 2.8: Spectral power distribution (SPD) of solar radiation at sea level under a U.S. standard atmosphere, adapted from Ref. 137.

The SNR due to solar radiation $\mathrm{SNR}_\mathrm{Solar}$ is the ratio of return power P_r to solar radiation power P_Solar. This is a conservative approach, since P_Solar can be subtracted

from P_{r} while true noise is variable. From Equations 2.13 and 2.43,

$$\mathrm{SNR}_{\mathrm{Solar}} = \frac{P_{\mathrm{r}}}{P_{\mathrm{Solar}}} \tag{2.44}$$

$$\approx 16 \frac{T_l}{\mathrm{SPD}_{\mathrm{Solar}} \times A_{\mathrm{S}} \Delta\lambda_{\mathrm{F}}} P_{\mathrm{s}} \tag{2.45}$$

2.7.1.5 Thermal radiation

The thermal radiation spontaneously emitted from the ocean surface layer can be approximated as blackbody radiation and depends only on temperature T_{K}. The thermal radiance L_λ of a blackbody at temperatures 10 °C and 20 °C are displayed in Figure 2.9. Thermal radiance L_λ, expressed in spectral units of wavelength in µm, is given by the following expression:[138]

$$L_\lambda = \frac{2 \times 10^{24} hc^2}{\lambda^5} \frac{1}{\exp\left(\frac{10^6 hc}{\lambda k_{\mathrm{B}} T_{\mathrm{K}}}\right) - 1} \tag{2.46}$$

where k_{B} is the Boltzmann constant and thermal radiance L_λ is expressed in units of $\mathrm{W\,m^{-2}\,sr^{-1}\,\mu m^{-1}}$. The thermal power P_{Thermal} that enters the telescope can be estimated by

$$P_{\mathrm{Thermal}} = L_\lambda T_l A_{\mathrm{S}} \frac{A_{\mathrm{t}}}{l^2} \Delta\lambda_{\mathrm{F}} \tag{2.47}$$

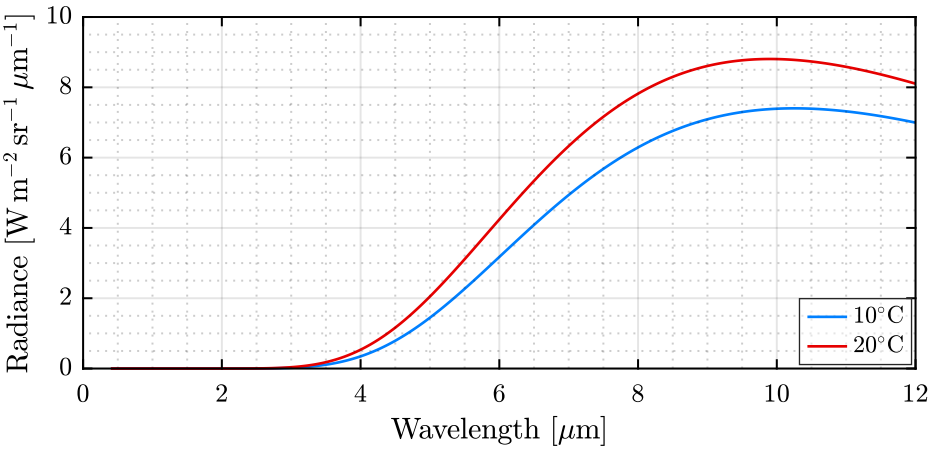

Figure 2.9: Thermal radiation.

The SNR due to thermal radiation, $\mathrm{SNR}_{\mathrm{Thermal}}$, is the ratio of return power P_{r} to

thermal radiation power P_{Thermal}. From Equations 2.13 and 2.47,

$$\text{SNR}_{\text{Thermal}} = \frac{P_{\text{r}}}{P_{\text{Thermal}}} \tag{2.48}$$

$$\approx 16 \frac{\rho T_l}{\pi L_\lambda A_{\text{S}} \Delta\lambda_{\text{F}}} P_{\text{s}} \tag{2.49}$$

2.7.2 Total SNR

The total SNR for the detection of a pulse that has propagated through a background atmosphere is calculated by adding the SNR due to all noise sources in quadrature as follows:

$$\text{SNR} = \left(\sum_i \text{SNR}_i^{-2} \right)^{-1/2} \tag{2.50}$$

$$= \left(\text{SNR}_{\text{Shot}}^{-2} + \text{SNR}_{\text{Detector}}^{-2} + \text{SNR}_{\text{Speckle}}^{-2} + \text{SNR}_{\text{Solar}}^{-2} + \text{SNR}_{\text{Thermal}}^{-2} \right)^{-1/2} \tag{2.51}$$

where it has been assumed that the noise components are uncorrelated.[136]

Table 2.1: Parameters used to model single pulse SNR as a function of wavelength illustrated in Figure 2.10.

Description	Symbol	Value
Energy of pulse sent	E_{s}	50 µJ
Duration of pulse sent	τ_{p}	100 ns
Altitude	l	500 m
Transmission	T_l^2	1
Temperature	T_{K}	288 K
Telescope radius	r_{t}	10 cm
Telescope FoV	θ_{t}	4 mrad
Bandwidth of spectral filter	$\Delta\lambda_{\text{F}}$	10 nm
Bandwidth of detector (filtered)	Δf_{D}	5 MHz
Detector NEP 1.0 µm – 2.5 µm	S_{D}	10.1 pW/$\sqrt{\text{Hz}}$
Detector NEP 2.5 µm – 4.0 µm	S_{D}	2.0 pW/$\sqrt{\text{Hz}}$
Detector NEP 4.0 µm – 5.0 µm	S_{D}	5.0 pW/$\sqrt{\text{Hz}}$

The SNR was modelled as a function of wavelength for the detection of a return pulse which was emitted from an altitude of 500 m at Nadir angle, propagated through a transparent atmosphere, and reflected from an ocean surface. The DIAL SNR model is illustrated in Figure 2.10 while the model parameters are listed in Table 2.1. The energy of the pulse sent, $E_{\text{s}} = 50$ µJ, and the pulse duration, $\tau_{\text{p}} = 100$ ns, were chosen based on previous Q-switching demonstrations in the 3 µm wavelength band.[139,140] The SNR calculations are based on single shot pulses only, i.e., no averaging. If a pulse repetition rate of 10 kHz and an averaging time of 0.1 s were used, the SNR would

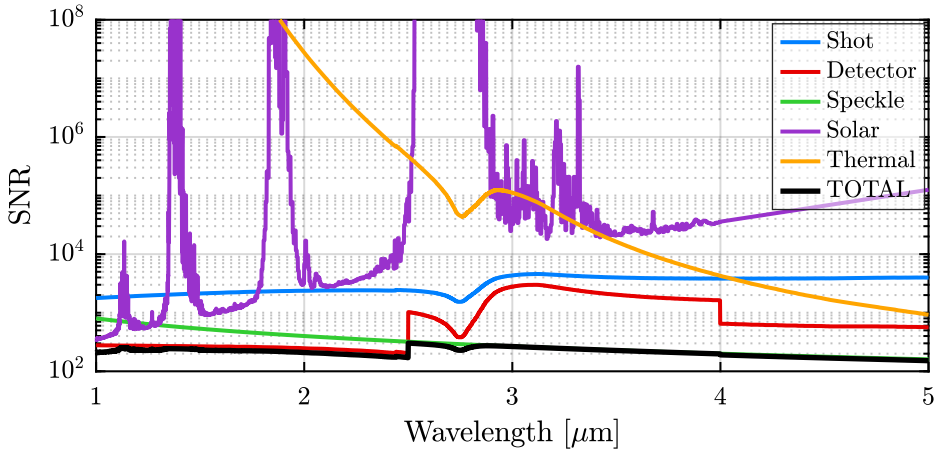

(a) Logarithmic scale showing each SNR component and the total SNR.

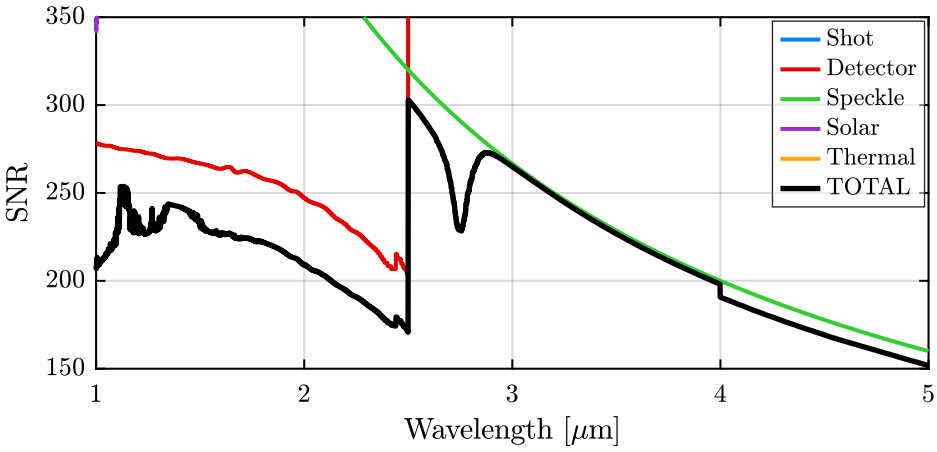

(b) Linear scale showing the total SNR.

Figure 2.10: Modelled SNR as a function of wavelength for the detection of a single return pulse reflected from an ocean surface. The atmosphere is assumed to be transparent to the laser pulse such that $T_l^2 = 1$. The parameters used to model the SNR are listed in Table 2.1.

improve by a factor of $\sqrt{10\,\text{kHz} \times 0.1\,\text{s}} = 32$. The SNR, modelled using the parameters listed in Table 2.1, was limited by either detector or speckle noise over the entire spectral region modelled.

Three different commercially available detectors, equipped with preamplifiers, were used to model $\text{SNR}_{\text{Detector}}$ in the spectral region 1 µm – 5 µm. These were (i) Thorlabs PDA10D2 (1.0 µm $\leq \lambda <$ 2.5 µm); (ii) Vigo PVI-2TE-4 MIPDC-F-10 (2.5 µm $\leq \lambda <$ 4.0 µm); and (iii) Vigo PVI-4TE-5 MIPDC-F-20 (4.0 µm $\leq \lambda <$ 5.0 µm). The solar SPD data illustrated in Figure 2.8 was extrapolated from 4 µm to 5 µm to model $\text{SNR}_{\text{Solar}}$. The steps in $\text{SNR}_{\text{Detector}}$ at $\lambda = 2.5$ µm and $\lambda = 4.0$ µm are due to the different NEPs of the detectors, as listed in Table 2.1. The dips in $\text{SNR}_{\text{Detector}}$, SNR_{Shot}, and $\text{SNR}_{\text{Thermal}}$ at $\lambda = 2.75$ µm are due to the change in spectral reflectance of sea water illustrated in

Figure 2.7. A large telescope FoV $\theta_t = 4\,\text{mrad}$ was chosen to improve $\text{SNR}_{\text{Speckle}}$ by averaging over a large area of the ocean surface. This is achieved at the expense of reducing $\text{SNR}_{\text{Thermal}}$ and, less significantly, $\text{SNR}_{\text{Solar}}$.

The SNR in this model shows that:

i. SNR is highest (>200) in the spectral regions 1.0 µm – 2.0 µm and 2.5 µm – 4.0 µm;

ii. Detectability in the spectral region 1.0 µm – 2.5 µm is limited by $\text{SNR}_{\text{Detector}}$ (for the case of the Thorlabs PDA10D2 detector considered in this analysis);

iii. Detectability in the spectral region 2.5 µm – 5.0 µm is limited by $\text{SNR}_{\text{Speckle}}$;

The combined Figures 2.6 and 2.10 show that within the spectral region 3.4 µm – 4.0 µm, there is a combination of (i) relatively high SNR; (ii) high atmospheric transparency; and (iii) strong spectral line intensities for three diesel exhaust gases – NO_2, H_2CO, and SO_2. These absorption lines can be viewed with higher resolution in Appendix A, Figures A.4, A.5, and A.6. The detectability of these gases, as well as CO, are investigated in Section 2.8.

2.8 Target gas assessment

The flow rates of diesel exhaust constituents were calculated and compared with background concentrations in Section 2.3. The spectral line intensities of diesel exhaust constituents within atmospheric windows were identified in Section 2.4. The SNR of a return pulse was modelled over a broad spectral region in Section 2.7.

In this Section, the strong line intensities of the main diesel exhaust constituents which are accessible within atmospheric transmission windows are analysed further. The absorption features of CO, NO_2, H_2CO, and SO_2 are presented in Sections 2.8.1, 2.8.2, 2.8.3, and 2.8.4 respectively. The line intensities of these molecules, as well as atmospheric absorption, are illustrated within the spectral regions that the molecules are most likely to be detectable, effectively showing selected spectral regions of Figure 2.6 in higher resolution. Furthermore, gas cell simulations are presented to show the absorption features of these gases in such a way that they can be scaled easily. The values of the simulated gas concentrations were chosen to be factors of ten that result in low levels of absorption ($< \sim 5\,\%$), i.e., absorption levels that vary almost linearly with concentration if the concentration is changed within a factor of five or so. The gas cell absorptions were simulated using the spectral tool SpectralCalc. In each case, the length of the simulated gas cell was set to 1 km.

2.8.1 Carbon monoxide

The absorption features of CO in the spectral region 2.30 µm – 2.43 µm are illustrated in Figure 2.11. Figure 2.11a illustrates the line intensities of CO and atmospheric absorption while Figure 2.11b illustrates the absorption within a 1000 ppm m CO gas cell. The strongest absorption lines are located in the 2.33 µm wavelength band.

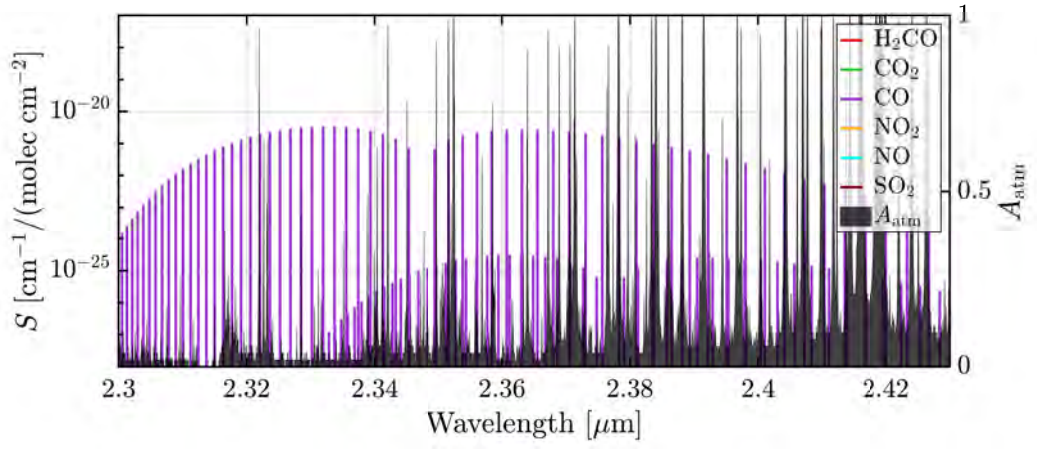

(a) Spectral line intensities S (left axis) with atmospheric absorption A_{atm} (right axis) overplotted.

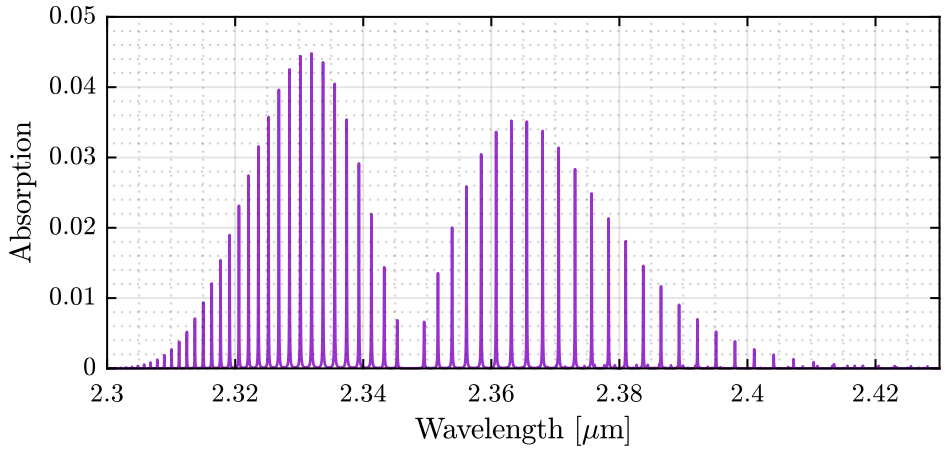

(b) Gas cell simulation. The 1 km gas cell had a CO concentration of 1 ppm resulting in a concentration length of 1000 ppm m.

Figure 2.11: Absorption features of CO in the spectral region 2.30 µm – 2.43 µm.

The flow rate and typical urban background concentration of CO are comparable with those of NO_2. The CO line strengths in the 2.33 µm wavelength band are within an order of magnitude of the NO_2 line strengths in the 3.43 µm wavelength band. A comparison of Figures 2.11 and 2.12 show a weaker absorption in CO than NO_2 for a given concentration length that, when combined with lower SNR in the 2.33 µm wavelength band than the 3.43 µm wavelength band, will mean that the lidar sensitivity

for CO detection is lower when compared with the NO_2 case. The estimated lidar sensitivities are listed in Table 2.2.

2.8.2 Nitrogen dioxide

In the context of diesel engine exhaust gas, NO_x is usually limited to NO and NO_2.[141] The estimated flow rate of NO_x from a 1000 kW diesel engine shown in Figure 2.2 was calculated from the NO_x emission factor provided by the United States Environmental Protection Agency.[98] However, the breakdown concentrations of NO and NO_2 were not provided by Ref. 98. These relative concentrations are affected by fuel mixture, temperature, and engine load.[142] The diesel exhaust concentration ratio NO_2/NO_x was assumed to be 10 %.[141,143] More information on the breakdown of NO_x concentrations in diesel exhaust can be found in Section A.3.1.

However, once the exhaust is discharged into the atmosphere, NO can react with O_3 to form NO_2 on a time scale of tens of minutes.[144] Although most of the Earth's atmospheric ozone is found in the stratosphere, 10 % – 15 % is found in the troposphere and the concentration at marine sea level is around 10 ppb – 50 ppb.[119,145] The chemistry of NO_x in the troposphere is briefly described below.[144]

$$NO + O_3 \rightarrow NO_2 + O_2$$

During the day, NO_2 can be photolysed by photons with energy $h\nu$.

$$NO_2 + h\nu \rightarrow NO + O$$

regenerating ozone

$$O + O_2 + M \rightarrow O_3 + M$$

where M denotes any third body that possesses the required energy for the reaction. Nitric oxide is also converted to NO_2 by reactions with hydroperoxyl (HO_2)

$$NO + HO_2 \rightarrow NO_2 + OH$$

and organic peroxy radicals (RO_2)

$$NO + RO_2 \rightarrow NO_2 + RO$$

During the day, NO_2 and NO are interconverted on a time scale of minutes by the above reactions. During the night, the photolysation process that reduces NO_2 to NO cannot take place and the concentration of NO_2 relative to NO can increase

significantly.[144] The background concentration of NO fluctuates significantly from day to night as a result of these chemical reactions. At night time, the background concentration of NO can diminish to <1 % of the background NO_2 concentration.[144]

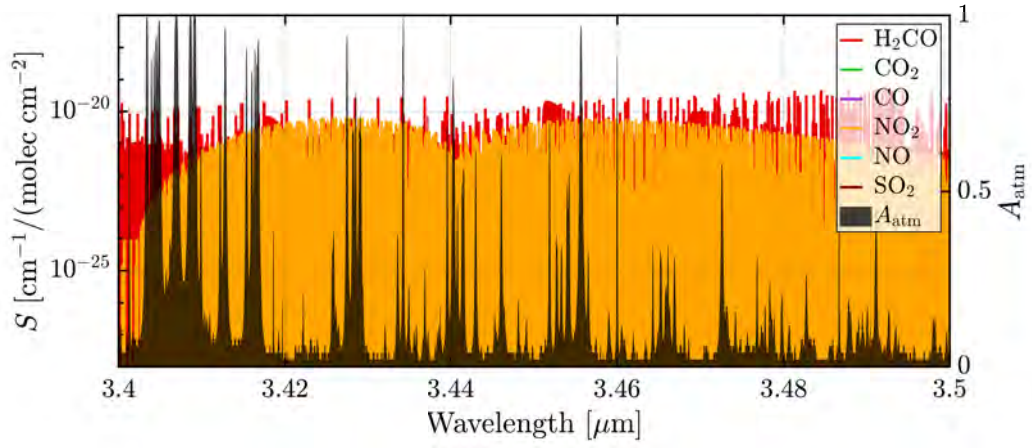

(a) Spectral line intensities S (left axis) with atmospheric absorption A_{atm} (right axis) overplotted.

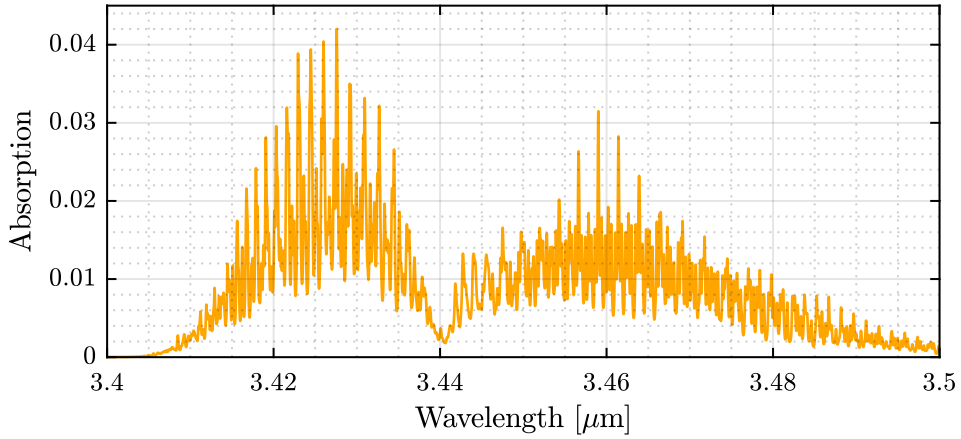

(b) Gas cell simulation. The 1 km gas cell had a NO_2 concentration of 0.1 ppm resulting in a concentration length of 100 ppm m.

Figure 2.12: Absorption features of NO_2 in the spectral region 3.40 µm – 3.50 µm.

The absorption features of NO_2 in the spectral region 3.4 µm – 3.5 µm are presented in Figure 2.12. Figure 2.12a illustrates the line intensities of NO_2 and atmospheric absorption while Figure 2.12b illustrates the absorption within a 100 ppm m NO_2 gas cell. The strongest absorption lines are located in the 3.425 µm wavelength band.

Fibre lasers which emit light near 3.5 µm have advanced considerably in recent years.[63] In the year 2016, Henderson-Sapir et al.[61] demonstrated a widely tunable mid-IR fibre laser with peak wavelengths in the 3.45 µm to 3.47 µm spectral region. Demonstrations of active Q-switching were followed by the same group in the year 2018.[67] These lasers are modelled and discussed in Chapter 3. A similar fibre laser was

gain-switched by Jobin et al.[146] which emitted 3.55 µm light. The 6.8 µJ gain-switched pulses were 33 ns wide with a repetition rate of 15 kHz.

2.8.3 Formaldehyde

The International Agency for Research on Cancer (IARC) has classified formaldehyde (H_2CO) as a human carcinogen (Group 1).[147] The estimated flow rate of H_2CO in diesel exhaust, illustrated in Figure 2.2, is several orders of magnitude lower that those of NO_2 and CO, and one order of magnitude lower than the flow rate of SO_2 when ULSDF is used. However, H_2CO is characterised by strong absorption lines, accessible in the transparent windows of the atmosphere, when compared with those of the three other gases considered.

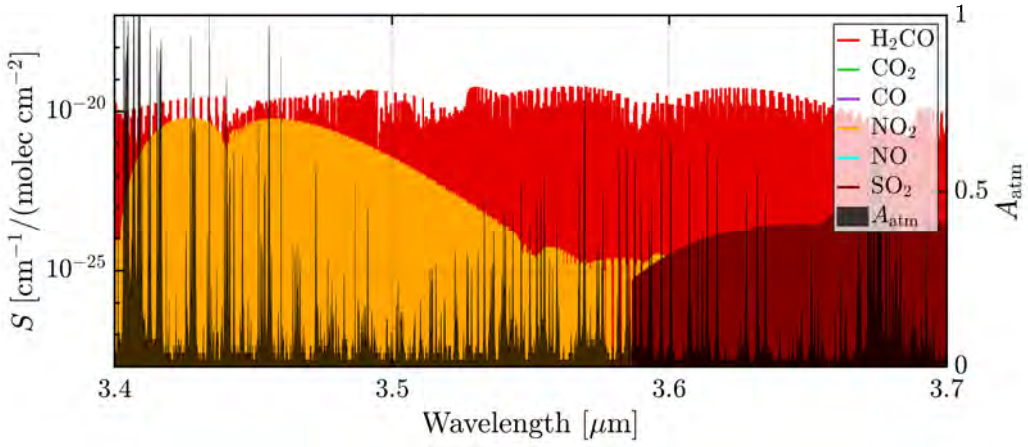

(a) Spectral line intensities S (left axis) with atmospheric absorption A_{atm} (right axis) overplotted.

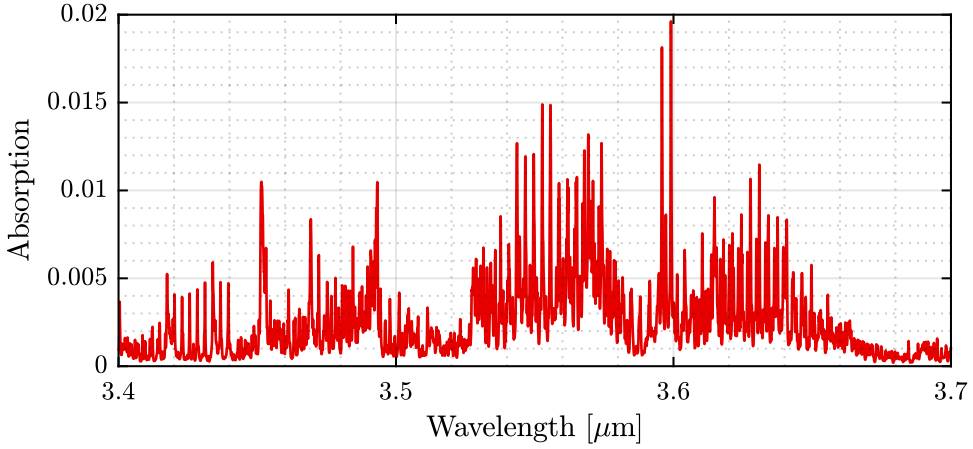

(b) Gas cell simulation. The 1 km gas cell had a H_2CO concentration of 0.01 ppm resulting in a concentration length of 10 ppm m.

Figure 2.13: Absorption features of H_2CO in the spectral region 3.40 µm – 3.70 µm.

The absorption features of H_2CO in the spectral region 3.4 µm – 3.7 µm are illustrated in Figure 2.13. Figure 2.13a illustrates the line intensities of H_2CO and atmospheric absorption while Figure 2.13b illustrates the absorption within a 10 ppm m H_2CO gas cell. The strongest absorption lines are located in the 3.60 µm wavelength band.

The lidar sensitivity estimates presented in Table 2.2 show that the lidar sensitivity is lowest (best) for detection of H_2CO in the 3.60 µm wavelength band when compared with detection of CO, NO_2, and SO_2. However, the background and exhaust plume concentrations of H_2CO are also lower when compared with the three other gases.

2.8.4 Sulfur dioxide

The flow rate of SO_2 illustrated in Figure 2.2 was calculated from the emission factor of ULSDF, which has a sulfur content of <15 ppm, since there is a global trend to reduce sulfur content in diesel fuel due to the harmful effects of SO_2 emissions. This global trend is illustrated in Appendix A.3.2. However, as explained in Section 2.1, MARPOL Annex VI will reduce the allowed sulfur content in marine fuel outside emission control areas from 3.5 % to 0.5 % (m/m) from 1 January 2020. This revised permissible limit is more than 300 times higher than the sulfur content in ULSDF.

The absorption features of SO_2 in the spectral region 3.95 µm – 4.05 µm are illustrated in Figure 2.14. Figure 2.14a illustrates the line intensities of SO_2 and atmospheric absorption while Figure 2.14b illustrates the absorption within a 1000 ppm m SO_2 gas cell. The strongest absorption lines are located in the 3.98 µm wavelength band.

The lidar sensitivity estimates presented in Table 2.2 show that the lidar sensitivity is worst for detection of SO_2 in the 3.98 µm wavelength band when compared with detection of CO, NO_2, and H_2CO. The background and exhaust plume (calculated for ULSDF) concentrations of SO_2 are also low when compared with the three other gases. Therefore, typical concentrations of SO_2 in the background atmosphere and exhaust plumes will be difficult to detect using DIAL technology.

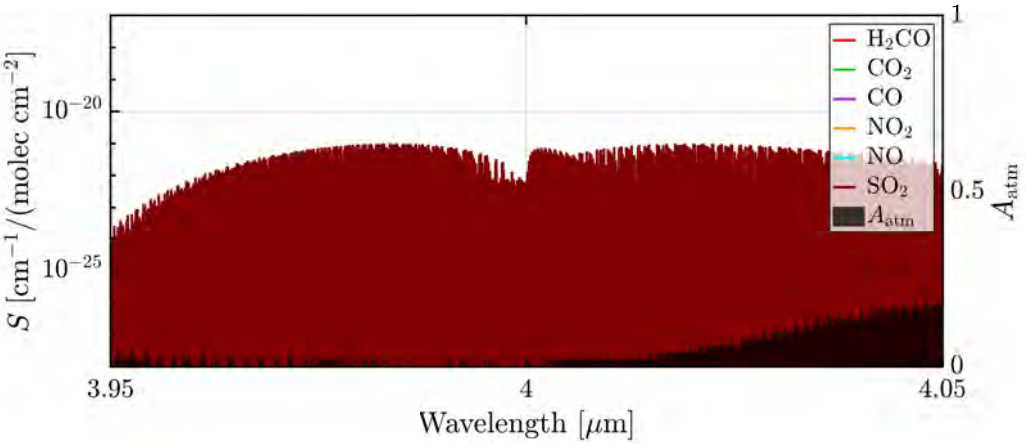

(a) Spectral line intensities S (left axis) with atmospheric absorption A_{atm} (right axis) overplotted.

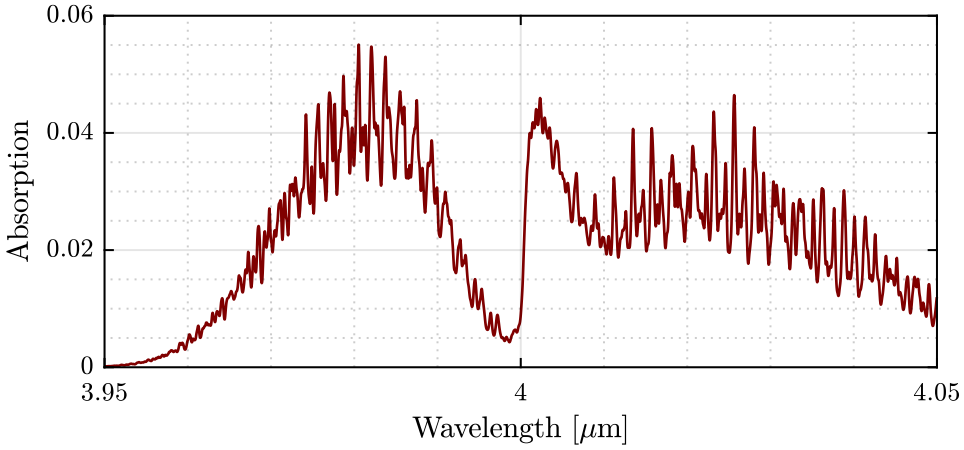

(b) Gas cell simulation. The 1 km gas cell had a SO_2 concentration of 1 ppm resulting in a concentration length of 1000 ppm m.

Figure 2.14: Absorption features of SO_2 in the spectral region 3.95 µm – 4.05 µm.

2.9 Lidar sensitivity estimates

SNRs and lidar sensitivities S_{L} were calculated for the target gases and spectral lines discussed in Section 2.8. A summary of these estimates is presented in Table 2.2. Note that the SNR calculations presented in Table 2.2 are based on single shot measurements. Significant noise improvements can be achieved with high pulse repetition rates and spatial averaging. If an averaging time of 0.1 s and a repetition rate of 10 kHz are used, as explained in Section 2.7.2, this would allow the averaging of 1000 pulses and therefore increase the SNR by a factor of 32. The spatial resolution for an aircraft speed of 100 m s^{-1} would be 100 m s^{-1} × 0.1 s = 10 m. The estimated improvement in lidar sensitivity by averaging 1000 pulses is included in Table 2.2.

When 1000 pulses are averaged, the lidar sensitivity S_{L} is below the urban back-

Table 2.2: SNR and lidar sensitivity S_{L} estimates for detection of CO, NO_2, H_2CO, and SO_2. The concentration lengths $2lC_{\mathrm{tg}}$ and absorptions A_{2l} of the simulated gas cells that were used in lidar sensitivity estimates are listed. Background atmospheric concentrations, World Health Organization (WHO) guidelines, and U.S. Environmental Protection Agency (EPA) standards are listed as well as their concentration lengths for a 1 km path length. The concentrations of these gases in exhaust plumes 1 km downwind from a 1000 kW point source are included.

	CO λ=2.33 µm	NO_2 λ=3.43 µm	H_2CO λ=3.60 µm	SO_2 λ=3.98 µm
Gas cell $2lC_{\mathrm{tg}}$ [ppm m]	1.0×10^{3}	1.0×10^{2}	1.0×10^{1}	1.0×10^{3}
Gas cell A_{2l}	4.5×10^{-2}	4.0×10^{-2}	2.0×10^{-2}	5.5×10^{-2}
SNR (single pulse)	1.8×10^{2}	2.3×10^{2}	2.2×10^{2}	2.0×10^{2}
S_{L} (single pulse) [ppm m]	1.2×10^{2}	1.1×10^{1}	8.3×10^{-1}	2.5×10^{2}
S_{L} (1000 averaged) [ppm m]	4.0×10^{0}	3.6×10^{-1}	2.8×10^{-2}	8.4×10^{0}
Remote background [ppm]	4.0×10^{-2} [119]	2.0×10^{-5} [119,144]	2.5×10^{-4} [148]	5.0×10^{-5} [119]
Urban background [ppm]	2.0×10^{-1} [119]	6.0×10^{-1} [119,144]	1.0×10^{-2} [119,149]	1.5×10^{-2} [119,150]
WHO guideline [ppm]	3.0×10^{1} (1 hr mean) (indoor) [147]	1.0×10^{-1} (1 hr mean) [151]	7.9×10^{-2} (30 min mean) (indoor) [147,152]	1.9×10^{-1} (10 min mean) [151]
U.S. EPA standard [ppm]	3.5×10^{1} [153]	1.0×10^{-1} (1 hr mean) [153]	–	5.0×10^{-1} (3 hr mean) [153]
Plume [ppm]	7.8×10^{-3}	1.6×10^{-3}	6.7×10^{-7}	6.0×10^{-6}
Remote background $\times$1000 m [ppm m]	4.0×10^{1}	2.0×10^{-2}	2.5×10^{-1}	5.0×10^{-2}
Urban background $\times$1000 m [ppm m]	2.0×10^{2}	6.0×10^{2}	1.0×10^{1}	1.5×10^{1}
WHO guideline $\times$1000 m [ppm m]	3.0×10^{4}	1.0×10^{2}	7.9×10^{1}	1.9×10^{2}
U.S. EPA standard $\times$1000 m [ppm m]	3.5×10^{4}	1.0×10^{2}	–	5.0×10^{2}
Plume $\times$120 m [ppm m]	9.3×10^{-1}	1.9×10^{-1}	8.0×10^{-5}	7.2×10^{-4}

ground concentration length for each of the four gases considered. In particular, sensitivities are at least one order of magnitude below the urban background for the cases of CO, NO_2, and H_2CO. Each sensitivity is also below the World Health Organization (WHO) guidelines and United States Environmental Protection Agency (EPA) standards listed in Table 2.2. This result shows that there is a potential to use DIAL technology for environmental monitoring of at least four diesel exhaust gases over polluted regions such as cities, their coasts, and shipping ports.

The plume analysis suggests that NO_x emissions from point sources could be monitored remotely for the cases of engine loads >10,000 kW, such as ocean going vessels and cruise ships. The NO_2 concentration in an exhaust plume was calculated for an engine load of 1000 kW assuming a NO_x controlled engine and ignoring post emission chemistry that increases the NO_2/NO ratio in the atmosphere. The concentration of NO_2 in an exhaust plume 1 km downwind from a point source was calculated for the conservative case that ignores these chemical reactions. Post emission ozone driven conversion of NO to NO_2 could mean that the concentration of NO_2 would be up to six times higher.

The exhaust plume concentration of SO_2 was calculated for ULSDF (15 ppm). The combination of engine load and sulfur content would need to be increased by five orders of magnitude for the potential detection of SO_2 emitted from a point source. For example, 15 % sulfur content per 10,000 kW of engine load. Therefore, DIAL technology is unlikely to be suitable for detecting SO_2 emitted from a single point source.

2.10 Conclusion

A feasibility study has been presented that investigates the potential use of DIAL technology for detecting diesel exhaust gases remotely. In this study, four exhaust gas constituents have been identified as the most likely target gases for remote detection – CO in the 2.3 µm wavelength band, NO_2 and H_2CO in the 3.5 µm wavelength band, and SO_2 in the 4.0 µm wavelength band. The likely sensitivities of DIAL systems to detect these gases has been analysed. When 1000 pulses are averaged, the lidar sensitivity S_L is at least one order of magnitude below the urban background concentration length for the cases of CO, NO_2, and H_2CO. Although SO_2 may not be a suitable target molecule for diesel exhaust gas emitted from most point sources, there could be a potential to remotely target illegal use of diesel fuel containing high levels of sulfur. If so, then the spectral region 3.95 µm – 4.05 µm would be of interest.

The possible detections of CO, NO_2, H_2CO and SO_2 offer a real possibility of de-

tecting diesel exhaust emissions using DIAL. There are a number of possible variations to the analysis that may achieve significant improvement in SNR, such as the following:

1. Increase averaging in post processing at the expense of horizontal resolution;
2. Nature may provide a significant increase in NO_2 concentration due to post emission ozone chemistry, which could increase plume concentration of NO_2 by a factor of six;
3. Urban or regional topographical scatterers, rather than an ocean surface, are expected to have higher reflectance that could result in a significant increase in return power.[117]

Given these improvements, it is very likely that diesel exhaust emissions could be detected by a downward looking DIAL system mounted on an airborne platform flying within an altitude of 500 m.

This analysis was performed using a conservative approach that targets exhaust emissions using a low-reflectance topographical scatterer (ocean surface). The study is applicable to marine environments such as shipping ports or shipping routes and demonstrates high potential detectability in regional and urban environments also. This work can be extended in the future to assess the detectability of exhaust gases emitted in urban and industrial environments, where the background atmosphere is heavily polluted, to identify the major sources of emissions for environmental monitoring and control.

Chapter 3
Modelling Fibre Lasers

This Chapter includes the following published article on pages 60–84:

> A. Malouf, O. Henderson-Sapir, M. Gorjan, D. J. Ottaway. Numerical modeling of 3.5 µm dual-wavelength pumped erbium-doped mid-infrared fiber lasers. *IEEE Journal of Quantum Electronics*, 52(11):1–2, Nov 2016.

The article presents a numerical model that was developed to simulate 3.5 µm dual-wavelength pumped (DWP) Er^{3+}-doped fibre lasers. The simulations provide insight and optimisation techniques to improve the performance of these lasers. The model simulates ionic and photonic interactions in the time domain as well as the spatial domain along the fibre, while most previously reported models solve for the steady state condition only. This model was validated against three experiments reported in literature and can be adapted to simulate any rare earth doped fibre laser.

Also included in this Chapter, Section 3.5, are revised contributions made to the following published article:

> O. Henderson-Sapir, A. Malouf, N. Bawden, J. Munch, S. D. Jackson, D. J. Ottaway. Recent advances in 3.5 µm erbium-doped mid-infrared fiber lasers. *IEEE Journal of Selected Topics in Quantum Electronics*, 23(3):6–14, May 2017.

This article includes Q-switch modelling of a 3.5 µm DWP Er^{3+}-doped fibre laser. Simulations were performed to study Q-switch behaviour in the time domain so that the performance of Q-switched 3.5 µm lasers could be predicted and optimised. The contributions made to this article were revised to provide more detail about the optimum repetition rate for Q-switching. The article is presented in Appendix B for convenience and supports the revised contributions presented in Section 3.5.

3.1 Background

Most reported numerical models of fibre lasers simulate the steady state condition only.[154–158] Several models were developed to study Er^{3+}-doped ZBLAN fibre lasers that operate on the 2.8 µm transition ($^4I_{11/2} \rightarrow {}^4I_{13/2}$). ZBLAN is a heavy metal fluoride glass of composition ZrF_4-BaF_2-LaF_3-AlF_3-NaF and the most common fluorozirconate (ZrF_4) glass. Parameters such as ion-doping concentration and fibre length were optimised by solving for the steady state conditions numerically.

The significance of interionic processes in 2.8 µm Er^{3+}-doped ZBLAN fibre lasers were investigated by Gorjan et al.[159] using a time-dependent model that implemented the fourth order Runge-Kutta (RK4) method. The laser was conventionally pumped by a single pump source. The simulated fibre length was divided into discrete length elements. The time step for the numerical iterations was set to the time required for light to traverse a single fibre element. Therefore, the temporal and spatial dynamics were coupled throughout the simulations.

Gorjan et al.[159] kindly provided this MATLAB model to our group at The University of Adelaide. Our plan was to adapt the model to simulate the DWP experiment reported by Henderson-Sapir et al.[62]. However, the fibre length of this experiment was only 20 cm, which was considerably shorter than the 4 m long fibre modelled by Gorjan et al.[159]. The shorter length elements, and therefore proportionally shorter time steps, resulted in many more time steps for a given total simulation time. The execution time for a 20 ms simulation of a 20 cm fibre would have been 170 hours (if the simulation was not terminated before completion), which was excessively long when compared with 6.5 hours for a 4 m long fibre.[160]

New code was developed as part of an Honours project, prior to candidature, to model the DWP experiment reported by Henderson-Sapir et al.[62]. This single-clad fibre laser experiment is referred to as 'H2014' in the published article on pages 60–84. The code was partially optimised for speed by solving the set of rate equations of all length elements in a single 2D matrix. Execution times were reduced by a factor of 18.5 (from 170 hours to 9 hours for the 20 cm fibre and from 6.5 hours to 21 min for the 4 m fibre). Thus it became viable to develop the model further. During the Honours project, the H2014 experiment was modelled and good agreement with experimental data was achieved.[160]

During candidature, the code was developed further to model two reported double-clad DWP fibre laser experiments (referred to as 'H2016' and 'F2016' in the published article on pages 60–84). The H2014 simulations were repeated when any changes were made to the algorithm. Simulations of the H2014, H2016, and F2016 experiments were

performed, analysed, and compared with experimental data at each stage of model development until good agreement was achieved for all three experiments. The model was then developed to simulate and study Q-switching behaviour in a DWP fibre laser. The model was also further optimised for speed.

3.2 Introduction

This Chapter presents a numerical model, written in MATLAB, that simulates the performance of 3.5 µm dual-wavelength pumped (DWP) Er^{3+}-doped fluorozirconate glass fibre lasers. Development of the model began prior to candidature as an Honours project.[160] The project was motivated by the need to simulate the DWP laser developed by Henderson-Sapir et al.[62] and optimise its performance. During candidature, the model was developed further to simulate three newly reported DWP fibre lasers and predict Q-switching behaviour for one of these laser systems.

The modelling work performed during candidature can be summarised as follows:

(i) The laser output power of three DWP Er^{3+}-doped 3.5 µm fibre lasers, reported in literature during the year 2016, were modelled showing good agreement with reported values. This work was published and is presented on pages 60–84.

(ii) Q-switching was implemented into the model and a Q-switched 3.5 µm DWP Er^{3+}-doped fibre laser was simulated for various Q-switch repetition rates. This work was published and revisions to this work are presented in Section 3.5.

(iii) The model code was optimised for speed. This work is presented in Section 3.6.

The model simulates the physical processes that occur within the fibre gain medium. The interactions that occur in these DWP systems are more complex than most conventional lasers due to the existence of two pumps, two possible competing laser transitions (2.8 µm and 3.5 µm), multiple excited state absorption processes and multiple interionic interactions. These complexities motivated the need to develop a model that was flexible enough to adapt to any fibre laser system.

This Chapter introduces the principles of 3.5 µm Er^{3+}-doped fibre lasers and the designs that were modelled in Section 3.3. The published article "Numerical modeling of 3.5 µm dual-wavelength pumped erbium-doped mid-infrared fiber lasers" is presented on pages 60–84. Section 3.4 examines an excited state absorption process of the second pump P_2 that was reported by Maes et al.[66] after the presented modelling work was completed. Q-switch modelling of a 3.5 µm Er^{3+}-doped fibre laser is presented in Section 3.5. This Section elaborates on contributions made to the article published by Henderson-Sapir et al.[63]. Attempts made to optimise the model code for speed are summarised in Section 3.6. Finally, conclusions are presented in Section 3.7.

3.3 Dual-wavelength pumped 3.5 µm fibre lasers

A comparison between conventional pumping (CP) and DWP is illustrated in Figure 3.1(a) with an energy level diagram. The CP approach excites ions directly from the ground state to the upper laser level with a single 655 nm pump source.[64] The 3.5 µm laser transition is followed by fast multi-phonon (MP) decay into a long lived energy state, $^4I_{11/2}$. Alternatively, the DWP technique combines two pump sources to excite ions to the upper laser level. The first pump P_1 excites Er^{3+} ions into the long lived $^4I_{11/2}$ state, which we refer to as the "virtual ground state". The second pump P_2 excites ions from this virtual ground state to the upper laser level. The DWP technique is more energy efficient than the single-wavelength CP approach because it reduces the quantum defect by exploiting a long lived excited state, $^4I_{11/2}$, that would otherwise cause bottlenecking and limit laser performance.[62]

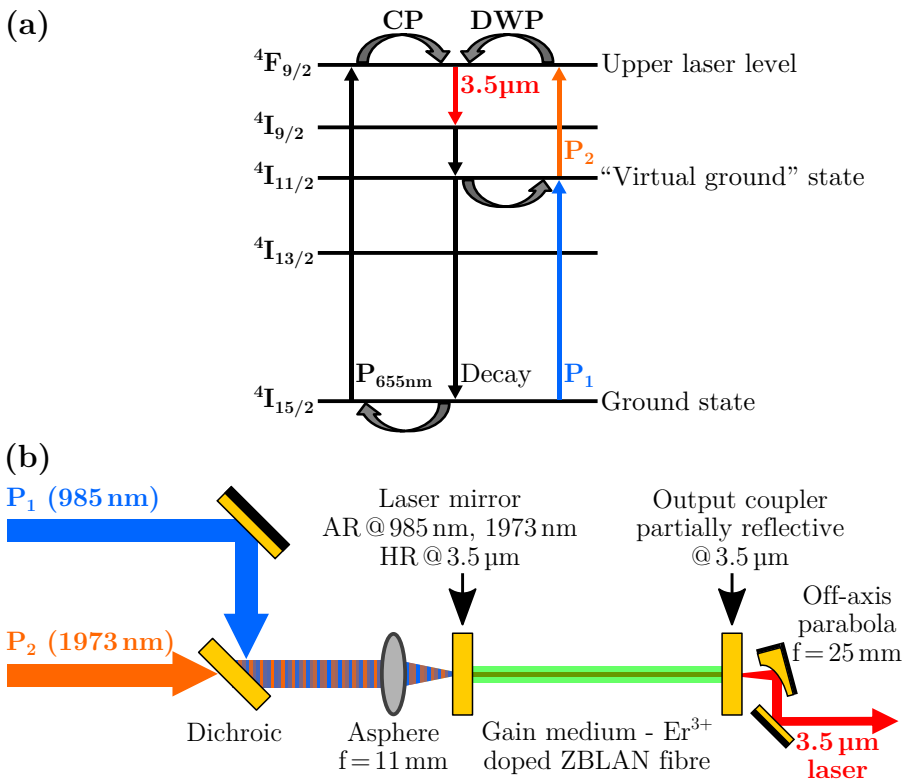

Figure 3.1: Dual-wavelength pumping technique of a 3.5 µm Er^{3+}-doped ZBLAN fibre laser. (a) Energy levels of Er^{3+} ions showing pump and laser transitions for conventional pumping (CP)[64] and dual-wavelength pumping (DWP).[161] (b) Schematic showing that pumps P_1 and P_2 are mode matched and launched into the fibre gain medium.[161]

A schematic of a DWP fibre laser system is shown in Figure 3.1(b).[62,161] Two pumps, P_1 and P_2, which emit light in two different wavelength bands, are mode matched and

launched into a single clad Er^{3+}-doped ZBLAN fibre gain medium. The resonator mirror butted to the input end of the fibre is anti-reflective (AR) at both pump wavelengths and highly reflective (HR) at 3.5 µm, while the output coupler is partially reflective at 3.5 µm. Henderson-Sapir et al.[61] and Fortin et al.[60] reported demonstrations of 3.5 µm DWP fibre lasers using the same type of double-clad Er^{3+}-doped zirconium fluoride fibre where P_1 was cladding-pumped and P_2 was core-pumped. Henderson-Sapir et al.[61] used discrete highly reflective and output coupler mirrors butt-coupled to the fibre tips while Fortin et al.[60] used an all fibre geometry including a fibre Bragg grating, written directly into the fibre, as the output coupler.

The model was calibrated and validated against the laser output powers of three 3.5 µm DWP fibre lasers that used the same type of double-clad fibre – one reported by Henderson-Sapir et al.[61] where P_1 power was held fixed at 2 W and two reported by Fortin et al.[60] where P_1 power was set to 3.5 W and 6.5 W. The simulated fibre properties were common to all three experiments while uncertain parameters, such as losses at resonator mirrors, were treated as variables within reasonable uncertainties that were estimated from literature. Approximately 5,000 simulations, submitted in 300 job arrays, were performed on supercomputers and analysed during candidature to validate the model against these experiments.

In addition to predicting laser output power, the model also provides time-domain information with high temporal resolution. The evolution of energy level populations over time provides valuable insight into laser threshold conditions, the fast changes that occur immediately following threshold, and steady state populations. This model has become a valuable tool for optimising fibre laser design and performance.

Statement of Authorship

Title of Paper	Numerical Modeling of 3.5 µm Dual-Wavelength Pumped Erbium-Doped Mid-Infrared Fiber Lasers
Publication Status	Published
Publication Details	A. Malouf, O. Henderson-Sapir, M. Gorjan, D. J. Ottaway. *IEEE J. Quantum Electron.*, 52(11):1–2, Nov 2016. doi: 10.1109/JQE.2016.2611440.

Principal Author

Principal Author	Andrew Malouf		
Contribution to the Paper	Model development, optimisation, and implementation; simulations; data analysis; figures; writing of manuscript.		
Overall Percentage	70 %		
Signature		Date	*15/03/2019*

Co-Author Contributions

By signing the Statement of Authorship, each author certifies that:

i. the candidate's stated contribution to the publication is accurate (as detailed above);
ii. permission is granted for the candidate to include the publication in the thesis; and
iii. the sum of all co-author contributions is equal to 100 % less the candidate's stated contribution.

Co-Author	Ori Henderson-Sapir		
Contribution to the Paper	Supervision of project; assistance with information, theory and data analysis; assistance with writing and editing of manuscript; corresponding author.		
Signature		Date	*17/03/2019*

Co-Author	Martin Gorjan		
Contribution to the Paper	Provision of code that was useful for model development; corresponding author.		
Signature		Date	*18/03/2019*

Co-Author	David J. Ottaway		
Contribution to the Paper	Supervision of project; assistance with theory, numerical methods, and application ideas; assistance with writing and editing of manuscript; corresponding author.		
Signature		Date	*16/03/2019*

Numerical Modelling of 3.5 µm Dual-Wavelength Pumped Erbium-Doped Mid-Infrared Fibre Lasers

Abstract

The performance of mid-infrared Er^{3+}-doped fibre lasers has dramatically improved in the last few years. In this paper we present a numerical model that provides valuable insight into the dynamics of a dual-wavelength pumped fibre laser that can operate on the 3.5 µm and 2.8 µm bands. This model is a much needed tool for optimising and understanding the performance of these laser systems. Comparisons between simulation and experimental results for three different systems are presented.

I Introduction

New mid-infrared laser sources will enable significant advances in a wide range of applications including spectroscopy,[3] remote sensing,[29] non-invasive medical diagnosis,[162] and defence countermeasure.[25] The mid-infrared spectral range is of particular interest in molecular spectroscopy,[163] since strong absorption features of many molecules (including hydrocarbons) are found there. The fundamental absorption lines for molecules containing bonds between hydrogen and carbon, nitrogen or oxygen are located between 2.8 µm and 4 µm.[163]

Dual-wavelength pumping (DWP) of an Er^{3+}-doped ZBLAN fluoride glass fibre is an efficient method of enabling a 3.5 µm laser at room temperature. This method takes advantage of long-lived excited states that cause bottlenecks which normally limit laser performance.[62] Recent work has demonstrated that emission between 3.3 µm and 3.8 µm can be achieved on the $^4F_{9/2} \rightarrow {}^4I_{9/2}$ transition when DWP is used.[61]

A numerical model has been developed to provide valuable insight into laser performance, the significance of competing processes, and the interactions that occur at the atomic and photonic level. The model can be used to analyse system design and predict optimum fibre specifications.

Several numerical models have been developed to study lasers that operate on the 2.8 µm transition in Er^{3+}-doped fibre lasers. Gorjan et al.[159] numerically investigated the significance of interionic processes in Er^{3+}-doped ZBLAN while Li et al.[157] numerically optimised parameters such as doping concentration. We present a model that has been developed and experimentally validated against three published DWP systems[60–62] operating on the 3.5 µm transition. We discuss the factors that limit their performance and methods of optimisation. The model can be adapted to any fibre

laser system.

The paper is organised as follows: Section II introduces the scientific and mathematical basis of the numerical model. Sections III and IV describe the validation procedure for the model. In Section V we discuss the findings and potential optimisations. Finally, conclusions are presented in Section VI.

II Basis of numerical model

The energy level transitions in Er^{3+} that are associated with the DWP system are illustrated in Figure 3.2.[61,164] Most decay processes are omitted for brevity but would simply be represented by arrows connecting each excited state to each level below it. A comparison of conventional pumping (CP)[64] and DWP[62] techniques used to generate 3.5 µm lasing (L_2) are included in the left of Figure 3.2. The CP technique pumps ions from ground level $^4I_{15/2}$ (1) directly to the upper laser level $^4F_{9/2}$ (5) using one 655 nm pump source (P_{655nm}).

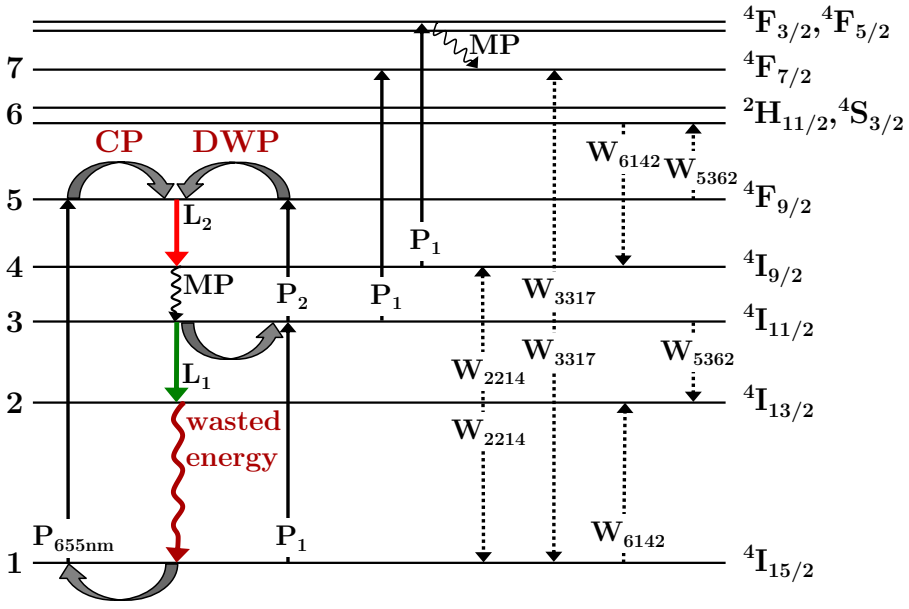

Figure 3.2: The energy levels of erbium ions showing DWP transitions due to pump absorption of the first (P_1) and second (P_2) pumps, 2.8 µm lasing (L_1), 3.5 µm lasing (L_2), and energy transfer processes W_{ijkl}. A comparison between conventional pumping (CP) and dual-wavelength pumping (DWP) techniques is illustrated on the left. Two important multi-phonon (MP) decay processes are illustrated while other decay processes are omitted for brevity.

The DWP technique uses a pump source with a wavelength of 966 – 985 nm[60,61] (P_1) to excite ions from the ground level $^4I_{15/2}$ (1) to level $^4I_{11/2}$ (3), and a pump source with a wavelength of 1973 – 1976 nm[60,61] (P_2) to excite ions from levels $^4I_{11/2}$ (3) to $^4F_{9/2}$ (5). DWP takes advantage of the long lifetime of level $^4I_{11/2}$ (3) which acts as an

elevated "virtual" ground state and cycles ions between levels $^4I_{11/2}$ (3) and $^4F_{9/2}$ (5). DWP significantly increases efficiency compared with CP since less energy is wasted by decay from level $^4I_{11/2}$ (3) back to the ground state. Low P_2 powers enable lasing at 2.8 µm (L_1) on the $^4I_{11/2} \rightarrow {}^4I_{13/2}$ transition.

A numerical model, titled "Fibre Laser Atomic and Photonic Populations" (FLAPP), was developed in MATLAB[165] to solve the rate equations listed in Section 'Rate equations'. This model is mathematically similar to that described by Gorjan et al.[159].

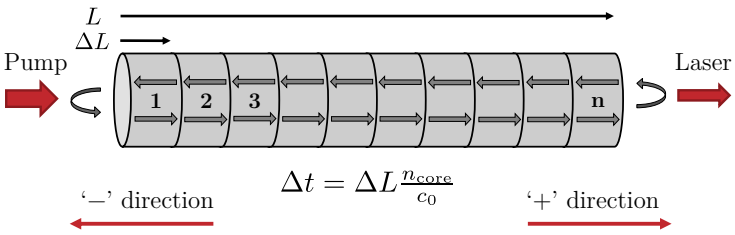

Figure 3.3: Numerical iteration of photon propagation in a fibre divided into n length elements. Photons propagate in the '+' or '−' direction. n_{core} is the refractive index of the fibre core and c_0 is the speed of light in a vacuum. The time step Δt is defined as the time required for light to traverse a single fibre element of length $\Delta L = \frac{L}{n}$.

This model solves the atomic and photonic populations at discrete sections of the fibre. This is achieved by dividing the fibre into a number of length elements n as illustrated in Figure 3.3. The rate equations are solved at each time step for each length element using the fourth order Runge-Kutta (RK4) method. Time and space are coupled such that the time step Δt is defined as the time required for light to traverse a single fibre element of length $\Delta L = \frac{L}{n}$.[159] The photonic populations are shifted one length element at each time step. At the fibre ends, these populations are reflected from, or transmitted through, the resonator mirrors.

The model FLAPP is an enhancement of that developed by Gorjan et al.[159] because it solves the rate equations for a single 2D population matrix that contains all populations of all fibre elements. This results in a significant reduction in computational time. The model also uses 3D parameter matrices so that parameters may be varied for multiple parallel simulations.

Pump absorption

The first pump has a wavelength between 966 nm[60] and 985 nm[62] depending on the experiment and is labelled P_1. This pump launches photons into either the core[62] or the inner cladding[60,61] at one end of the fibre. The ions that absorb these pump photons are excited from energy level $^4I_{15/2}$ (1) to level $^4I_{11/2}$ (3) by ground state absorption (GSA).

The second pump, P_2, has a wavelength between 1973 nm[62] and 1976 nm[60] depending on the experiment and is launched into the fibre core. The ions in level $^4I_{11/2}$ (3) that absorb photons from the second pump are excited to level $^4F_{9/2}$ (5). The model allows for pumping from either end of the fibre or from both ends simultaneously.

There are two excited state absorption (ESA) processes associated with the first pump – one from level $^4I_{11/2}$ (3) to level $^4F_{7/2}$ (7) and one from level $^4I_{9/2}$ (4) to level $^4F_{3/2}$ followed by fast multi-phonon decay to level $^4F_{7/2}$ (7). The latter excited state absorption is treated as a direct transition from levels $^4I_{9/2}$ (4) to $^4F_{7/2}$ (7) due to the fast multi-phonon decay.

Relaxation

Each excited energy level has an intrinsic lifetime, τ, and relaxation rate, $r{=}\tau^{-1}$ which includes radiative (fluorescence) and non-radiative multi-phonon (MP) decay. Relaxation from an upper level i to a lower level j has an associated branching ratio β_{ij} where $\sum_{j=1}^{i-1}\beta_{ij}{=}1$. Then the relaxation rate r_{ij} from an upper level i to lower level j is given by $r_{ij}{=}\beta_{ij}r_i{=}\beta_{ij}\tau_i^{-1}$.

Lasing

Pump absorption of P_1 and P_2 photons creates a population inversion between the $^4I_{9/2}$ (4) and $^4F_{9/2}$ (5) energy levels. Spontaneous emission (radiative decay) from level $^4F_{9/2}$ (5) to level $^4I_{9/2}$ (4) initiates lasing at a wavelength of 3.5 µm. Similarly, radiative decay from level $^4I_{11/2}$ (3) to level $^4I_{13/2}$ (2) can initiate lasing at a wavelength of 2.8 µm.

The rate of spontaneous emission R_{sp} is proportional to the population of the upper laser level N_{upper}. The rate of stimulated emission R_{se} is proportional to the laser photon density F_{laser} multiplied by N_{upper}. Note that laser photons may be reabsorbed by ions in the lower laser level N_{lower}, reducing the effective gain of stimulated emission. The rate of absorption is proportional to F_{laser} and N_{lower}. The cross sections of these transitions are elaborated in Section 'Cross sections'.

Interionic processes

Energy transfer processes are non-radiative energy exchanges that occur between ions. The significance of these interactions is often dependent on doping concentration[156,166] which determines the mean spacing between ions and hence the probability of interactions.

The relevant energy transfer process W_{ijkl} describes the non-radiative energy exchange between two ions initially in levels i and j that transition to levels k and l. The

energy transfer processes in Er^{3+}-doped ZBLAN that have been published in literature are W_{2214}, W_{3317}, W_{6142}, and W_{5362}.[164,166] The rate W_{ijkl} is expressed in units of volume per unit time.

Rate equations

The atomic and photonic rate equations are stated below with spatial and time dependence omitted for brevity. A detailed explanation of each term follows.

The atomic rate equations are:

$$\frac{\mathrm{d}N_7}{\mathrm{d}t} = -\sum_{i=1}^{6} r_{7i}N_7 + R_{\mathrm{P_1abs_{37}}}F_{\mathrm{P_1}} + R_{\mathrm{P_1abs_{47}}}F_{\mathrm{P_1}} + W_{3317}N_3^2 \tag{3.1}$$

$$\frac{\mathrm{d}N_6}{\mathrm{d}t} = r_{76}N_7 - \sum_{i=1}^{5} r_{6i}N_6 - W_{6142}N_6N_1 + W_{5362}N_5N_3 \tag{3.2}$$

$$\frac{\mathrm{d}N_5}{\mathrm{d}t} = \sum_{i=6}^{7} r_{i5}N_i - \sum_{i=1}^{4} r_{5i}N_5 + R_{P_2abs_{35}}F_{P_2} - R_{L_2se_{54}}F_{L_2} - W_{5362}N_5N_3 \tag{3.3}$$

$$\frac{\mathrm{d}N_4}{\mathrm{d}t} = \sum_{i=5}^{7} r_{i4}N_i - \sum_{i=1}^{3} r_{4i}N_4 - R_{\mathrm{P_1abs_{47}}}F_{\mathrm{P_1}} + R_{\mathrm{L_2se_{54}}}F_{\mathrm{L_2}} + W_{2214}N_2^2 + W_{6142}N_6N_1 \tag{3.4}$$

$$\frac{\mathrm{d}N_3}{\mathrm{d}t} = \sum_{i=4}^{7} r_{i3}N_i - \sum_{i=1}^{2} r_{3i}N_3 + R_{\mathrm{P_1abs_{13}}}F_{\mathrm{P_1}} - R_{\mathrm{P_1abs_{37}}}F_{\mathrm{P_1}} - R_{\mathrm{P_2abs_{35}}}F_{\mathrm{P_2}} - R_{\mathrm{L_1se_{32}}}F_{\mathrm{L_1}} - 2W_{3317}N_3^2 - W_{5362}N_5N_3 \tag{3.5}$$

$$\frac{\mathrm{d}N_2}{\mathrm{d}t} = \sum_{i=3}^{7} r_{i2}N_i - r_{21}N_2 + R_{\mathrm{L_1se_{32}}}F_{\mathrm{L_1}} - 2W_{2214}N_2^2 + W_{6142}N_6N_1 + W_{5362}N_5N_3 \tag{3.6}$$

$$\frac{\mathrm{d}N_1}{\mathrm{d}t} = \sum_{i=2}^{7} r_{i1}N_i - R_{\mathrm{P_1abs_{13}}}F_{\mathrm{P_1}} + W_{2214}N_2^2 + W_{3317}N_3^2 - W_{6142}N_6N_1 \tag{3.7}$$

$$N_{\mathrm{core}} = \sum_{i=1}^{7} N_i \tag{3.8}$$

where N_i is the population density of ions in energy level i, N_{core} is the doping density of ions in the fibre core, F is the photonic population number density, and r_{ij} is the intrinsic relaxation rate from level i to j. $R_{\mathrm{P}_k\mathrm{abs}_{ij}}$ is the rate of pump absorption of pump P_k with transitions from level i to j and $R_{\mathrm{L}_k\mathrm{se}_{ij}}$ is the rate of stimulated emission of laser L_k with transition from level i to j. W_{ikjl} is the rate of interionic interactions resulting in transitions from levels i and j to k and l.

The absorption and stimulated emission rates include the populations of the upper and lower laser energy levels and the cross sections of transitions between them.

$$R_{\mathrm{P}_k\mathrm{abs}_{ij}} = v\left(\sigma_{\mathrm{P}_k\mathrm{abs}_{ij}}N_i - \sigma_{\mathrm{P}_k\mathrm{em}_{ji}}N_j\right) \tag{3.9}$$

$$R_{\mathrm{L}_k\mathrm{se}_{ij}} = v\sigma_{\mathrm{L}_k\mathrm{se}_{ij}}\left(b_iN_i - \frac{g_i}{g_j}b_jN_j\right) \tag{3.10}$$

$$= v\left(\sigma_{\mathrm{L}_k\mathrm{em}_{ij}}N_i - \sigma_{\mathrm{L}_k\mathrm{abs}_{ji}}N_j\right) \tag{3.11}$$

where $v{=}\frac{c_0}{n_{\mathrm{core}}}$ is the speed of light inside the fibre, approximated to be constant for pump and laser wavelengths. $\sigma_{\mathrm{P}_k\mathrm{abs}_{ij}}$ and $\sigma_{\mathrm{P}_k\mathrm{em}_{ji}}$ are the effective cross sections of absorption and emission of pump P_k for the transition between levels i and j. $\sigma_{\mathrm{L}_k\mathrm{se}_{ij}}$ is the cross section of stimulated emission of laser L_k for the transition from level i to j. $\sigma_{\mathrm{L}_k\mathrm{em}_{ij}}$ and $\sigma_{\mathrm{L}_k\mathrm{abs}_{ji}}$ are the effective cross sections of emission and absorption of laser L_k. b_i and b_j are the Boltzmann factors of the upper and lower laser sublevels i and j. g_i and g_j are the degeneracies of the upper and lower laser sublevels.

For Er^{3+} ions, each energy level is split into $(2J{+}1)\,/2$ Stark levels, where J is the total angular momentum quantum number, leaving Kramers degeneracy.[167] Therefore, the Stark levels in Er^{3+} (having odd number of electrons) have degeneracies $g_i{=}g_j{=}2$.[156]

Photonic population densities are calculated for propagation in each of the '+' and '−' directions illustrated in Figure 3.3. Note that we calculate the photonic populations inside the core only since only these populations are available to interact with the Er^{3+} ions. The mode fields extend outside the core for wavelengths that have fibre V parameters smaller than 2.4 (see Section 'Mode overlap') such that only the single transverse mode is guided. Therefore, we include a mode overlap factor Γ to correct for rates of change of population density within the core.[168]

The photonic rate equations are:

$$\frac{\mathrm{d}F^{\pm}_{\mathrm{P}_1}}{\mathrm{d}t} = \Gamma_{\mathrm{P}_1}\left[-R_{\mathrm{P}_1\mathrm{abs}_{13}} - R_{\mathrm{P}_1\mathrm{abs}_{37}} - R_{\mathrm{P}_1\mathrm{abs}_{47}}\right]F^{\pm}_{\mathrm{P}_1} + R_{\mathrm{P}_1\mathrm{loss}}F^{\pm}_{\mathrm{P}_1} \tag{3.12}$$

$$\frac{\mathrm{d}F^{\pm}_{\mathrm{P}_2}}{\mathrm{d}t} = \Gamma_{\mathrm{P}_2}\left[-R_{\mathrm{P}_2\mathrm{abs}_{35}}F^{\pm}_{\mathrm{P}_2}\right] + R_{\mathrm{P}_2\mathrm{loss}}F^{\pm}_{\mathrm{P}_2} \tag{3.13}$$

$$\frac{\mathrm{d}F^{\pm}_{\mathrm{L}_1}}{\mathrm{d}t} = \Gamma_{\mathrm{L}_1}\left[R_{\mathrm{L}_1\mathrm{se}_{32}}F^{\pm}_{\mathrm{L}_1} + R_{\mathrm{L}_1\mathrm{sp}_{32}}\right] + R_{\mathrm{L}_1\mathrm{loss}}F^{\pm}_{\mathrm{L}_1} \tag{3.14}$$

$$\frac{\mathrm{d}F^{\pm}_{\mathrm{L}_2}}{\mathrm{d}t} = \Gamma_{\mathrm{L}_2}\left[R_{\mathrm{L}_2\mathrm{se}_{54}}F^{\pm}_{\mathrm{L}_2} + R_{\mathrm{L}_2\mathrm{sp}_{54}}\right] + R_{\mathrm{L}_2\mathrm{loss}}F^{\pm}_{\mathrm{L}_2} \tag{3.15}$$

where $F^{\pm}$ is the density of pump P_k of laser L_k photons propagating in the '±' direction and Γ is the mode overlap factor of the photon field as defined in Section 'Mode overlap'. $R_{\mathrm{L}_k\mathrm{loss}}$ and $R_{\mathrm{P}_k\mathrm{loss}}$ are the loss rates of laser and pump photons. $R_{\mathrm{L}_k\mathrm{sp}_{ij}}$ is the spontaneous emission rate of laser L_k photons from level i to j.

The rate term for spontaneous emission is given by

$$R_{\mathrm{L}_k \mathrm{sp}_{ij}} = \frac{f_{\mathrm{accept}}}{2} f_{\mathrm{rad}} r_{ij} N_i \tag{3.16}$$

where f_{accept} is the probability of acceptance of a spontaneously emitted photon being trapped in the fibre in either direction of propagation, and f_{rad} is the probability that the relaxation is radiative.

Cross sections

For two nondegenerate states of manifold sublevels i and j, the emission and absorption cross sections will be equal, i.e., $\sigma_{ij}{=}\sigma_{ji}$.[169] In the case of rare earth ions doped into a host, any 'level' is actually a manifold of sublevels and a transition of energy separation $h\nu$ can occur between multiple pairs of sublevels. The energy of each sublevel is slightly dependent on the host because variations in the local electric fields cause Stark shifts. The inhomogeneous nature of glass hosts means that effective sublevel energy positions are blurred rather than discrete.

The populations of each sublevel is dependent on thermal distribution and can be estimated by multiplication of the total level population by the Boltzmann factor of the sublevel. Therefore, a cross section must be defined at a particular frequency within the spectral bandwidth of the transition. A cross section derived from experimental measurement of absorption or emission spectra is an *effective* cross section, i.e., inclusive of the sublevel Boltzmann factor, at a given temperature.

Measured energy level positions and Stark splitting of Er^{3+} at 13 K are provided by Huang et al.[167] in units of cm^{-1}. We use this data and the McCumber relation[170] to calculate effective emission cross sections from absorption cross sections and vice versa. The McCumber relation considers that the population of each sublevel is determined by the Boltzmann population distribution and is expressed as follows:

$$\frac{\sigma_{\mathrm{em}}(\nu)}{\sigma_{\mathrm{abs}}(\nu)} = \frac{Z_1}{Z_2} \exp\left(\frac{E_{\mathrm{zl}} - h\nu}{kT}\right) = \exp\left(\frac{\epsilon - h\nu}{kT}\right) \tag{3.17}$$

where σ_{em} and σ_{abs} are the cross sections of emission and absorption at frequency ν for the transition between a lower energy level 1 and an upper energy level 2. $Z_i{=}\sum_j \exp\left(\frac{-E_j}{kT}\right)$ are the partition functions of the lower and upper energy levels that each form manifolds of sublevel energies E_j, k is the Boltzmann constant, and T is the temperature, assumed to be 300 K. E_{zl} is the zero-line energy difference between levels 1 and 2, defined to be the energy separation between the lowest sublevels of the two manifolds, and $h\nu$ is the photon energy. Letting $\frac{Z_1}{Z_2}\exp\left(\frac{E_{\mathrm{zl}}}{kT}\right) = \exp\left(\frac{\epsilon}{kT}\right)$ in Equation 3.17, where ϵ is a constant, shows that σ_{em} and σ_{abs} are equal at only one

frequency ν.

Mode overlap

A Gaussian intensity profile is a good approximation for a single mode field inside a step index fibre.[168] The intensity of each mode has a central peak and tends to zero away from longitudinal axis of the fibre. We define the mode overlap Γ at any given wavelength as the fraction of the power in the mode that overlaps the core. Only the overlapped portion of the mode is available to interact with the Er^{3+} ions. The entire mode, however, will be affected by gain or loss as a result of these interactions.

To estimate the mode overlap Γ of single mode operation, we take the approach of calculating the fraction of power transmitted through a circular aperture of radius equal to the fibre core radius a. This applies to the case of a lowest order mode only, which is well approximated by a Gaussian beam.

The intensity I of a Gaussian beam inside the fibre at a distance r from the longitudinal axis may be derived from the equation for the complex wave amplitude $\tilde{u}(x, y, z)$ given by Siegman.[169] Intensity is given by $I(r)=I_0 \exp\left(-2\frac{r^2}{w^2}\right)$ where w is the mode field radius. Then, using integration by substitution, we can calculate the mode overlap factor Γ as the ratio of power inside the core P_{core} of radius a to total power in the mode P_{mode}.

$$\Gamma = \frac{P_{\text{core}}}{P_{\text{mode}}} = \frac{\int_0^{2\pi}\int_0^{a} I(r) r \mathrm{d}r \mathrm{d}\phi}{\int_0^{2\pi}\int_0^{\infty} I(r) r \mathrm{d}r \mathrm{d}\phi} = 1 - \exp\left(-2\frac{a^2}{w^2}\right) \tag{3.18}$$

The mode field radius (or spot size) w for step index, single-mode fibres is estimated by the Marcuse empirical formula:[171]

$$w \approx a\left(0.65 + \frac{1.619}{V^{3/2}} + \frac{2.879}{V^6}\right) \tag{3.19}$$

where V is a parameter for step-index fibres defined by $V=\frac{2\pi}{\lambda} a\,(NA)$ and NA is the numerical aperture.

The mode overlap Γ of a highly multi-mode beam, such as the clad pumping of a double clad fibre, is estimated to be the ratio $A_{\text{core}}/A_{\text{clad}}$, where A_{core} and A_{clad} are the cross sectional areas of the core and clad and A_{clad} includes the area of the core.

The relation between the photon density inside the core F to total power in the mode P_{mode} is given by

$$F(\nu) = \frac{\bar{I}_{\text{core}}(\nu)\, n_{\text{core}}(\nu)}{h\nu c_0} = \Gamma(\nu)\,\frac{P_{\text{mode}}(\nu)\, n_{\text{core}}(\nu)}{Ah\nu c_0} \tag{3.20}$$

where ν is the photon frequency, A is the cross sectional area of the core, and $\bar{I}_{\text{core}}=\frac{P_{\text{core}}}{A}$

is the mean intensity inside the core in the transverse plane, i.e., the transverse intensity profile inside the core is assumed to be uniform.

Any change in photon population is distributed throughout the mode which extends beyond the fibre core. The mode overlap factor is implemented in the photonic rate equations to convert from rates of change of photon population in the mode F_{mode} to rates of change of photon population inside the fibre core F.

$$\frac{dF}{dt} \approx \frac{\Delta F}{\Delta t} = \Gamma \frac{\Delta F_{\text{mode}}}{\Delta t} \tag{3.21}$$

Loss rate

The loss rate is calculated from an internal loss coefficient that arises from scatter and absorption of pump and laser photons due to the glass host. This loss rate does not include transmission losses through resonator mirrors. The loss of laser photons is given by:

$$(\phi(z))_{\text{loss}} = \phi_0 \exp(-\alpha z) \tag{3.22}$$

where $\phi(z)$ is the number of photons (proportional to power) at distance z along the fibre propagating in either direction, ϕ_0 is the number of photons at z=0, and α is the measured *internal loss coefficient*, assumed to be constant along the length of the fibre. Therefore, the loss over a single fibre element length ΔL in time step Δt is

$$\left(\frac{\Delta\phi}{\Delta t}\right)_{\text{loss}} \approx \frac{\exp(-\alpha \Delta L) - 1}{\Delta t}\phi_0 \tag{3.23}$$

The rates of internal loss R_{loss} from the photonic rate Equations 3.14 and 3.15 at each wavelength λ are given by

$$\left(\frac{\mathrm{d}F}{\mathrm{d}t}\right)_{\text{loss}} = R_{\text{loss}} \approx \frac{\exp(-\alpha \Delta L) - 1}{\Delta t} \tag{3.24}$$

Two types of resonator mirror losses are also implemented in the model. The first is a *scattering loss* that reduces transmission without affecting reflection. The second is a *reflection efficiency* that reduces the effective mirror reflectivity without affecting transmission.

III Simulation parameters

The model, FLAPP, was tested on three experiments published in literature with their respective properties listed in Table 3.1. The first experiment (H2014)[62] used a single clad fibre manufactured by IR-Photonics (IRP). The second (H2016)[61] and third (F2016)[60] experiments used the same design double clad fibre manufactured by Le Verre Fluoré (LVF) that had a lower doping. The first pump was launched into the inner cladding and the second pump was launched into the core. This double clad fibre has a circular inner cladding (diameter 260 µm) with two parallel flats (separated by 240 µm). The second experiment used discrete highly reflective (HR) and output coupler (OC) mirrors butt-coupled to the fibre whereas the third experiment used an all fibre geometry including a fibre Bragg grating (FBG), written directly into the fibre, as the output coupler.

Table 3.1: Experimental properties.

Property	H2014[62]	H2016[61]	F2016[60]	Unit
Manufacturer	IRP	LVF	LVF	
Cladding	single	double	double	
Er^{3+}	1.7	1.0	1.0	mol.%
a	5.25	8.25	8.25	µm
NA(core)	0.150	0.125	0.125	
L	0.18	2.80	4.30	m
$R_{OC}(3.5\,\mu m)$	90	80	55	%
OC type	mirror	mirror	FBG	
$R_{HR}(3.5\,\mu m)$	99	99	90	%
HR type	mirror	mirror	mirror	
P_1 power	0.194	2.0	6.5, 3.5	W
P_1 pumping	core	clad	clad	
λ_{P_1}	985	977	966-974	nm
λ_{P_2}	1973	1973	1976	nm

Tables 3.2, 3.3, and 3.4 list the simulation parameters that were sourced and calculated from multiple references, including Refs. 156,159,161,167,172–176. Parameters found to be in good agreement with multiple independent sources were held fixed in the simulations. Such parameters include the absorption cross section of P_1, stimulated emission cross section of L_1, mirror reflectivities at each wavelength, and intrinsic lifetimes of levels $^4I_{13/2}$ (2) and $^4I_{11/2}$ (3). Parameters with larger uncertainties were altered independently, within their stated uncertainties, to test their significance. These parameters were likely to affect final results significantly if varied by 25 % or so from measured or published values. Such parameters include absorption cross section of pump P_2, stimulated emission cross section of the 3.5 µm laser transition, the cross relaxation parameter W_{5362}, and lifetimes of levels $^4I_{9/2}$ (4) and $^4F_{9/2}$ (5).

Table 3.2: Simulation parameters of pumps and lasers.

Property	H2014[62]	H2016[61]	F2016[60]	Unit	Ref.
λ_{P_1}	985	977	968	nm	
λ_{P_2}	1973	1973	1976	nm	
$\sigma_{P_1abs_{13}}$	9.30	19.5	8.56	$10^{-26}\,m^2$	173
$\sigma_{P_1abs_{37}}$	2.00	9.30	30.7	$10^{-26}\,m^2$	173
$\sigma_{P_1abs_{47}}$	25.5	13.5	2.10	$10^{-26}\,m^2$	173
$\sigma_{P_2abs_{35}}$	30.0	30.0	30.0	$10^{-26}\,m^2$	161
$\sigma_{P_1em_{31}}$	11.5	16.1	4.45	$10^{-26}\,m^2$	167,173
$\sigma_{P_1em_{73}}$	6.75	21.1	44.0	$10^{-26}\,m^2$	167,173
$\sigma_{P_1em_{74}}$	47.8	17.4	1.70	$10^{-26}\,m^2$	167,173
$\sigma_{P_2em_{53}}$	36.1	36.1	37.5	$10^{-26}\,m^2$	161,167
λ_{L_1}	2800	2800	2800	nm	
λ_{L_2}	3470	3470	3440	nm	
$\sigma_{L_1em_{32}}$	45.0	45.0	45.0	$10^{-26}\,m^2$	176
$\sigma_{L_2em_{54}}$	12.0	12.0	10.8	$10^{-26}\,m^2$	64,161
b_2	0.210	0.210	0.210		167
b_3	0.350	0.350	0.350		167
b_4	0.575	0.575	0.427		167
b_5	0.435	0.435	0.308		167
R_{OC} (3.5 µm)	87	58	55	%	
R_{HR} (3.5 µm)	99	99	86	%	
α (3.5 µm)	0.060	0.035	0.035	m^{-1}	

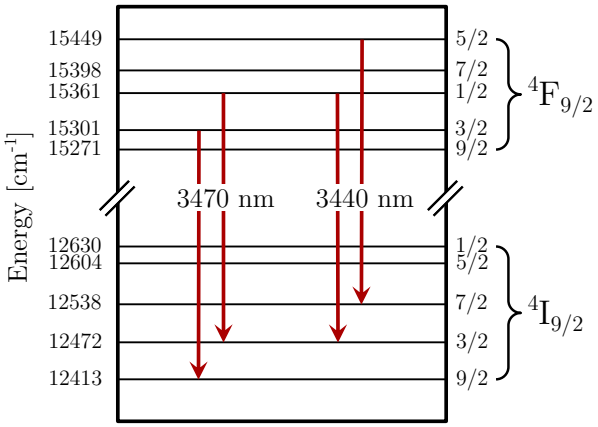

Figure 3.4: Stark splitting in Er^{3+}-doped ZBLAN and predicted laser transitions of lasers developed by Henderson-Sapir et al.[61,62] (3470 nm) and Fortin et al.[60] (3440 nm). Each arrow connects a pair of Stark levels that correspond to the predicted transitions of the associated wavelengths. The energy data was sourced from Ref. 167 and the assignment order of Stark levels was sourced from Ref. 177.

The emission cross sections, σ_{P_1em} and σ_{P_2em}, of the first and second pumps were calculated from absorption measurements[161] using McCumber theory. The effective stimulated emission cross section σ_{L_2em} of the 3.5 µm laser was estimated using the 3.5 µm fluorescence spectrum given by Többen[64] and the Füchtbauer-Ladenburg equation.[161] The 3.5 µm laser transitions, predicted from measured Stark split energy levels,[167] is

shown in Figure 3.4. The Boltzmann factors b_i of the Stark split upper and lower energy levels were calculated using the partition function Z of each level as follows:

$$b_i = \frac{\exp\left(\frac{-E_i}{kT}\right)}{Z} = \frac{\exp\left(\frac{-E_i}{kT}\right)}{\sum_i \exp\left(\frac{-E_i}{kT}\right)} \tag{3.25}$$

where k is the Boltzmann constant and T is the temperature, assumed to be 300 K. The Boltzmann factors b_i were then summed for each predicted laser transition for each level.

The simulation reflectivities of the butt-coupled mirrors are lower than their specified values since the light is incident from a ZBLAN fibre (refractive index n_{core}=1.48) rather than from air. The dielectric coatings of the mirrors used in experiments H2014[62] and H2016[61] is proprietary information and, therefore, we had to make our own predictions about their composition and number of layers. We also performed 0° reflectivity measurements on the 90 % and 80 % output couplers that resulted in 90±1 % and 75±1 % respectively. The simulation reflectivities were calibrated to give good agreement with the slope efficiencies of experimental data.

The intrinsic lifetimes τ_i and branching ratios β_{ij} in Er^{3+}-doped ZBLAN that were used in each simulation are listed in Table 3.3.

Table 3.3: Spectroscopic parameters of Er^{3+}.

Parameters	Value	Source
τ_2	9.9 ms	174
τ_3	7.9 ms	174
τ_4	8.0 µs	174
τ_5	177 µs	174
τ_6	530 µs	174
τ_7	5.0 µs	178
β_{21}	1	174
β_{32}, β_{31}	0.182, 0.818	174
β_{43}, β_{41}	0.999, 0.001	174
$\beta_{54}, \beta_{53}, \beta_{52}, \beta_{51}$	0.808, 0.008, 0.009, 0.175	174
$\beta_{65}, \beta_{64}, \beta_{63}, \beta_{62}, \beta_{61}$	0.285, 0.029, 0.014, 0.193, 0.479	174
β_{76}, β_{71}	0.990, 0.010	178

The interionic parameters used in the simulations are listed in Table 3.4 and are consistent with the weakly interacting regime in recent literature.[156,159,164] Interionic processes in Er^{3+}-doped ZBLAN fibres are currently not fully understood and a future direct measurement of their strength in fibres (compared with bulk glass) would be beneficial. There are discrepancies in literature regarding the rate values of the significant processes and their dependence on doping concentration, particularly between

bulk glass and fibre.[156,159,166,174] ZBLAN composition and quality of fibre draw may vary between suppliers and draws. This variation may result in different distributions of Er^{3+}-ions[179] which affect the rates at which interionic processes occur.

Table 3.4: Simulation parameters of interionic processes.

Parameters	Value ($10^{-24}\,m^3\,s^{-1}$)	Ref.
W_{2214}	0.40	156,164
W_{3317}	0.08	156,164
W_{6142}	0.10	156,164
W_{5362}	17.0	164

The upper and lower energy levels of the 3.5 µm laser transition are highly populated in the DWP system compared with the more common singly pumped 2.8 µm Er^{3+}-doped ZBLAN fibre laser. The work of Bogdanov[174] shows that further processes, including reverse processes, are possible. These processes could have a greater affect on the 3.5 µm DWP system than the 2.8 µm fibre laser. One example of such a process is W_{3251}[174] that would transfer ions from the virtual ground state $^4I_{11/2}$ (3) to the upper laser level $^4F_{9/2}$ (5). This process was not included in the model since, to the best of our knowledge, no direct measurement of its value has been made.

IV Model validation

We identified a list of parameters that were either measured directly or published in literature and held those parameters fixed in simulations. We then varied the remaining variable parameters slightly, within their published uncertainties or our estimate of their bounds, until we found a cohesive set of parameters that gave good agreement with experimental results. These values were therefore maintained for the three systems H2014,[62] H2016,[61] and F2016.[60]

Steady state results gave excellent agreement between the cases where both pumps were switched on simultaneously and where P_1 was switched on 20 ms prior to P_2. Therefore, we switched both pumps on simultaneously for all presented simulations. The number of fibre elements n chosen for each system was determined by finding the minimum n such that the variation between successive simulations was negligible. These were n_{H2014}=10, n_{H2016}=28, and n_{F2016}=43.

Time domain – H2014[62]

In this section, we study the time evolution of the atomic populations and intracavity laser power. We also show that 20 ms is sufficient time to reach steady state. In each of the following two examples, the power of pump P_1 is held fixed at 194 mW.

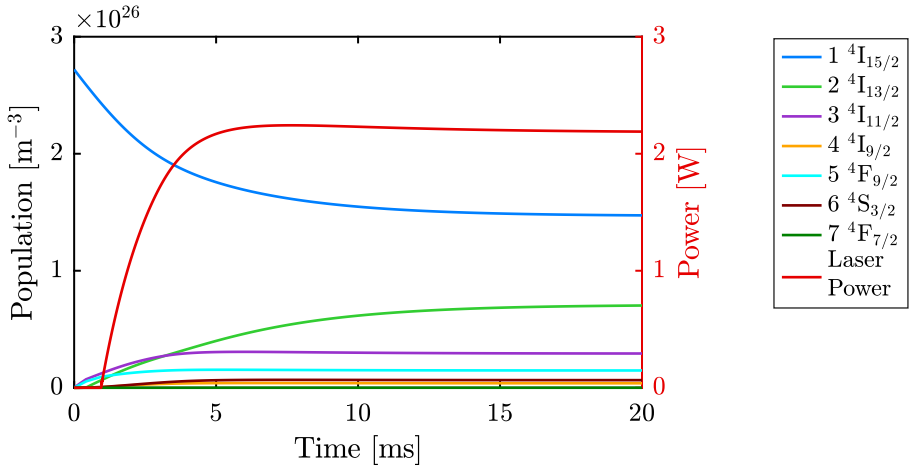

Figure 3.5: Modelled atomic populations of experiment H2014 by Henderson-Sapir et al.[62]. The populations are calculated midway along the fibre in the case where pump P_1 operates at 194 mW and P_2 operates at 2 W CW. The intracavity 3.47 µm laser power propagating in the '+' direction is plotted against the right axis.

In Figure 3.5 the atomic populations in the middle fibre element are shown (left axis) as these approximate the mean population along the fibre. The intracavity 3.47 µm laser power midway along the fibre, propagating in the '+' direction, is also shown (right axis). Pump P_2 operates at 2 W CW.

The threshold condition for lasing is reached at around 1 ms, after which the laser power increases rapidly over the following 4 ms. When threshold is reached, the population in level $^4F_{9/2}$ (5) remains fairly constant beyond 1 ms. A large population is bottlenecked in level $^4I_{13/2}$ (2) due to its relatively long intrinsic lifetime of τ_2=9.9 ms. Therefore steady state for this system is reached at around 20 ms, making 20 ms duration simulations sufficient for steady state analysis.

Intracavity laser power immediately after threshold is illustrated in Figure 3.6. For both laser transitions, the well known relaxation oscillations[169] are observed. The relaxation oscillations are stronger on the 2.8 µm laser emission than the 3.5 µm emission due to the higher stimulated emission cross section on the 2.8 µm transition. This means that 3.5 µm transition relaxation oscillations have a lower frequency and damp out prior to full power being reached. The figure also illustrates that the 2.8 µm laser operates at low power (20 mW intracavity power) and is gradually suppressed by the build-up of ions in its lower lasing level $^4I_{13/2}$ (2).

Lasing occurs at 2.8 µm on the $^4I_{11/2} \rightarrow {}^4I_{13/2}$ transition when pump P_1 is fixed at 194 mW and the power of P_2 is low. An interesting experimental observation occurs whilst pulsing P_2 at low power in which lasers pulse alternately between wavelengths of 3.47 µm and 2.8 µm. Our simulations have reproduced this behaviour as illustrated in Figure 3.7. This figure shows the modelled intracavity laser power when pump P_2

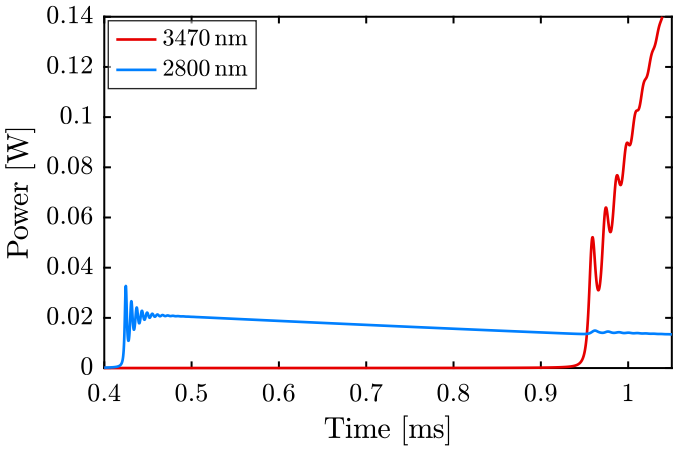

Figure 3.6: Modelled intracavity laser power of experiment H2014 by Henderson-Sapir et al.[62] immediately after threshold of the 2.8 µm and 3.47 µm lasers. The power is calculated midway along the fibre in the case where pump P_1 operates at 194 mW and P_2 operates at 2 W CW. The figure illustrates oscillatory behaviour at each laser wavelength immediately after threshold. The powers plotted are for lasers propagating in the '+' direction only.

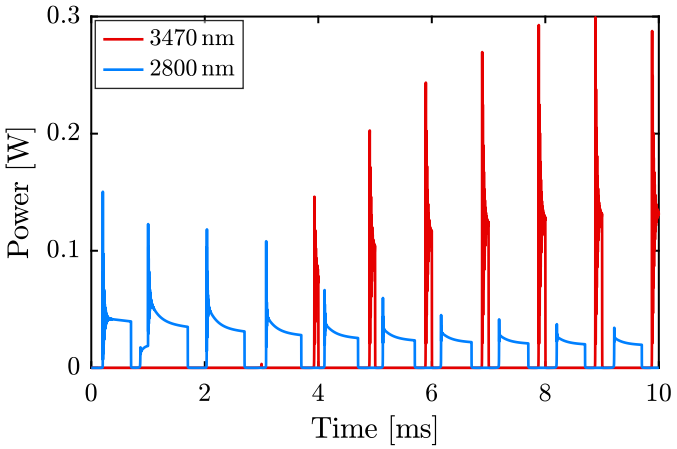

Figure 3.7: Modelled intracavity laser power of experiment H2014 by Henderson-Sapir et al.[62,180] in low power pulsed operation. The power is calculated midway along the fibre over a 10 ms simulation. Pump P_2 operates at 200 mW with 300 µs pulses at a repetition rate of 1 kHz. Lasers pulse alternately between wavelengths of 2.8 µm and 3.47 µm.

is pulsed at low power (200 mW peak) with 300 µs pulses at a repetition rate of 1 kHz. For this phenomenon to be observed, the power of P_2 needs to be low enough to retain a sufficient population in the $^4I_{11/2}$ (3) level between pulses to enable lasing at 2.8 µm.

Laser output power – H2014[62]

The model calculates pump and laser transmission in both the '+' and '−' directions since both resonator mirrors are partially transmissive at each of the pump and laser wavelengths. In all of our simulations, the pumps are launched into the '−' end of the fibre and the output coupler is located at the '+' end of the fibre. Therefore, all transmission results that follow are transmissions in the '+' direction.

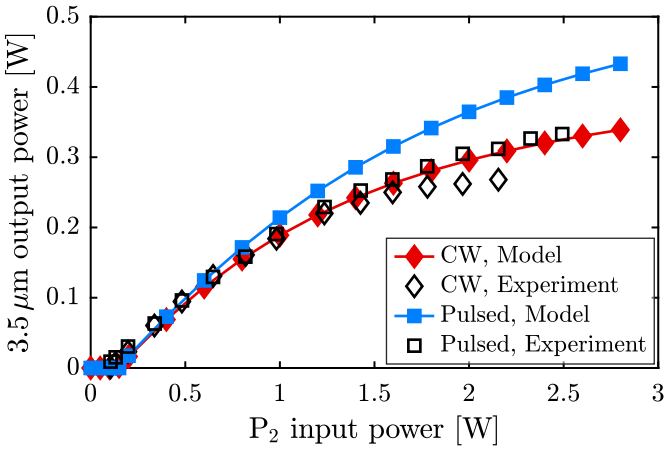

Figure 3.8: Modelled 3.47 µm laser output power of experiment H2014 by Henderson-Sapir et al.[62] for CW and pulsed operation.

Modelled 3.47 µm laser output power of experiment H2014 as a function of incident P_2 power is presented in Figure 3.8. The plot shows reasonable agreement between modelled and experimental data for both CW and pulsed operation.[180] The modelled threshold power matches experiment well at just above 100 mW. Modelled slope efficiencies and the non-linear power saturations are also closely matched to experiment.

When pulsed, the 1973 nm pump operated at a frequency of 1 kHz and a duty cycle of 30 %. The experimental pulse power was determined by dividing the average transmitted power (detected by a slow thermopile) by the duty cycle of the pulse (0.3 in this case).

The model predicts a higher saturation level than seen in experiment. This may be explained by a slight misalignment of the fibre that develops at the pump input end due to thermal expansion against the butt-coupled HR mirror. The fibre tip, initially heated by P_1 core pumping, expands further with increasing P_2 power since scattered pump light that is not launched into the core is absorbed by the fibre coating. The misalignment results in saturation of laser power.

Pump transmission – H2014[62]

Modelled CW pump transmission of experiment H2014 is presented in Figure 3.9. Transmission of both pumps P_1 and P_2 are shown. The plot shows good agreement between modelled and experimental data for both pumps. Nearly all of the P_1 power is absorbed before reaching the output coupler. The transmission of pump P_2 is dependent upon populations in levels $^4I_{11/2}$ (3) and $^4F_{9/2}$ (5) as well as pump absorption and emission cross sections (see Equation 3.9). The calculated populations in levels $^4I_{11/2}$ (3) and $^4F_{9/2}$ (5) are dependent on parameters that have considerable uncertainties including launch efficiency, the cross relaxation rate W_{5362}, and the lifetimes of the 3.5 µm laser levels $^4F_{9/2}$ (5) and $^4I_{9/2}$ (4).

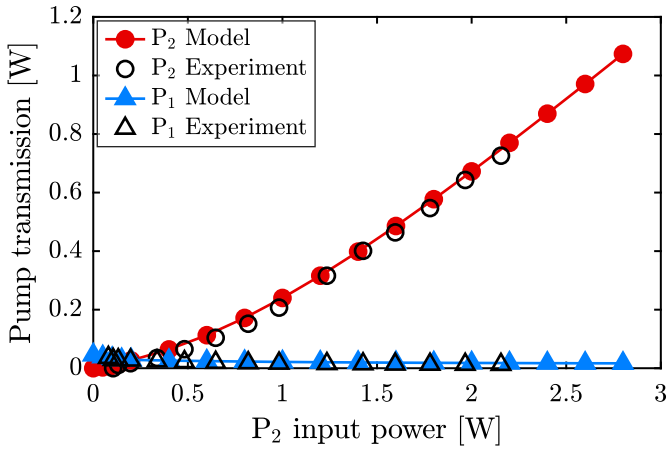

Figure 3.9: Modelled CW pump transmission of experiment H2014 by Henderson-Sapir et al.[62] for the 985 nm (P_1) and 1973 nm (P_2) pumps. The incident power of P_1 was held fixed at 194 mW while the incident power of P_2 was varied.

Laser output power – H2016[61] and F2016[60]

Modelled 3.5 µm laser output powers of experiments H2016 and F2016 are presented in Figure 3.10. The plot shows good agreement between modelled and experimental data for each simulation. In each simulation, the power of P_1 is held fixed and the power of P_2 is incremented by 500 mW from 0 W to near the maximum power used in experiment.

The H2016 experiment is plotted against incident pump power. The modelled launch efficiencies of pumps P_1 and P_2 were 90 % and 86 % respectively. The F2016 experiments are plotted against launched pump power by setting the launch efficiency of P_1 to 100 %. However, the launch efficiency of P_2 was set to 72 % to match the slope efficiency of experimental data. The modelled wavelength of P_1 in experiment F2016 was 968 nm which gave good agreement with the power saturation of 'F3.5'.

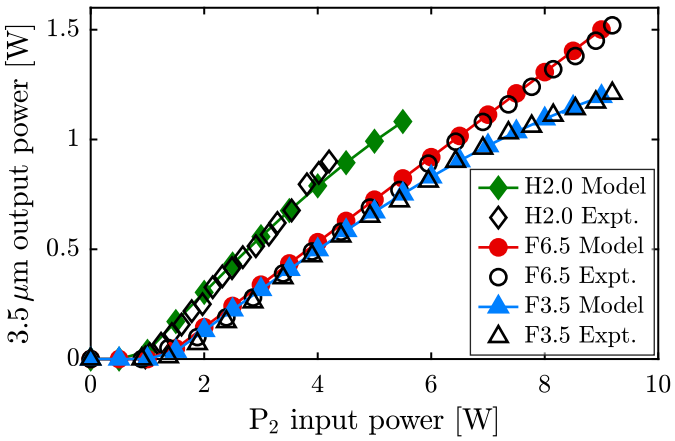

Figure 3.10: Modelled 3.5 µm laser output powers of experiments H2016 by Henderson-Sapir et al.[61] and F2016 by Fortin et al.[60]. 'H2.0' refers to the experiment H2016 in which P_1 operated at 2.0 W. 'F6.5' and 'F3.5' refer to experiments F2016 in which P_1 operated at 6.5 W and 3.5 W respectively.

V Discussion

Experiment H2014 by Henderson-Sapir et al.[62]

Modelled populations as functions of incident P_2 power are presented in Figure 3.11. These populations are averaged over the length of the fibre once steady state has been reached. The 3.47 µm laser output power is also overplotted against the right axis to show the relation between laser output power and steady state populations.

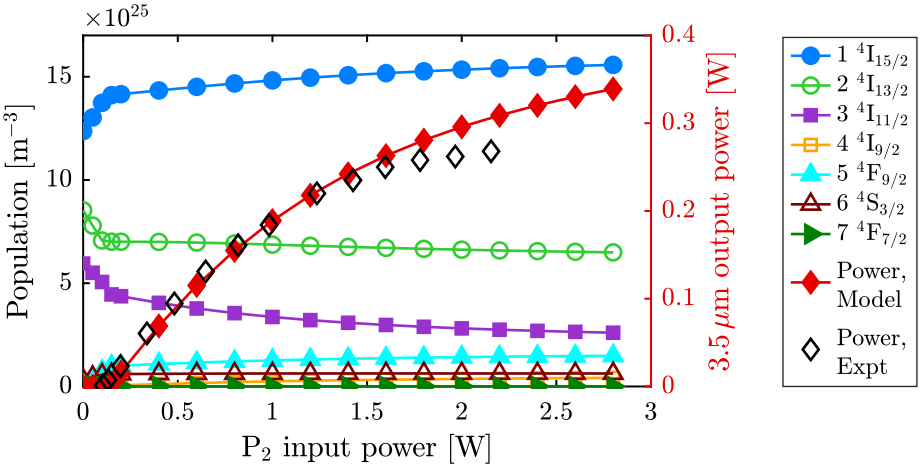

Figure 3.11: Modelled populations of experiment H2014 by Henderson-Sapir et al.[62] as a function of P_2 pump power. The populations are averaged over the length of the fibre at the end of a 20 ms simulation. The 3.47 µm laser output power is plotted against the right axis to show the relation between laser output power and steady state populations.

Below threshold, the population of the $^4I_{11/2}$ (3) level decreases significantly with increasing P_2 power as its population is pumped to the upper laser level $^4F_{9/2}$ (5). This decrease is closely followed by a decrease in the population of level $^4I_{13/2}$ (2), as relaxation from the depleting $^4I_{11/2}$ (3) level is reduced. The population of the ground state increases as ions are effectively returned to the ground state. This is most likely due to ions in the now populated upper laser level $^4F_{9/2}$ (5) returning to the ground state by radiative decay r_{51}=989 s^{-1}. Another likely path is cross relaxation W_{5362} up to level $^4S_{3/2}$ (6) followed by decay to the ground state, either directly (r_{61}=904 s^{-1}) or via level $^4I_{13/2}$ (2) (r_{62}=364 s^{-1}). This cross relaxation process becomes significant as the population of the $^4F_{9/2}$ (5) level increases.

Once threshold is achieved, the population of the $^4F_{9/2}$ (5) level is almost clamped due to gain saturation. Perfect clamping is not achieved due to the accumulation of ions in the lower laser level $^4I_{9/2}$ (4). Further increases in the rate of stimulated emission cause this lower lasing state population to gradually increase. This forces the population in level $^4F_{9/2}$ (5) to slightly increase so that threshold round trip gain is maintained. Lasing causes a significant increase in the transfer rate of ions from the $^4I_{9/2}$ (4) state to the $^4I_{11/2}$ (3) state, thereby limiting the effect on depopulation of this level by P_2 pumping.

The non-linear behaviour seen in Figures 3.8 and 3.11 at P_2 powers greater than 1 W can be explained by power saturation due to the limited supply of ions in level $^4I_{11/2}$ (3) available for pumping to the upper laser level $^4F_{9/2}$ (5). Further evidence of this is the increase in relative P_2 transmission seen in Figure 3.9 above 1 W.

The gain medium becomes transparent to the P_2 pump when the population of level $^4I_{11/2}$ (3) is 20 % higher than the population of level $^4F_{9/2}$ (5). This is calculated based on the effective P_2 emission cross section that was calculated from the effective pump absorption cross section using McCumber theory. In Figure 3.11, the ratio of populations in levels $^4I_{11/2}$ (3) to $^4F_{9/2}$ (5) is 1.75 when the incident P_2 power is 2.8 W. This occurs because the population of the $^4I_{11/2}$ (3) level decreases and the population of the $^4F_{9/2}$ (5) level increases due to bottlenecking of population in the $^4I_{9/2}$ (4) as mentioned earlier. The population of the $^4I_{11/2}$ (3) level is reduced in two ways. Firstly, more ions are stored in the two levels above it. Secondly, the increase in level $^4F_{9/2}$ (5) increases the number of ions that escape the cycle between the virtual ground state $^4I_{11/2}$ (3) and upper laser level $^4F_{9/2}$ (5). This is because the spontaneous emission rate from the $^4F_{9/2}$ (5) level to the ground state is nine times higher than decay from the $^4I_{11/2}$ (3) level. The cross relaxation process W_{5362} increases this further.

Parameter significance

In this section we investigate the impact of changes in the lower laser level $^4I_{9/2}$ (4) lifetime and the energy exchange process W_{5362}. The benchmark values are those listed in Tables 3.3 and 3.4. The steady state 3.47 µm output power as a function of incident P_2 pump power is presented in Figure 3.12 for a variety of lower laser state lifetimes and W_{5362} values. In each case, the fibre is pumped by CW pump sources.

The intrinsic lifetime of the lower laser level is reduced by factors of two and ten from the benchmark value τ_4=8.0 µs. The results clearly show that a dominant limitation on laser performance is the bottlenecking of ions in the lower laser level $^4I_{9/2}$ (4) since the power saturation is removed when the lifetime of this state is reduced by a factor of 10. Ions that accumulate in this lower laser level $^4I_{9/2}$ (4) are delayed in their return to the virtual ground state $^4I_{11/2}$ (3) and limit the potential rate of P_2 absorption. The population of ions in level $^4I_{9/2}$ (4) are available to absorb photons of the 3.5 µm transition and reduce the net rate of laser photon generation.

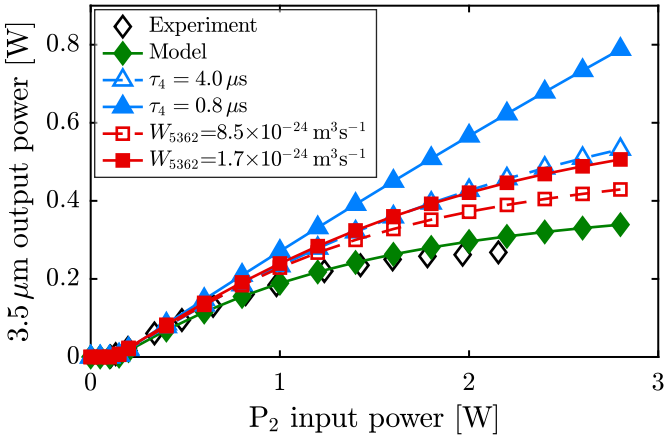

Figure 3.12: Modelled CW 3.47 µm laser output powers as functions of P_2 pump power based on variations of experiment H2014 by Henderson-Sapir et al.[62]. The intrinsic lifetime τ_4 of the lower laser level $^4I_{9/2}$ (4) and the cross relaxation parameter W_{5362} are reduced by factors of 2 and 10 separately.

The cross relaxation parameter W_{5362} is reduced by factors of two and ten from the benchmark value W_{5362}=17.0×10^{-24} m^{3}s^{-1}.[164] The rate at which these interionic interactions occur is proportional to the populations in levels $^4I_{11/2}$ (3) and $^4F_{9/2}$ (5). This interionic process limits the laser performance by depleting ions from the virtual ground level $^4I_{11/2}$ (3) as well as the upper laser level $^4F_{9/2}$ (5) which reduces stimulated emission and pump absorption. The plot of the reduced W_{5362}=1.7×10^{-24} m^{3}s^{-1} illustrates the negative effect this parameter has on laser performance by reducing slope efficiency and increasing power saturation. It is worth noting that significantly

reducing this parameter does not remove the power saturation completely as this is dominated by the lower lasing state lifetime. The effect of this energy transfer also reduces significantly when double clad fibres and lower doping densities are used as described below.

To understand what processes are important in governing the performance of the DWP laser, we calculated the transition rates as functions of incident P_2 pump power. The most significant transition rates are averaged over the length of the fibre and plotted in Figure 3.13. The most significant transition is from levels $^4I_{11/2}$ (3) to $^4F_{9/2}$ (5) by P_2 pump absorption. The non-linearity of this pump absorption, as well as stimulated emission, illustrates power saturation due to depletion of ions in level $^4I_{11/2}$ (3) as discussed earlier. The population of the lower laser level $^4I_{9/2}$ (4) is fed mainly by stimulated emission and non-radiative transitions from the $^4F_{9/2}$ (5) level and hence the rate of decay from this state grows with the power of the second pump.

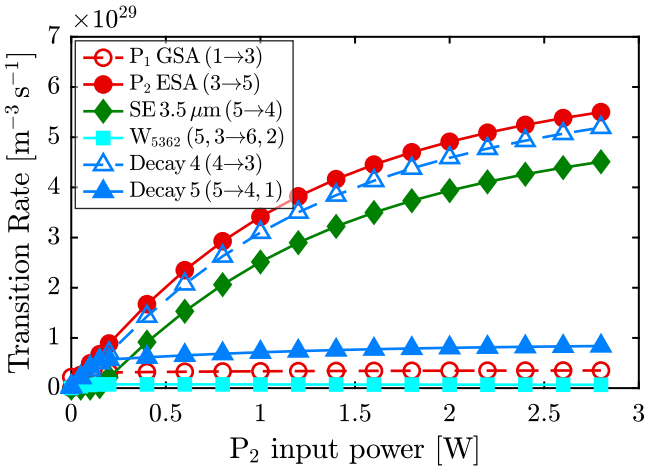

Figure 3.13: Modelled transition rates of experiment H2014 by Henderson-Sapir et al.[62]. Rates are averaged over the length of the fibre and plotted as functions of incident P_2 pump power. The transitions are pump absorption of P_1 and P_2 (P_1 GSA and P_2 ESA), stimulated emission (SE) of the 3.5 µm laser, the cross relaxation process W_{5362}, and the decay rates from the lower (4) and upper (5) laser levels.

The variations in the transition rates as functions of incident P_2 pump power around threshold are plotted in Figure 3.14. Below threshold, approximately 18 % of ions in the upper laser level $^4F_{9/2}$ (5) decay to the ground state, exiting the second pump cycle. Beyond threshold of the 3.47 µm laser, stimulated emission increases sharply and causes a faster return of ions to the $^4I_{11/2}$ (3) level.

At P_2 power levels below 70 mW the rate of stimulated emission due to the 2.8 µm laser transition is more significant than W_{5362}. Above 70 mW, the 2.8 µm laser is suppressed by absorption of the P_2 pump and its subsequent reduction of the $^4I_{11/2}$ (3) population. The rate in which ions leave level $^4F_{9/2}$ (5) by the energy transfer process

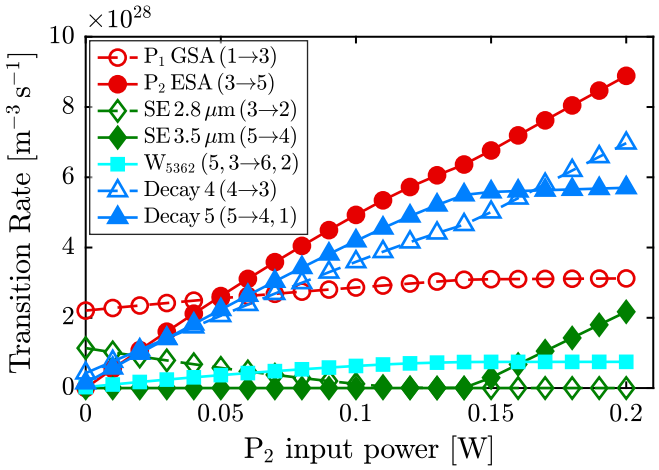

Figure 3.14: Modelled transition rates of experiment H2014 by Henderson-Sapir et al.[62] around threshold. The rates are averaged over the length of the fibre and plotted as functions of incident P_2 pump power. The transitions are pump absorption P_1 and P_2 (P_1 GSA and P_2 ESA), stimulated emission (SE) of the 2.8 µm and 3.5 µm lasers, the cross relaxation process W_{5362}, and the decay rates of the lower (4) and upper (5) laser levels.

W_{5362} rises until threshold is reached at which point it flattens considerably. The rate in which ions are excited by P_2 shows signs of initial saturation until the threshold of the 3.47 µm laser is reached and then it resumes its linear increase.

Experiments H2016 by Henderson-Sapir et al.[61] and F2016 by Fortin et al.[60]

The simulations F6.5 and F3.5 presented in Figure 3.10 are particularly sensitive to the wavelength of P_1 due to steep variation in ground state absorption between 965 nm and 972 nm.[173] The P_1 source used in these experiments was a 974 nm laser diode, however the actual wavelength of operation was stated to be "closer to 966 nm at the low power range used in these experiments".[60] The wavelength 968 nm provided the best fit to experimental data. This wavelength also corresponds to the peak of the excited state absorption for the ${}^4I_{11/2} \rightarrow {}^4F_{7/2}$ transition. The rate of excited state absorption in the H2.0 simulation is more sensitive to variations in wavelength since at 977 nm the change in cross section with wavelength is significant.

Modelled transition rates of experiment H2016[61] as functions of incident P_2 pump power is plotted in Figure 3.15. The rates of stimulated emission and P_2 absorption are closer to linearity compared with those of the shorter 18 cm core-pumped fibre in experiment H2014.[62] This is due to the longer interaction length of this 2.8 m fibre and the lower power density of P_1 in the core which prevents bleaching of the ${}^4I_{11/2}$ (3) level.

The modelled laser output power as a function of fibre length for fixed powers

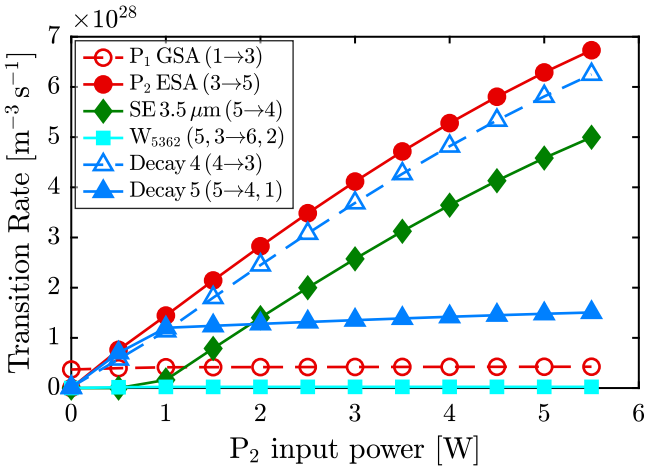

Figure 3.15: Modelled transition rates of experiment H2016 by Henderson-Sapir et al.[61]. The rates are averaged over the length of the fibre and plotted as functions of incident P_2 pump power. The transitions are pump absorption of P_1 and P_2 (P_1 GSA and P_2 ESA), stimulated emission (SE) of the 3.5 µm laser, the cross relaxation process W_{5362}, and the decay rates of the lower (4) and upper (5) laser levels.

of both P_1 and P_2 is presented in Figure 3.16. The model predicts an optimal fibre length of 3.4 m for the H2016[61] H2.0 system when the second pump operates at 4 W. Laser power decreases sharply below 2.6 m interaction lengths and decreases moderately above 3.6 m. An optimal fibre length of 2.5 m is predicted for the F2016[60] F6.5 system when the second pump operates at 9 W. This implies a potential increase in laser power of 10 % compared with the experimental fibre length of 4.3 m.

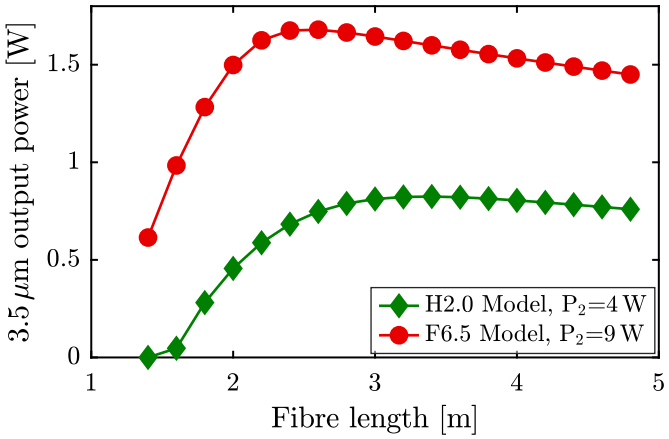

Figure 3.16: Modelled laser output power as function of fibre length based on parameters from experiments H2016 by Henderson-Sapir et al.[61] (H2.0) and F2016 by Fortin et al.[60] (F6.5). The H2.0 simulation had P_2 power fixed at 4 W and the F6.5 simulation had P_2 power fixed at 9 W.

Modelled laser output power as a function of output coupler reflectivity for fixed

powers of P_2 is presented in Figure 3.17. The plot shows how optimum output coupler reflectivity decreases with increasing power of the second pump. An optimal reflectivity of 74 % is predicted for the H2.0[61] system when the second pump operates at 4 W and 76 % reflectivity at 2 W. An optimal reflectivity of 24 % is predicted for the F6.5[60] system when the second pump operates at 9 W. This implies a potential increase in laser power of 22 % compared with the experimental output coupler reflectivity of 55 %.

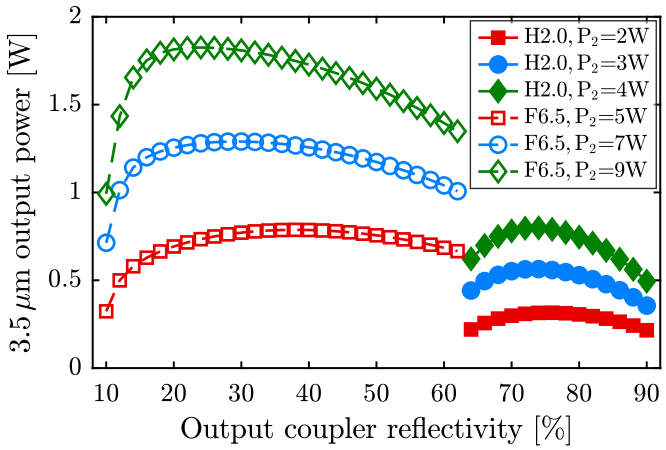

Figure 3.17: Modelled laser output power as a function of output coupler reflectivity based on parameters from experiments H2016 by Henderson-Sapir et al.[61] (H2.0) and F2016 by Fortin et al.[60] (F6.5). The H2.0 simulation had the power of P_2 fixed at 4, 3, and 2 W. The F6.5 simulation had the power of P_2 fixed at 9, 7, and 5 W.

VI Conclusions

An extensive numerical model of DWP 3.5 µm Er^{3+}-doped fibre lasers has been presented and validated against results from three published experiments. The model provides valuable insight into atomic and photonic interactions in both time and position along the fibre and enables the optimisation of parameters such as fibre length, output coupler reflectivity, doping concentration, and pump wavelengths. The model may be extended to other dopant ions and fibres.

The limitations on DWP laser performance include the accumulation of ions in the lower laser level and the escape of ions from the second pump cycle. The dominant escape processes are the decay from the upper laser level to ground state and, in high Er^{3+}-doping concentrations, the cross relaxation process W_{5362}.

Future work includes FLAPP upgrade to account for laser wavelength shifting with second pump power and investigation into interionic processes by further modelling. Better understanding of interionic processes would enable us to improve optimisation of doping and potential co-doping concentrations. We also intend to optimise the

wavelength of the first pump for laser power and slope efficiency to achieve the optimum balance of ground and excited state absorptions.

Acknowledgements

The authors would like to thank eRSA (South Australian provider of high performance computing) for provision of computer resources.

3.4 Excited state absorption of the second pump

Excited state absorption of the second pump P_2, when operated at a wavelength of 1976 nm, was reported by Maes et al.[66] after the article[181] presented in this Chapter was published. This ESA is a transition from the upper laser level $^4F_{9/2}$ to the $^4F_{7/2}$ level, depleting the upper laser level population and providing an additional path that escapes the main pump cycle.

Although the absorption cross section of the $^4F_{9/2} \rightarrow {}^4F_{7/2}$ transition was estimated to be only ∼2.3 % of the cross section for the $^4I_{11/2} \rightarrow {}^4F_{9/2}$ transition, the authors claim that this ESA is significant enough to completely quench 3.4 µm laser emission when P_1 power is low and P_2 power is high. This is explained by bleaching of the virtual ground state $^4I_{11/2}$ by P_2 and, consequently, a significant population in the upper laser level $^4F_{9/2}$ available for second ESA. The second ESA of P_2 would provide another mechanism for ions to exit the lasing cycle. Ions in the $^4F_{7/2}$ state (lifetime τ_7=5 µs) quickly relax into the thermally coupled $^2H_{11/2}$ and $^4S_{3/2}$ levels. According to reported branching ratios,[174] 67 % of these ions escape the P_2 cycle by decaying into the $^4I_{15/2}$ and $^4I_{13/2}$ levels.

However, the strong quenching effect reported by Maes et al.[66] appears inconsistent with experimental results reported earlier by Fortin et al.[60] which show no evidence of laser quenching at similar powers of P_1 and P_2. This may be partially attributed to the higher slope efficiency reported by Maes et al.[66] (29 %) when compared with the experiment reported by Fortin et al.[60] (19 %).

The possibility of second ESA of P_2 was proposed earlier by the author of this thesis in his Honours thesis (not published) following analysis of Stark split energy levels in Er^{3+}-doped ZBLAN glass.[160] The fluorozirconate glass reported by Maes et al.[66] was Er^{3+}:ZrF_4 and no Stark level analysis of this glass has been reported in literature. The following analysis for second ESA of P_2 is based on Er^{3+}-doped ZBLAN glass and, therefore, some shifting of Stark levels relative to the fluorozirconate glass reported by Maes et al.[66] can be expected.

Figure 3.18 represents the possible energy transitions between Stark split levels of Er^{3+}-doped ZBLAN glass when the P_2 wavelength is 1976 nm (or photon energy is 5061 cm^{-1}). The Stark split energy positions were measured in Er^{3+}-doped ZBLAN glass at 13 K by Huang et al.[167]. The width of each energy level, as well its position, determines the range of possible photon energies that can be absorbed between any Stark level pair. There are seven possible ESA transitions (ESA_1) between the virtual ground state $^4I_{11/2}$ and the upper laser level $^4F_{9/2}$ and one possible transition (ESA_2) between the $^4F_{9/2}$ and $^4F_{7/2}$ states.

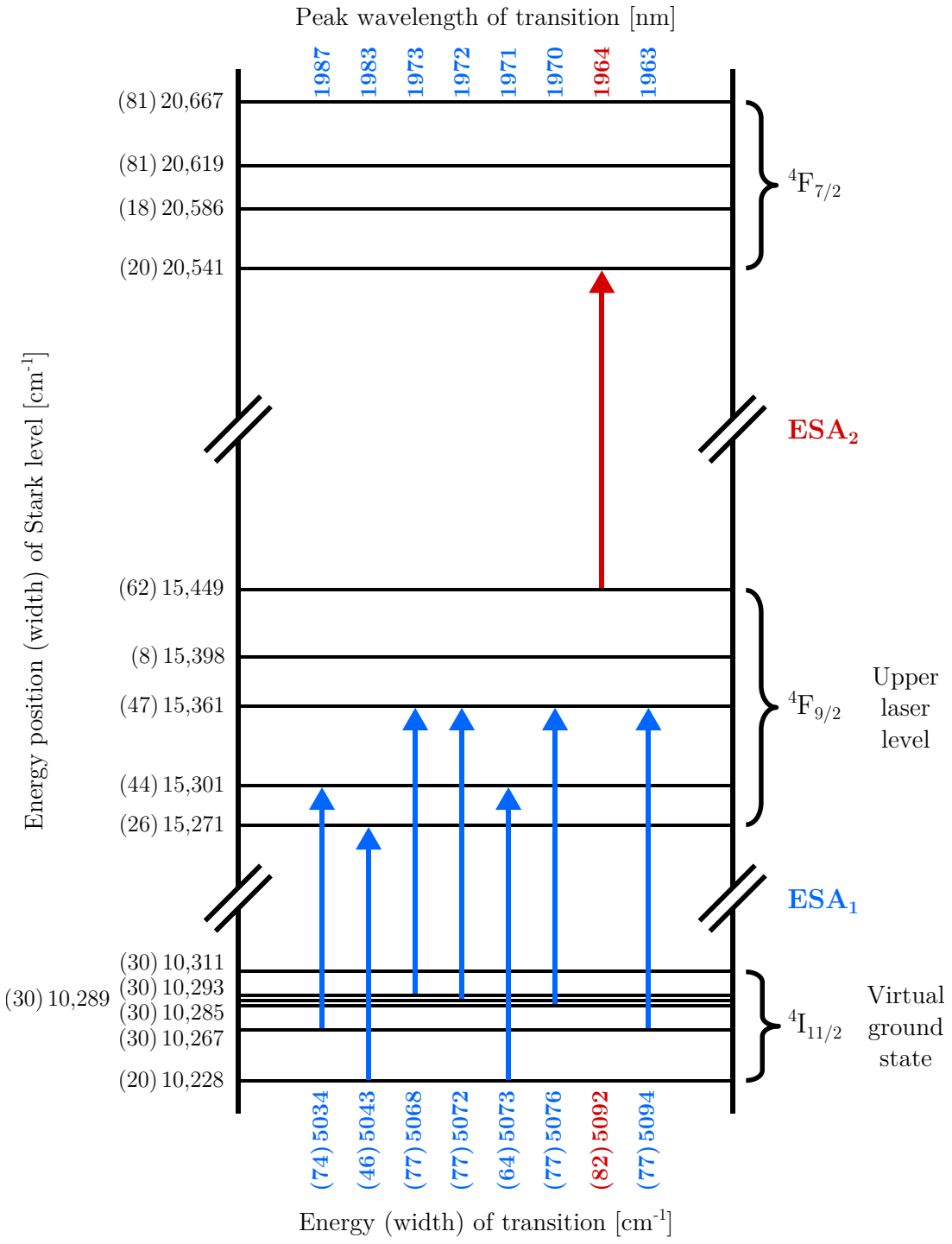

Figure 3.18: Excited state absorption transitions between Stark split energy levels in Er^{3+}-doped ZBLAN when P_2 wavelength is 1976 nm (or photon energy is 5061 cm^{-1}). Each arrow represents one possible ESA transition. The energy that separates each pair of Stark levels, and the width of each transition, are labelled at the bottom. The peak wavelength of each transition is labelled at the top. The energy data was sourced from Ref. 167.

The ESA_2 transition starts from the highest Stark level within the $^4F_{9/2}$ manifold (calculated Boltzmann factor is 0.12 at 300 K) and is terminated at the lowest Stark level within the $^4F_{7/2}$ manifold. The peak wavelength for this transition is 1964 nm. Therefore, Maes et al. [66] suggested that ESA_2 is significant enough to completely quench lasing when P_2 operates at a peak wavelength that is 12 nm longer than the peak wavelength of the energy transition while only 12 % of the $^4F_{9/2}$ population is available for absorption at the P_2 wavelength. Since ESA_2 removes ions from the main pump cycle, the significance of ESA_2 may be amplified by multi-loop processes. That is, ESA_2 transitions from 12 % of the $^4F_{9/2}$ population could become significant over many pump cycles, even when the cross section of the absorption is small, because ions are removed from the main pump cycle.

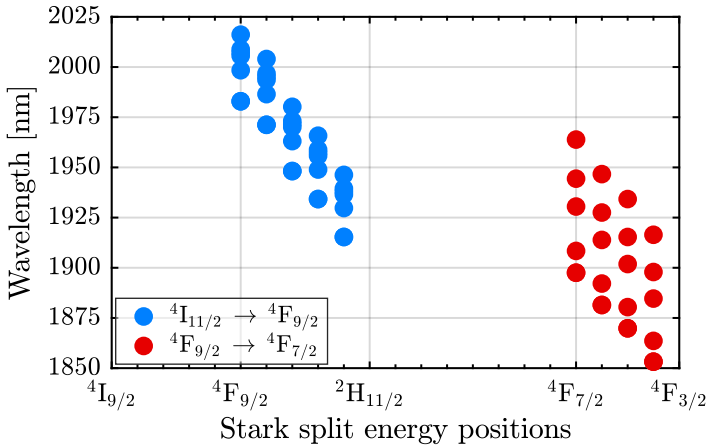

Figure 3.19: Energy transitions between Stark levels of Er^{3+}-doped ZBLAN due to absorption by photons with energies near those of the second pump P_2.

All possible $^4I_{11/2} \rightarrow {}^4F_{9/2}$ and $^4F_{9/2} \rightarrow {}^4F_{7/2}$ transitions between Stark split levels are represented in Figure 3.19. Each tick mark along the horizontal axis represents one Stark split energy position (evenly spaced for clarity) while the tick marks above the axis labels represent the lowest Stark split energy position within each energy manifold. Each marker represents a possible energy transition from one Stark level to another. The markers are placed at the final Stark level position, given by the horizontal axis, that results from absorption by a photon with wavelength given by the vertical axis. For example, a photon with wavelength 1973 nm has an energy that closely matches energy transitions from Stark split levels within the $^4I_{11/2}$ manifold to the second and third Stark split levels of $^4F_{9/2}$. It can be seen that there are five Stark split levels in the $^4F_{9/2}$ manifold and therefore five markers in each Stark split level of the $^4F_{7/2}$ manifold.

The red marker at the lowest Stark level of the $^4F_{7/2}$ manifold and at a wavelength

of 1964 nm corresponds to the ESA_2 transition in Figure 3.18. At wavelengths shorter than ∼1964 nm, the $^4F_{9/2} \rightarrow {}^4F_{7/2}$ transitions presented in Figure 3.19 may explain the small peaks observed in measured absorption spectra reported by Henderson-Sapir et al.[63].

Second ESA of P_2 has not been implemented in the FLAPP model at this stage, although it can be implemented easily if necessary. The model has shown good agreement with reported measurements without the inclusion of second ESA P_2.[181] If the process does indeed exist, it may be overcome by increasing P_1 power or possibly by shifting the wavelength of P_2 to slightly longer values. Further validity of this process is required by direct measurement near the P_2 wavelength to determine its relevance to DWP under normal pumping regimes. Stark level analysis on the same glass used to manufacture the fibres, at laser operating temperature, would provide more reliable data for future modelling.

3.5 Q-switch modelling

This Section includes revised contributions made to the following published article:

> O. Henderson-Sapir, A. Malouf, N. Bawden, J. Munch, S. D. Jackson, D. J. Ottaway. Recent advances in 3.5 µm erbium-doped mid-infrared fiber lasers. *IEEE Journal of Selected Topics in Quantum Electronics*, 23(3):6–14, May 2017.

3.5.1 Simulation

The model FLAPP presented in this Chapter was updated to predict Q-switching behaviour of fibre lasers. Performing these simulations enables various laser system designs to be tested before committing to costly purchases of ZBLAN fibres and components. Since the model provides time domain information, it can be used to investigate the temporal evolution of a laser pulse and the energy level population dynamics at discrete locations along the fibre. In future work, the model may be developed to simulate gain-switching and mode-locking.

Q-switching was implemented into the model by enabling the reflectivity of the output coupler mirror to be switched between on (low loss) and off (high loss) states according to a user specified repetition frequency and duty cycle. The switching time was modelled to be instantaneous. This approach is reasonable for the case where the buildup time of simulated pulses is much longer than the rise time of a Q-switch (∼100 ns for acousto-optic modulators). The model update was intended to predict and optimise peak power of laser pulses generated by Q-switching. In future work,

finite switching times could be implemented to simulate real switches more accurately if required.

The 3.5 µm fibre laser system H2016[61] modelled in this Chapter (pages 60–84) was the base system for the following Q-switch simulations. The properties of the H2016 system are listed in Tables 3.1 and 3.2. The power of the first pump was set to 2 W and 4 W while the power of the second pump was held fixed at 5.5 W.

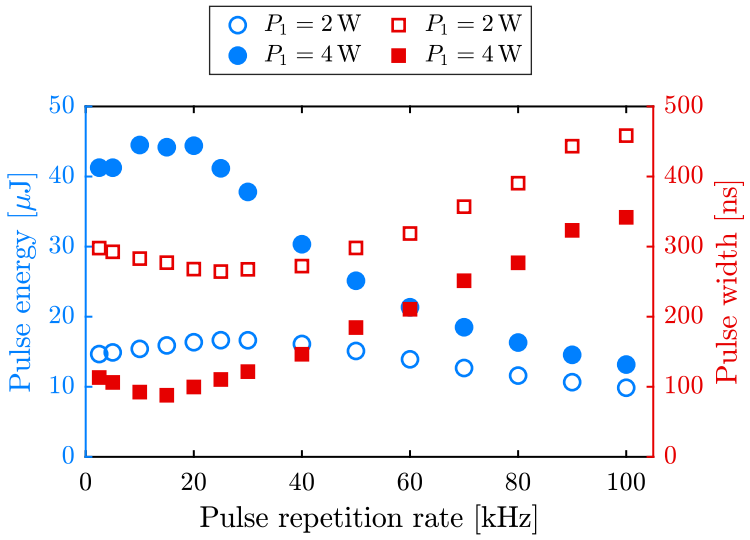

Figure 3.20: Simulated pulse energy and pulse width as functions of Q-switch repetition rate. The Q-switch on-time was held fixed at 5 µs. The model parameters are based on the 3.5 µm fibre laser system H2016[61] modelled in this Chapter under CW operation.

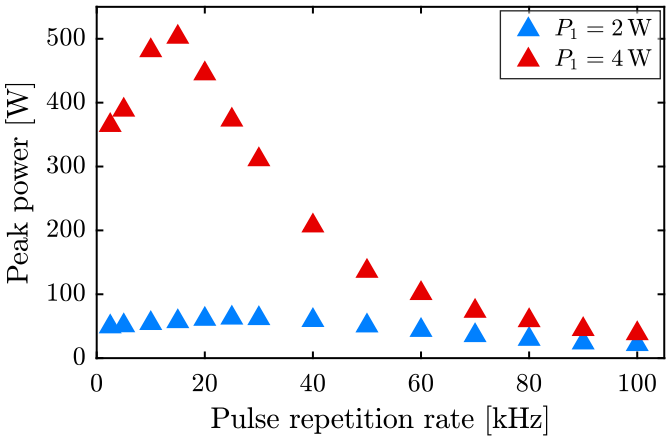

Figure 3.21: Simulated peak power of laser output pulses calculated from pulse energies and pulse widths displayed in Figure 3.20

The Q-switch on-time was held fixed at 5 µs while the Q-switch repetition rate was varied between 2.5 kHz (400 µs period) and 100 kHz (10 µs period). To ensure a stable

pulse train, three simulations were performed for each Q-switch repetition rate. The first simulation was performed over 20 ms, without Q-switching, to establish CW steady state conditions. The final populations became the initial conditions of the second simulation, for which Q-switching was implemented over 20 ms of simulation time to establish conditions for a stable pulse train. Finally, a simulation was performed over 500 µs with high time resolution so that the fast dynamics of the Q-switched pulses could be analysed.

The energies and widths of the laser output pulses during the final 500 µs simulation were calculated at each pulse repetition rate and are presented in Figure 3.20. The pulse energies were averaged by integrating the laser output power over the simulation time and dividing by the number of pulses during the simulation. The pulse widths were estimated from the full width at half maximum (FWHM) of Gaussian fits to each pulse. Then the peak powers were calculated by dividing the pulse energies by the pulse widths and are presented in Figure 3.21.

When the first pump operates at 2 W, the highest peak power is 63 W at 25 kHz pulse repetition rate (pulse energy 17 µJ and pulse duration 264 ns). At 4 W of pump power, an optimum peak power of 500 W is predicted at 15 kHz pulse repetition rate (pulse energy 44 µJ and pulse duration 88 ns).

The energy level population densities while Q-switching were investigated for high peak power pulses. Figure 3.22 shows the population densities over time when Q-switch repetition rates were set to 5 kHz, 15 kHz, and 25 kHz. The power of the first pump was set to 4 W in each case and the populations were averaged along the length of the fibre. The upper laser level population drops to a minimum in less than a microsecond after the Q-switch is switched on in all cases.

At 5 kHz, the upper laser level $^4F_{9/2}$ is saturated well within the Q-switch off-time, while the virtual ground state $^4I_{11/2}$ population is flat, indicating bleaching of the second pump. At 25 kHz, the Q-switch is switched on as the population of the $^4F_{9/2}$ level is still increasing almost linearly and before it could otherwise saturate. At 15 kHz, the optimum repetition rate for peak power, the Q-switch is switched on as the upper laser level $^4F_{9/2}$ approaches saturation. At this rate, the balance between the $^4I_{11/2}$ state population available for pump absorption and the Q-switch off-time available for ions to build up in the upper laser level results in the highest upper laser level population as the Q-switch is switched on, when compared with the 5 kHz and 25 kHz cases.

Figure 3.23 shows P_2 pump absorption over time when the Q-switch repetition rates were set to 5 kHz, 15 kHz, and 25 kHz. The absorption was calculated over the entire fibre length. The pump absorption is bleached during the Q-switch cycle when

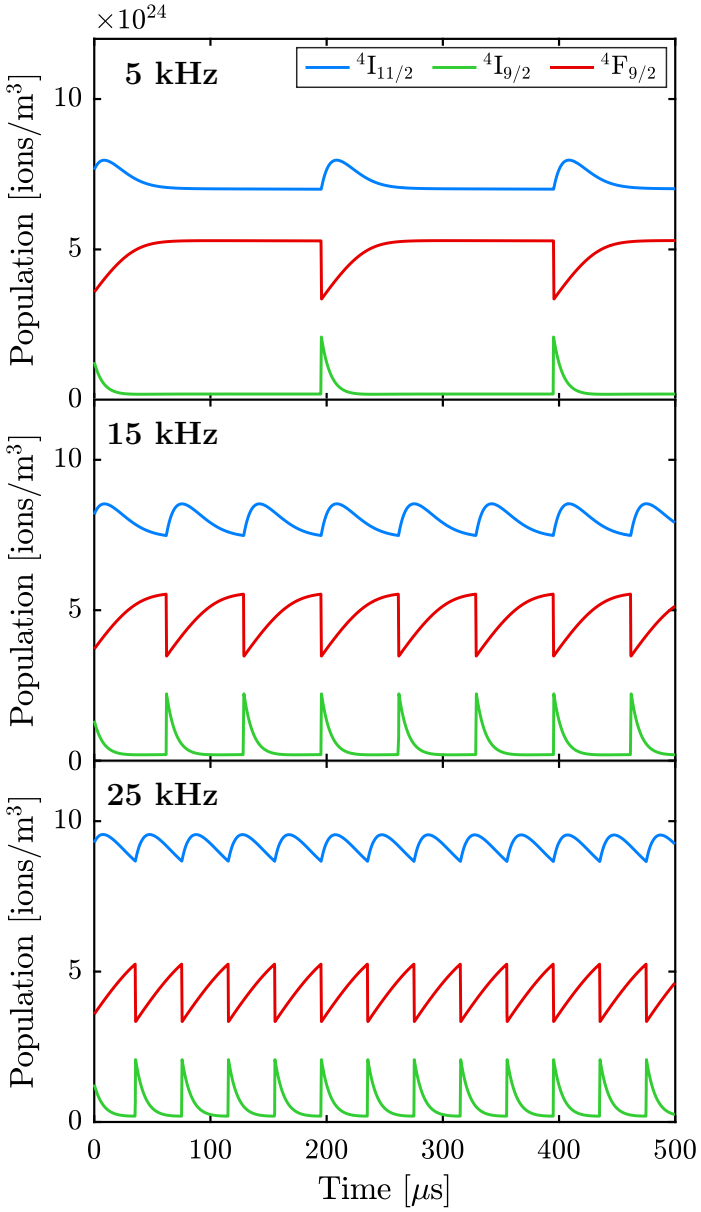

Figure 3.22: The time dependent behaviour of the spatially averaged population densities along the fibre when Q-switched at 5 kHz, 15 kHz, and 25 kHz. The incident P_1 power was 4 W.

the repetition rate is 5 kHz. At 25 kHz, the Q-switch is switched on while the pump absorption is still high in comparison with the bleached level of the 5 kHz case. The Q-switch cycle replenishes the $^4I_{11/2}$ state via stimulated emission fast enough to prevent any bleaching of the pump absorption. At the optimum repetition rate of 15 kHz, the Q-switch is switched on just before the pump absorption begins to bleach.

In conclusion, the model has been used to predict performance of the H2016[61] 3.5 µm DWP fibre laser system when a Q-switching mechanism is added to this system. Analysis in the time domain provides insight into the evolution of energy level

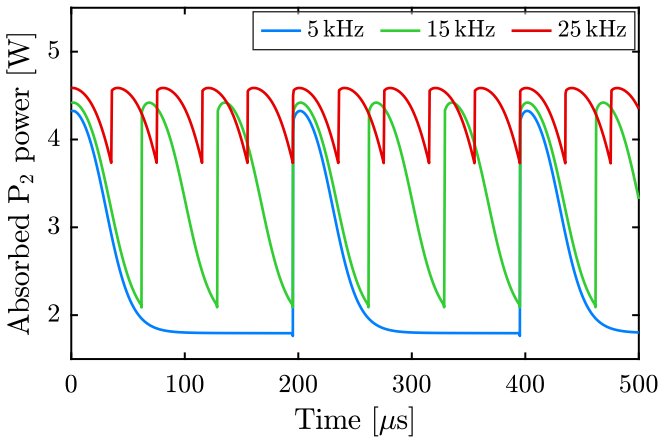

Figure 3.23: Absorbed pump P_2 power over time while Q-switching at 5 kHz, 15 kHz, and 25 kHz. The P_2 power launched into the fibre was 4.7 W and the absorption was calculated over the entire fibre length. The incident P_1 power was 4 W.

populations with time and how deviations from the optimal Q-switch repetition rate are detrimental to laser performance. Q-switching can be analysed in the time domain from numerous other perspectives, such as pump absorption, to provide more information for improving laser performance.

3.5.2 Comparison with experiment

The Q-switching simulations were soon followed by the first demonstration of an actively Q-switched 3.5 µm fibre laser.[67] The H2016[61] experiment, modelled in this Chapter (pages 60–84), was adapted for Q-switching using the same pump sources, fibre, and resonator mirrors. Several components were inserted between the output end of the fibre and the output coupler – a collimating lens, a dichroic mirror to remove pump light, a CaF_2 window at Brewster's angle to force linear polarisation, and an acousto-optic modulator (AOM) to Q-switch the cavity. The incident power of P_1 was 4.3 W (compare with 4.0 W used in Q-switch simulations) while P_2 power was 3.6 W (compare with 5.5 W used in Q-switch simulations). The P_2 power was limited by pulse stability and damage to the fibre from high peak power laser pulses.

Stable Q-switching was achieved with AOM repetition rates between 5 kHz and 100 kHz and Q-switch on-times between 4 µs and 10 µs (compare with 5 µs used in Q-switch simulations). The Q-switch repetition rate that resulted in the maximum pulse energy was 15 kHz which is in agreement with simulations presented in Section 3.5.1. Measured pulse energies were consistently ∼20 % of simulated values for all repetition rates (5 kHz – 100 kHz) showing good qualitative agreement. For example, the maximum measured pulse energy was 7.8 µJ while the maximum simulated pulse

energy was 44 µJ. Measured pulse widths were longer than simulated values by factors between 3 and 5.

The disagreements between simulation and experiment are firstly explained by the lower P_2 power (3.6 W) used in experiment, when compared with the P_2 power (5.5 W) used in simulations. The output of the Q-switch experiment was unstable when the P_2 power exceeded 3.6 W. Secondly, the simulations were performed with ideal Q-switching when no extra loss processes (other than the Q-switch itself) were added to the system. In the experiment, however, losses were introduced by the components added for Q-switching and the coupling of the laser beam to the fibre core in free space. Thirdly, the Q-switch on-times used in experiment varied between 4 µs and 10 µs while being held fixed at 5 µs during simulations. Finally, there is a spontaneous emission rate term used in all simulations to initiate lasing. The spontaneous emission rate could be more significant during Q-switch operation, since lasing is initiated on shorter time scales, when compared with CW operation.

In conclusion, the simulations were successful in predicting an optimal repetition rate for Q-switching. The model could not have predicted limitations in P_2 power due to the damage threshold of the fibre and pulse stability. In future work, the Q-switching simulations could be repeated with adjusted parameters that match the experiment reported by Bawden et al.[67] more closely. The parameters that require adjustment are the power of both pumps, Q-switch on-times, losses from added components, and coupling efficiency of the laser beam to the fibre core at the output end. Comparisons between experiment and future simulations could be made to confirm the validity of the model and study Q-switching in 3.5 µm DWP fibre lasers further. At this point in candidature, the continuation of Q-switch modelling was passed on to Nathaniel Bawden, PhD candidate at The University of Adelaide, to aid development in Q-switching the 3.5 µm DWP fibre laser, while the author's focus shifted to the study of saturable absorption in graphene presented in Chapters 4, 5, and 6.

3.6 Code optimisation for speed

Several approaches were investigated to optimise the code for speed, including parallelisation and compilation, using graphical processor units (GPUs) as well as central processor units (CPUs). This work was performed during candidature by Albert Kong (graduate student, The University of Adelaide) under supervision by Andrew Malouf. The aim was to reduce execution time of the main loop.

At each time step, the DWP laser models presented on pages 60–84 solved 15 rate equations (7 energy levels and 2×4 photonic populations) four times (RK4 method)

for each fibre element. Optimisation tests were performed for the case of the H2016[61] experiment, where the length of the fibre was divided into 28 elements. The average execution time of a 20 ms simulation, which required ∼40 million time steps, was reduced from 5.5 hours to 1.5 hours by moving the main loop and a group variable initialisations into a separate function.

3.6.1 Parallelisation

The main loop iterated over each time step while a nested loop solved the rate equations over four iterations in accordance with the RK4 method. Each iteration is sequential and, therefore, cannot be parallelised. Alternatively, the rate equations for each fibre element could be parallelised. Attempts were made to execute parallelised code on GPUs and CPUs. However, the execution times were increased significantly, since any speed advantage gained from parallelisation was dominated by communication overhead.

3.6.2 Compilation

The MATLAB execution engine uses just-in-time (JIT) compilation. Alternatively, a MATLAB function can be compiled into a MATLAB executable (MEX) file and called by a MATLAB script. The main loop was removed from the main script, placed in a separate function, and compiled into a MEX file. Execution time was improved by a factor of 1.6 (from 5.5 hours to 3.5 hours). We found that when the initialisation of main loop variables was performed within the function, rather than the main script, execution time was reduced further. Finally, and unexpectedly, we found that not compiling the function at all resulted in the shortest execution time, which was reduced by a factor of 3.7 (from 5.5 hours to 1.5 hours). That is, the shortest execution time was achieved by removing the main loop from the main script, placing the main loop into a separate function, initialising all main loop variables *within* the function, and *not* compiling that function. This unexpected result may be attributed to function arguments being stored in CPU cache and accessed faster from the cache than from main memory. Therefore, JIT compilation was effective when compared with MEX compilation provided that memory was utilised efficiently.

3.7 Conclusion

A numerical model that simulates the performance of 3.5 µm DWP Er^{3+}-doped zirconium-based fluoride glass fibre lasers has been presented. The model can provide

time-domain information with high resolution, predict laser output power, and is a valuable tool for the optimisation of fibre laser performance. The model was calibrated and validated against the laser output powers of three 3.5 µm DWP fibre lasers published in literature. The optimum Q-switch repetition rate of one 3.5 µm DWP fibre laser, reported by,[61] was predicted by simulation.

In the future, more modelling could be performed to simulate the Q-switching demonstrated by Bawden et al.[67]. Gain-switching and mode-locking algorithms could potentially be implemented into the model to predict and compare laser pulses generated by these techniques. Alternative numerical methods that use adaptive step sizes, such as method of lines, rather than fixed step sizes could be investigated for accuracy and computational efficiency. Sujecki[182] developed an algorithm that used the finite difference method and method of lines approach to model Q-switching in Er^{3+}-doped fluoride fibre lasers that operate on the 2.8 µm transition. The method of lines uses discrete spatial derivatives and continuous time derivatives. The equations are firstly solved for the steady state condition. Then time domain numerical analysis that uses an adaptive step size is performed, effectively enabling space and time to be decoupled. Adaptive step sizes require less steps than fixed step sizes and are therefore more computationally efficient. A method of lines algorithm could be implemented into the model presented in this Chapter for comparison of simulation results, particularly in the time domain, and execution times.

Chapter 4
Graphene Properties

Graphene is a 2D material with unique properties. It has a linear energy dispersion, broadband saturable absorption, high electron mobility, and ultrafast electronic relaxation time.[183] Graphene has been used extensively as a saturable absorber to passively mode-lock ultrafast lasers.[70,87–95] Compared to traditional semiconductor saturable absorber mirrors (SESAMs) and single-walled carbon nanotubes, graphene has an extremely broad wavelength response, a high modulation depth, and low saturation intensity.[87] The modulation depth can be extended by stacking multiple layers of graphene.[184,185]

The graphene properties presented in this Chapter, combined with the growing demand for mode-locked mid-IR lasers, motivated the need to investigate the response of graphene to high intensity mid-IR radiation experimentally and assess its potential as a mode-locking element for mid-IR lasers. These experiments are detailed in Chapters 5 and 6. This Chapter introduces the properties of graphene and the concepts which underpin the experiments.

4.1 Background

Graphene, a 2D allotrope of carbon, is a flat monolayer sheet of carbon atoms bonded in a hexagonal honeycomb lattice. By comparison, graphite, carbon nanotube and fullerene are 3D, 1D, and 0D allotropes of carbon respectively. Graphite is made out of stacks of graphene layers that are weakly coupled by van der Waals forces.[186] Graphene can sustain current densities six orders of magnitude higher than copper, has extremely high thermal conductivity, and is impermeable to gases.[187] Its charge carriers have zero effective mass and exhibit extremely high intrinsic mobility.[187]

The 2010 Nobel Prize for Physics was shared by Andre Geim and Kostya Novoselov for "groundbreaking experiments regarding the two-dimensional material graphene".

Graphene was extracted from graphite by a mechanical exfoliation process commonly referred to as the "Scotch-tape method" or micromechanical cleavage.[188] This process, which suffers from poor reproducibility, can produce graphene up to several mm^2 in area.[183,187]

One attractive alternative to mechanical exfoliation for graphene production is epitaxial growth of graphene on a hexagonal substrate such as silicon carbide (SiC). This process uses the carbon that exists in the substrate to form a graphene surface. The SiC is heated to temperatures between 1273 K and 1773 K causing the surface silicon to sublimate leaving a carbon-rich coating.[189]

Chemical vapour deposition (CVD) is a process that produces high quality graphene on a metal substrate such as copper foil and can be transferred onto another substrate.[190] The copper surface is pre-treated with chemical etching to remove impurities and flatten the surface. Gas molecules containing carbon are combined in a high-temperature reaction chamber. The carbon atoms are disassociated by pyrolysis on the copper substrate that is a catalyst for the reaction. The catalyst reduces the temperature required for reactions to occur. Once cooled, the graphene is coated with a polymer support layer such as polymethyl methacrylate (PMMA) and transferred by a wet chemical process. The PMMA is removed by a solvent such as acetone.[191]

4.2 Introduction

This Chapter describes the unique properties of graphene that make it such an ideal broadband saturable absorber material for laser mode-locking. In Section 4.3, the graphene lattice is described in real space and reciprocal space, since both lattice descriptions are required to derive expressions for the energy dispersion. The energy dispersion relations of graphene are reported extensively in literature. However, their derivations are often omitted or incomplete. In Section 4.4, expressions for the energy dispersion are stated while their derivations can be found in Appendix C.2. Two expressions are stated – one for all k-space (Equation 4.10) and one for the regions (in k-space) where the dispersion is linear (Equations 4.11 and 4.12). The energy dispersions in single layer and trilayer graphene are described and illustrated. The optical properties of graphene that are most relevant to this work are described in Section 4.5. These properties include saturable absorption, two-photon absorption, ultrafast carrier lifetimes, and threshold estimates for laser induced damage. Previous demonstrations of graphene mode-locked lasers are discussed in Section 4.6. Finally, conclusions are presented in Section 4.7.

4.3 Lattice structure

4.3.1 Carbon bonds

The carbon atom has six electrons distributed in the configuration $1s^2 2s^2 2p^2$. In graphene, sp^2 hybridisation occurs when the 2s, $2p_x$, and $2p_y$ orbitals combine to form three new orbitals equally separated by 120° in the xy-plane,[6,192,193] as illustrated in Figure 4.1. Strong covalent σ bonds are formed that give rise to a hexagonal structure. The σ bonds are responsible for the strength and mechanical properties of the lattice.[194]

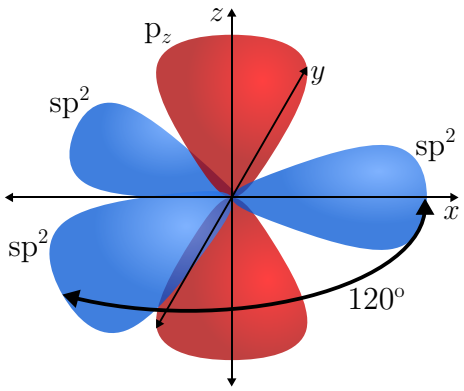

Figure 4.1: Graphene orbitals. Each carbon atom has three sp^2 hybridised orbitals, equally separated by 120° in the xy-plane, that form strong covalent σ bonds with neighbouring atoms. The p_z orbital, orientated perpendicular to the graphene plane, forms one π bond with one of three neighbouring atoms and is responsible for the valence and conduction bands in graphene.[6,192,193]

There is one π electron per carbon atom that does not contribute to the σ bonds. The $2p_z$ orbital, orientated perpendicular to the graphene plane, forms a π bond that is weaker than the σ bonds. Each atom forms one π bond with one of its three neighbouring atoms. These π bonds form the π band (valence band) and π^* band (conduction band) that are responsible for the unusual electronic properties of graphene.[195] Since each atom contributes one π electron, graphene is considered to be a half filled system where, in the ground state, the valence band is completely filled and the conduction band is empty. The π electrons, situated either side of the lattice plane, are responsible for the high electron mobility in graphene.[187]

The real lattice exists in real space, the set of all position vectors $\mathbf{r} = (x, y)$, while the reciprocal lattice exists in reciprocal space (k-space), the set of all wave vectors $\mathbf{k} = (k_x, k_y)$. Each lattice representation is related to the other by a Fourier transform. Both lattice descriptions are important for understanding the energy band structure of graphene.

4.3.2 Real lattice

Two neighbouring carbon atoms in graphene, although chemically equivalent, are located in inequivalent environments. The hexagonal structure cannot be spanned by the same set of primitive translation vectors (linearly independent basis vectors) and, therefore, is not a Bravais lattice (a lattice which *can* be spanned by linearly independent basis vectors). The condition for a 2D Bravais lattice is given by Equation 4.1. The hexagonal structure of graphene, however, can be described by two interleaving triangular Bravais *sublattices*, A and B,[192,193] as illustrated in Figure 4.2.

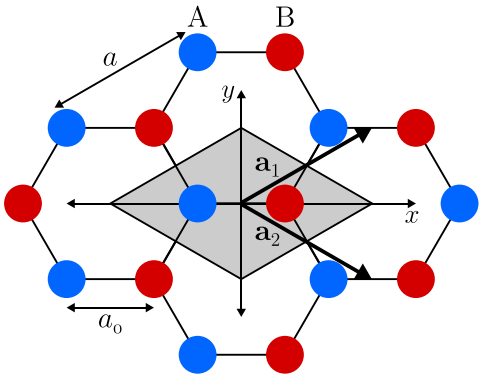

Figure 4.2: Real lattice. The primitive unit cell shown shaded contains two neighbouring carbon atoms – one from each interleaving triangular sublattice A (blue) and B (red). Linear combinations of the primitive translation vectors $\mathbf{a}_1$ and $\mathbf{a}_2$ span the triangular Bravais lattice points $\mathbf{R}$ and define the coordinates of the unit cells.[192,193]

The primitive unit cell contains two neighbouring carbon atoms, one from each sublattice. Therefore, the hexagonal structure is a triangular Bravais lattice of unit cells with a two-atom basis. If the origin of this Bravais lattice was chosen, for example, to be at an atom site from sublattice A, the lattice vectors would span sublattice A. The lattice vectors $\mathbf{R}$ are the set of all linear combinations of the primitive translation vectors $\mathbf{a}_1$ and $\mathbf{a}_2$ and define the positions of the unit cells.

$$\mathbf{R} = n_1\mathbf{a}_1 + n_2\mathbf{a}_2 \qquad n_1, n_2 \in \mathbb{Z} \tag{4.1}$$

The choice of primitive translation vectors is not unique.[186,195–199] In this work, the primitive translation vectors of the Bravais lattice are:

$$\mathbf{a}_1 = \frac{a}{2}\left(\sqrt{3}, 1\right), \qquad \mathbf{a}_2 = \frac{a}{2}\left(\sqrt{3}, -1\right) \tag{4.2}$$

where $a = \sqrt{3}a_0$ is the lattice constant in real space and $a_0 = 1.42\,\text{Å}$ is the distance between nearest neighbour atoms.[200]

4.3.3 Reciprocal lattice

The reciprocal lattice is defined with respect to the triangular Bravais lattice.[192,193,201] Each point in the reciprocal lattice corresponds to a set of lattice planes in real space. All wave vectors $\mathbf{k}$ of a plane wave must have the same periodicity as the real space Bravais lattice.[201] That is,

$$e^{i\mathbf{k}\cdot(\mathbf{r}+\mathbf{R})} = e^{i\mathbf{k}\cdot\mathbf{r}} \tag{4.3}$$

$$e^{i\mathbf{k}\cdot\mathbf{R}} = 1 \tag{4.4}$$

$$\mathbf{k}\cdot\mathbf{R} = 2\pi n, \qquad n \in \mathbb{Z} \tag{4.5}$$

Equation 4.5 describes the condition for discrete values of $\mathbf{k}$ with respect to the real lattice vectors $\mathbf{R}$.

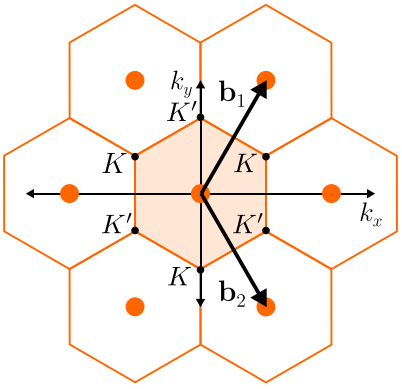

Figure 4.3: Reciprocal lattice. Linear combinations of the primitive translation vectors $\mathbf{b}_1$ and $\mathbf{b}_2$ span the reciprocal lattice points $\mathbf{K}$. The lattice points are shown by the filled orange circles and the lattice constant is $4\pi/\sqrt{3}a$. The first Brillouin zone is the primitive unit cell shown shaded while the neighbouring unit cells are shown without shading. The symmetric points K and K' are located (in k-space) at the vertices of the first Brillouin zone.[192,193]

The reciprocal lattice is illustrated in Figure 4.3. The reciprocal primitive translation vectors $\mathbf{b_1}$ and $\mathbf{b_2}$ are perpendicular to the real space planes with magnitude equal to the inverse interplanar spacing multiplied by 2π.[201]

$$\mathbf{b}_1 = \frac{2\pi}{\sqrt{3}a}\left(1, \sqrt{3}\right), \qquad \mathbf{b}_2 = \frac{2\pi}{\sqrt{3}a}\left(1, -\sqrt{3}\right) \tag{4.6}$$

Thus the reciprocal lattice constant is $4\pi/\sqrt{3}a$. Note that $\mathbf{b}_1 \perp \mathbf{a}_2$ and $\mathbf{b}_2 \perp \mathbf{a}_1$. Each point in the reciprocal lattice corresponds to a set of parallel lattice planes in real space.[201] Further illustrations that relate the real lattice planes with the reciprocal

lattice points are provided in Appendix C, Figure C.1. The set of all reciprocal space lattice vectors $\mathbf{K}$ is given by

$$\mathbf{K} = m_1\mathbf{b}_1 + m_2\mathbf{b}_2, \qquad m_1, m_2 \in \mathbb{Z} \tag{4.7}$$

The first Brillouin zone is the Wigner-Seitz cell (a primitive unit cell) of the reciprocal lattice.[201] Every possible $\mathbf{k}$ is equivalent to just one vector in the first Brillouin zone. The vertices of the first Brillouin zone are termed the K and K' points.[186] The K and K' points are positioned in k-space at:

$$K = \left(\frac{2\pi}{\sqrt{3}a}, \frac{2\pi}{3a}\right), \left(0, -\frac{4\pi}{3a}\right), \left(-\frac{2\pi}{\sqrt{3}a}, \frac{2\pi}{3a}\right) \tag{4.8}$$

$$K' = \left(\frac{2\pi}{\sqrt{3}a}, -\frac{2\pi}{3a}\right), \left(0, \frac{4\pi}{3a}\right), \left(-\frac{2\pi}{\sqrt{3}a}, -\frac{2\pi}{3a}\right) \tag{4.9}$$

These symmetric K and K' points are significant because the band gap is zero at these points and the energy dispersion is linear in the vicinity of these points. These unique properties are described further in Section 4.4 and a derivation of the linear energy dispersion relation is detailed in Appendix C.2.

4.4 Electronic band structure

4.4.1 Single layer graphene

The tight binding model is commonly used to describe the electronic band structure in graphene.[186,192,193,195–199] This approach assumes that electrons are tightly bound to the atoms that they belong to. The energy dispersion $E(\mathbf{k})$ of graphene is stated in Equation 4.10 in terms of the real lattice constant a described in Section 4.3.2. This expression is derived using the tight binding approach to a first approximation, which assumes that π electrons may 'hop' between neighbouring atoms only.[196] The derivation of Equation 4.10 is detailed in Appendix C.2 using the lattice description given in Section 4.3.2, since this derviation is often omitted or incomplete in literature.

The tight binding approach with nearest neighbour hopping is adequate for a qualitative description of the energy dispersion in graphene, particularly in the low energy dispersion regime which is most relevant to this work.[198] The energy dispersion of graphene, derived from the tight binding approach with nearest neighbour hopping

only, is given by[192,193,196,198]

$$E(\mathbf{k}) = E_0 \pm \gamma \sqrt{1 + 4\cos\left(\frac{\sqrt{3}a}{2}k_x\right)\cos\left(\frac{a}{2}k_y\right) + 4\cos^2\left(\frac{a}{2}k_y\right)} \tag{4.10}$$

where E_0 is the onsite energy and γ is the hopping integral, or overlap integral, for nearest neighbour hopping. Each of these parameters are described mathematically in the derivations presented in Appendix C.2.

The onsite energy E_0 of the π electron is determined by the Hamiltonian of a single atom, assumed to be isolated, *and* the perturbed potential due to all other atoms in the lattice. The value of E_0 is often treated as zero for illustration purposes since it only displaces the energy dispersion graph vertically.[195,197,198] The value of the hopping parameter γ is determined empirically.[198]

In the low energy dispersion regime, the dispersion relation in Equation 4.10 can be simplified to

$$E_K - E_0 = \pm\hbar v_\mathrm{F}|\mathbf{k} - K|, \quad |\mathbf{k} - K|a \ll 1 \tag{4.11}$$

and

$$E_{K'} - E_0 = \pm\hbar v_\mathrm{F}|\mathbf{k} - K'|, \quad |\mathbf{k} - K'|a \ll 1 \tag{4.12}$$

in the vicinity of the K and K' points respectively, where $v_\mathrm{F} = \sqrt{3}a\gamma/2\hbar \approx 10^6\,\mathrm{m\,s^{-1}} \approx c/300$ is the Fermi velocity (or electronic group velocity).[183,186] Derivations of Equations 4.11 and 4.12 are also presented in Appendix C.2.

Comparison of Equations 4.11 and 4.12 with the energy formula of special relativity $E = (p^2c^2 + m^2c^4)^{1/2}$, where momentum $p = \hbar k$, shows that charge carriers in graphene mimic relativistic particles with zero rest mass and speed v_F.[202] That is, the speed v_F of charge carriers in graphene is a constant, independent of momentum. This behaviour is one of the most intriguing aspects about graphene and is responsible for much of its research attention.[195]

The valence (π) and conduction (π^*) bands of graphene are described by the energy dispersion relation in Equation 4.10. This relation is a first approximation calculated using the tight binding approach with nearest neighbour hopping only. The energy dispersion is illustrated in Figure 4.4. The hopping parameter γ used in the model was $-2.7\,\mathrm{eV}$.[198] There is a zero band gap at the vertices of the Brillouin zone, i.e. the K and K' points given in Equations 4.8 and 4.9, where the band structure is conical and the dispersion is linear. The density of states at the Fermi level $E - E_0 = 0$ is zero.[203,204]

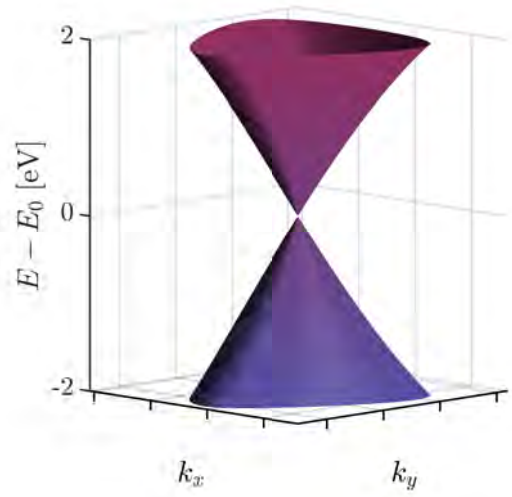

(a) Energy dispersion centred on the K and K' points.

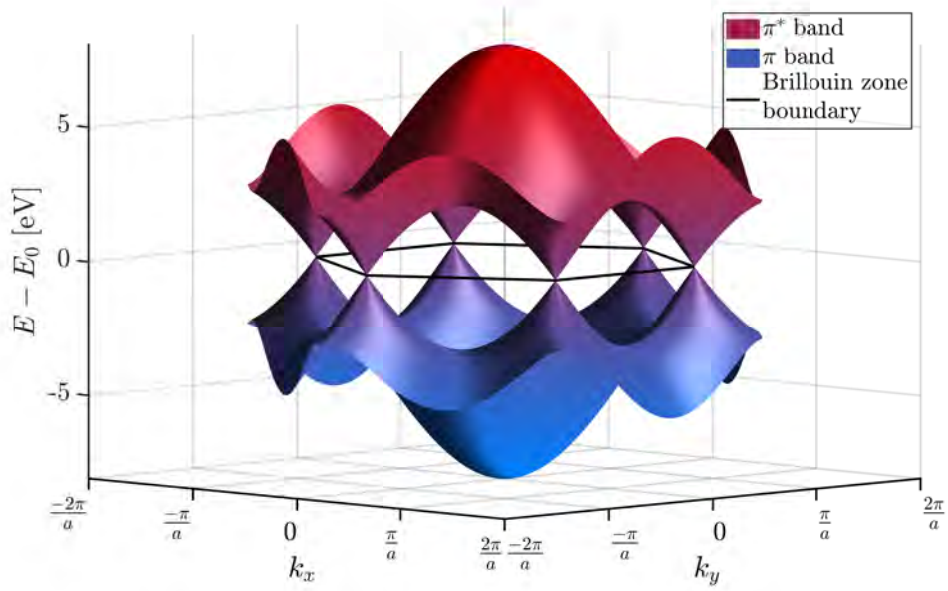

(b) Energy dispersion centred on the first Brillouin zone. The first Brillouin zone is the hexagonal region bounded by the black lines in the $E - E_0 = 0$ plane.

Figure 4.4: Energy dispersion of graphene. The energies E were calculated using the tight binding approximation for nearest neighbour hopping only. The π band ($E - E_0 < 0$) and π^* band ($E - E_0 > 0$) touch at the K and K' points. The conical band structures centred on the K and K' points show linear dispersion near the Fermi level $E - E_0 = 0$.

Figure 4.4a shows the conical band structure (Dirac cones) and linear dispersion near the K and K' points (Dirac points). By comparison, semiconductors tend to have quadratic dispersion. Figure 4.4b shows the valence (π) and conduction (π^*) bands to just beyond the first Brillouin zone.

The zero band gap and linear dispersion of graphene give rise to the broadband saturable absorption properties described in Section 4.5.1. The combination of (i) zero band gap; (ii) linear dispersion; and (iii) previously demonstrated near-IR lasers mode-locked using graphene saturable absorbers (discussed in Section 4.6); suggested that graphene would be an ideal broadband saturable absorber in the mid-IR and, therefore, motivated the study of graphene presented in this Chapter as well as Chapters 5 and 6.

4.4.2 Multilayer graphene

The saturable absorption modulation depth can be extended by stacking multiple layers of graphene as described in Section 4.5.1. In stacks of multiple graphene layers, two consecutive layers are normally oriented in such a way that the atoms in one of the two sublattices of one layer are directly above half of the atoms in the neighbouring layer. The second sublattice sits above the empty hexagon centres. The shortest distance between carbon atoms in different layers is 3.4 Å.[186] Each additional graphene layer introduces two more energy bands to the stack and coupling between layers leads to hopping terms between the π orbitals in adjacent layers.[186] In ordered few layer graphene, the characteristic linear dispersion of single layer is either replaced or augmented by pairs of split hyperbolic bands.[205]

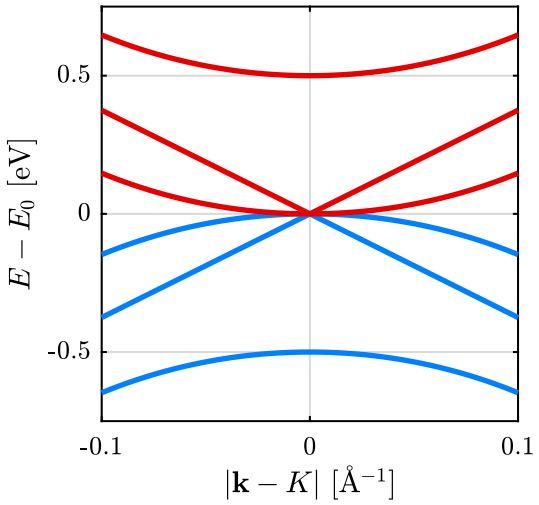

Figure 4.5: Energy band illustration for trilayer graphene.[186,205–207]

An illustration of the band structure in ordered trilayer graphene is presented in Figure 4.5.[186,205–207] The three pairs of energy bands give rise to nine possible interband energy transitions. A photon with photon energy $E_{\text{ph}} = h\nu$, for example, may be absorbed via one of nine possible interband transitions, provided that E_{ph} is higher than the largest band gap $\sim$1 eV (1.2 µm) at $|\mathbf{k} - K| = 0$.[205] Furthermore, at high

optical intensity, band separations of $2E_{\text{ph}}$ may be bridged by two-photon absorption. Therefore, when $E_{\text{ph}} < \sim 1\,\text{eV}$ ($\lambda > \sim 1.2\,\mu\text{m}$), the number of possible interband transitions is higher for the two-photon absorption process than single photon absorption. Two-photon absorption is described in Section 4.5.2 and experimental results presented in Chapter 6 show that it limits the effective modulation depth of multilayer graphene in the mid-IR and is detrimental to its performance as a laser mode-locking material.

4.5 Optical properties

Despite being only one atom thick, graphene absorbs 2.3 % of incident low intensity light, independent of wavelength λ, while reflectance is negligible (<0.1 %).[208] The wavelength independence is due to the linear energy dispersion given by Equations 4.11 and 4.12 and illustrated in Figure 4.4a. As the intensity of incident light is increased, the absorption of light by graphene decreases and the absorption *saturates*, as illustrated graphically in Figure 4.7. This saturable absorption property, combined with fast recovery times and linear dispersion, make graphene an ideal material for passively mode-locking ultrafast lasers over a broad spectral range.[183,209,210]

At higher incident light intensity, two-photon absorption can become significant, particularly in multilayer graphene[211–213] as discussed in Section 4.4.2, and reduce the otherwise full extent of the saturable absorption (i.e. reduce the effective *modulation depth* of the absorption). The affect of two-photon absorption on effective modulation depth in trilayer graphene is shown by experiment in Chapter 6. At even higher intensity levels, the optical damage threshold of graphene may be exceeded, causing the breaking of carbon bonds and subsequent ejecting of material.[214–216]

In this Section, the concepts of saturable absorption, two-photon absorption, carrier lifetimes, and optical damage in graphene are introduced. These concepts are directly related to the experimental work presented in Chapters 5 and 6. Saturable absorption, two-photon absorption, and the optical damage threshold of graphene were measured in the spectral region between 1.55 µm and 3.5 µm (0.35 eV to 0.80 eV) using a tunable laser source that emitted 100 fs pulses. The details of the experiment are presented in Chapter 5 followed by published results in Chapter 6.

4.5.1 Saturable absorption

Graphene is a saturable absorber, i.e. the absorption of light decreases with increasing intensity. Figure 4.6 illustrates the saturable absorption of light in graphene using the low energy dispersion band structure described in Section 4.4 and neglecting E_0 by letting $E_0 = 0$. Low intensity light with photon energy $E_{\text{ph}} = h\nu$ is readily absorbed,

exciting π electrons from the valence band to the conduction band, leaving a vacancy (hole) in the valence band. At high light intensity, electron excitations occur at such a high rate that there is insufficient time for them to decay back down from the conduction band to the valence band before the valence band is depleted. Further absorption is rejected by Pauli blocking and the absorption *saturates*.[87,88,217]

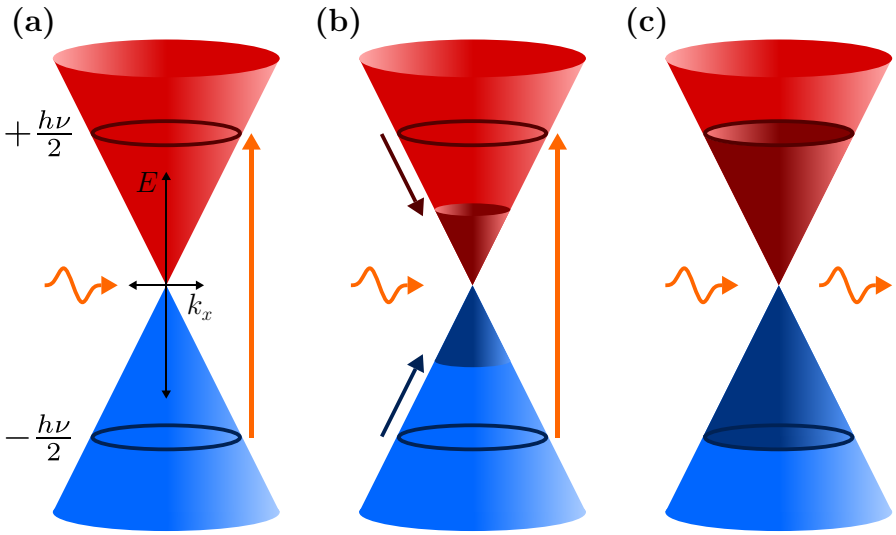

Figure 4.6: Absorption of light in graphene. Each figure depicts the low energy dispersion of graphene, centred on a K or K' point in k-space, where the k_y-axis (not shown) points into the page. **(a)** Light with photon energy $E_{\text{ph}} = h\nu$ is absorbed and electrons are excited from the valence band (π band) to the conduction band (π^* band). **(b)** The photogenerated carriers thermalise within sub picoseconds. An equilibrium electron and hole distribution is approached through intraband phonon scattering and electron-hole recombination. **(c)** At high radiation intensity, the photogenerated carriers cause the states near the edge of the conduction and valence bands to fill, causing Pauli blocking and saturating the absorption.[87]

Saturable absorption in graphene is described as a function of light intensity I by the following equation for the absorption coefficient $\alpha(I)$:[87]

$$\alpha(I) = \alpha_{\text{s}}(I) + \alpha_{\text{ns}} \tag{4.13}$$

$$= \frac{\alpha_0}{1 + \frac{I}{I_{\text{s}}}} + \alpha_{\text{ns}} \tag{4.14}$$

where $\alpha_{\text{s}}(I)$ is the saturable absorption coefficient, α_{ns} is the non-saturable absorption coefficient, α_0 is the modulation depth parameter, and I_{s} is the saturation intensity, i.e., the intensity required to reduce the saturable absorption coefficient to half of its unbleached value. The units of the absorption parameters α_0, α_{s}, and α_{ns} are treated as dimensionless (rather than inverse length) throughout this work because graphene is a 2D material.

The intensity dependent transmission $T(I)$ through graphene, therefore, is given by

$$T(I) = \exp\left[-\left(\frac{\alpha_0}{1+\frac{I}{I_s}} + \alpha_{ns}\right)\right] \tag{4.15}$$

Equations 4.14 and 4.15 are derived in Appendix C.3 for a two energy level system. The transmission T expressed in Equation 4.15 is shown graphically in Figure 4.7 to illustrate saturable absorption behaviour in graphene over a broad intensity range. The saturation intensity was assumed to be $I_s = 1\,\mathrm{GW\,cm^{-2}}$ for the illustration. In Chapter 6, it will be shown that the saturation intensity increases with increasing photon energy E_{ph} and that $I_s = 1\,\mathrm{GW\,cm^{-2}}$ when $E_{ph} = 0.8\,\mathrm{eV}$ ($\lambda = 1.55\,\mu\mathrm{m}$). The values for the absorption parameters α_0 and α_{ns} were chosen to give 2.3 % absorption at low intensity and 1.3 % modulation depth for illustration purposes.[88,208] The modulation depth can be extended by stacking multiple layers of graphene.[184,185]

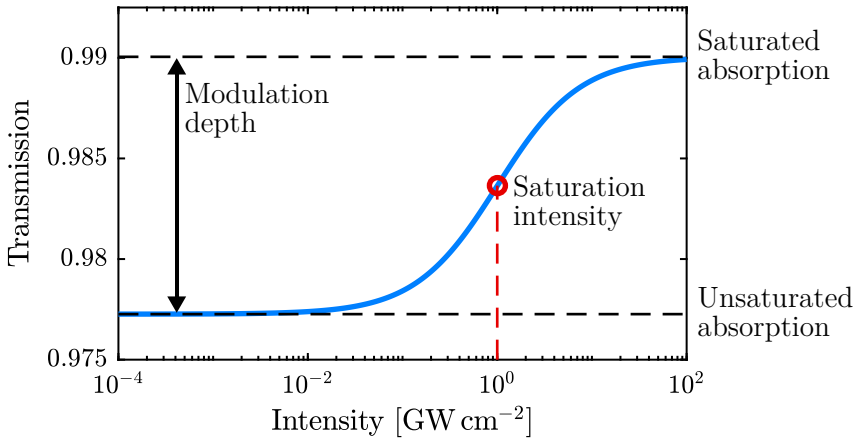

Figure 4.7: Modelled intensity dependent transmission of light through graphene. The transmission is calculated from Equation 4.15 using the parameters $\alpha_0 = 0.013$, $\alpha_{ns} = 0.010$, and saturation intensity $I_s = 1\,\mathrm{GW\,cm^{-2}}$ for illustration purposes.[88,208] The modulation depth is the difference in transmission between the completely saturated and completely unsaturated levels.

The saturation intensity I_s of graphene has been shown to depend on the radiation wavelength, λ.[185,218] Yamashita et al.[218] suggested that I_s has a wavelength λ dependence given by the empirical relationship $I_s = 2.7/\lambda^6$, where I_s and λ are expressed in units of $\mathrm{GW\,cm^{-2}}$ and µm respectively. The empirical fit was made to saturation intensities sourced from literature that were measured using radiation wavelengths ranging between 780 nm and 1560 nm (0.8 eV to 1.6 eV). However, the graphene samples used in the experimental data of the empirical fit were fabricated by various methods, including chemical exfoliation techniques to produce colloidal suspensions of graphene flakes[219] and exfoliation of graphite in water by sonication to incorporate graphene

flakes into a host polymer.[88] Therefore, there was considerable variation in the quality of the graphene samples and (for the cases of suspended graphene flakes) variations in the radiation angle of incidence to the graphene planes. Furthermore, the pulse durations of the laser sources used to measure the saturation intensities ranged between 80 fs[219] and 1 ps.[87]

When the measurements of saturation intensity presented in Chapter 6 were combined with other measurements reported in literature that were performed using (i) graphene fabricated by CVD, epitaxy, or mechanical exfoliation; and (ii) radiation directed at normal angle of incidence to the graphene plane (unlike the case of randomly orientated suspensions of graphene flakes); the dependence of photon energy E_{ph} on saturation intensity I_{s} was shown to fall into two distinct regimes of laser pulse duration, τ_{p}. When $\tau_{\mathrm{p}} \leq 500\,\mathrm{fs}$, the saturation intensity I_{s} was proportional to the third power of photon energy E_{ph}. However, when $\tau_{\mathrm{p}} \geq 1\,\mathrm{ps}$, the saturation intensity I_{s} was found to have a square root dependence. The measurements of saturation intensity I_{s} and their dependence on photon energy E_{ph} are presented in Chapter 6.

4.5.2 Two-photon absorption

Two-photon absorption (2PA) in graphene has also been reported in literature,[211–213] although far less extensively than saturable absorption. The two-photon absorption process is the simultaneous absorption of two photons causing an interband electronic transition and can be a significant absorption process when the intensity of light is high enough. The energy gap of the transition is equivalent to the combined energy of the two photons, i.e., $E_{\mathrm{2PA}} = 2h\nu$. The transition creates an electron in the conduction band and a hole in the valence band.

The rate of two-photon absorption with respect to path length has I^2 dependence. Therefore, the expression for transmission given in Equation 4.15 is modified to include two-photon absorption as follows:[211]

$$T(I) = \exp\left[-\left(\frac{\alpha_0}{1+\frac{I}{I_{\mathrm{s}}}} + \alpha_{\mathrm{ns}} + \beta I\right)\right] \tag{4.16}$$

where β is the two-photon absorption coefficient, measured in units of $\mathrm{cm^2\,GW^{-1}}$ throughout this work because graphene is a 2D material.

The strength of two-photon absorption depends on the number of layers in a graphene stack and the photon energy.[211] As illustrated in Figure 4.5, each additional layer in a stack introduces a pair of energy bands in the dispersion relation and, therefore, increases the number of possible interband transitions that can occur by photon

absorption for a given photon energy.[186] The strength of two-photon absorption in graphene has been shown to decrease with photon energy over a broad spectral region, although resonant features may occur in β as a function of E_{ph} due to stacking orientation and interlayer coupling.[211]

Two-photon absorption in graphene was observed in the experimental work presented in Chapters 5 and 6. Transmission measurements of high intensity radiation, in the spectral region between 1.55 µm and 3.5 µm (0.35 eV to 0.80 eV), through trilayer graphene showed that the effective modulation depth was affected by two-photon absorption. The two-photon absorption coefficient β was quantified at each wavelength by fitting Equation 4.16 to transmission measurements. A resonant peak was observed at 3.2 µm (0.39 eV) and the location of this peak agrees with quantum perturbation theory proposed for bilayer graphene.[211] The transmission measurements and quantification of the two-photon absorption parameter β show that two-photon absorption does limit the effective modulation depth of multilayer graphene and, therefore, will affect its performance as a mode-locking element. The strength of the affect is stronger with increasing wavelength, particularly above 2.5 µm (below 0.5 eV).

4.5.3 Lifetimes

The relaxation of photogenerated carriers in graphene is described by two distinct time scales. The fast recovery time $\tau_1 \approx 200$ fs may be attributed to carrier-carrier intraband scattering, while the slower recovery time $\tau_2 \approx 1.5$ ps may be explained by interband electron-hole recombination and carrier-phonon scattering. These carrier dynamics have been measured by various groups using ultrafast pump-probe spectroscopy.[219–221]

Dawlaty et al.[220] measured carrier relaxation times in epitaxial graphene layers grown on SiC wafers using a Ti:sapphire mode-locked laser that emitted ∼85 fs pulses with a 780 nm centre wavelength at a repetition rate of 81 MHz. They found an initial fast relaxation transient τ_1 in the 70 fs – 120 fs range followed by a slower relaxation process τ_2 in the 0.4 ps – 1.7 ps range. The slower relaxation time was found to be inversely proportional to the degree of crystalline disorder in the graphene layers as measured by Raman spectroscopy.

Shang et al.[221] measured the carrier dynamics in graphene films on CaF_2 in the mid-IR probe region between 3.15 µm and 5.0 µm (2600 cm^{-1} – 3100 cm^{-1}) using femtosecond pump-probe spectroscopy. They showed a fast relaxation τ_1 in the range 140 fs – 300 fs, which was attributed to a superposition of several ultrafast intraband and interband decay channels. The slow recovery τ_2 was in the 1.4 ps – 1.6 ps range and attributed to phonon scattering. Moreover, the fractional amplitudes of the bi-exponential fits varied with probe photon energy. For example, at a probe wavelength

of 3.85 µm (2600 cm^{-1}), the decay components were $\tau_1 = 250$ fs and $\tau_2 = 1.4$ ps, and the fractional amplitudes were $A_1 = A_2 = 0.5$, resulting in a mean lifetime of 820 fs. At the shorter probe wavelength of 3.2 µm (3100 cm^{-1}), the measured decay rates were $\tau_1 = 120$ fs and $\tau_2 = 1.56$ ps, the fractional amplitudes were $A_1 = 0.74$ and $A_2 = 0.26$ respectively, and the mean lifetime was therefore 500 fs.

4.5.4 Damage threshold

Roberts et al.[214] defined the threshold condition for laser induced damage in graphene as the point that a single laser pulse exposure creates a hole in the carbon lattice. The single-shot damage threshold was measured in the femtosecond pulse regime using a laser source with a centre wavelength of 790 nm. The damage threshold peak intensities were 2.7 TW cm^{-2}, 0.9 TW cm^{-2}, and 0.3 TW cm^{-2} for pulse durations 50 fs, 200 fs, and 1.6 ps respectively. The corresponding damage threshold fluences were 135 mJ cm^{-2}, 180 mJ cm^{-2}, and 480 mJ cm^{-2} respectively. Below the single-shot damage limit, multiple ultrafast pulse exposures led to the formation of defects. The ultrafast excitation breaks carbon bonds, thus increasing the number of lattice defects which in turn leads to the formation of smaller and smaller nano-crystallites. For example, exposure to 50 fs pulses with peak intensity $I = 10$ GW cm^{-2} caused graphene samples to degrade substantially after 10^8 exposures, corresponding to ∼1.5 days of continuous laser exposer at a 1 kHz repetition rate.

Currie et al.[215] distinguish between thermal and non-thermal effects that lead to damage in graphene. A CW laser source can cause thermal damage by photon absorption and subsequent energy dissipation through phonons which, at sufficient incident optical energy, can be violent enough to break carbon bonds. The energy from femtosecond laser pulses is transferred at rates significantly faster than the phonon relaxation time. Thus, hot electrons are created and then cooled by transferring their energy to phonons on a time scale shorter than thermal diffusion and are thus capable of breaking carbon bonds and ejecting material. Single layer CVD graphene samples were illuminated with 50 fs pulses that had a centre wavelength of 800 nm and a 40 µm spot diameter. Damage occurred at optical pulse fluences ranging between 14 mJ cm^{-2} and 66 mJ cm^{-2}. Pulse fluences below this range were not investigated and therefore damage at fluences below 14 mJ cm^{-2} cannot be ruled out.

A more conservative estimate of the optical damage threshold in graphene was reported by Lee et al.[216]. The damage threshold intensity I_{dam} was estimated to be 2 GW cm^{-2} using a light source with a centre wavelength of 1560 nm, pulse width 210 fs, 86 MHz repetition rate, and 4.4 ± 0.6 µm beam diameter. The damage threshold intensity I_{th} corresponds to a threshold fluence of $F_{\mathrm{dam}} = 0.42$ mJ cm^{-2}. Optical damage

resulted from high peak power of the laser source rather than from heat due to the average power.

In the work presented in Chapter 5, Section 5.8, the damage threshold of graphene was measured in the spectral region between 1.55 µm and 3.5 µm (0.35 eV to 0.80 eV) using a tunable laser source that emitted 100 fs pulses. The measurements were performed by systematically incrementing the radiation intensity incident on a sacrificial sample of monolayer graphene until damage could be observed visually using a microscope with 10× magnification. The sacrificial sample was repeatedly translated (horizontally) across the beam waist so that any laser induced damage could be observed in rows, rather than single spots, for easier identification. The measured damage thresholds were wavelength dependent and ranged between $60 \pm 11\,\mathrm{GW\,cm^{-2}}$ ($\lambda = 1.55\,\mu\mathrm{m}$) and $191 \pm 33\,\mathrm{GW\,cm^{-2}}$ ($\lambda = 2.50\,\mu\mathrm{m}$). The damage threshold intensity measured when $\lambda = 1.55\,\mu\mathrm{m}$ is more than a magnitude higher than the measurement reported by Lee et al.[216], while the measured threshold fluence was within an order of magnitude higher. The measured damage threshold intensities and fluences are listed in Table 5.4 and an image of laser induced damage in graphene, produced deliberately while performing the damage threshold measurements, can be found in Figure 5.7.

4.6 Graphene mode-locked lasers

When a saturable absorber is placed in a laser cavity, the transmission of the high intensity components of the laser radiation is higher than the lower intensity components. Short pulse generation is therefore favoured and CW radiation is suppressed, which can be used to achieve mode-locking. For ultrashort pulse generation, a saturable absorber with a fast recovery time, such as graphene, is required to stabilise the mode-locking, while a slower recovery time could facilitate laser self-starting.[86,222]

Graphene mode-locked fibre lasers were first demonstrated in the telecommunication band ∼1.5 µm (0.8 eV) and subpicosecond pulses were achieved.[87–89] Solid state lasers in the 1 µm,[90,91] 2 µm,[92,93] and 2.5 µm[94,95] wavelength bands have also been mode-locked using graphene. Tolstik et al.[95] achieved a pulse duration of 41 fs at a repetition rate of 108 MHz in a Cr:ZnS laser. The wavelength was centred at 2.4 µm with a 190 nm spectral bandwidth. They compared the performance of single layer, bilayer, and trilayer graphene mounted on a mirror. The maximum pulse energy, 2.3 nJ, was achieved using bilayer graphene and the average output power was 250 mW.

The longest wavelength demonstrated in a graphene mode-locked laser is 2.78 µm (0.4 eV) in which 42 ps pulses were achieved.[70] The 4 – 6 layer graphene stack, fabricated by the CVD method, was coated onto a gold cavity mirror to mode-lock the Er^{3+}-doped

ZBLAN fibre laser. The linear absorption of the multilayer graphene was ∼12 % and its modulation depth and saturation intensity were ∼10 % and 2 MW cm^{-2} respectively. The mode-locked pulses were 42 ps wide with a repetition rate of 25.4 MHz and an average output power of 18 mW.

The 42 ps pulses achieved by Zhu et al.[70] at a wavelength of 2.78 µm were significantly longer than the 41 fs pulses achieved by Tolstik et al.[95] at 2.4 µm. The transmission measurements presented in Chapter 6 show that the effective modulation depth of trilayer graphene decreases with wavelength and is limited by two-photon absorption. The transmission measurements showed that the effective modulation depth dropped from 2 % to 1 % when the wavelength was increased from 2.5 µm (0.50 eV) to 2.8 µm (0.44 eV). Therefore, the performance of multilayer graphene as a mode-locking element is expected to reduce with increasing wavelength and may explain why ultrashort pulses are difficult to achieve beyond the 2.5 µm band.

4.7 Conclusion

The unique properties of graphene that underlie its performance as a saturable absorber in the mid-IR spectral region have been described in this Chapter. The energy dispersion is linear in the vicinity of the K and K' points, where the band gap is zero. The combination of linear dispersion, Pauli blocking at high intensity, and ultrafast response times make graphene a promising broadband saturable absorber for passive mode-locking. Graphene mode-locked lasers have been demonstrated in the near-IR domain but not beyond the 3 µm wavelength band. In the spectral region above 2.5 µm (below 0.5 eV), two-photon absorption becomes significant enough to limit the effective modulation depth of the absorption and reduce the performance of multilayer graphene as a mode-locking element (shown in Chapter 6). The characterisation of trilayer graphene, by experiment, in the spectral region between 1.55 µm and 3.5 µm (0.35 eV to 0.80 eV) is presented in Chapters 5 and 6 to investigate the performance limitations of graphene for mode-locking mid-IR lasers.

Chapter 5
Graphene Under Illumination: Experiment

This Chapter provides details of an experiment performed to measure the response of graphene to high intensity radiation. The intensity dependent transmission through trilayer graphene was measured in the spectral region between 1.55 µm and 3.5 µm (0.35 eV to 0.80 eV) using the z-scan technique and a tunable laser source. The purpose of this experiment was to study saturable absorption behaviour in graphene and assess the potential use of graphene for mode-locking mid-IR lasers. The results from this experiment, presented in Chapter 6, will show that the effective modulation depth of multilayer graphene is affected by two-photon absorption, which will be detrimental to the performance of multilayer graphene when used as a saturable absorber to mode-lock mid-IR lasers.

5.1 Background

The nonlinear optical properties of graphene have been measured by numerous groups and reported in literature.[70,87,89,185,211–213,217,223] Several of these groups showed that the saturation intensity increases with photon energy by repeating transmission measurements using a series of different wavelength bands rather than just one.[185,212,213,223] However, besides one report of a measurement performed in the 2.8 µm wavelength band,[70] no measurements of saturation intensity beyond the 2.4 µm band[213] were found in literature. To the best of our knowledge, measurements of transmission through graphene had not been performed using one sample and one fixed pulse duration over a broad spectral range in the mid-IR.

Furthermore, as outlined in Section 4.6, there have been few reported demonstrations of ultrashort pulses achieved using graphene as a mode-locking element beyond

the 2.5 µm wavelength band. The characterisation of graphene in the mid-IR spectral region was important for determining its effectiveness as a saturable absorber for mode-locking mid-IR lasers, such as the 3.5 µm DWP fibre lasers modelled in Chapter 3.

5.2 Introduction

The experiment detailed in this Chapter was designed and optimised to measure small changes (<1 %) in transmission of light. All measurements of transmission through graphene presented in this work were performed using the same graphene sample, tunable laser source, and pulse duration (100 fs). Once the experiment design was optimised for sensitivity, the experiment conditions were kept as consistent as possible between measurements that were performed using different source radiation wavelengths. Only the source radiation wavelength, spectral filters, and power attenuation were changed between transmission measurements.

The design of this experiment was optimised for measurement sensitivity. The main challenges encountered while designing this experiment were to:

i. achieve measurement sensitivity levels <0.5 %;

ii. reduce effects of source power fluctuations;

iii. reduce effects of beam wander;

iv. avoid laser induced damage to the graphene.

These challenges will be addressed throughout this Chapter. Once the experiment design was optimised, the procedure for measuring the intensity dependent transmission using any given wavelength of radiation could be summarised as follows:

i. measure the intensity profile of the beam;

ii. determine the beam waist location and spot size;

iii. measure the damage threshold intensity of graphene;

iv. determine the minimum attenuation required to avoid laser induced damage to graphene;

v. perform a z-scan transmission measurement through an uncoated CaF_2 window;

vi. perform the z-scan transmission measurement through graphene mounted on a CaF_2 window;

vii. data analysis.

These procedures were repeated at each of the following radiation wavelength bands: 1550 nm, 2000 nm, 2500 nm, 2800 nm, 3200 nm, and 3500 nm. Each procedure will be described throughout this Chapter. The telecommunications wavelength band 1550 nm was included so that measurements could be compared with others reported in literature,[87–89,185,213] while the wavelength bands 2800 nm and 3500 nm were included because these are competing laser transitions of the Er^{3+}-doped fluorozirconate glass fibre lasers modelled in Chapter 3.

The optimised design of the z-scan is outlined in Section 5.3 and illustrated in Figure 5.1a. This design was used in all z-scan measurements presented in Chapter 6. The graphene samples used during design optimisation, damage threshold measurements, and transmission measurements throughout this experiment are described in Section 5.4. The properties and limitations of the tunable laser source are described in Section 5.5 followed by characterisations of the optical filters used throughout the experiment in Section 5.6. The method and results of beam intensity profile measurements are presented in Section 5.7. The approach taken to measure the laser induced damage threshold of graphene is described in Section 5.8 and estimates are presented. Finally, the z-scan process is described in further detail and transmission measurements are presented in Section 5.9. The significance of the z-scan results will be discussed in the published article contained in Chapter 6.

5.3 Experiment design

This experiment was designed to measure the intensity dependent transmission of laser pulses through graphene using the z-scan technique.[224,225] Relative transmission measurements were performed using beams that were split to propagate along reference and signal arms. A schematic of the z-scan experiment is illustrated in Figure 5.1a. The tunable laser source (TLS) emitted 100 fs pulses at a 1 kHz repetition rate. The beam was spectrally filtered to block unwanted spectral components, such as residual pump light, and was attenuated with neutral density (ND) filters to prevent laser induced damage to the graphene. A mid-IR polariser (Thorlabs LPMIR050) prevented the possibility of polarisation drifts proceeding to the beamsplitter (BS) and varying the ratio of reflectance to transmittance.

The experiment was designed to ensure that the z-scan would span a wide range of intensities (over four orders of magnitude) so that the full range of saturable absorption (i.e. the modulation depth) could be observed. This intensity range was predicted theoretically in Section 4.5.1 from Equation 4.15 and can be found illustrated in Figure 4.7. The combination of z-scan range (150 mm), lens focal length (f=75 mm), and

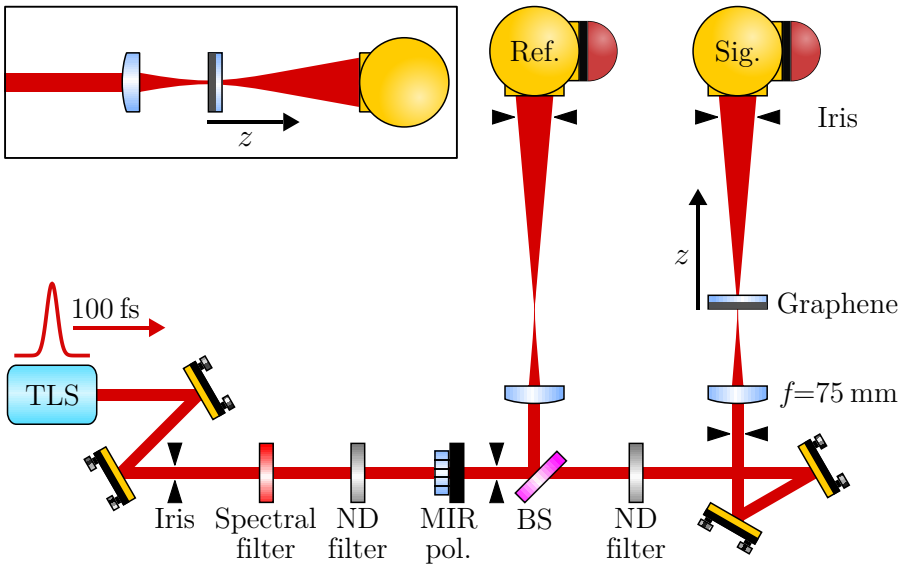

(a) Schematic of z-scan experiment.

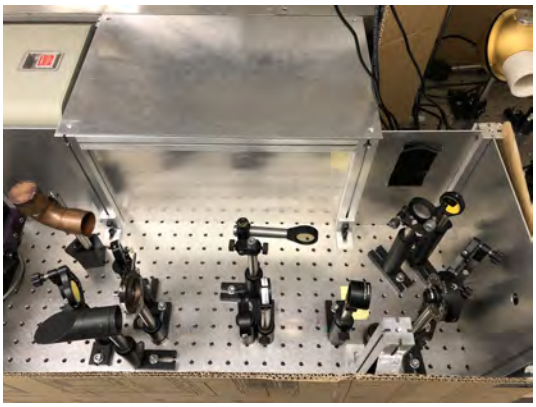

(b) Source area.

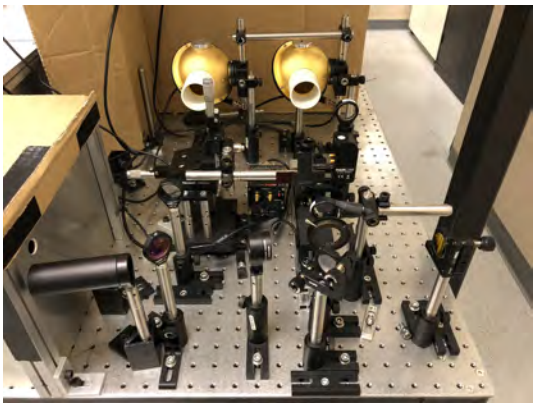

(c) Measurement area.

Figure 5.1: Experiment design for z-scan transmission measurements. The spectrally filtered beams were attenuated by neutral density (ND) filters to prevent laser induced damage to the graphene. The mid-IR (MIR) polariser prevented polarisation drifts incident on the beamsplitter (BS), which split the beam into a reference path and signal path. The graphene sample was placed in the signal path and translated along z from the focal point by up to 150 mm. Each beam entered an integrating sphere attached to a detector. The source area contained unfiltered, high intensity radiation that was dumped and isolated from the measurement area using aluminium sheets to prevent scattered (triggered) pulses of light from entering the detection system.

graphene sample size (⌀ 25.4 mm) were chosen to meet this objective.

The beam was split into a reference path and signal path using a CaF_2 beamsplitter (BS, Thorlabs BSW511) coated for the 1 µm – 6 µm spectral range. Each beam was focussed by a CaF_2 plano convex lens (f=75 mm). The spot radius w_0 at the focal point was between 54 µm and 78 µm, depending on the wavelength, as measured and listed in Table 5.3. Each detection system included a gold integrating sphere (Newport

819D-GL-4) and PbSe detector (Thorlabs PDA20H-C), suitable for the 1.5 µm to 4.8 µm spectral region. Detections of both the reference and signal beams enabled the effects of source power fluctuations to be (mostly) cancelled out.

The integrating spheres were implemented to minimise the effects of beam wander. Furthermore, the large expanded beam (∼30 mm diameter) incident on the internal grainy surface of each integrating sphere meant that fluctuations in detected power, due to a combination of local variations in the sphere surfaces and beam wander, were minimised. The beams that entered each integrating sphere were closely matched in power, as well as size, to establish comparable detector responses. This beam matching design enabled a measurement sensitivity of <0.5 % to be achieved.

During each z-scan, the graphene sample was initially placed at the focal point of the signal lens and translated by up to 150 mm in the direction of beam propagation, $\vec{z}$. At each sample position z, the pulse energies of the signal and reference beams were measured simultaneously, both with and without the sample in the beam path, to minimise the effects of source power fluctuation and drift. A motorised translation stage (Thorlabs MTS50/M-Z8) with 50 mm travel was used to increment the sample along $\vec{z}$ from each of three fixed positions that extended the maximum possible z-scan range from 50 mm to 150 mm.

The sample was held by a motorised flipper (Thorlabs MFF101/M) that was mounted on the motorised translation stage and that enabled the sample to be flipped into and out of the signal beam. In this way, the time between measurements was minimised, reducing effects from source power fluctuations. Customised software, developed using MATLAB, was used to command the motorised stage, motorised flipper, and an oscilloscope (Rigol DS4012). The averages of 2048 waveforms were acquired from the reference and signal channels at each position z and each flipper position. The transmission $T^{(z)}$ at each sample position z was calculated from the expression

$$T^{(z)} = \frac{E_{\mathrm{sig}}^{(z)} / E_{\mathrm{ref}}^{(z)}}{E_{\mathrm{sig0}}^{(z)} / E_{\mathrm{ref0}}^{(z)}} \tag{5.1}$$

where $E_{\mathrm{sig}}^{(z)}$ and $E_{\mathrm{ref}}^{(z)}$ are the averaged pulse energies detected by the signal and reference detectors respectively at position z when the sample was in the signal beam, and $E_{\mathrm{sig0}}^{(z)}$ and $E_{\mathrm{ref0}}^{(z)}$ are the energies detected when the sample was removed from the beam path. Note that although four pulse energies were measured at each position z, only $E_{\mathrm{sig}}^{(z)}$ had any dependence on intensity I (and therefore position z).

The experimental setup was divided into two sections – a source area and a measurement area. Photographs of these two sections are presented in Figures 5.1b and 5.1c that provide real images to associate with the schematic representation in Fig-

ure 5.1a. Laser pulses were emitted from the left side of the source area (Figure 5.1b) and exited out through a circular aperture in the aluminium sheet at the right. The laser was aligned to the beamsplitter using the pair of beam steering mirrors located near the source, one iris immediately following the mirrors, and the aperture in the aluminium sheet. The beam was filtered spectrally, attenuated, and polarised in the source area which was enclosed to prevent leakage of scattered (triggered) pulses of light into the detection system.

The filtered, attenuated, and polarised beam entered the measurement area (Figure 5.1c) from the circular aperture in the aluminium sheet at the left. The beam was split into signal and reference paths. The signal beam was attenuated further to closely match the power of the reference beam and its alignment was optimised using a second pair of beam steering mirrors. Each beam was focused by a lens (f=75 mm) before entering an integrating sphere connected to a PbSe detector. The graphene sample was translated along the signal path from the focal point toward the integrating sphere by a distance of up to 150 mm during each z-scan.

5.4 Graphene samples

The graphene samples measured throughout this experiment were produced by the CVD method described in Section 4.1 and transferred onto CaF_2 substrates. All z-scan transmission measurements presented in Chapter 6 were performed on one trilayer graphene sample produced and transferred by Graphenea, Spain. The quality of the graphene, before and after the experiment, was validated by Raman spectroscopy explained and illustrated in the published article contained in Chapter 6. The trilayer was formed by three separate transfers of single layer graphene onto a ⌀ 25.4 mm CaF_2 substrate. The large sample size was chosen so that a large beam could be transmitted through the graphene and, therefore, the transmission could be measured over a large range of intensities (four orders of magnitude) during any single z-scan. The trilayer configuration was chosen for the following reasons:

i. multilayer graphene enabled the study of interactions between layers;

ii. the modulation depth of graphene could be tuned by the number of layers, which added importance to the study of multilayer graphene;

iii. trilayer graphene could be produced without compromising the material quality when compared with the quality of single layer graphene production;

iv. saturable absorption was more likely to be observed in trilayer graphene than in single layer graphene due to the higher modulation depth of trilayer graphene and limitations in measurement sensitivity.

Preliminary experiments were performed on 6 – 8 layer graphene (rather than single or few layer graphene) so that nonlinear absorption processes were more likely to be observed during experiment design and optimisation. The 6 – 8 layer Trivial Transfer Graphene™ was supplied by ACS Material and transferred onto a ⌀ 12.7 mm CaF_2 substrate using the wet transfer process in accordance with user instructions provided by the supplier. The graphene was supplied with a PMMA coating on one side. The sample was released into deionised water, transferred onto the substrate, baked, and immersed in preheated acetone to remove the PMMA. A single layer graphene sample was also produced by the same method and then used as a sacrificial sample for damage threshold estimates presented in Section 5.8.

Fourier transform infrared (FTIR) spectra of the trilayer graphene sample (TLG on CaF_2) and an uncoated CaF_2 window are shown in Figure 5.2. The transmission through TLG alone, calculated from the two spectra, increases a few percent with wavelength over the spectral region from 1.5 µm to 4.0 µm, which is also observed in transmission measurements presented in Chapter 6 in the low intensity regime and has been reported in literature.[205,226] The light source in the PerkinElmer FT-IR Spectrum Two spectrometer was low power CW and was not expected to cause any nonlinear absorption processes in the graphene. The CaF_2 substrate was chosen for its low absorption in the mid-IR. Graphene has negligible reflectivity.[208] Therefore, the FTIR spectrum of the TLG on CaF_2 sample was affected by non-saturated absorption (∼2.3 % per layer[208]) in the graphene and Fresnel reflections from the front and back face of the CaF_2 substrate. The small absorption features around 3.5 µm in the CaF_2 only spectrum are not observed in the TLG on CaF_2 spectrum, nor in CaF_2 spectra provided by the supplier (Thorlabs). Therefore, the features around 3.5 µm in the calculated TLG spectrum are expected to be non-physical.

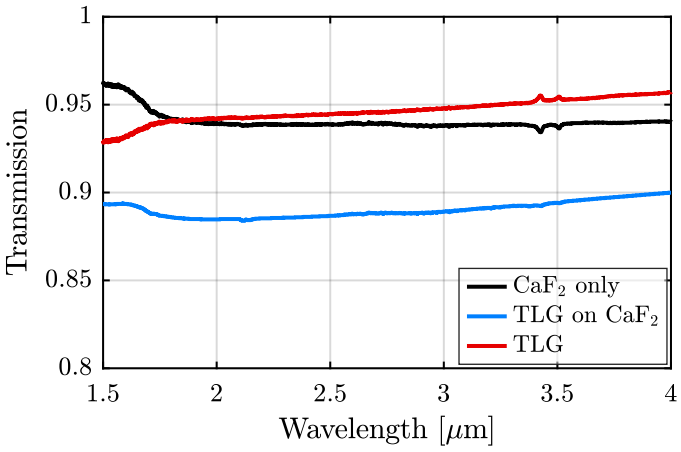

Figure 5.2: FTIR spectra of a CaF_2 substrate and the trilayer graphene (TLG) on CaF_2. The TLG transmission was calculated from the two above mentioned spectra.

5.5 Tunable laser source

The TLS was an optical parametric amplifier (Light Conversion TOPAS-C) pumped by an 800 nm regenerative amplifier system (Spectra Physics Spitfire Pro XP). The pulse duration was 100 fs (full width at half maximum) and the repetition rate was 1 kHz. The components of the OPA and their properties are listed in Appendix D, Table D.1. The TOPAS-C included a difference frequency generation (DFG) crystal (1 mm thick $AgGaS_2$). Light converted by DFG was emitted along with higher frequency components (signal, idler, and 800 nm pump light) that were filtered out using long pass (LP) and band pass (BP) filters while transmission measurements were performed.

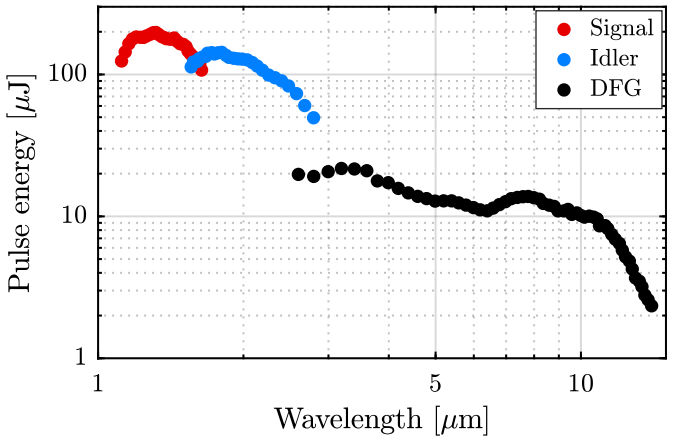

Figure 5.3: Laser source TOPAS-C 09690 tuning curves. Where the tuning curves overlap, the operator may choose a light source from either tuning curve.

According to the TOPAS-C performance specifications, the signal wave was tunable

from 1150 nm to 1600 nm while the idler wave was tunable from 1600 nm to 2600 nm. Figure 5.3 shows the tuning curves of the TOPAS-C following initial installation (December, 2009).

Table 5.1: Light emitted from the tunable laser source (TOPAS-C) that was used to measure transmission through graphene. The average power P_{avg} was measured at three locations – (i) the TOPAS output; (ii) after the spectral filter; and (iii) after the signal lens when the signal beam was not attenuated by ND filters. The spectral filters are described in Section 5.6.1.

λ [nm]	Pol.	Signal (V) [nm]	Idler (H) [nm]	Light source	Spectral filter	P_{avg} TOPAS [mW]	P_{avg} Spectral filter [mW]	P_{avg} Signal lens [mW]
1550	V	1550.00	1660.52	Signal	LP1500+ BP1550	173	3.80	1.35
2000	H	1338.01	2000.00	Idler	LP1500	190	56.0	27.2
2500	H	1180.11	2500.00	Idler	LP1500	135	20.0	9.4
2800	H	1244.44	2253.22	DFG	LP2500	92	3.0	1.0
3200	H	1280.00	2145.32	DFG	LP2500	83	2.5	0.9
3500	H	1302.16	2085.82	DFG	LP2500	100	3.2	1.2

The transmission measurements were performed using radiation in the spectral region between 1.55 µm and 3.5 µm (0.35 eV to 0.80 eV). The wavelengths are listed in Table 5.1 along with their signal and idler components, the spectral filters used, and the average power measured at three locations. The signal was vertically polarised (V) while the idler and DFG were horizontally polarised (H). Where the tuning curves overlapped, as illustrated in Figure 5.3, the light source was chosen according to the optics available to filter out unwanted spectral components. For the case when wavelength $\lambda = 1550$ nm, a 1550 nm half waveplate (Thorlabs WPH05M-1550) was used to rotate the polarisation from V to H so that all transmission measurements were performed using horizontally polarised light for consistency. The average power was measured at three locations – (i) the TOPAS output; (ii) after the spectral filter; and (iii) after the signal lens (where the graphene sample would be placed) without attenuation by ND filters.

The source power was observed to fluctuate or drift over several time scales while transmission measurements were performed. The effects of fast power fluctuations were removed by averaging 2048 pulses. The source power also oscillated with a period of ∼8 min, which can be observed in z-scan data presented in Figure 5.9. After considerable investigation, these oscillations were attributed to the laboratory air conditioning cycle and were an unavoidable noise source. This meant that the time between measurements while the sample was in and out of the beam path at each z location needed

to be minimised. Finally, the source power drifted over a time scale of several hours, particularly within the first five hours after the laser source was switched on. Therefore, each z-scan was started at least five hours after the source was turned on and was completed within approximately two hours.

Observations of beam wander were made while each beam profile was measured. Each beam profile was measured using a knife edge that blocks part of the beam. The beam wandered in both the horizontal and vertical directions and added considerable difficulty to measuring the beam profile for each wavelength of radiation. These beam profile measurements, as well as the approach taken to overcome beam wander effects, are documented in Section 5.7.

The main challenges in achieving $<0.5\,\%$ measurement sensitivity were due to laser source instability described in this Section.

5.6 Optical filters

5.6.1 Spectral filters

Three spectral filters – 1550 nm band pass (BP1550), 1500 nm long pass (LP1500), and 2500 nm long pass (LP2500) – were used to block unwanted spectral components (such as 800 nm pump light) emitted from the source. Optical density spectra of the filters are presented in Figure 5.4 to show that when these filters were used in accordance with Table 5.1, the unwanted spectral components of source radiation were filtered out. The spectra were measured using a Cary 5000 UV-Vis-NIR spectrophotometer (0.75 µm – 3.3 µm) and a PerkinElmer FT-IR Spectrum Two spectrometer (1.3 µm – 6.0 µm). The optical density of the LP2500 filter was also measured at wavelengths 1.55 µm, 2.0 µm, and 2.5 µm using the OPA femtosecond laser source to confirm that it was consistent with Figure 5.4a (and not Figure 5.4b).

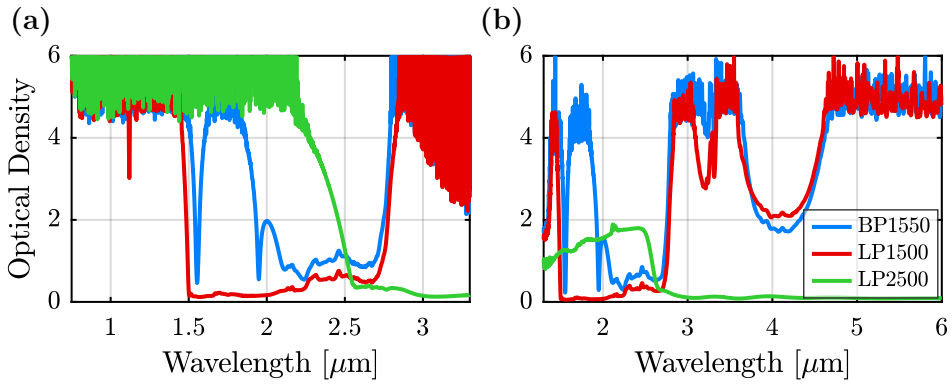

Figure 5.4: Optical density spectra of spectral filters used in z-scan transmission measurements. The three filters were a 1550 nm band pass (BP1550), 1500 nm long pass (LP1500), and 2500 nm long pass (LP2500). **(a)** Optical density spectra in the spectral region between 0.75 µm and 3.3 µm measured using a Cary 5000 UV-Vis-NIR spectrophotometer. **(b)** Optical density spectra in the spectral region between 1.3 µm and 6.0 µm measured using a PerkinElmer FT-IR Spectrum Two spectrometer.

5.6.2 Neutral density filters

A set of ND IR filters were characterised during the preliminary stages of this experiment and FTIR spectra can be found in Appendix D.2.1. These germanium ND filters were supplied by Spectrogon and designed for the 2 µm – 16 µm spectral region. However, these filters caused the beam path to deviate, possibly due to a slight wedge in each filter. The attenuated power was too low for beam alignment and, therefore, the beam had to be aligned while it was unattenuated. Therefore, it was necessary that the ND filter did not deviate the beam path and that the wavelength dependent optical density of the ND filter was known. Therefore, the Spectrogon IR ND filters were not suitable for this experiment.

Table 5.2: OD of ND UV filters for each radiation wavelength used to measure the transmission through graphene.

λ [nm]	NDUV 01A	NDUV 02A	NDUV 03A	NDUV 04A	NDUV 05A	NDUV 06A	NDUV 10A	NDUV 20A	NDUV 30A
1550	0.03	0.14	0.26	0.39	0.51	0.67	1.09	1.70	2.07
2000	0.03	0.14	0.28	0.45	0.58	0.74	1.21	1.82	2.10
2500	0.04	0.15	0.30	0.50	0.64	0.80	1.29	1.90	2.08
2800	0.07	0.20	0.34	0.55	0.69	0.90	1.38	1.94	2.07
3200	0.03	0.16	0.32	0.53	0.68	0.86	1.36	1.98	2.05
3500	0.04	0.17	0.34	0.56	0.71	0.89	1.40	2.02	2.05

Alternatively, a set of ND UV filters (Thorlabs, fused silica reflective) were observed to be suitable, despite being designed for the 200 nm – 1200 nm spectral region, and were used throughout all z-scans and damage threshold measurements. Unlike the ND IR

filters, the ND UV filters did not deviate the beam path. FTIR spectra of these filters can be found in Appendix D, Figure D.2. However, a peak in the optical density in the 2.8 µm wavelength band was not consistent with observations made using the OPA femtosecond laser source. Therefore, the optical densities of all the ND UV filters were measured directly using the OPA femtosecond laser source and the z-scan detection system illustrated in Figure 5.1. The measurements were performed using all z-scan radiation wavelengths and are listed in Table 5.2. These values were used to determine the beam attenuation throughout all z-scan transmission measurements presented in Chapter 6 and damage threshold measurements described in Section 5.8.

5.7 Beam profiles

The intensity profiles of each beam were measured using the knife edge technique.[227,228] A schematic of the knife edge measurement setup is presented in Figure 5.5. The knife edge was made up of two razor blades at right-angles in the xy-plane and mounted on a XYZ translation stage. One razor blade edge was aligned vertically for measuring the horizontal spot size $w_x(z)$ while the other was aligned horizontally for measuring the vertical spot size $w_y(z)$.

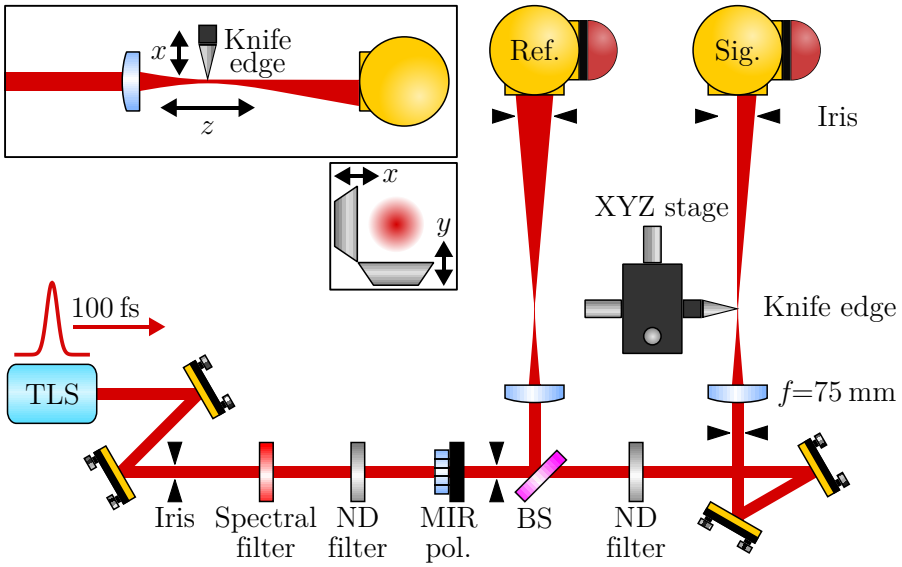

Figure 5.5: Schematic for M^2 measurements. The knife-edge consisted of a pair of razor blades aligned at right angles and mounted on a 3-axis linear stage. The vertically aligned blade was used to measure the beam size in the horizontal (x) direction while the horizontally aligned blade was used to measure the beam in the vertical (y) direction. The beam size was measured at a range of z positions either side of the beam waist to determine the beam propagation parameter M^2.

The spot sizes $w_x(z)$ and $w_y(z)$ were measured at ~17 discrete z positions either

side of the beam waist, with a higher concentration of measurements taken close to the beam waist, to determine the beam propagation described by Equation 5.2. The spot size $w_x(z)$, for example, was measured by taking the absolute difference between razor positions along the x-direction that clip the beam to 90 % and 10 % of its total average power. The difference was multiplied by the factor 0.78 to obtain the ($1/e^2$ intensity half-width) spot size $w_x(z)$.[227] The vertical spot size $w_y(z)$ was measured similarly.

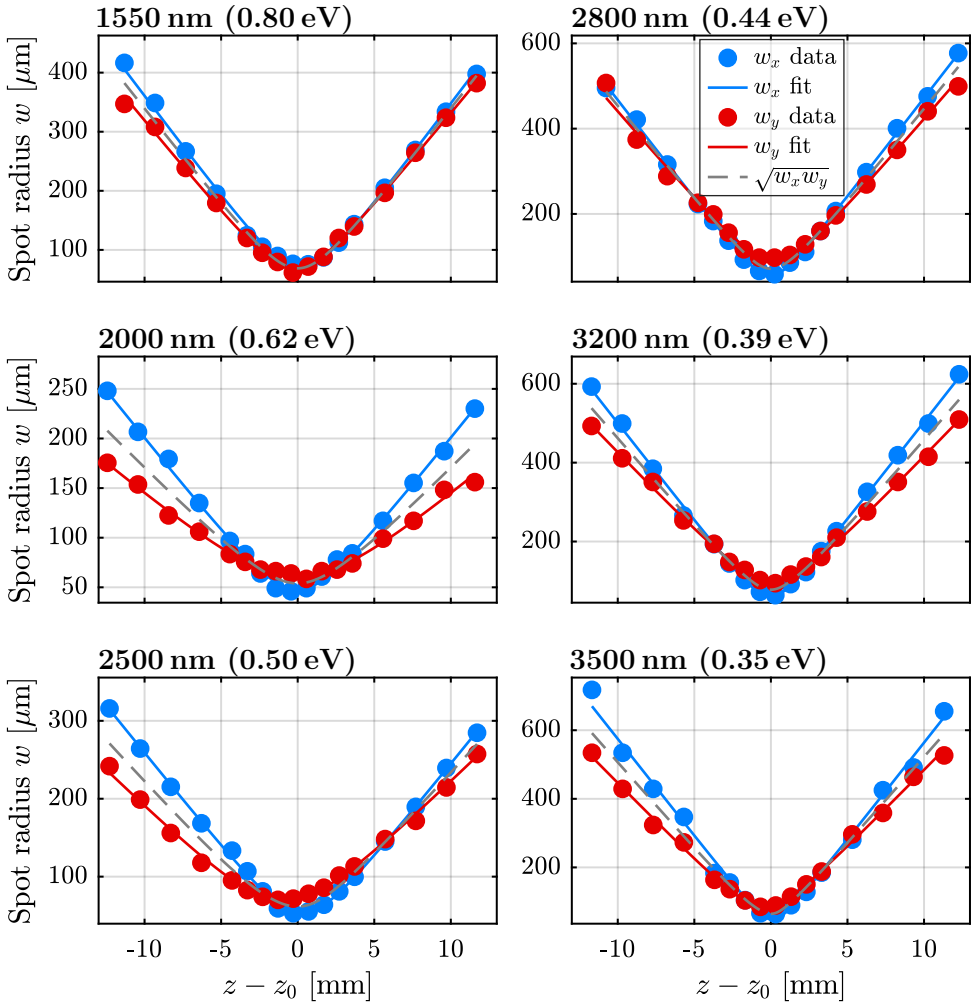

Figure 5.6: Beam profile measurements for each radiation wavelength fitted to the function given by Equation 5.2.

The data were fitted to the free-space propagation function for the spot radius $w(z)$ of real beams given by[228]

$$w(z) = w_0 \left[1 + \left(\frac{M^2 \lambda (z - z_0)}{\pi w_0^2}\right)^2\right]^{\frac{1}{2}} \tag{5.2}$$

to determine the M^2 parameters (M_x^2 and M_y^2) and beam waist spot sizes (w_{0x} and

w_{0y}) of each beam. The beam propagation parameter M^2 represents the degree of variation of the beam from an ideal Gaussian beam ($M^2 = 1$).

The knife edge measurements of each beam are presented graphically in Figure 5.6 while fitted values are listed in Table 5.3. The spot sizes $w_x(z)$ and $w_y(z)$ were estimated from the fitted function, given by Equation 5.2, which therefore determined the beam area $A_{\text{beam}}(z) = \pi w_x(z) w_y(z)$. The function $\sqrt{w_x w_y}$ was calculated from the fitted functions $w_x(z)$ and $w_y(z)$ and its minimum value was the estimate for the spot size w_0 of the beam at the waist location and determined the position $z - z_0 = 0$. The distance from the back of the focussing lens to the waist location, z_{w-l}, was determined from the location of the knife edge position $z - z_0 = 0$ for the z-scan transmission measurements presented in Chapter 6. The beam intensities $I(z)$ for all z-scan positions z in each transmission measurement were calculated from the beam area $A_{\text{beam}}(z)$ and the measured peak power.

Table 5.3: Summary of beam profile measurements. The half-width spot sizes were measured in the horizontal (x) and vertical (y) directions using a knife edge and fitted to the function given by Equation 5.2. The distance z_{w-l} is the distance from the back of the lens to the waist location $z - z_0 = 0$ determined by the knife edge measurements illustrated in Figure 5.6.

Wavelength [nm]	M_x^2	M_y^2	w_{0x} [µm]	w_{0y} [µm]	w_0 [µm]	z_{w-l} [mm]
1550	4.91	4.34	69.7	67.3	68.8	76.3
2000	1.46	1.27	47.6	61.2	54.0	79.4
2500	1.64	1.69	52.8	69.1	61.5	79.3
2800	2.87	4.38	54.8	92.5	71.4	79.8
3200	2.93	4.06	59.9	101.2	77.9	79.7
3500	2.44	3.48	47.9	84.8	64.7	80.7

The effects of source power fluctuations and beam wander were reduced by detecting the pulses that arrived at both the signal and reference detectors. The peak heights of the pulses were measured using the oscilloscope after any DC component was subtracted. The signal-to-reference ratio of pulse peaks, while the knife edge did not clip the signal beam, was recorded in a spreadsheet. A range of possible pulse peak values that could have arrived at the reference detector was determined from observations of source power fluctuations and were subsequently entered into a spreadsheet. The corresponding range of possible signal pulse peaks when the knife edge clipped 90 % and 10 % of the signal power were then calculated from the range of possible reference peaks and signal-to-reference ratio. The possible reference and clipped signal peaks formed a lookup table for the beam profile measurement. The knife edge was then translated to positions that reduced the signal-to-reference ratios to 90 % and 10 % of the unclipped value.

The spot size measurement at each z position needed to be performed quickly ($<\sim$3 s) to avoid effects of beam wander. At each z position, the approximate spot size was estimated from averaging numerous attempted measurements. Then quick translations of the knife edge were performed to check that the estimated value was reproducible.

5.8 Damage threshold

The damage threshold of graphene was estimated to determine an upper bound for the maximum peak intensity used in each z-scan. A sacrificial sample of single layer CVD graphene on CaF_2 was used to estimate the damage threshold at each radiation wavelength. The graphene was transferred onto a CaF_2 substrate by the wet transfer process described in Section 5.4.

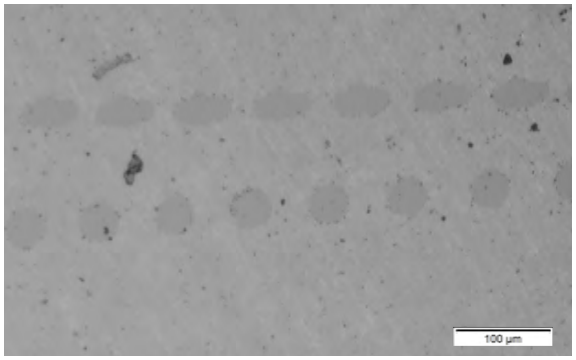

Figure 5.7: Laser induced damage in single layer graphene. The spots shown are damage due to single-shot laser pulses. The sacrificial graphene sample was repeatedly translated in a systematic horizontal zigzag motion, across the beam waist, and observed under a microscope to determine if the damage threshold intensity was exceeded. The sample was raised by a 100 µm thick spacer between each measurement.

The sacrificial sample was repeatedly translated (horizontally) across the beam waist in a zigzag motion so that any laser induced damage could be observed in rows, rather than single spots, for easier identification. The zigzag motion translated the sample horizontally (x-direction) across the beam while making sub-millimetre translations along the beam axis (z-direction) repeatedly to ensure that the sample passed through the beam waist. The laser induced damage was observed under an optical microscope (Olympus BX51) with 5× and 10× magnification. A photographic image of laser induced damage in graphene, produced deliberately while performing the damage threshold measurements, is shown in Figure 5.7.

The estimated damage threshold intensities I_{dam} and fluences F_{dam} are listed in Table 5.4. The peak intensity $I_{\text{peak}} = 2P_{\text{peak}}/\pi w_0^2$ of each beam was estimated using

Table 5.4: Damage threshold estimates for single layer CVD graphene. The damage was identified by visual observation under an optical microscope with 10× magnification. The laser pulse duration was 100 fs.

λ [nm]	I_{dam} [GW cm^{-2}]	F_{dam} [mJ cm^{-2}]
1550	59.8 ± 10.9	2.99 ± 0.54
2000	131.1 ± 19.5	5.05 ± 0.52
2500	191.2 ± 32.7	9.56 ± 1.64
2800	124.6 ± 29.6	6.23 ± 1.48
3200	116.6 ± 4.0	5.83 ± 0.20
3500	144.9 ± 21.5	7.25 ± 1.08

the beam waist spot size w_0 measurements presented in Section 5.7. The peak intensity was adjusted by attenuation using the ND UV filters listed in Table 5.2. The discrete levels of attenuation determined the upper and lower bounds of the damage threshold estimates presented in Table 5.4.

The maximum peak intensity of the beams used in z-scan transmission measurements through graphene was less than one third of the estimated (lower bound) damage threshold intensity listed in Table 5.4.

5.9 Z-scans

An overview of the z-scan design was presented in Section 5.3. This Section provides additional detail to the z-scan measurement method.

The graphene sample was held by a motorised flipper that was mounted on a 50 mm motorised translation stage. The motorised translation stage was mounted on a custom designed track that had three fixed location settings (0 mm, 50 mm, and 100 mm) to extend the z-scan range from 50 mm up to 150 mm. The sample was translated from z=0 mm to z=50 mm in 0.5 mm increments and from z=50 mm to z=150 mm in 1.0 mm increments. The z-scan procedure was automated with customised software that was developed using MATLAB. The software commanded the oscilloscope, motorised translation stage, and motorised flipper. The automation was important for consistency between measurements and speed to minimise effects from source power fluctuation and drift. It also enabled the experimenter to perform other tasks while the z-scan was in process.

The basic automated workflow could be summarised as follows:

Stage: Go to position z;
Flipper: In;
Oscilloscope: Run; Pause for averaging; Stop; Acquire data;

Flipper: Out;
Oscilloscope: Run; Pause for averaging; Stop; Acquire data;

The workflow was repeated for each position z of the motorised stage.

Each acquired waveform was the average of 2048 waveforms. Any more averaging extended the total duration of the z-scan and introduced effects from source power drift over several hours. The averaged waveforms were acquired from the reference and signal channels at each position z and each flipper position (in and out of the beam path). The use of the flipper ensured that the transmission measurement was calibrated at every stage position z to reduce effects from source power drift.

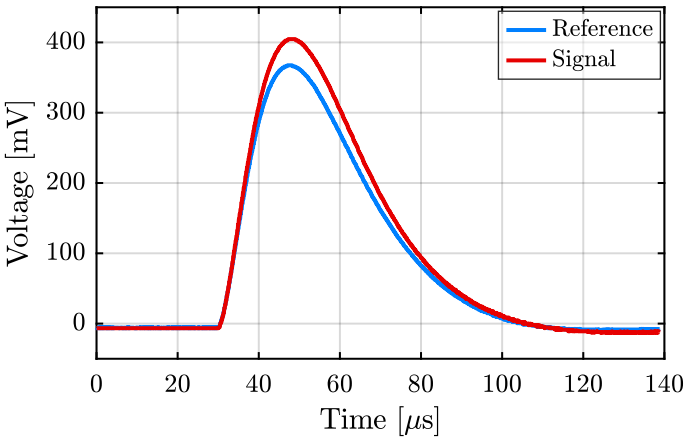

Figure 5.8: Typical pulse waveforms acquired from the oscilloscope and converted to units of time and voltage. Each waveform is the average of 2048 waveforms and the averaging was performed by the oscilloscope.

The waveform data was read in 8-bit unsigned integer format (decimal range 0 to 255). The X-increment, Y-increment, and Y-origin were used to convert the acquired waveform into units of time and voltage. An example of the acquired waveforms, converted to units of time and voltage, is presented in Figure 5.8. The waveform pulse durations are much longer than 100 fs due to the slow detector response time. The rise time $(1 - 1/e)$ of the detector response (an impulse response) was 8 µs while the fall time was 26 µs.

The DC level was then subtracted from each waveform and an integration window was defined for all pulse waveforms. The pulses were integrated and the transmission $T^{(z)}$ at each sample position z was calculated from the expression given in Equation 5.1.

The z-scan transmission data for each wavelength is presented in Figures 5.9 and 5.10. Figure 5.9 illustrates the integrated reference and signal pulses while Figure 5.10 illustrates the transmission, calculated from the pulse integrals, as a function of sample position z.

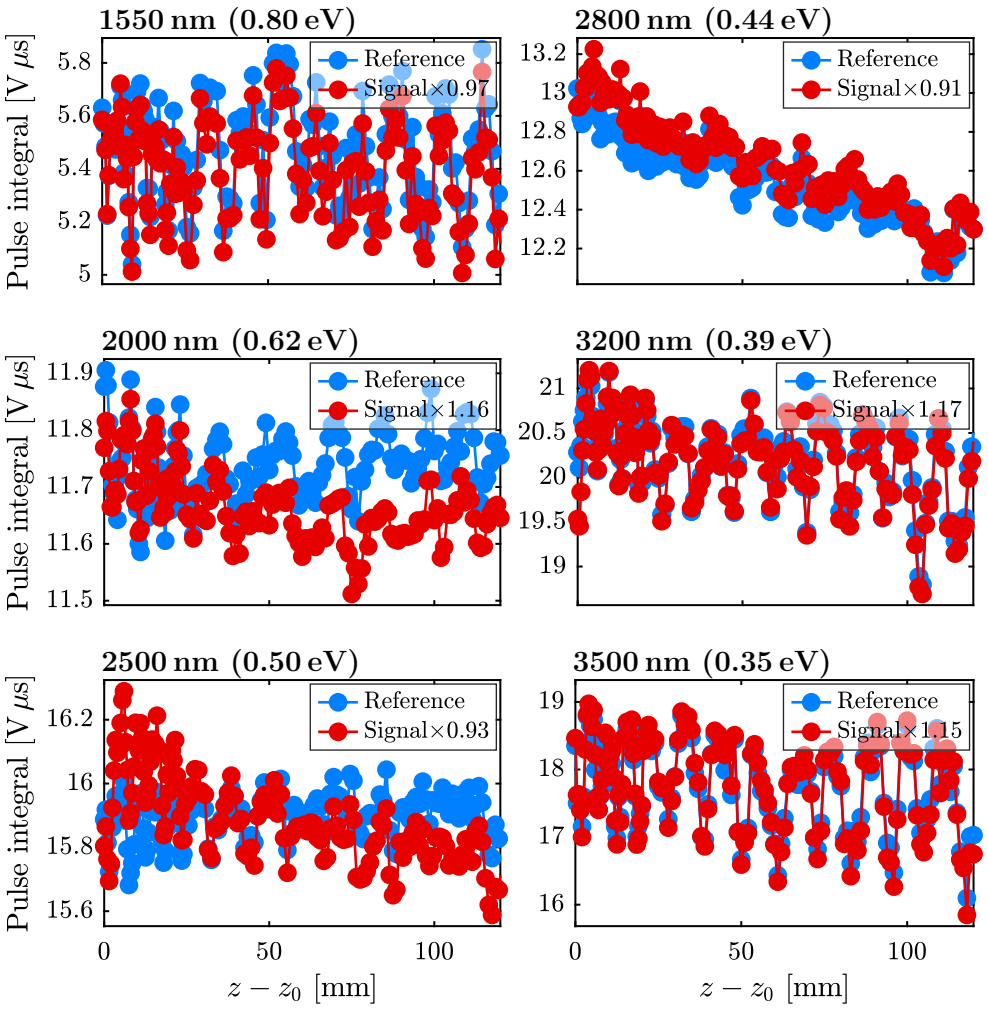

Figure 5.9: Pulse integrals for transmission through graphene. The signal has been multiplied by a factor that equates the signal with the reference at $z - z_0 = 0$ for easier comparison between the two data sets. The periodic structure in the data matched the cycle of the air conditioner in the laser lab.

The integrated signal pulses illustrated in Figure 5.9 were multiplied by a factor that equates the signal with the reference at $z - z_0 = 0$ for easier comparison between the reference and signal data. There is a periodic structure in both data sets due to source power fluctuations. The period of oscillations was observed to be ∼8 min and the fluctuations in source power were attributed to the laboratory air conditioning cycle. This was an unavoidable noise source that was reduced by implementation of the motorised flipper to calibrate the transmission measurement at each sample position z.

The transmission at each position z was calculated from the pulse integral data illustrated in Figure 5.9 using Equation 5.1 and is presented in Figure 5.10. The dip in transmission at the beam waist location $z - z_0 = 0$ was attributed to two-

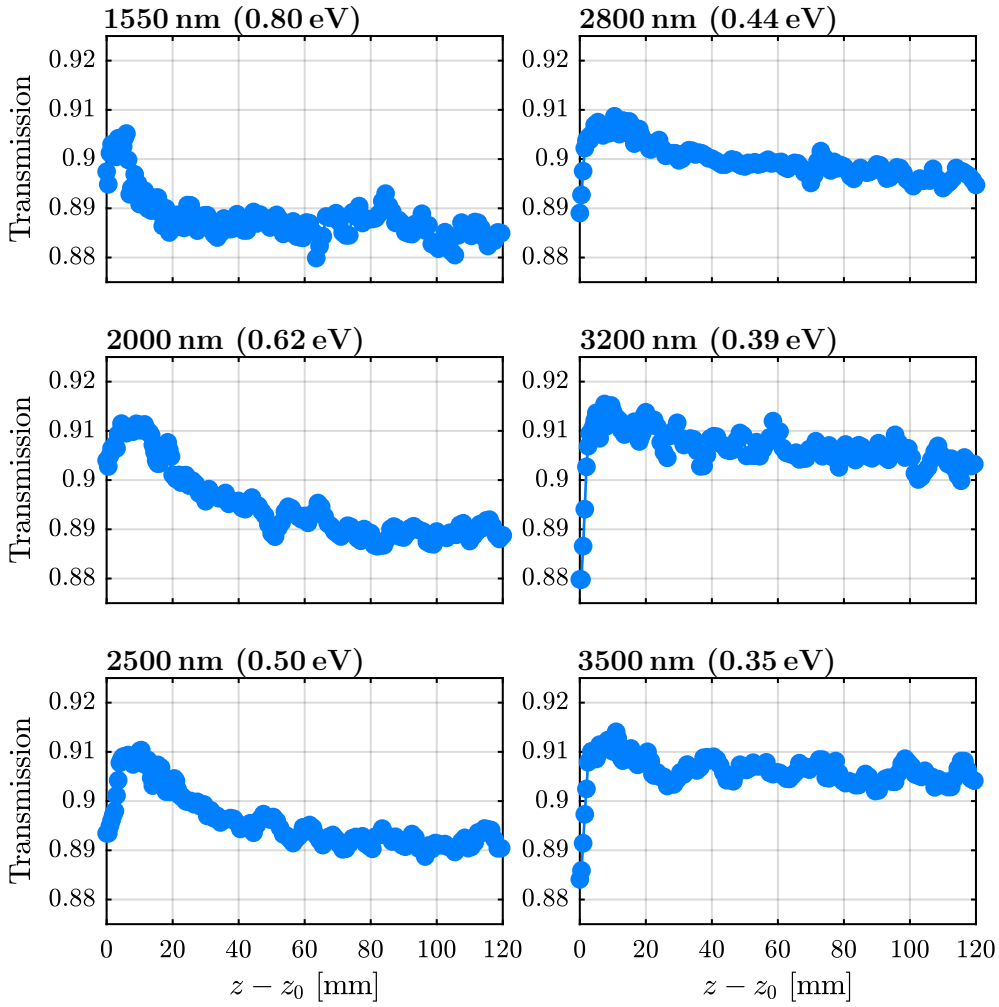

Figure 5.10: Transmission through trilayer graphene on CaF_2. The transmission was calculated from the integrated pulses presented in Figure 5.9.

photon absorption while the transmission peak that follows was attributed to saturable absorption. These processes will be validated in Chapter 6 after the transmission data has been analysed as a function of intensity.

The beam intensity was calculated as a function of z-scan position z using the beam propagation function in Equation 5.2 and beam profile measurements described in Section 5.7. The beam intensities of each z-scan, which span four orders of magnitude, can be found illustrated in Appendix D, Figure D.3.

The transmission data was then converted from functions of position z to functions of intensity I and fitted to Equation 4.16, the equation for transmission through graphene that includes saturable absorption and two-photon absorption processes. The saturation intensity I_s, saturable absorption coefficient α_0, and non-saturable absorption coefficient α_{ns}, and two-photon absorption parameter β were estimated from the curve fit. The significance of these final results are discussed within the published

article on pages 140–148 while the fitted parameters are listed in Table 6.1.

The transmission through a CaF_2 window (Thorlabs WG51050) was also measured in each wavelength band, using the z-scan technique, to rule out any nonlinear effects in the substrate. No intensity dependence on transmission was observed. The z-scans of the CaF_2 window can be found in Appendix D, Figures D.4 and D.5.

5.10 Conclusion

This Chapter has described the design, equipment, methods, and challenges of the z-scans performed to measure the response of graphene to high intensity radiation in the spectral region between 1.55 µm and 3.5 µm (0.35 eV to 0.80 eV). The final optimised experiment design was described in Sections 5.3 and 5.9 and illustrated in Figure 5.1a, while much of the optimisation process was omitted for brevity.

Final z-scan transmission measurements were presented in Figures 5.9 and 5.10 as functions of sample position z. Nonlinear transmission features were observed that were attributed to saturable absorption and two-photon absorption processes in graphene. These processes will be validated in Chapter 6 after the transmission data has been analysed as a function of intensity. The significance of the results from this experiment will be discussed in Chapter 6.

Chapter 6
Graphene Under Illumination: Results

This Chapter includes the following published article on pages 140–148:

> A. Malouf, O. Henderson-Sapir, S. Set, S. Yamashita, D. J. Ottaway. Two-photon absorption and saturable absorption of mid-IR in graphene. *Applied Physics Letters*, 114(9):091111, 2019.

The article provides the first reported measurement of the transmission of high intensity radiation through graphene, using a single sample and a fixed pulse duration, over a wide spectral region in the near to mid-IR. The purpose of this work was to study saturable absorption behaviour in graphene and assess the potential use of graphene for mode-locking mid-IR lasers.

The well known z-scan technique was used to measure the intensity dependent transmission of near to mid-IR radiation through graphene (as described in Chapter 5). The parameters associated with saturable absorption and two-photon absorption were quantified from the transmission data (listed in Table 6.1). The saturable absorption properties of graphene play a crucial role in its performance as a laser mode-locking element. This work shows that the effective modulation depth of multilayer graphene is affected by two-photon absorption, which will be detrimental to the performance of multilayer graphene when used as a saturable absorber to mode-lock mid-IR lasers.

The saturation intensities measured are compared with other reported measurements for cases of graphene produced in uniform sheets (as opposed to, for example, randomly orientated flakes in a composite or colloidal suspension). When the measured saturation intensities were compared with others reported in literature, they fell into two distinct pulse duration regimes and so two empirical relationships between saturation intensity and photon energy are proposed. These results provide insight into

graphene absorption processes at high intensity and their relationship with photon energy.

6.1 Background

This Section provides only a brief background, since the properties of graphene were described in Chapter 4 and the experimental details were provided in Chapter 5.

Recent work on the development of ultrafast lasers shows the enormous potential of graphene as a widely broadband saturable absorber that is ideal for passive mode-locking.[87–95] In spite of these important advances in understanding the absorption properties of graphene, the relationship between photon energy and saturation intensity, as well as two-photon absorption, remains poorly understood.

In previous work, researchers have measured the saturation intensity of multilayer graphene using photon energies in the visible and near-IR spectral regions.[87–89,185,211–213,217] Only several researchers have reported observations of two-photon absorption in graphene.[211–213] In this work, saturable absorption and two-photon absorption processes in the spectral region between 1.55 µm and 3.5 µm (0.35 eV to 0.80 eV) are observed and analysed.

6.2 Introduction

This Chapter investigates the response of graphene to high intensity radiation in the spectral region between 1.55 µm and 3.5 µm (0.35 eV to 0.80 eV). The results of the z-scan experiment that was detailed in Chapter 5 are presented and analysed in this Chapter. Chapter 5 concluded with z-scan transmission measurements presented as functions of sample position z. Preliminary observations of saturable absorption and two-photon absorption were made from the z-scan transmission data illustrated in Figure 5.10.

The transmission data were then converted from functions of sample position z to functions of intensity I and fitted to Equation 4.16, the expression for transmission through graphene that includes saturable absorption and two-photon absorption processes. The saturation intensity I_s, saturable absorption coefficient α_0, non-saturable absorption coefficient α_{ns}, and two-photon absorption parameter β were estimated from the fitted transmission functions.

The published article "Two-photon absorption and saturable absorption of mid-IR in graphene" is presented on pages 140–148. The fitted absorption parameters are illustrated graphically within the article while their values are listed in Section 6.3,

Table 6.1. Note that the published article presented in this Chapter includes references made to Supplementary Material. Although the Supplementary Material document is not included in this thesis, its content is covered in more detail throughout Chapter 5 and Table 6.1 of this Chapter. Finally, conclusions are presented in Section 6.4.

Statement of Authorship

Title of Paper	Two-Photon Absorption and Saturable Absorption of Mid-IR in Graphene
Publication Status	Published
Publication Details	A. Malouf, O. Henderson-Sapir, S. Set, S. Yamashita, D. J. Ottaway. *Appl. Phys. Lett.*, 114(9):091111, 2019. doi: 10.1063/1.5088641.

Principal Author

Principal Author	Andrew Malouf		
Contribution to the Paper	Design, perform, and optimise experiments; develop algorithms for experiment and data analysis; figures; writing of manuscript.		
Overall Percentage	80 %		
Signature		Date	*15/03/2019*

Co-Author Contributions

By signing the Statement of Authorship, each author certifies that:

i. the candidate's stated contribution to the publication is accurate (as detailed above);
ii. permission is granted for the candidate to include the publication in the thesis; and
iii. the sum of all co-author contributions is equal to 100 % less the candidate's stated contribution.

Co-Author	Ori Henderson-Sapir		
Contribution to the Paper	Supervision of project; assistance with experiment design and preliminary experiments, data analysis, and editing of manuscript; corresponding author.		
Signature		Date	*17/03/2019*

Co-Author	Sze Set		
Contribution to the Paper	Advice and support; provision of test samples; corresponding author.		
Signature		Date	*20/03/2019*

Co-Author	Shinji Yamashita		
Contribution to the Paper	Advice and support; provision of test samples; corresponding author.		
Signature		Date	*01/04/2019*

Co-Author	David J. Ottaway		
Contribution to the Paper	Supervision of project; assistance with experiment design, data analysis, comparison of results with literature, and editing of manuscript; corresponding author.		
Signature		Date	*16/03/2019*

Two-photon absorption and saturable absorption of mid-IR in graphene

Abstract

We report on the response of graphene to high intensity mid-IR radiation and show that graphene exhibits saturable absorption and significant two-photon absorption in the spectral region from 1.55 µm to 3.50 µm (0.35 eV to 0.80 eV). We find that the effective modulation depth of multilayer graphene is limited by two-photon absorption which will affect its performance as a laser mode-locking element. The measured saturation intensities of femtosecond pulses were found to depend on the third power of photon energy when we combined our results with others reported in literature, while those of longer pulses were found to have a square root dependence.

I Introduction

The optical and electronic properties of graphene are important for a number of applications including solar cells, photodetectors, light-emitting devices, and touch screens.[183] Graphene has also been used extensively as a saturable absorber to mode-lock ultrafast lasers because it has broadband saturable absorption (SA), large modulation depth, and ultrafast relaxation time.[70,87–91,94,218] Graphene mode-locked fibre lasers were first demonstrated in the telecommunication band ∼1.5 µm (0.8 eV)[87–89] and subpicosecond pulses were achieved. The longest wavelength demonstrated in a graphene mode-locked laser is 2.8 µm (0.4 eV) in which 42 ps pulses were achieved.[70] There is currently an urgent need to understand the mid-IR saturation properties of graphene to facilitate growing demand for mode-locked mid-IR laser sources in fields such as molecular spectroscopy and medicine.[14,163]

Graphene has a variety of interesting electronic properties including linear dispersion near the Dirac points, zero bandgap, and charge carriers that have speed $v \approx 10^6\,\mathrm{m\,s^{-1}}$ and mimic relativistic particles with zero rest mass.[202] The electronic band structure can be described using a tight-binding Hamiltonian.[196] Pauli blocking at high intensity combined with ultrafast response times and linear dispersion make graphene an ideal broadband saturable absorber for passive mode-locking.[183,209,210] Compared to traditional semiconductor saturable absorber mirrors (SESAMs) and single-walled carbon nanotubes, graphene has an extremely broad wavelength response, high modulation depth and low saturation intensity.[87] The modulation depth can be extended by stacking multiple graphene layers.[184,185]

The saturation intensity, I_s, has been suggested to have a wavelength λ dependence given by the empirical relationship $I_s = 2.7/\lambda^6$, where I_s and λ are expressed in units of GW/cm^2 and µm respectively.[218] The empirical fit was made to saturation intensities measured using wavelengths between 780 nm and 1560 nm (0.8 eV to 1.6 eV). However, this relationship did not hold for some extremely small reported values of I_s.[87,90] We present a revised empirical fit to I_s measured with wavelengths between 435 nm and 3.5 µm (0.4 eV to 2.9 eV).

Two-photon absorption (2PA) has been observed in the spectral region between 435 nm and 2400 nm (0.5 eV to 2.9 eV)[211–213] and a theoretical explanation of this strong interaction has been proposed.[211] The strength of 2PA is greater in stacked layers than single layer graphene due to the increased number of energy bands caused by interlayer coupling and thus a greater number of possible electronic transitions.[211] The effective modulation depth of graphene is limited by 2PA which can be detrimental to passive mode-locking.[229]

In this work, we study the saturation behaviour of trilayer graphene mounted on CaF_2 using the well known z-scan technique to measure intensity dependent transmission.[224,225] We use a 100 fs tunable laser source at a range of wavelengths, ranging from 1.55 µm (0.80 eV), where measured saturation intensity is compared with values in literature,[87,89,218] up to 3.5 µm (0.35 eV), where recent advances have been made in fibre lasers.[60,61,63,82,146,181,230] We show that 2PA limits the effective modulation depth, as well as the slope of the nonlinear transmission curve, at mid-IR wavelengths. We also show that saturation intensities of femtosecond pulses follow the empirical relation $I_s \propto E_{ph}^3$ where E_{ph} is the photon energy, while for longer pulses, $I_s \propto \sqrt{E_{ph}}$. We report transmission measurements of high-intensity radiation through graphene using a single sample and a fixed pulse duration over a wide spectral region in the near to mid-IR.

The SA and 2PA processes are described by Equation 6.1 where $I = I(z')$ is the intensity and z' is the depth into the material. The absorption parameters α_0, α_{ns}, and β are the saturable, non-saturable, and 2PA parameters respectively. The non-saturable coefficient α_{ns} is included because saturable absorbers are generally imperfect and do not saturate absorption down to zero.[222,231]

$$\frac{dI}{dz'} = -\left[\frac{\alpha_0}{1+\frac{I}{I_s}} + \alpha_{ns} + \beta I\right] I \tag{6.1}$$

We make no assumptions about the change in intensity *within* the sample and treat the trilayer thickness as dimensionless and unity such that $dz' = 1$. The transmission

T is then described by Equation 6.2,

$$T(I) = \exp\left[-\left(\frac{\alpha_0}{1+\frac{I}{I_s}} + \alpha_{ns} + \beta I\right)\right] T_{sub} \tag{6.2}$$

where T_{sub} is the transmission through the substrate. Note that in this expression, the units of β are inverse intensity and the SA parameters α_0 and α_{ns} are dimensionless.

II Experiment

The intensity dependent transmission of mid-IR radiation through graphene was measured using the z-scan technique. Graphenea (Spain) produced the undoped graphene using chemical vapor deposition (CVD) and transferred three monolayers separately onto the face of a 25 mm diameter, 5 mm thick CaF_2 window (Thorlabs WG51050). This sample was used for all the transmission measurements in this experiment. The tunable light source was an optical parametric amplifier (Light Conversion TOPAS-C) pumped by an 800 nm regenerative amplifier system (Spectra Physics Spitfire Pro XP). The pulse duration was 100 fs full width at half maximum and the repetition rate was 1 kHz. The intensity dependent transmission was measured at six wavelengths – 1550 nm, 2000 nm, 2500 nm, 2800 nm, 3200 nm, and 3500 nm. Measurements at longer wavelengths were limited by signal-to-noise. See Supplementary Material for more detail on the z-scan procedure.

Raman spectra

The quality of the graphene sample was assessed using Raman spectroscopy and scanning Raman microscopy. The Raman spectra of the CVD single layer graphene used to produce the trilayer sample, as provided by the supplier (Graphenea, Spain), are presented in Figure 6.1a. These single layers were stacked on a CaF_2 substrate to form the trilayer graphene used in this experiment. The most prominent features in the Raman spectra of graphene are the G band near 1600 cm^{-1} and G′ band near 2700 cm^{-1}. The large intensity of the G′ band relative to the G band is explained by a triple resonance process that can occur due to graphene's linear dispersion.[232] The D band arises from the breathing modes of the hexagonal sp^2 carbon rings and requires the presence of a defect for its activation.[233]

Raman maps were measured at 1 mm and 1 µm spacings after the experiment was completed to analyse the degrees of uniformity and disorder in the graphene sample. The laser excitation wavelength used for the Raman maps was 532 nm (2.33 eV) with a ∼1 µm spot size. The ratio of the integrated G band to G′ band over the area

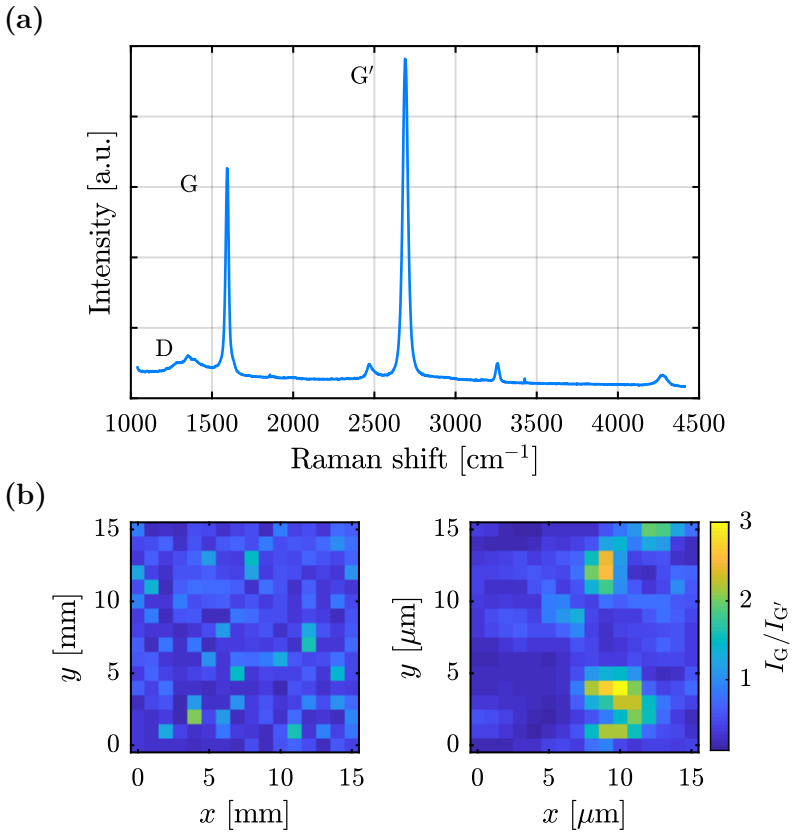

Figure 6.1: (a) Raman spectra of single layer CVD graphene used to produce the trilayer sample used in this experiment. The graphene was transferred onto a SiO_2/Si substrate. The spectrum was taken with a laser excitation wavelength of 532 nm (2.33 eV). (b) Raman maps of the central areas of the graphene sample at 1 mm (left) and 1 µm (right) spacings. The color scale shows the ratio $I_G/I_{G'}$ of integrated peaks.

of the sample is shown by the color map in Figure 6.1b. The variations may be explained by local changes in stacking orientation which affect the degree of coupling between layers[234] and variations in distance between layers. Although the quality of the graphene is high, it is not crystalline. The orientation of each layer is random and an inhomogeneous residue of polymethyl methacrylate (PMMA), resulting from the wet-transfer of CVD graphene, may exist between the layers. The higher ratio of $I_G/I_{G'}$ exhibits the Raman signature of a strong coupling between the layers while the lower ratio resembles single layer graphene. The ratio $I_D/I_G \approx 0.1$ was averaged over all Raman map locations indicating that no significant disorder was introduced since the graphene was produced.[233]

The Raman maps show that large variations in the degree of coupling between graphene layers occur on the scale of several µm^2. As the smallest spot radius used in the z-scan transmission measurements was 65 µm, any effects from variations in layer coupling are averaged over the relatively large beam area and are thus not likely to

change with beam location. See Supplementary Material for Fourier transform infrared (FTIR) spectra of the graphene sample.

III Results and Discussion

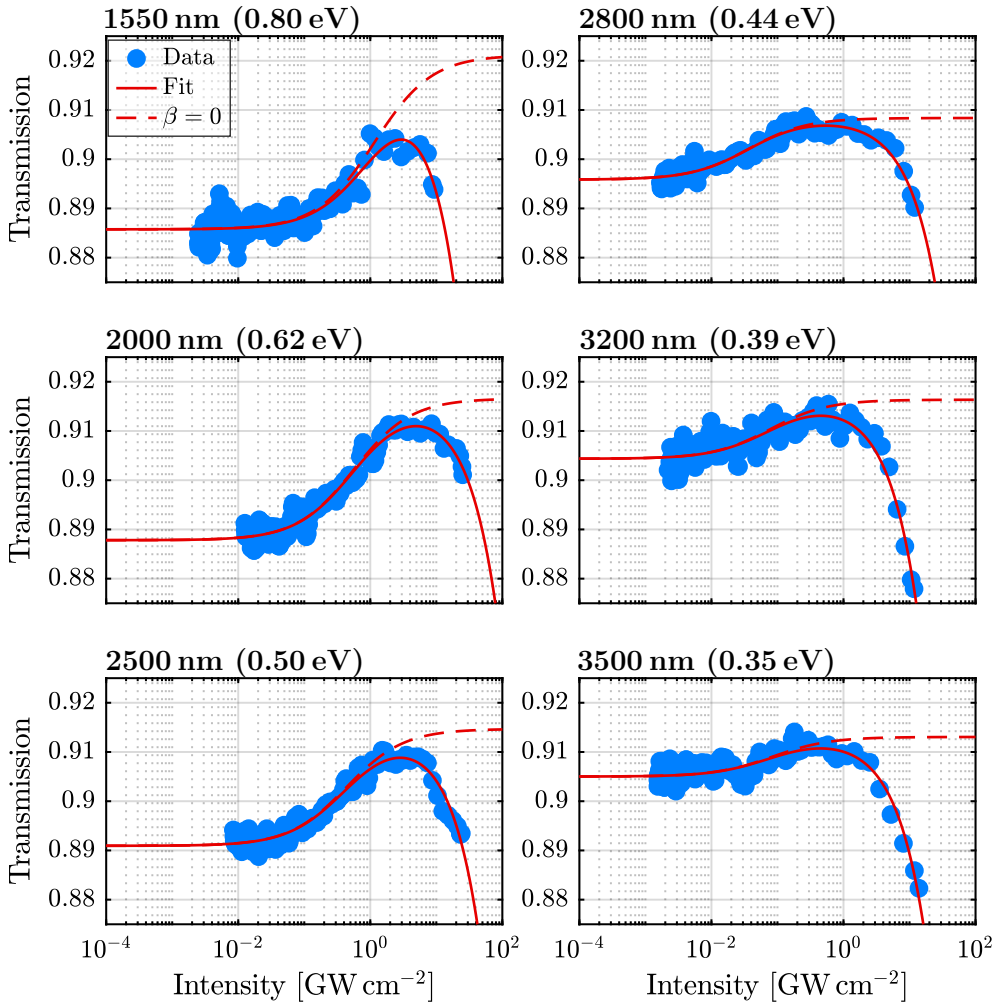

Figure 6.2: Z-scan transmission measurements presented as functions of intensity. The data is fitted to Equation 6.2 and the absorption processes SA and 2PA are observed. The fit function is then altered by setting $\beta = 0$ to qualitatively show the effect of SA without 2PA.

The transmission T of femtosecond pulses at each wavelength were measured at each position z and converted to a function of intensity I. The transmission data were then fitted to Equation 6.2 and are presented in Figure 6.2. The data at all wavelengths show an increase in transmission with intensity that is consistent with SA. At intensities above $\sim$1 GW cm^{-2}, the I^2 dependence of 2PA dominates the effects of SA and the transmission rolls off. At wavelengths 2.8 µm (0.44 eV), 3.2 µm (0.39 eV), and 3.5 µm (0.35 eV), the transmission reduces to well below unsaturated values. Sim-

ilar observations have been made in the near-IR regime with bilayer graphene[211] as well as SESAMs.[229] The highest peak intensities incident on the graphene were limited to below damage thresholds determined by experiment at each wavelength. See Supplementary Material for listed damage thresholds.

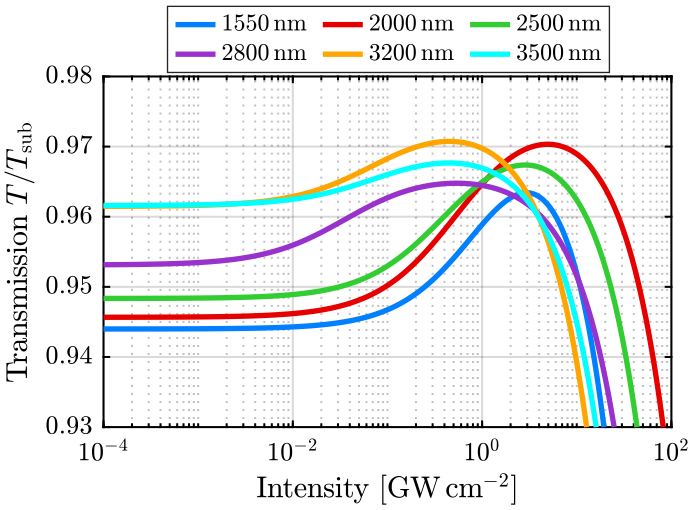

Figure 6.3: Transmission fit functions normalised to the transmission of the CaF_2 substrate at each wavelength.

The transmission functions fitted to Equation 6.2 were normalised to the transmission of the CaF_2 substrate at each wavelength and are presented in Figure 6.3. There are several interesting features displayed here. Firstly, the low intensity transmission increases with wavelength, which is also observed in the FTIR spectra presented in the Supplementary Material. This is in agreement with some reports in literature,[94,235] however it does contradict other reports of a completely flat absorption spectrum[208,220] and may be due to an interaction between the graphene and the CaF_2 substrate. Secondly, the saturation intensity decreases with wavelength with the exception of 2.8 µm (0.44 eV) where I_s is the lowest of all wavelengths. Thirdly, the modulation depth is highest at 2.0 µm (0.62 eV) and lowest at 3.5 µm (0.35 eV). The effective modulation depth and slope of the nonlinear transmission curve are reduced by 2PA.

The fitted absorption parameters for SA and 2PA are shown graphically in Figure 6.4. Resonant features in 2PA are observed with a peak at around 3200 nm (0.39 eV) which may be explained by interlayer coupling. This peak location agrees with quantum perturbation theory used for the case of AB stacked bilayer graphene.[211] There is insufficient data to resolve a possible second peak below 2000 nm (above 0.62 eV) that may exist due to three layer coupling. The sum of the SA parameters decreases with wavelength which corresponds to the transmission increase in the low intensity regime. See Supplementary Material for listed values of the fitted absorption parameters α_0,

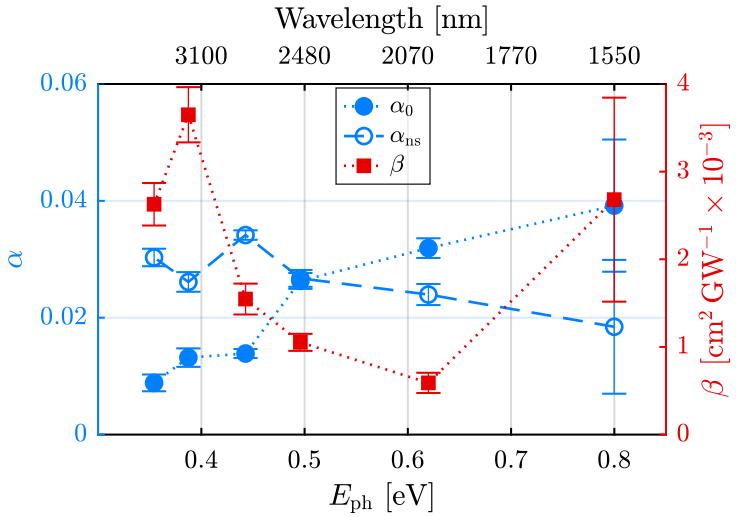

Figure 6.4: Fit parameters α_0 and α_{ns} for SA (left axis) and β for 2PA (right axis). Connecting lines are included for a guide to the eye.

α_{ns}, and β.

The measured saturation intensities, I_s, and saturation fluences, F_s, are presented in Figure 6.5 as functions of photon energy, E_{ph} (See Supplementary Material for the listed values), and compared with measurements published in literature.[70,87,89,185,211–213,217,223] In each case, graphene sheets were produced by either mechanical exfoliation, epitaxy, or CVD and the direction of incident radiation was perpendicular to the graphene plane. Cases for graphene flakes suspended in a solution or polymer were excluded from the analysis because the angle of incidence is not uniform and the incident beam is more likely to interact with flake edges where disorder is high. One reported measurement of I_s for graphene produced by spin coating is also included in Figure 6.5 for comparison, since the graphene was mounted on a flat glass substrate and the radiation was at normal incidence.[236]

The relationship between I_s and E_{ph} is affected by incident pulse duration, τ_p, relative to the carrier lifetime. The relaxation of photogenerated carriers in graphene is described by two distinct time scales, $\tau_1 \approx 140\,\text{fs}$ and $\tau_2 \approx 1.56\,\text{ps}$, where τ_1 may be attributed to carrier-carrier intraband scattering while τ_2 may be explained by carrier-phonon intraband scattering or electron-hole recombination.[87,220,221] The fractional amplitudes of the biexponential fits are $A_1 \approx 0.74$ for time constant τ_1 and A_2 for τ_2,[221] which result in a mean lifetime of $\tau_{avg} \approx 500\,\text{fs}$. The saturation intensity data in Figure 6.5 are divided into two pulse duration regimes, $\tau_p \leq 500\,\text{fs}$ and $\tau_p \geq 1\,\text{ps}$, where the boundary between the two regimes is comparable with the mean carrier lifetime. Each set of data were fitted to $I_s = aE_{ph}^b$ and $F_s = cE_{ph}^d$, where a, b, c and d are the fit parameters. The saturation intensity of graphene produced by spin coating[236]

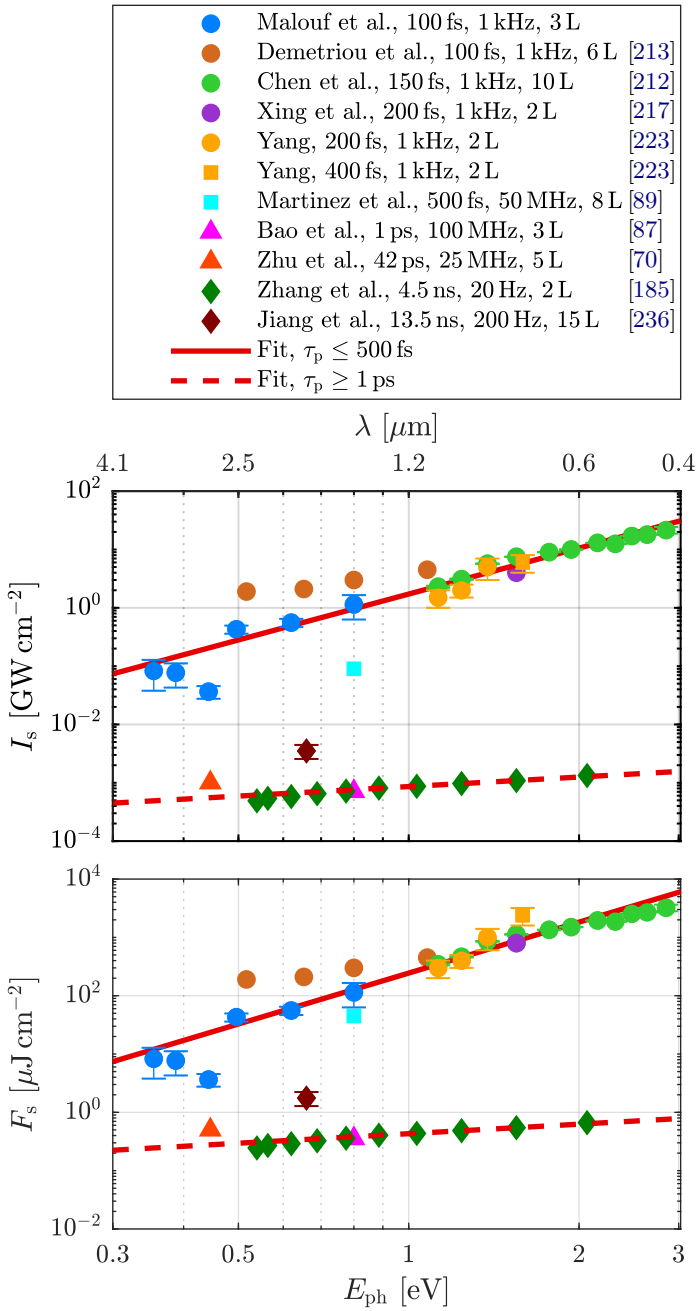

Figure 6.5: Comparison of measured saturation intensities I_s and saturation fluences F_s in literature as functions of photon energy E_{ph}. The data are sorted by laser pulse duration. Laser pulse repetition rates and number of graphene layers (L) are listed in the legend. The data are divided into two pulse duration regimes, $\tau_p \leq 500$ fs and $\tau_p \geq 1$ ps, and fitted separately.

is significantly higher than the case for CVD graphene[185] when measured with similar photon energy and pulse duration, which is likely due to high disorder as a result of the spin-coating process. Therefore, I_s and F_s for the spin-coated graphene were excluded from the fits.

In the short pulse regime, the I_s parameters are $a_1 = 0.2 \pm 0.1$ and $b_1 = 2.6 \pm 0.3$ while the $F_s = \tau_p I_s$ parameters are $c_1 = 2.4 \pm 0.1$ and $d_1 = 2.9 \pm 0.2$. In the long pulse regime, $F_s = \tau_{avg} I_s$, and the fit parameters are $a_2 = 8.6 \pm 0.5 \times 10^{-4}$, $b_2 = 0.54 \pm 0.10$, $c_2 = 0.43 \pm 0.02$, and $d_2 = 0.54 \pm 0.10$. That is, the empirical fits suggest that $I_s \propto E_{ph}^3$ and $F_s \propto E_{ph}^3$ when incident pulse durations are below the mean carrier lifetime. In the case of longer pulses, $I_s \propto \sqrt{E_{ph}}$ and $F_s \propto \sqrt{E_{ph}}$.

IV Conclusion

We have characterised the response of trilayer graphene to high intensity radiation between 1.55 µm and 3.50 µm (from 0.35 eV to 0.80 eV). We have shown that multilayer graphene exhibits SA and 2PA in response to 100 fs pulses. Resonant features in 2PA were observed over the spectral region measured, however more data is required to resolve these features. The 2PA limits the effective modulation depth and can be detrimental to mode-locking ultrafast lasers. Saturation intensities of femtosecond pulses are shown empirically to be proportional to the third power of photon energy, while those of longer pulses are shown to have a square root dependence.

Supplementary Material

See Supplementary Material for z-scan procedure, transmission measurements, absorption and saturation intensity values, method of beam profile measurement, damage thresholds, and FTIR spectra.

Acknowledgments

The authors thank Tak W. Kee and Patrick Tapping for the femtosecond laser facilities and Jason Gascooke for performing Raman measurements. The authors are grateful to Elizaveta Klantsataya for useful discussions. The authors acknowledge the expertise, equipment, and support provided by the Australian National Fabrication Facility (ANFF) at Flinders University. This research was supported by the Australian Research Council through ARC LIEF Grant LE098974 and the South Australian Government Premier's Research and Industry Fund (PRIF).

6.3 Absorption parameters

The saturable absorption parameters (α_0, α_{ns}, and I_s) and two-photon absorption parameter (β) that were fitted to the z-scan transmission measurements using Equation 4.16 are listed in Table 6.1.

Table 6.1: Fitted absorption parameters.

λ [nm]	E_{ph} [eV]	α_0 [10^{-2}]	α_{ns} [10^{-2}]	β [10^{-3} cm^2 GW^{-1}]	I_s [GW cm^{-2}]	F_s [μJ cm^{-2}]
1550	0.80	3.92 ± 1.13	1.85 ± 1.15	2.68 ± 1.16	$(1.14 \pm 0.51) \times 10^{0}$	$(1.14 \pm 0.51) \times 10^{2}$
2000	0.62	3.19 ± 0.17	2.40 ± 0.18	0.59 ± 0.17	$(5.57 \pm 0.90) \times 10^{-1}$	$(5.57 \pm 0.90) \times 10^{1}$
2500	0.50	2.63 ± 0.14	2.67 ± 0.14	1.05 ± 0.10	$(4.28 \pm 0.68) \times 10^{-1}$	$(4.28 \pm 0.68) \times 10^{1}$
2800	0.44	1.39 ± 0.08	3.41 ± 0.08	1.55 ± 0.18	$(3.65 \pm 0.89) \times 10^{-2}$	$(3.65 \pm 0.89) \times 10^{0}$
3200	0.39	1.32 ± 0.16	2.61 ± 0.17	3.65 ± 0.32	$(7.72 \pm 3.43) \times 10^{-2}$	$(7.72 \pm 3.43) \times 10^{0}$
3500	0.35	0.89 ± 0.14	3.03 ± 0.15	2.63 ± 0.24	$(8.30 \pm 4.51) \times 10^{-2}$	$(8.30 \pm 4.51) \times 10^{0}$

6.4 Conclusion

The results presented in this article are the culmination of research in the unique properties of graphene presented in Chapter 4 and the z-scan experiment presented in Chapter 5 which was optimised for measurement sensitivity. Results of the z-scan transmission measurements show that the effective modulation depth of multilayer graphene is affected by two-photon absorption, which will be detrimental to the performance of multilayer graphene when used as a saturable absorber to mode-lock mid-IR lasers.

This work has shown that when measured saturation intensities are compared with reported measurements for cases of graphene produced in the form of uniform sheets only, rather than composites or colloidal suspensions of graphene flakes, those saturation intensities fall into two distinct pulse duration τ_p regimes. Two empirical relationships between saturation intensity I_s and photon energy E_{ph} were proposed: (i) $I_s \propto E_{ph}^3$ when $\tau_p \leq 500\,\text{fs}$; and (ii) $I_s \propto \sqrt{E_{ph}}$ when $\tau_p \geq 1\,\text{ps}$. These results provide new insight into graphene absorption processes at high intensity and their relationship with photon energy and pulse duration.

The future directions that may stem from this work are extensive. Now that the challenges of measuring small changes in nonlinear absorption have been met and understood, the experiment design is well established for z-scan measurements of transmission through any material. Various numbers of graphene layers, for example, may be studied and compared over a broad spectral range to extend the study of nonlinear absorption processes in graphene and their dependence on photon energy. With further

optimisation of experiment design, or use of a more stable tunable laser source, single layer graphene could be studied in the mid-IR spectral region. Although the modulation depth of single layer graphene is only ∼1.3 %, it is not expected to be affected by two-photon absorption processes[211] and this should be confirmed by experiment in the mid-IR spectral region.

Furthermore, saturable absorbers other than graphene can be characterised and compared with the response of graphene presented in this work. This would be particularly important in the mid-IR spectral region beyond the 2.5 µm wavelength band where, as this work has shown, the effective modulation depth of multilayer graphene is considerably affected by two-photon absorption. In fact, this work shows that the search for an effective mid-IR laser mode-locking element should extend beyond multilayer graphene to other saturable absorber materials. The response of single layer graphene to high intensity radiation in the mid-IR is yet to be measured.

Chapter 7
Conclusion

7.1 Summary

Progress in mid-IR lasers will achieve the high-brightness, widely broadband sources needed for applications in remote sensing, medicine, and defence. Three approaches were implemented in this thesis to advance mid-IR lasers.

Firstly, a DIAL application was proposed for the detection of diesel exhaust gases in the atmosphere (Chapter 2). Diesel engine exhaust, classified as a Group 1 carcinogen, contains three gas constituents that could be detected remotely by an airborne DIAL system. Carbon monoxide is a suitable target gas in the 2.3 µm wavelength band, while nitrogen dioxide and formaldehyde are suitable targets in the 3.5 µm band. When 1000 pulses are averaged, the lidar sensitivity estimates for the detection of these gases were at least one order of magnitude below the urban background concentration lengths. The results of this feasibility study are presented in such a way that they are easily scalable, while the method adopted could be repeated for other conditions, such as different backscattering surfaces (i.e. other than an ocean surface) or different target gases (such as methane). The 3.5 µm dual-wavelength pumped fibre lasers modelled in Chapter 3 may continue to develop into suitable light sources for detection of nitrogen dioxide or formaldehyde using a DIAL system in the future.

Secondly, a numerical model was developed to simulate fibre laser processes and performance (Chapter 3). This was the first theoretical study of 3.5 µm lasers. The model was validated against three reported experiments and simulates the ionic and photonic interactions in 3.5 µm dual-wavelength pumped fibre lasers with a high temporal resolution, while most previously reported models solve for the steady state condition only. The evolution of energy level populations over time provides valuable insight into laser threshold conditions, the fast changes that occur immediately following threshold, and steady state populations. Furthermore, in the Q-switch mode of operation, the time

evolution of pulses and energy level populations enable the study of Q-switching behaviour and the optimisation of Q-switch repetition rate. This model, adaptable to almost any fibre laser design, has become a valuable tool for designing and optimising laser output power in either CW or Q-switch modes of operation.

Thirdly, graphene was studied and characterised to understand its potential suitability for mode-locking mid-IR lasers (Chapters 4, 5, and 6). Graphene mode-locked lasers have been demonstrated in the near-IR domain but not beyond the 3 µm wavelength band. This work was motivated by the broadband saturable absorption properties of graphene combined with the growing demand for ultrafast mid-IR laser sources. The unique properties that give rise to broadband saturable absorption in graphene were studied and presented (Chapter 4). These include linear energy dispersion, zero bandgap, and ultrafast electronic relaxation times. The response of graphene to high intensity radiation was measured in the spectral region between 1.55 µm and 3.50 µm using a 100 fs laser source and the z-scan technique (Chapter 5). The experiment was optimised to achieve transmission measurement sensitivity below 0.5 %, overcoming several challenges associated with laser source instability. The laser beam profile and damage threshold of graphene were measured in each wavelength band prior to each z-scan.

The intensity dependent transmission through trilayer graphene was measured in six wavelength bands – 1.55 µm, 2.0 µm, 2.5 µm, 2.8 µm, 3.2 µm, and 3.5 µm. Saturable absorption and two-photon absorption processes were observed and measured in each wavelength band (Chapter 6). The measured saturation intensities were combined with others reported in literature to find that saturation intensity depends on the third power of photon energy in the femtosecond regime while longer pulses show a square root dependence. Moreover, transmission measurements show that the effective modulation depth of multilayer graphene is affected by two-photon absorption which will be detrimental to mode-locking performance. This result explains why lasers beyond the 3 µm wavelength band have not been mode-locked using multilayer graphene.

7.2 Future directions

This research lays the foundation for a wide range of possible future directions.

The DIAL feasibility study presented in Chapter 2 demonstrates that detection of diesel exhaust gases in the atmosphere using DIAL technology is possible. Numerous assumptions were made to simplify the analysis. More detailed studies are required to estimate lidar sensitivity for any specific set of DIAL parameters and environmental conditions. The optimal wavelengths of the online and offline pulses for each target

gas need to be determined precisely to ensure that they are not attenuated by other gases. Now that the likelihood of diesel exhaust detection has been established, the methodology presented can be extended to other applications, such as searching for methane leaks in natural gas pipelines. Furthermore, this study motivates the need to advance dual-wavelength Q-switching techniques for mid-IR DIAL laser sources.

The fibre lasers modelled in Chapter 3 were 3.5 µm dual-wavelength pumped Er^{3+}-doped fibre lasers. Now that the model has been validated against several experiments, it can be easily adapted to any fibre laser design if the required parameters are known. This is beneficial for designing fibre lasers prior to purchasing costly equipment and fibre. Furthermore, the model could be developed to simulate the effects of a saturable absorber inside a laser cavity for passive Q-switching. The initial approach would be to include an intensity dependent transmission at the output coupler. The model could be used to predict and optimise the saturable absorber properties required to Q-switch a particular laser.

The z-scan experiment presented in Chapter 5 was optimised to measure small changes in transmission of light through trilayer graphene. Now that the experiment design and methodology have been established, the intensity dependent transmission through any saturable absorber can be measured. If multilayer graphene is not ideal for mode-locking mid-IR lasers, then what material is? Single layer graphene? Would two-photon absorption be observed in single layer graphene? Does single layer graphene have sufficient modulation depth for mode-locking mid-IR lasers? What about bilayer graphene? Ten layer graphene? What about black phosphorus or any other saturable absorber material? The emission wavelength of any laser could be used in z-scans of multiple saturable absorbers to compare their absorption properties and determine which materials are most suitable for mode-locking or Q-switching that laser.

When combined, the three approaches to advancing mid-IR lasers presented in this thesis form a powerful set of tools for designing mid-IR lasers in the future.

Appendix A
DIAL: Supporting Information

A.1 Spectral analysis of diesel exhaust molecules

A.1.1 Spectral line intensities

The spectral line intensities S of various diesel exhaust molecules and atmospheric absorption in the spectral region between 1 µm and 5 µm are presented in Figures A.1 – A.8, where each figure covers a 500 nm spectral region. The figures effectively expand part of Figure 2.6 to reveal molecular absorption features within atmospheric transmission windows with a higher resolution. The spectral regions where atmospheric absorption is low indicate which spectral lines are accessible within the transparent windows of the atmosphere. The absorption was modelled for a return pulse from an altitude of 500 m, i.e. a total path length of 1 km. The line intensities were sourced from the HITRAN2016 database.[9]

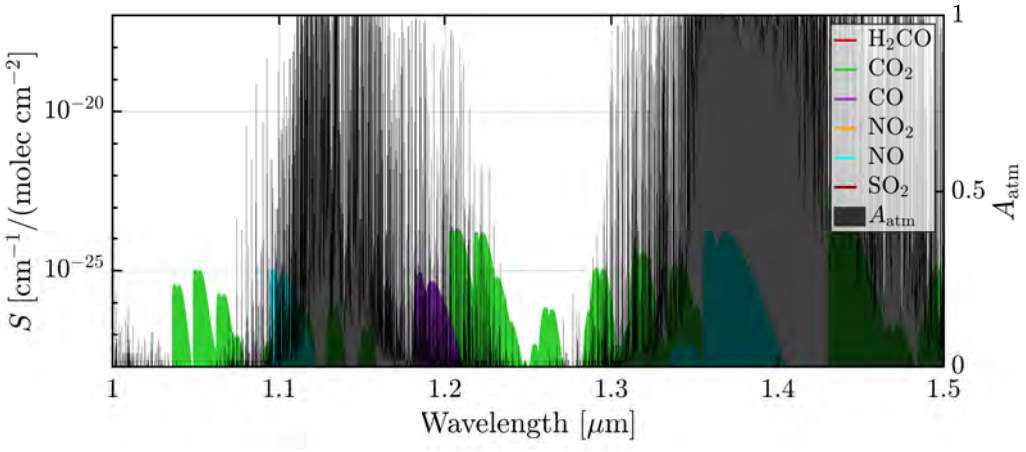

Figure A.1: The spectral line intensities S of various diesel exhaust molecules (left axis) with atmospheric absorption (right axis) overplotted. The spectral region is confined to 1.0 µm – 1.5 µm.

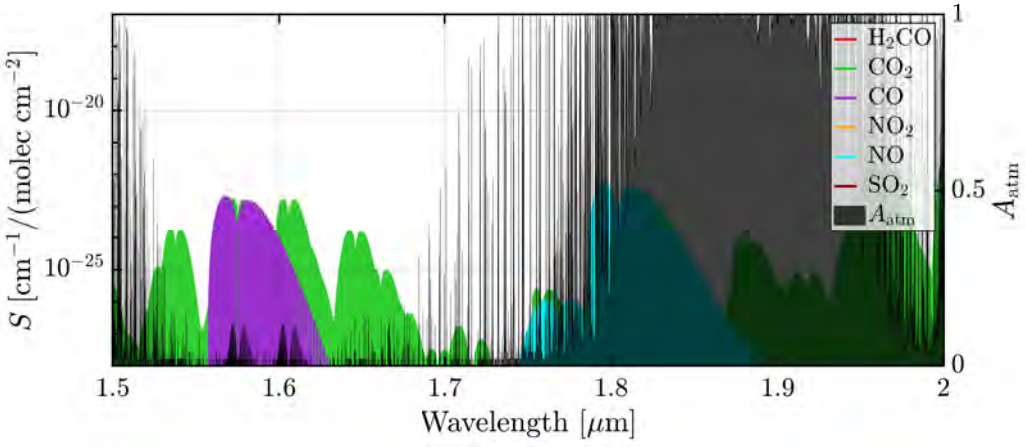

Figure A.2: The spectral line intensities S of various diesel exhaust molecules (left axis) with atmospheric absorption (right axis) overplotted. The spectral region is confined to 1.5 µm – 2.0 µm.

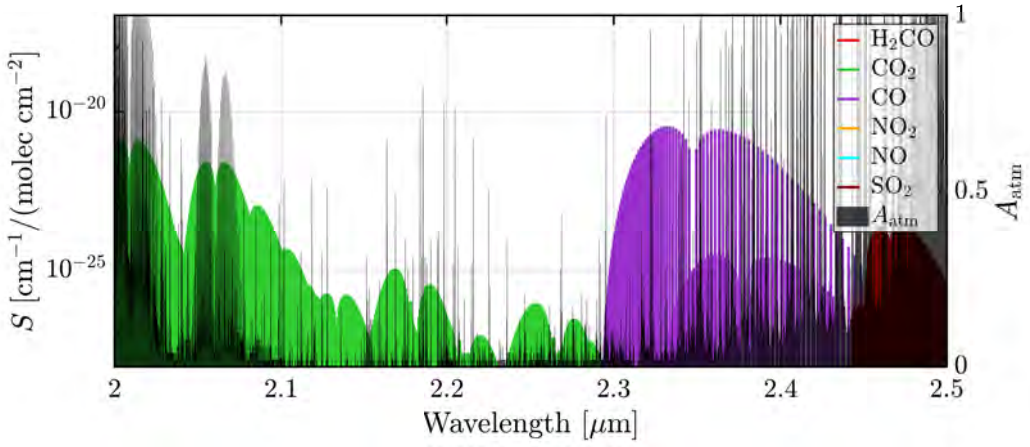

Figure A.3: The spectral line intensities S of various diesel exhaust molecules (left axis) with atmospheric absorption (right axis) overplotted. The spectral region is confined to 2.0 µm – 2.5 µm.

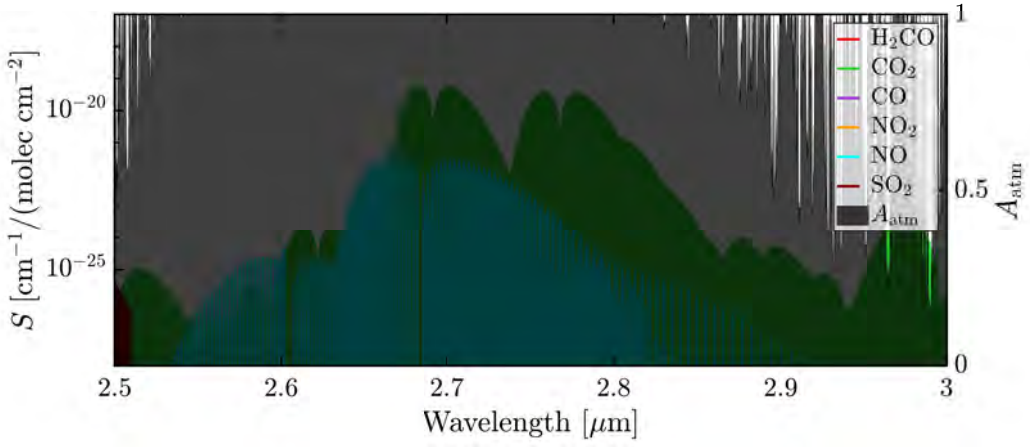

Figure A.4: The spectral line intensities S of various diesel exhaust molecules (left axis) with atmospheric absorption (right axis) overplotted. The spectral region is confined to 2.5 µm – 3.0 µm.

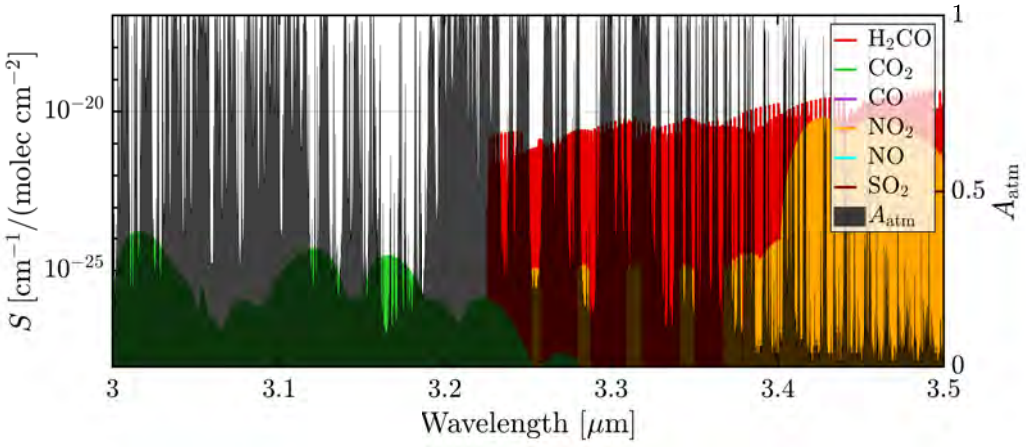

Figure A.5: The spectral line intensities S of various diesel exhaust molecules (left axis) with atmospheric absorption (right axis) overplotted. The spectral region is confined to 3.0 µm – 3.5 µm.

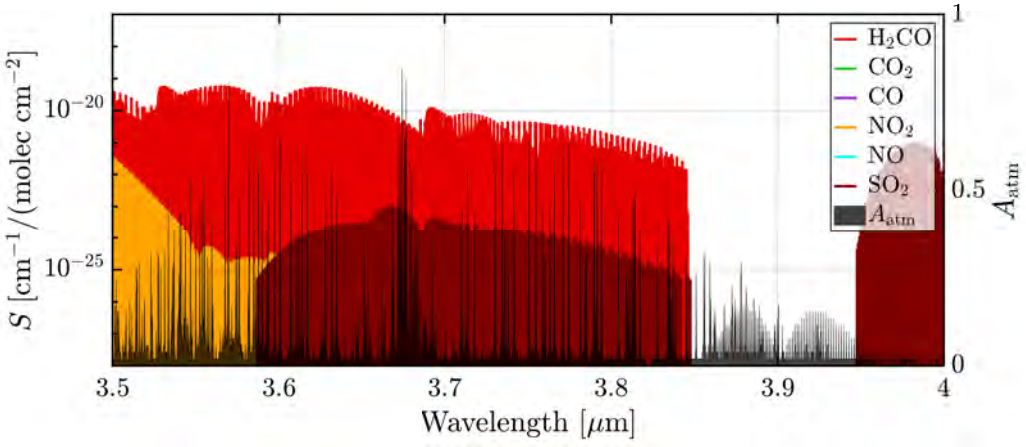

Figure A.6: The spectral line intensities S of various diesel exhaust molecules (left axis) with atmospheric absorption (right axis) overplotted. The spectral region is confined to 3.5 µm – 4.0 µm.

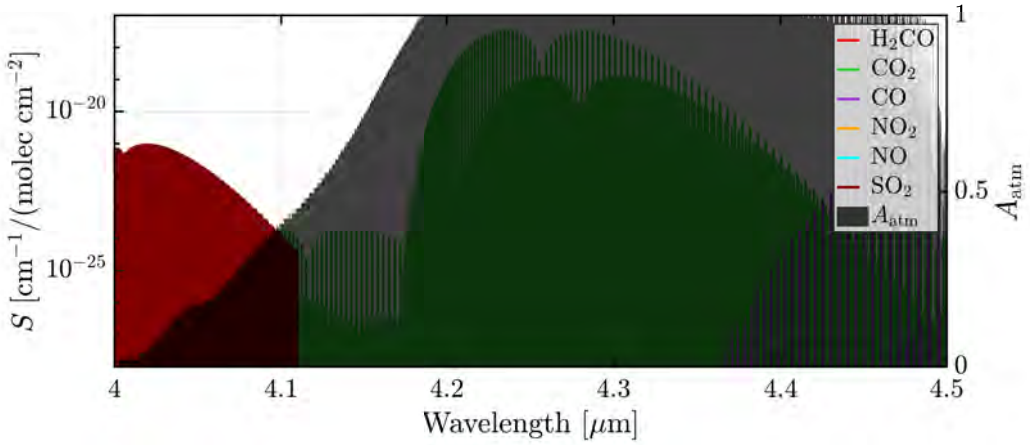

Figure A.7: The spectral line intensities S of various diesel exhaust molecules (left axis) with atmospheric absorption (right axis) overplotted. The spectral region is confined to 4.0 µm – 4.5 µm.

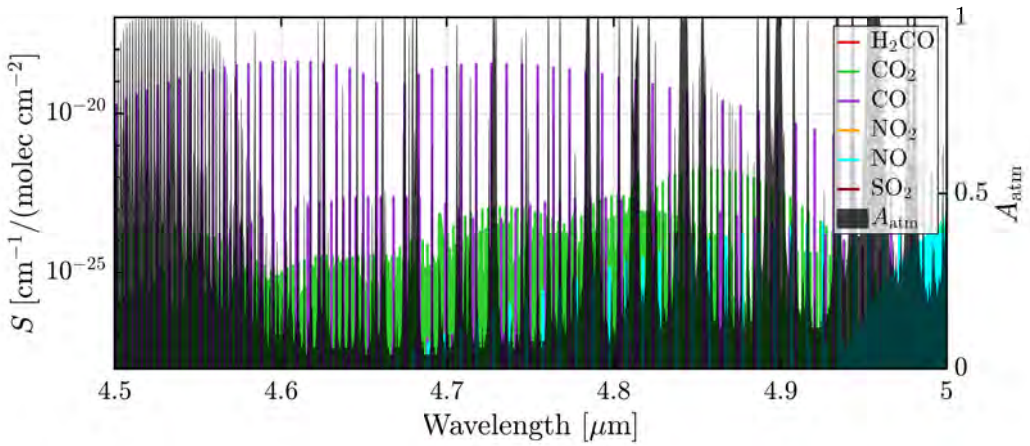

Figure A.8: The spectral line intensities S of various diesel exhaust molecules (left axis) with atmospheric absorption (right axis) overplotted. The spectral region is confined to 4.5 µm – 5.0 µm.

A.1.2 Absorption cross sections

The absorption cross sections of various diesel exhaust molecules in the spectral region between 2 µm and 12 µm are presented in Figure A.9. The cross sections for acetaldehyde and acrolein were sourced from the HITRAN2016 database[9] while the propylene cross sections were sourced from Ref. 125. Figure A.10 shows the absorption cross sections in the spectral region between 3.2 µm and 3.8 µm with atmospheric absorption overplotted. Absorption peaks within transmission windows include: propylene at wavelength 3.389 µm and cross section 1.64×10^{-19} cm^2, acetaldehyde at wavelength 3.650 µm and cross section 1.57×10^{-19} cm^2, and acrolein at wavelength 3.556 µm and cross section 1.52×10^{-19} cm^2.

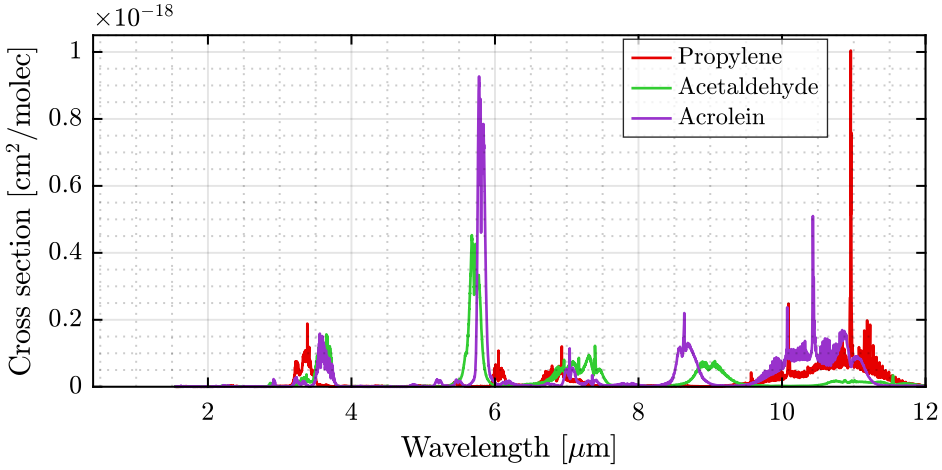

Figure A.9: Absorption cross sections of various diesel exhaust molecules measured near 298 K.

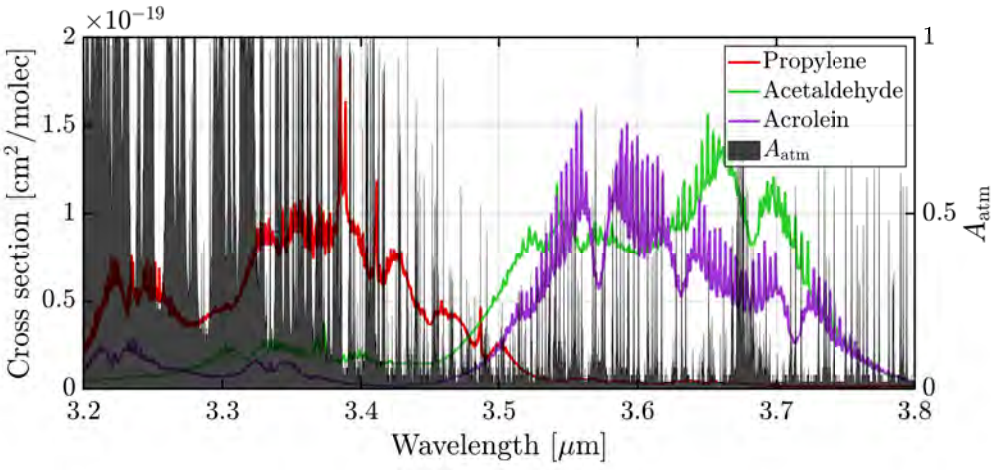

Figure A.10: Absorption cross sections of various diesel exhaust molecules measured near 298 K with atmospheric absorption overplotted.

A.1.3 Absorbance

The absorbance of diesel exhaust molecules in the spectral region between 2.5 µm and 12 µm are presented in Figure A.11. The absorbance data were sourced from the NIST database.[237] Figure A.12 shows the absorbance in the spectral region between 3.2 µm and 3.8 µm with atmospheric absorption overplotted. NIST state the following: "Important Note: All spectra were measured in the gas phase by GC/IR (gas chromatography / infrared spectroscopy), hence concentrations in the IR cell are not known or estimable. Molar absorption coefficients are not reported. This data provides only relative absorption coefficients as a function of wavelength which can be used for identification, not quantification." Therefore, the data was normalised to the highest peak within each spectrum. For some spectra, the highest peak occurs at a wavelength greater than 12 µm.

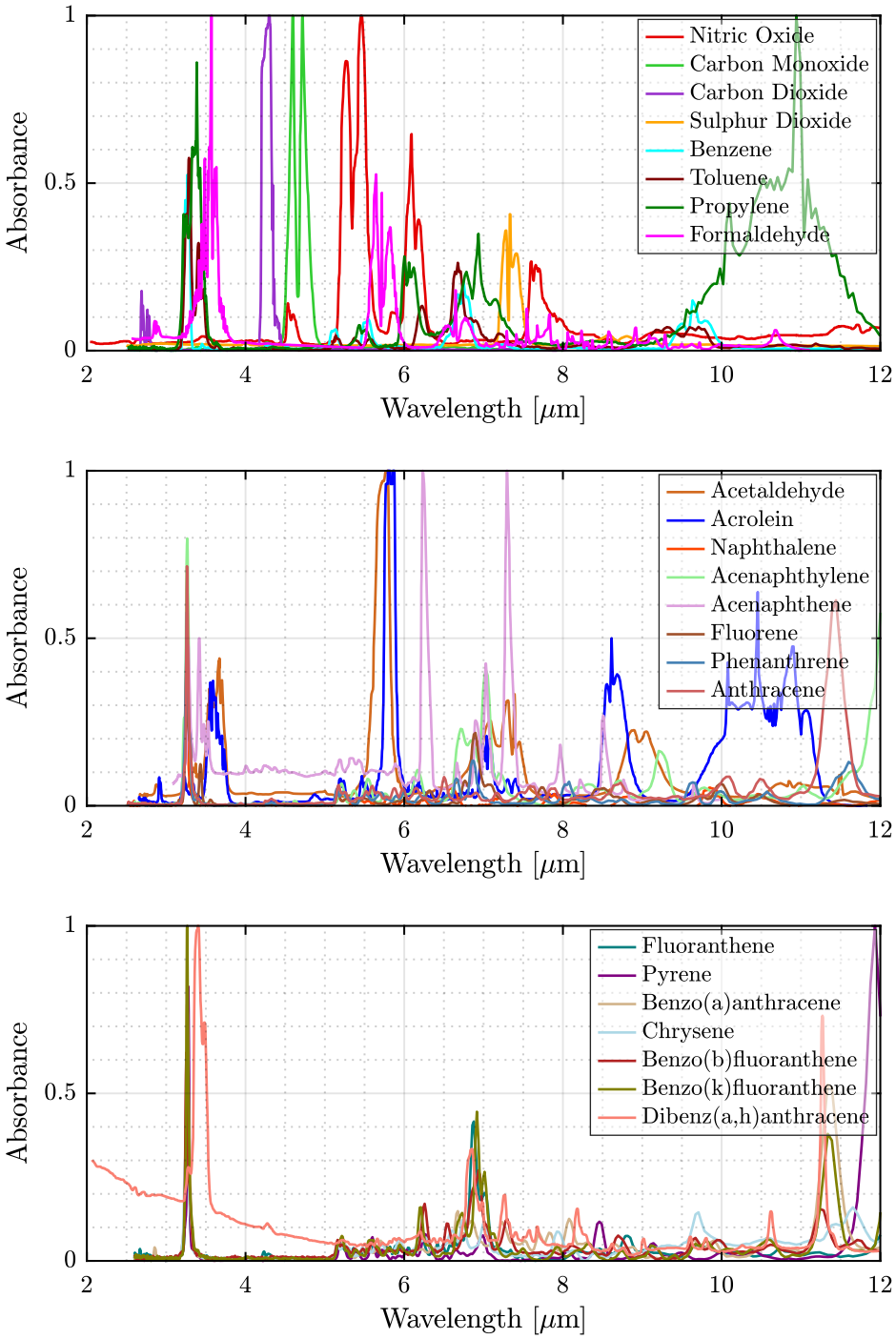

Figure A.11: Normalised absorbance of diesel exhaust molecules sourced from NIST data.[237] Note that the absorption peaks are only relative within each spectrum and are not relative from one spectrum to another.

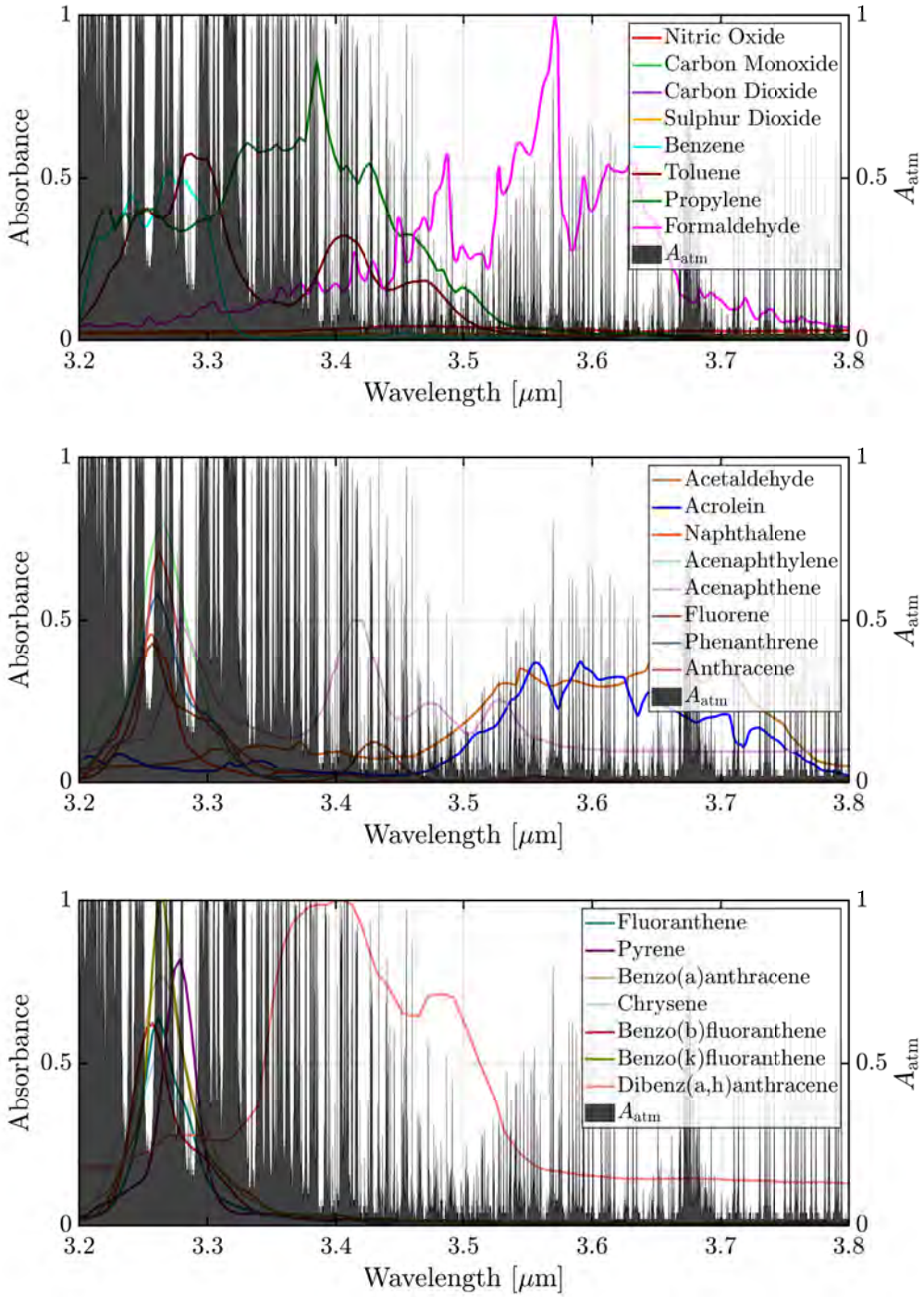

Figure A.12: Normalised absorbance of diesel exhaust molecules (left axis) sourced from NIST data[237] with atmospheric absorption (right axis) sourced from the HITRAN2016 database[9] overplotted. Note that the absorption peaks are only relative within each spectrum and are not relative from one spectrum to another. The spectral region is confined to 3.20 µm – 3.80 µm since this region contains most of the molecular absorption features within atmospheric transmission windows.

A.2 Spectral response of IR detectors

The spectral responses of Hamamatsu and Vigo IR detectors are shown in Figures A.13 and A.14 respectively.

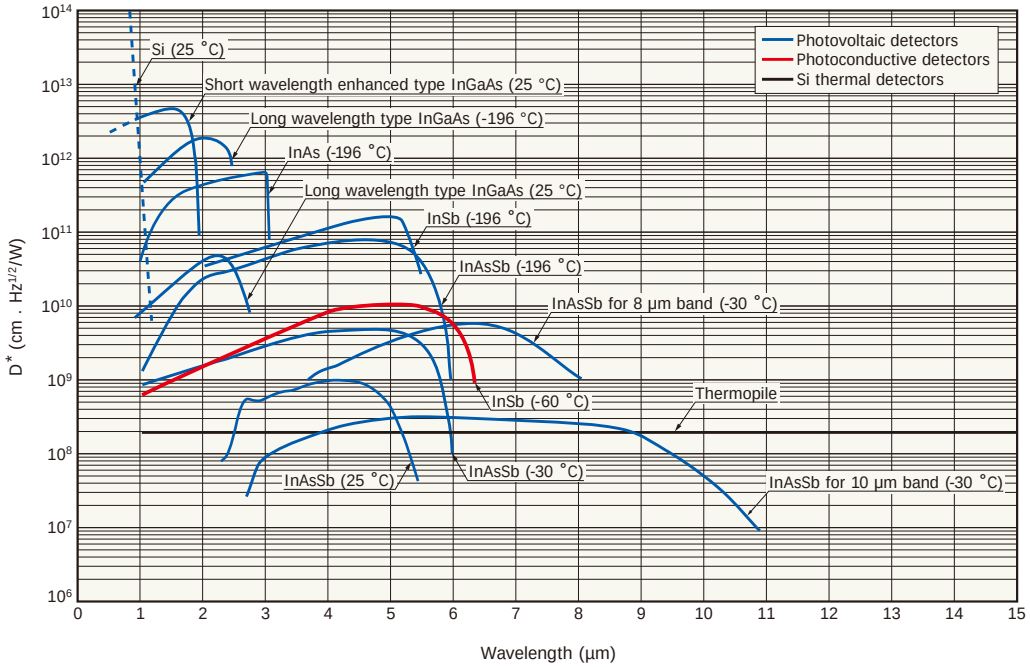

Figure A.13: Spectral response of Hamamatsu IR detectors. This illustration was sourced from the Hamamatsu selection guide for IR detectors, April 2019.

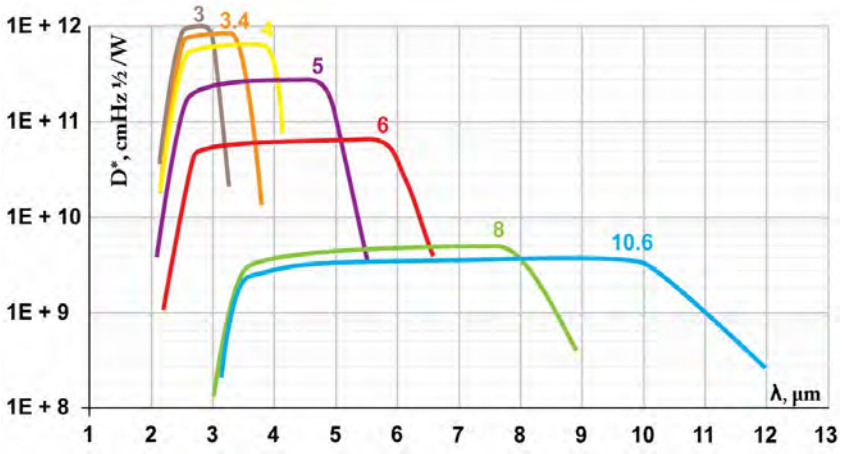

Figure A.14: Spectral response of Vigo PVI-4TE series IR detectors suitable for the 2 µm to 12 µm spectral range. This illustration was sourced from the Vigo catalogue for IR detectors, January 2017.

A.3 Diesel fuel

A.3.1 Nitrogen oxide breakdown in diesel exhaust

The maximum ratios of NO_2/NO_x in diesel engine exhaust may be up to 30 % but, under usual operating conditions, lies between 5% and 10%.[141] This ratio is affected by fuel mixture, temperature, and engine load.[142]

Measurements of NO_x emissions have been performed on a marine auxiliary diesel engine using various fuel mixtures and engine loads.[142] The experiments were performed using the turbocharged diesel engine equipped with a direct fuel injection and with the engine volume 6 l. Mixing of the biodiesel with the ultra low sulfur diesel fuel (ULSDF), using the ratios 0 %, 50 %, 80 % and 100 %, created the different testing fuels. The individual mixed fuels were marked ULSDF, B50:U50, B80:U20 and Biodiesel. Measured concentrations of NO_x, NO, and NO_2 are displayed in Figures A.15, A.16, and A.17 respectively. The ratio NO_2/NO_x ranges between 3 % (high engine load) and 32 % (low engine load) while NO/NO_x ranges between 60 % (low engine load) and 93 % (high engine load).

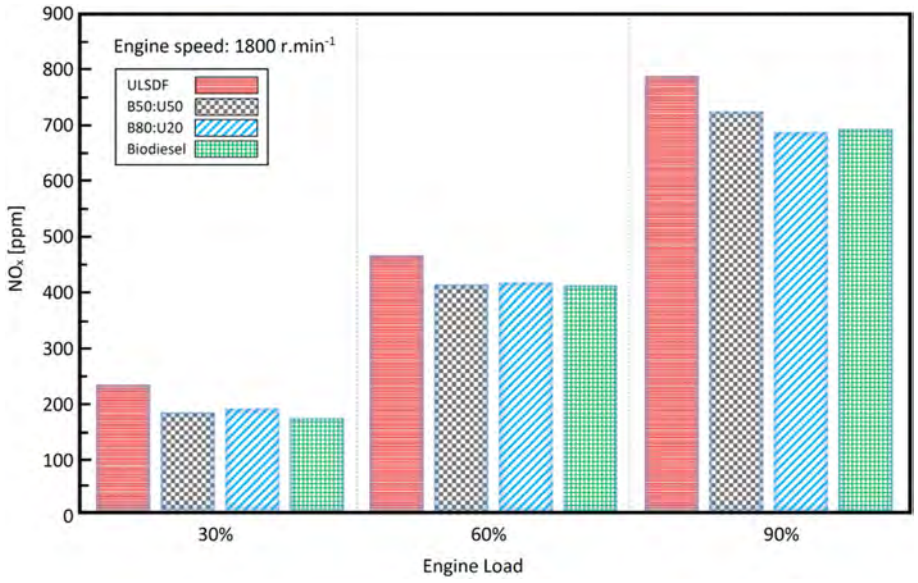

Figure A.15: Influence of different testing fuels on the NO_x emissions at the engine speed 1800 rpm.[142]

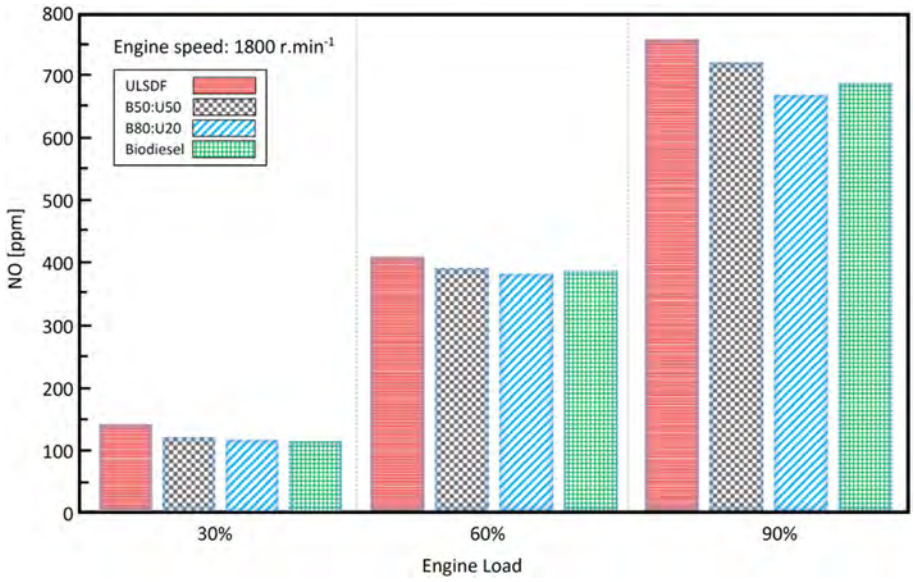

Figure A.16: Influence of different testing fuels on NO emissions at the engine speed 1800 rpm.[142]

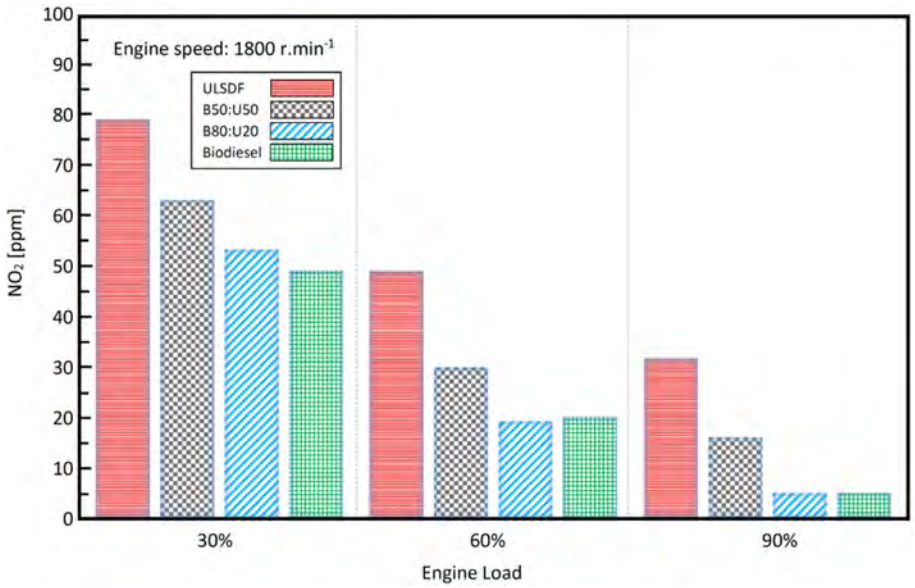

Figure A.17: Influence of different testing fuels on NO_2 emissions at the engine speed 1800 rpm.[142]

A.3.2 Sulfur content globally

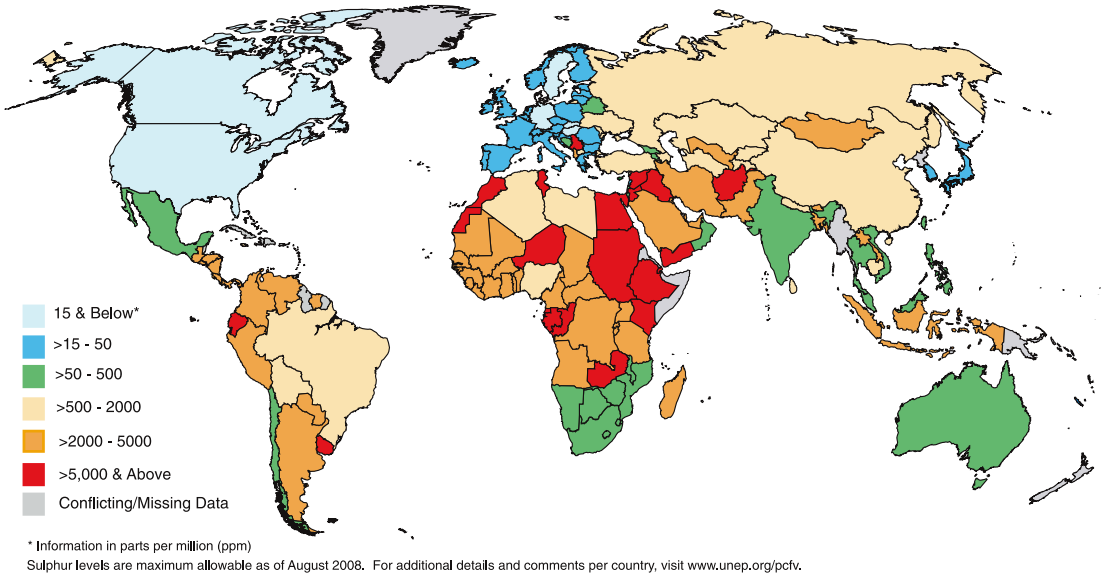

Figure A.18: Global status of sulfur levels in diesel fuels as at August 2008. This illustration was reported by UNEP.

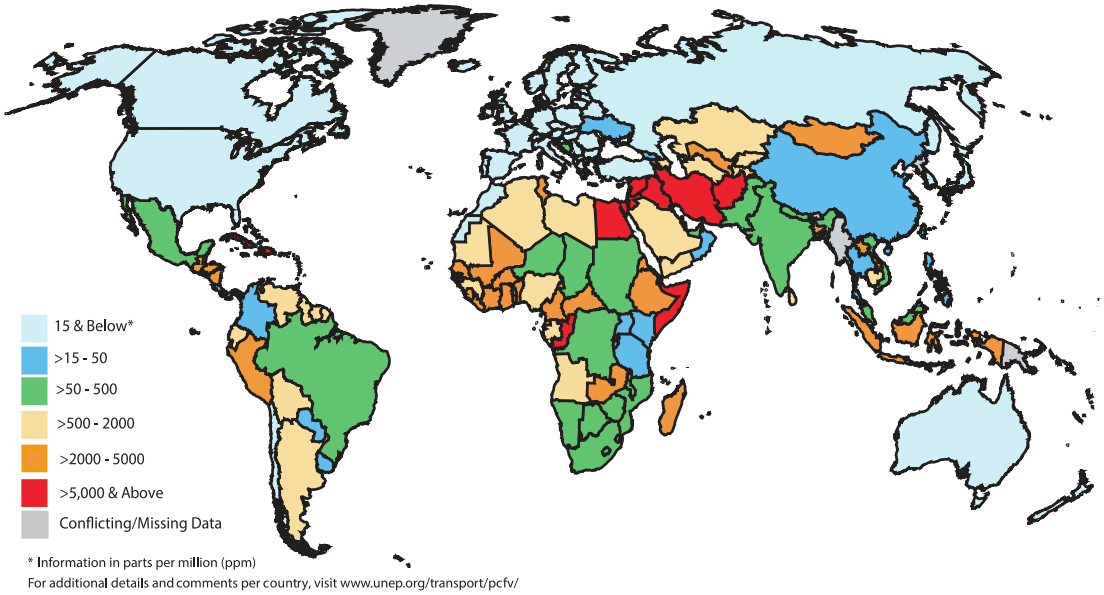

Figure A.19: Global status of sulfur levels in diesel fuels as at March 2017. This illustration was reported by UNEP.

Appendix B
Modelling Fibre Lasers: Supporting Information

This Appendix presents the following published article:

> O. Henderson-Sapir, A. Malouf, N. Bawden, J. Munch, S. D. Jackson, D. J. Ottaway. Recent advances in 3.5 µm erbium-doped mid-infrared fiber lasers. *IEEE Journal of Selected Topics in Quantum Electronics*, 23(3):6–14, May 2017.

This article is provided to support the material presented in Section 3.5.

IEEE JOURNAL OF SELECTED TOPICS IN QUANTUM ELECTRONICS, VOL. 23, NO. 3, MAY/JUNE 2017 0900509

Recent Advances in 3.5 μm Erbium-Doped Mid-Infrared Fiber Lasers

Ori Henderson-Sapir, *Member, IEEE*, Andrew Malouf, Nathaniel Bawden, Jesper Munch, Stuart D. Jackson, *Senior Member, IEEE*, and David J. Ottaway

(Invited Paper)

***Abstract*—The performance of mid-infrared Er^{3+}-doped fiber lasers has dramatically improved in the last few years. In this paper, we present an overview of the progress in 3.5 μm fiber lasers based on the dual-wavelength pumping approach. The cross section of the excited state absorption transition used by the 1973 nm second pump is found experimentally. A numerical simulation of the expected *Q*-switched behavior of this fiber laser is presented. This shows that increasing the power of the 977 nm pump is important to achieve high-peak power pulses.**

***Index Terms*—Laser, fiber, optics, optical, infrared, mid-infrared, erbium, Er^{3+}, ZBLAN, numerical, model, simulation, optimization, 3.5 μm, 2.8 μm, dual-wavelength.**

I. Introduction

IN THIS paper we review the current state of the art in rare-earth doped mid-infrared fiber lasers. The last decade has seen a continuing increase in the power available from mid-infrared sources. Significant attention has been given to sources such as optical parametric oscillators (OPOs) and amplifiers (OPAs), quantum cascade lasers (QC) and fiber lasers. The improvement in these sources have opened up many new possible applications in defense [1], environmental monitoring [2] and medicine [3]. Despite the advances, mid-infrared sources operating in the 3-4 μm band have lagged behind in terms of output power, portability, efficiency and beam quality.

Quantum cascade lasers have excelled at the longer wavelengths and the achievable wavelengths have recently been pushed further towards shorter wavelengths [4]. In recent years wavelengths as short as 3.2 μm have been demonstrated [5]. Compared with QCs, rare earth doped fiber lasers have the potential for efficient power scaling of high beam quality outputs. Moreover, their higher energy storage capability promises high peak powers, which are likely to be outside of QC capabilities. Recently, 3 μm fiber lasers have shown to exhibit power levels exceeding 30 W CW with peak powers exceeding 0.9 kW. [6], [7].

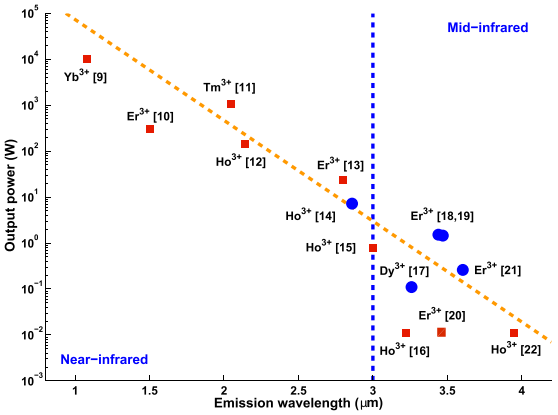

Fig. 1. Published laser power from rare-earth doped fiber laser as a function of operating wavelength [9]–[22]. The trend of reduced power as the wavelength increases (dashed orange line) is mostly a result of the energy difference between pump and laser photons. Recent development since 2012 [8] are marked with a blue circle. The Ho^{3+} based 3.9 μm laser required cryogenic cooling [22].

Infrared fiber lasers can now provide output over most of the wavelength range of 1-4 μm as can be seen in Fig. 1. The figure depicts the maximum average power demonstrated to-date from rare-earth doped fiber lasers. Originally, published in a review paper by Jackson [8] and updated for this paper it shows the state-of-the-art power achieved by fiber lasers at various wavelengths. It also demonstrates that until recently the output power versus wavelength follows a trend line that decreases exponentially with increasing wavelength until 3 μm, above which the laser power fell significantly to 10 mW.

The pioneering work done on demonstrating fiber lasers with wavelengths longer than 3 μm was done by a group from the Technischen Universität Braunschweig in Germany in the 1990's. They demonstrated lasers that operated at 3.2 μm [16] and 3.9 μm (cryogenically) [22] using Ho^{3+}:ZBLAN fiber and at 3.5 μm [20] using Er^{3+}:ZBLAN fiber. These lasers had high threshold and low slope efficiencies, particularly when operated at room temperature. The maximum average power levels were at the 10 mW level.

The low powers and efficiencies demonstrated previously in these lasers can be attributed to the following reasons. First, the high phonon energy of silica glass means that it is not transparent

Manuscript received August 1, 2016; revised September 28, 2016; accepted September 30, 2016. This work was supported in part by the South Australian Government through the Premier Research and Industry Fund and PSRF schemes and in part by the University of Adelaide.

O. Henderson-Sapir, A. Malouf, N. Bawden, J. Munch, and D. J. Ottaway are with the University of Adelaide, Adelaide, SA 5005, Australia (e-mail: ori.henderson-sapir@adelaide.edu.au; andrew.malouf@adelaide.edu.au; nathaniel.bawden@student.adelaide.edu.au; jesper.munch@adelaide.edu.au; david.ottaway@adelaide.edu.au).

S. D. Jackson is with the Department of Engineering, Macquarie University, Sydney, NSW 2109, Australia (e-mail: stuart.jackson@mq.edu.au).

Color versions of one or more of the figures in this paper are available online at http://ieeexplore.ieee.org.

Digital Object Identifier 10.1109/JSTQE.2016.2615961

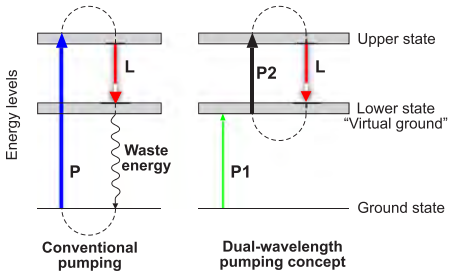

Fig. 2. The dual-wavelength pumping concept compared to ordinary ground-state based pumping.

beyond 2.4 μm and longer wavelength transitions are efficiently quenched by multi-phonon non-radiative decay. This requires the use of more exotic glasses, such as the fluoride glass ZBLAN which are less mechanically robust and have proven more difficult to fabricate and handle. In addition, many of the longer wavelength transitions are located high above the ground state, which means the lasing transition is inherently inefficient due to high quantum defect. Moreover, excited states located below the lasing transition often have long radiative lifetimes which are fully realized due to the required low phonon energy of the glass hosts. These long lifetimes trap ions and prevent them from returning to the ground state after lasing which depletes the ground state and reduces pump absorption. Therefore, the high quantum defect for the longer transitions, combined with less mature glasses and compounded by less efficient pump sources [23] are the main reasons behind the declining trend in laser power shown in Fig. 1. In the case of the ${}^4F_{9/2} \rightarrow {}^4I_{9/2}$ transition in erbium [20] we have recently found evidence that the high threshold in these experiments were likely caused by an energy exchange process that robs the top lasing state of ions [24].

We realized that the long-lived lower level excited states could be transformed from a hindrance to an advantage if they were used to significantly reduce the quantum defect of these laser. This could be achieved using dual-wavelength pumping (DWP) whose concept is illustrated in Fig. 2. Dual wavelength pumping uses one pump wavelength (P_1) to establish a population in one of the long-lived excited states which we have called a "virtual ground state". The lasing cycle then consists of pumping the ions to the top lasing state using a second pump (P_2), post-lasing the ions return to the virtual ground state and the cycle is repeated. In this way ions can undertake this lasing cycle a number of times before they drop to the ground state and need to be re-pumped to the virtual ground state using P_1. This technique offers the additional benefit of using infrared pump wavelengths that are more readily available at higher powers than the visible sources required for direct ground state pumping. Our initial work demonstrated this concept on the ${}^4F_{9/2} \rightarrow {}^4I_{9/2}$ transition in erbium [21], [25], [26]. Our first demonstration of mid-infrared DWP laser significantly surpassed the 10 mW barrier, achieved a slope efficiency of 25 % and brought the 3.5 μm Er^{3+} transition onto the trend line shown in Fig. 1. Further power scaling to 1.5 W output power was demonstrated recently by our group [19] and the Université Laval group [18] who used an all fiber approach.

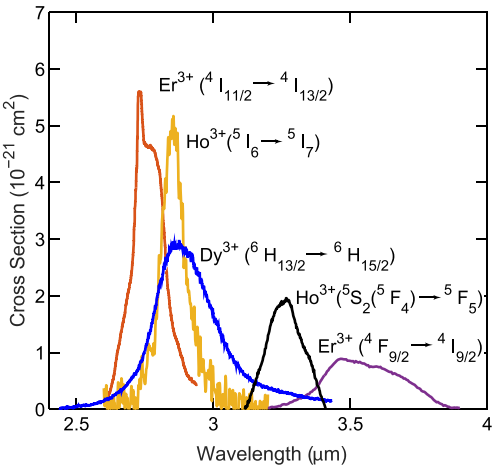

Fig. 3. Emission cross-sections of mid-infrared transitions in rare-earth doped ZBLAN glass. The 3.2 μm cross-section was calculated from the spontaneous emission spectrum in [16] in conjunction with spectroscopic data from [28] by applying the Fuchtbauer-Ladenburg method [29].

We expect that further power scaling of the 3.5 μm transition is achievable. To facilitate this we have recently finished a numerical model that emulates the 3.5 μm system [27]. This numerical codes allows us to simulate different conditions and various geometries prior to committing to purchase costly ZBLAN fibers. Moreover, our code allows us to investigate both the spatial and temporal development of the laser pulse along the fiber, therefore enabling the investigating of gain-switching and Q-switching. Both short pulse approaches are necessary for remote sensing applications and might allow 3.5 μm fiber lasers to replace costly OPOs as laser sources for remote sensing applications.

Results from Figs. 1 and Fig. 3, together with the results from Braunschweig Group [22] demonstrate that fiber lasers can span the entire 2.6-3.9 μm wavelength range, which covers the important light absorption "fingerprint" range of many organic compounds, some of them shown in Fig. 4. This development can open new applications for fiber lasers in spectroscopy that were not previously available.

In this paper we describe new experimental and modeling results which are important for improving the performance of DWP based 3.5 μm fiber lasers. First we show the optimal wavelength for the excited state pump source (P_2) in a DWP system is 1973 nm. We then present our experimental work to find the absorption and emission cross-sections curves associated with the second pump source.

In the following section we show phenomenologically that the emission spectra at the 3.5 μm band has a considerable dependence on the source of the ZBLAN glass used and its doping concentration which has ramifications for extending the

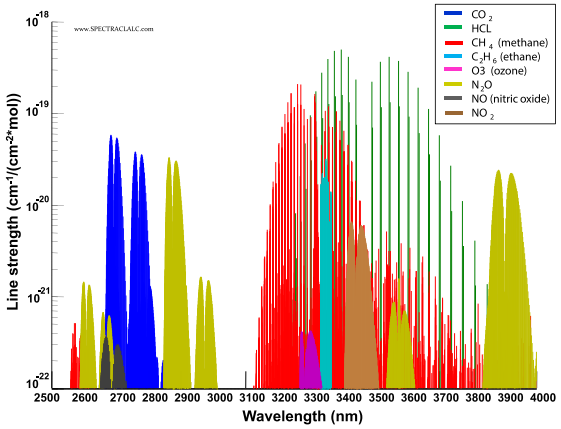

Fig. 4. Absorption of various gasses in the 2.5–4 μm spectral range. Note that the three most important greenhouse gases, water (not shown for brevity - many lines), carbon-dioxide and methane, are all present.

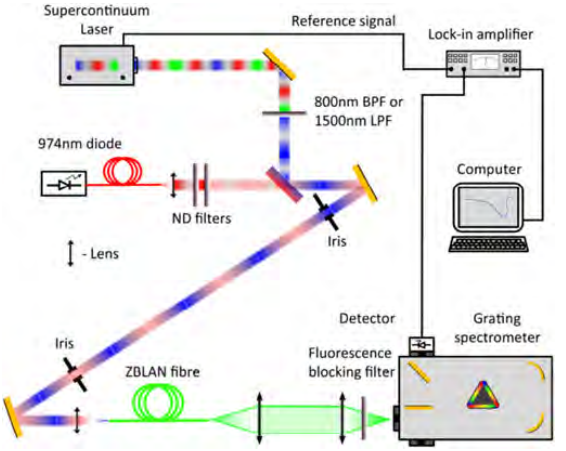

Fig. 6. Experimental setup for in-fiber pump-probe measurement for determining ${}^4I_{11/2} \rightarrow {}^4F_{9/2}$ transition cross-section. BPF - bandpass filter, LPF - longpass filter. For further details, see text.

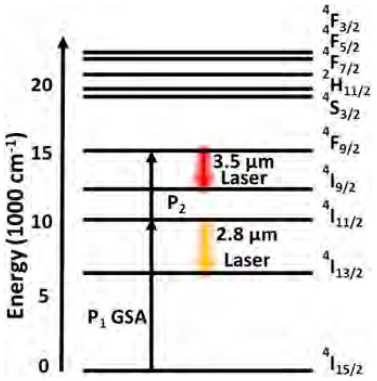

Fig. 5. Energy level diagram of Er:ZBLAN.

tuning range of this transition. We conclude by presenting a numerical analysis of a Q-switched DWP, 3.5 μm laser which is a necessary precursor for the evaluation of high peak-pulse lasers in this band for laser based remote sensing applications.

II. 2 μm Emission Cross-Section

To achieve efficient pumping of the DWP system by the second pump, it is important that its wavelength is close to the peak absorption of this transition (${}^4I_{11/2} \rightarrow {}^4F_{9/2}$) (see Fig. 5). In this section we present measurements using excited state spectroscopy to determine the relevant excited state cross-section for the first time in Er^{3+}:ZBLAN. Spectroscopic data available from Caspary [30], suggests that the transition has a zero-phonon transition wavelength of 1973 nm and no ground state-absorption (GSA) or excited-state absorption (ESA) transitions correspond to this wavelength band suggesting little interference in the measurements from other transitions. Existence of a weak excited-state absorption that originates from the ${}^4F_{9/2}$ state has been proposed by the Laval group [31] to explain their modeling results. This excited state absorption will not effect the results presented here because a significant population is not established in the ${}^4F_{9/2}$ state. The experimental set-up used to perform this measurement is illustrated in Fig. 6.

Determining the optimum ESA wavelength using a fiber compared with bulk has two major advantages. The increased interaction length allows small cross-sections to be measured and the fiber geometry ensures good spatial overlap between the probe beam and the excited state population established by the 974 nm pump. For the fiber experiments, we used a commercially available Er^{3+} doped ZBLAN fiber manufactured by FiberLabs. The fiber had a 3.6 μm core with an NA $= 0.28$ and 125 μm diameter cladding surrounded by polymer coating with 250 μm diameter. The doping concentration was low, 8×10^{19} ions/cm^3 or 0.5 mol% to minimize non-radiative energy transfer processes.

We determined the lineshape of the ESA transition using the experimental set-up illustrated in 6. Light from a 974 nm diode and a broadband supercontinuum source (SCS) was launched into an Er^{3+}:ZBLAN fiber. The 974 nm diode excited ions from the ground state and created a population at the ${}^4I_{11/2}$ level. The SCS probed the ${}^4I_{11/2} \rightarrow {}^4F_{9/2}$ transition at a variety of wavelengths to determine a relative transmission over a wide-band wavelength for a range of differing 974 nm pump powers. By determining the spatially averaged population of the ${}^4I_{11/2}$ level, this absorption spectra was used to calculate the absolute excited-state absorption cross-section.

In this experimental set-up, the pump and probe beams were launched into the fiber from the same direction. The pump beam was a 330 mW, 974 nm single mode, fiber-coupled laser diode (Thorlabs PL980P330J), which was collimated using an aspheric lens. Some measurements required neutral density filters

to attenuate the beam whilst maintaining a constant current and hence wavelength for the 974 nm laser diode.

The probe beam was generated by a Koheras SuprK supercontinuum source (SCS) with a power spectral density of 0.01 mW/nm in the band around 1970 nm. The single transverse mode output of the SCS enabled easy alignment and focusing into the fiber. The SCS was internally pulsed with a pulse duration of ~ 1 ns and a pulse repetition frequency (PRF) of 22.6 kHz. The TTL output from the SCS was used to synchronize the lock-in amplifier (LIA). Various filters were used to allow only a certain band of the SCS to be incident on the ZBLAN fiber.

The beam from the SCS was combined with the 974 nm beam on a 45° dichroic mirror (CVI Laser Optics). The dichroic mirror reflected the wavelength range of 1500-2400 nm while it transmitted the 974 nm beam. The combined beams were launched through an aspheric lens into the ZBLAN fiber. Chromatic dispersion of the launching aspheric lens resulted in large variations in launch efficiency at the different wavelengths used. This was especially noticeable when launching the 974 nm pump and the broadband SCS beam around 1900 nm band. The launching conditions were thus a trade-off between launched pump and probe power. This issue could be avoided in future experiments by using reflective focusing optics.

The launched beams interacted with the Er^{3+} ions by GSA and ESA transitions. The residual pump, probe and fluorescence emerging out of the fiber were collimated by an uncoated CaF_2 lens. Short wave fluorescence was filtered from the emerging beam using either a 1550 nm or 1150 nm longpass filter (Thorlabs). The remaining light was focused into the spectrometer (Princeton Instruments, Acton 2557) using an additional CaF_2 lens.

Visible and near-IR wavelengths were detected using a silicon photo-diode (Horiba DSS), while the 1970 nm band light was detected by an extended InGaAs biased photodiode detector (Thorlabs DET10D). The signal from the detector was fed into a LIA (Stanford Research System SRS830) for amplification and demodulation at the SCS frequency. The signal from the LIA was logged by computerized acquisition and control system (Princeton Instruments, SpectraHub).

An example of the change in the transmitted probe beam spectrum between 1500 nm and 2100 nm with changing 974 nm power is shown in Fig. 7. It shows a wide absorption band stretching between 1900 nm and 2020 nm, with its peak centered at 1973 nm. As expected, the depth of absorption was strongly dependent on the 974 nm power launched into the fiber.

In the case of a pump and probe measurement and following Pollnau *et al.* notation [32], the general case for the transmission ratio of a probe beam with and without a pump beam is

$$\frac{1}{N_e l}\ln\left(\frac{I_p}{I_u}\right) = \sigma_{\mathrm{GSA}} + \sum_i \frac{N_i}{N_e}\left[\sigma_{\mathrm{SE}}(i) - \sigma_{\mathrm{ESA}}(i)\right]. \quad (1)$$

In (1), we defined $N_e = \sum_i N_i$ as the total population density of all excited states, and the ratio of the transmitted probe power with the pump laser on and off is $(\frac{I_p}{I_u})$. σ_{GSA}, σ_{ESA} and σ_{SE}

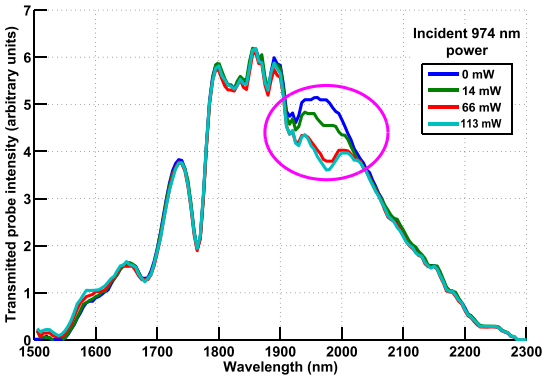

Fig. 7. Initial broadband transmission scan showing ${}^4I_{11/2} \rightarrow {}^4F_{9/2}$ ESA. The ellipse encompasses the ESA region of the 1973 nm absorption maximum. On the left side of the curves, we see hints of weak stimulated emission around the 1550 nm band.

are the absorption cross-sections of the ground and excited state transitions and the stimulated emission (SE) cross-sections, respectively.

The excited state absorption spectra of Fig. 7 was used to calculate the wavelength dependent cross-section for this transition using (2).

$$\sigma_{\mathrm{ESA}} = \frac{1}{N_{4_{I_{11/2}}} l}\ln\left(\frac{I_p}{I_u}\right). \quad (2)$$

To determine the absolute cross-section, accurate measurements of the population of the ${}^4I_{11/2}$ state ($N_{4_{I_{11/2}}}$ in (2)), the fiber length l and the probe beam transmission ratio $(\frac{I_p}{I_u})$ are required. The last term is readily obtained from a transmission measurement since it is independent of absolute power. This holds as long as the power levels are kept low to prevent bleaching of the population established by the pump. Obtaining the $N_{4_{I_{11/2}}}$ term accurately is considerably more challenging since it requires an absolute value. The procedure for achieving this is described below.

It should be noted that (2) assumes that there are no neighboring excited state absorptions whose wings overlap the excited absorption of interest. The data shown in Fig. 7, supported by the work of Caspary [30] shows that there are no significant ESA or SE bands which overlap the 1970 nm band. ESA and SE bands, which are further removed from the 1970 nm band can be identified in Fig. 7. A feature close to 1550 nm was the result of the ${}^4I_{15/2} \rightarrow {}^4I_{13/2}$ GSA transition combined with SE on the ${}^2H_{11/2} \rightarrow {}^4I_{9/2}$ transition. This SE transition starts at 1470 nm but the short edge was not measured in the scan of Fig. 7, because of the 1500 nm longpass filter used to eliminate second order shorter wavelengths from coming through the spectrometer.

We used the following additional pump-probe experiment to obtain the average population of the ${}^4I_{11/2}$ state at each 974 nm power level. The transmission through the fiber of a

weak 797 nm beam probed the ${}^4I_{15/2} \rightarrow {}^4I_{9/2}$ GSA transition. This experiment provided an absolute average value for the change in the mean ground population of the fiber. We observed a change in the transmission of the 797 nm beam, due to the bleaching of the ground state, ${}^4I_{15/2}$ due to high pump intensity.

As stated previously, the ${}^4I_{11/2}$ population cannot be calculated simply by using the absorbed power of the 974 nm pump because this required a very accurate knowledge of the coupling efficiency. Further, the pump wavelength (974 nm) is known to drive a number of excited state processes which further complicates this relationship.

When the 974 nm pump is switched on, the change in the ground population is

$$\begin{aligned}\Delta N_g &= N_{\text{ground with pump}} - N_{\text{ground}} = -N_e \\ &= -(N_{{}^4I_{13/2}} + N_{{}^4I_{11/2}} + N_{\text{Higher}}),\end{aligned} \tag{3}$$

where N_{Higher} is the population of all other excited states, beyond ${}^4I_{13/2}$, and ${}^4I_{11/2}$. N_{Higher} was small because of the combination of low pump power, low doping concentration and the short lifetimes of levels above ${}^4I_{11/2}$. In a case similar to ours, with CW 974 nm pumping Pollnau *et al.* showed numerically [33] that less than 1% of the population occupied levels above ${}^4I_{11/2}$. Hence, we disregard the N_{Higher} term in (3).

Pollnau *et al.* [33] also derived the ratio of population of the ${}^4I_{13/2}$ and ${}^4I_{11/2}$ levels to the total excited population and found that the population of these levels was dominated by the ratio of lifetimes of the energy levels. They found that this ratio held for doping densities up to almost 4 mol% doping of Er^{3+} ions [34], [35], which is considerably higher than the doping densities used in our experiment (0.5 mol%). We therefore used their result for the excited state population ratio of 33% and 66% for the ${}^4I_{13/2}$ and ${}^4I_{11/2}$ levels' occupation, respectively. Using these results together with (3), we find

$$N_{{}^4I_{11/2}} \simeq -\frac{2}{3}(\Delta N_g). \tag{4}$$

The change in the ground state population can be measured by observing the change in transmitted light in the 800 nm band of the SCS, with and without the 974 nm pump operating. This change in transmission corresponds to absorption by the ${}^4I_{15/2} \rightarrow {}^4I_{9/2}$ GSA transition and the relevant additional ESA transitions shown in reference (1).

$$\begin{aligned}N_{{}^4I_{11/2}} = \frac{1}{l}\ln\left(\frac{I_{\text{out 800 nm pump}}(\lambda_1)}{I_{\text{out 800 nm}}(\lambda_1)}\right) \\ \times \frac{1}{\frac{3}{2}\sigma_{\text{GSA}}(\lambda_1) - \frac{1}{2}\sigma_{\text{ESA}_{{}^4I_{13/2}}}(\lambda_1) - \sigma_{\text{ESA}_{{}^4I_{11/2}}}(\lambda_1)}\end{aligned} \tag{5}$$

Equation (5) holds so long as a significant population is not established in the ${}^4I_{9/2}$ state, which allows us to omit the stimulated emission term and obtain (5).

The combination of the low incident power of the SCS over the entire 800 nm band (0.2 mW) and short lifetime of the ${}^4I_{9/2}$ state (10 μs) ensures that this is true.

To determine the population of the ${}^4I_{11/2}$, it was necessary to know the GSA and ESA cross-sections for specific wavelengths. These cross-section were obtained from Pollnau *et al.* [33] ($\sigma_{\text{GSA}} = 6.7 \times 10^{-22}$ cm^2, $\sigma_{\text{ESA}_{{}^4I_{13/2}}} = 11.6 \times 10^{-22}$ cm^2 and $\sigma_{\text{ESA}_{{}^4I_{11/2}}} = 1.5 \times 10^{-22}$ cm^2) at 797 nm. To maximize the signal-to-noise, we chose a wavelength within the 800 nm band where GSA is dominant. From the work of Pollnau [33], the peak of the GSA transition occurs around 797 nm. We conducted an additional pump-probe scan at this band which confirmed the wavelength of the peak of the GSA transition. The peak of the ${}^4I_{15/2} \rightarrow {}^4I_{9/2}$ GSA transition was coincidentally at the intersection point of both ${}^4I_{13/2} \rightarrow {}^2H_{11/2}$ and ${}^4I_{11/2} \rightarrow {}^4F_{3/2}$ ESA transition cross-section curves. By using this wavelength, we were able to obtain the highest signal-to-noise and be least affected by ESA at the 800 nm band.

In the above derivation, all population densities are assumed to be the average values over the entire fiber length. The exponential absorption profile of the pump means that the local ion density at each position along the fiber is different. Under the assumptions of negligible effect of cross-relaxation (CR) and energy-transfer upconversion (ETU) processes and negligible loss in the fiber, the average ion densities are independent of the local population and depend only on the total pump power absorbed. These assumptions are believed to be valid in our case since the fiber used had low doping concentration and the pump power used was low, both minimizing the effects of CR and ETU processes.

The derivation by Pollnau *et al.* in [33] assumed that bleaching of the ground state was very limited. In their case, less than 15% of the population was in an excited state. In our case, due to the small core of the fiber, a large fraction of the population could be excited. Thus, in order to maintain the validity of the above derivation, it was necessary to reduce the pump power as much as possible while maintaining a reasonable signal to noise. The calculated ESA cross-section at 1973 nm was not accurate when using high 974 nm pump power which excited a significant fraction of the ion population.

After finding the ion density of the ${}^4I_{11/2}$ level with varying 974 nm pump power, a second measurement was performed using the same setup that was used to measure the 1973 nm absorption. From the transmission fraction and the ion population we could derive the absorption cross-section using (2).

The two experiments used a similar experimental setup to the one in Fig. 6 with slight variations. The 1500 nm longpass filter was replaced by an 800 nm bandpass filter for the first part of the experiment measuring the 800 nm transmission and was reverted back to the 1500 nm longpass filter for the second part of the experiment. A longer fiber, 65 cm long was used for both experiments to increase the absorption of the light and hence the signal level.

The absorption was linear up to about 25 mW of 974 nm pump, where saturation effects started occurring. Beyond this point the bleaching of the ground state significantly changes the likelihood of GSA. Moreover, ESA becomes signficant at higher power levels due to increased population at higher levels

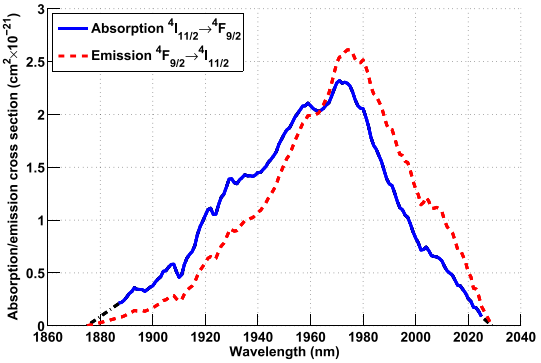

Fig. 8. ESA cross-section of the ${}^4I_{11/2} \rightarrow {}^4F_{9/2}$ transition based on measurement of bleaching of the ground. The black dot-dashed line represents extrapolation of the measured absorption data. Peak absorption cross-section value is $\sigma_{1973\mathrm{nm\,abs}} = 2.3 \pm 0.8 \times 10^{-21}$ cm^2 and emission peak value is $\sigma_{1973\mathrm{nm\,em}} = 2.6 \pm 0.9 \times 10^{-21}$ cm^2.

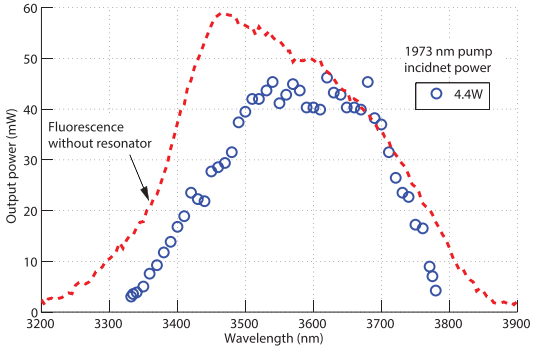

Fig. 9. Wavelength tuning obtained using 2.8 m long, 1 mol% Er^{3+}:ZBLAN fiber while employing the DWP method [19]. 5 W of 977 nm pump and 4.4 W of 1973 nm pump powers were used. The dashed line represents the fluorescence spectrum of the ${}^4F_{9/2} \rightarrow {}^4I_{9/2}$ without a resonator.

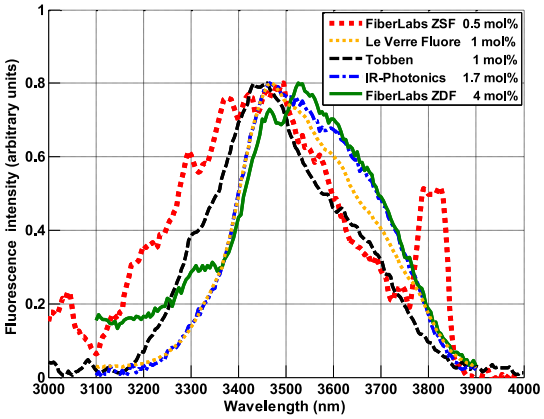

Fig. 10. Comparison of the normalize fluorescence from the ${}^4F_{9/2} \rightarrow {}^4I_{9/2}$ transition from different fiber varieties. The distinctive feature at 3820 nm in the FiberLabs ZSF curve is the result of stray light from the 1909 nm pump source.

than ${}^4I_{11/2}$ which causes the population ratio to deviate from one used to calculate (5).

By combining the results of the ion density from the 797 nm transmission measurement with the 1973 nm absorption at low pump powers a consistent cross-section of $\sigma_{1973\mathrm{nm}} = 2.3 \pm 0.8 \times 10^{-21}$ cm^2 was obtained. The relatively high uncertainty (30%) at these low power data arises from the lower signal-to-noise and instabilities of the SCS source.

The emission cross-section of the ${}^4F_{9/2} \rightarrow {}^4I_{11/2}$ transition can be inferred from the absorption cross-section using the McCumber relation [36] and it is shown in Fig. 8. Energy of the appropriate Stark levels required for this calculation can be found in [37]. We arrived at a peak emission cross-section of $\sigma_e = 2.6 \pm 0.9 \times 10^{-21}$ cm^2 with the wavelength dependency shown in Fig. 8. The value obtained of $\sigma_{1973\mathrm{nm}} = 2.3 \pm 0.8 \times 10^{-21}$ cm^2 is the first experimental value obtained for this ESA transition.

III. Variations in the 3.5 μm Emission Shape

In our previous work [19] we demonstrated a 450 nm wide tuning range on the transition centered on 3.5 μm band using the DWP method. Such wide tuning is significant to the future sensing of hydrocarbons which tend to have strong absorption lines closer to the short-wavelength edge of the tuning range illustrated in Fig. 9.

It is therefore imperative to ensure efficient operation at the shorter edge of the tuning range, which looks achievable since there is large variability in the fluorescence curves obtained from fibers made using slightly different compositions of ZBLAN and differing dopant concentrations. This is summarized in Fig. 10 which shows fluorescence curves obtained from four different fiber sources: Two fibers manufactured by FiberLabs, a single clad, 0.5 mol% fiber (ZSF) and a 4 mol% double clad fiber (ZDF). A third fiber manufactured by LeVerre Fluore (1 mol%) and a forth one made by IR-Photonics (1.7 mol%). The fluorescence from these four fibers was collected during our work. A fifth fiber (1 mol%) single clad, is from the work of Többen [20].

The large differences of the short and long edges of the fluorescence cannot be attributed to slight differences in calibration as they span over 100 nm on each side. Although the different curves were collected from fibers of different lengths, this should not significantly affect the fluorescence profile because the cross section of the fiber is low and re-absorption by the sparsely populated ${}^4I_{9/2}$ level was negligible

The origin of the difference between the fibers is not clear. Fig. 10 suggests that doping concentration might contribute to the location of the short edge. Understanding the causes and controlling the location of the short edge is essential for future spectroscopy application since the strongest fundamental absorption lines involving C-H bonds fall around 3.34 μm, well within the wavelength region mostly affected by the fluorescence short-edge variations.

IV. Q-Switching

Q-switching is a long established technique for producing short pulses with high peak power [38]. Such pulses are

extremely useful in remote sensing applications such as differential absorption lidar (DiAL), see for example [39]. In this section we investigate the likely Q-switching behavior of a 3.5 μm fiber laser using our time domain numerical model [27]. We evaluate the laser performance using the same parameters that were used to demonstrate 1.5 W level power operation [19]. The laser gain medium was a 2.8 m long, 1 mol% doped Er^{3+}:ZBLAN fiber. This double-clad fiber had a core diameter of 16 μm and a circular, double truncated cladding of 240/260 μm. The numerical apertures of the core and inner cladding were 0.12 and 0.46 respectively. Both ends of the fiber were butted against dichroic mirrors. At the pump input end, the mirror was 100% reflective at 3.5 μm while 80% and 90% transmissive at the 977 nm and 1973 nm pump wavelengths, respectively. The output dichroic was an 80% transmissive mirror at 3.5 μm.

This study presents results for the case where both pumps operate in CW modes suitable for high PRF remote sensing applications. Q-switching is simulated by repetitively switching the intra-cavity loss between high and low loss states. The switching time is modeled to be instantaneous and we show that build-up time of a pulse is in the order of microseconds. Therefore, slower switching times, such as those seen with acousto-optic type switches, would not alter the outcomes significantly.

We conducted a series of simulations to obtain a modeled Q-switched pulse train. Firstly, we performed 20 ms simulations with the power of the first (977 nm) pump set to 2 W and 4 W. This length of time is sufficient to reach a steady state population in the $^4I_{11/2}$ state (the "virtual ground state") which has a lifetime of 7.9 ms [35]. We then followed with further 20 ms simulations where the second (1973 nm) pump operated at 5.5 W (as used in our previous experiments [19]) and the Q-switch alternated between high and low loss states. The Q-switch on-time (low loss) was consistently 5 μs while the off-time (high loss) was determined by the PRF. This second simulation allowed the Q-switched pulse properties to stabilize. During this simulation, the saved data was down-sample for memory management reasons. Finally, we performed a third simulation of 500 μs duration with a high temporal resolution. This enabled us to analyze the system over the duration of a single pulse.

Simulations were conducted for PRFs ranging between 2.5 kHz and 100 kHz. The pulse duration and energy are illustrated in Fig. 11. The predicted minimum pulse duration and maximum pulse energy occur at a PRF of around 15 kHz and 25 kHz in the case when the first pump operates at 4 W and 2 W respectively . The maximum predicted peak power was 500 W which occurred when the pulse duration was 88 ns and the pulse energy was 44 μJ.

It is expected that the pulse energy increases with decreasing repetition rate for CW-pumped, repeatedly Q-switched laser, until the inverse of the upper state lifetime is reached (177 μs for the $^4F_{9/2}$ level in Er^{3+}:ZBLAN [35]). At this point, the increase plateaus. An example can be seen in the low power curve in Fig. 5 of the paper by Chang *et al.* [40]. The behavior predicted for this DWP system is different in a number of ways. Firstly, the peak energy is achieved around 20 kHz which is considerably higher than the inverse of the upper state lifetime ($\sim$5 kHz). Secondly, when the peak energy is reached, the energy of the

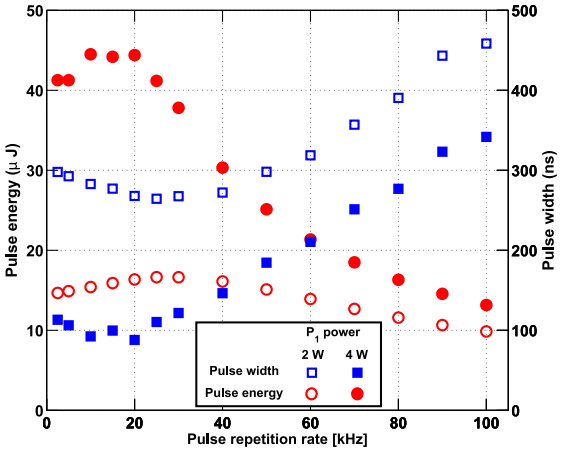

Fig. 11. Simulated pulse energy and pulse width for Q-switched operation using 2.8 m long, 1 mol% Er^{3+}:ZBLAN fiber while employing the DWP method. 2 W and 4 W of 977 nm pump and 5.5 W of 1973 nm pump powers were used. The Q-switching frequency was varied as part of the simulation.

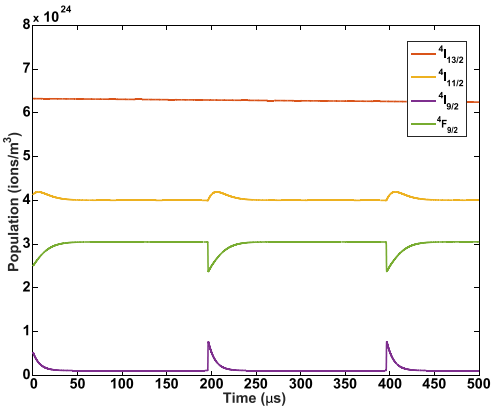

Fig. 12. The time dependent behavior of the spatially averaged population density along the fiber when pulsing at 5 kHz. The power of the 977 nm pump was set to 2 W.

pulses decline as the pulse duration is decreased. This behavior can be explained when the time dependent population of critical states is evaluated.

The time dependent population densities averaged over the fiber are plotted for the cases of 5 kHz and 25 kHz in Figs. 12 and 13 respectively. When the 5 kHz PRF is considered, it becomes apparent that the upper lasing state population saturates well before the end of the pump cycle. This can be explained by the bleaching of the second pump transition. It also means that the pulse energy can be increased by increasing the power of the 977 nm pump since this will increase the population in the $^4I_{11/2}$ level and hence increase the saturation intensity of the second pump. The reduction in pulse energy as the PRF decreases can be described by a more subtle effect. In this regime, a slightly higher time average population is maintained in the

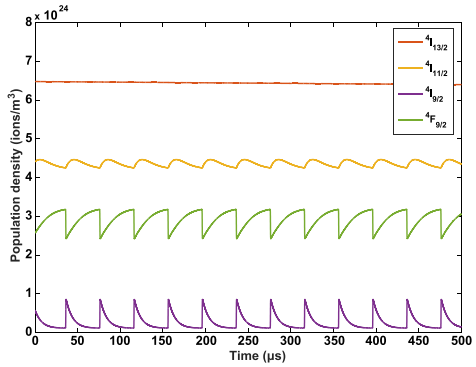

Fig. 13. The time dependent behavior of the spatially averaged population density along the fiber when pulsing at 25 kHz The power of the 977 nm pump was set to 2 W.

$^4F_{9/2}$ state for the lower repetition rate case. This means more ions can exit this state by spontaneous processes, hence leave the lasing cycle resulting in a reduced population in the $^4I_{11/2}$ state. This lowers the saturation intensity of the second pump and reduces the inversion at the time of Q-switching . This simulation demonstrates that for Q-switched operation, higher levels of the 977 nm pump are highly desirable.

V. Conclusion

In this paper we have reviewed the current state of the art in rare-earth doped mid-infrared fiber lasers with a particular emphasis on systems that utilize dual-wavelength pumping.

We have measured the excited state absorption cross section of the $^4I_{11/2} \rightarrow^4 F_{9/2}$ transition in erbium using excited state absorption spectroscopy in fibers for the first time. This transition is used when DWP is used to generate lasing emission around 3.5 μm. The data presented shows that the peak absorption of this transition is located at 1973 nm. We used the McCumber relationship to derive the stimulated emission cross section of this transition as well. Accurate knowledge of both the emission and absorption cross section of this transition are important to accurately numerically model the performance of DWP erbium lasers.

We have presented an initial investigation of the remaining steps that will be required to make these DWP lasers suitable for remote hydrocarbon sensing using DiAL. This included a comparison of the fluorescent curves of the 3.5 μm transition for fibers with differing concentrations and ZBLAN formulation. This shows the exciting possibility that it may be possible to extend the performance of the $^4F_{9/2} \rightarrow^4 I_{9/2}$ to shorter wavelength. Pulsed operation is important for lasers that are used in DiAL, hence we present a numerical investigation of a Q-Switched 3.5 μm laser. This study showed that sub 100 ns duration pulses are theoretically possible with corresponding peak powers of 500 W. This modeling also showed that high levels of 977 nm pump are more important for pulsed operation compared with CW operation to prevent bleaching of the virtual ground state that is established by the 977 nm pump.

Acknowledgement

The authors would like to thank eRSA (South Australian provider of high performance computing) for the provision of computer resources.

References

[1] B. Molocher, "Countermeasure laser development," in *Proc. Eur. Symp. Opt. Photon. Defence Security*, 2005, Paper 598902.
[2] B. M. Walsh, H. R. Lee, and N. P. Barnes, "Mid infrared lasers for remote sensing applications," *J. Lumin.*, vol. 169, pp. 400–405, 2016.
[3] S.-S. Kim *et al.*, "Potential and challenges for mid-infrared sensors in breath diagnostics," *IEEE Sensors J.*, vol. 10, no. 1, pp. 145–158, Jan. 2010.
[4] Y. Yao, A. J. Hoffman, and C. F. Gmachl, "Mid-infrared quantum cascade lasers," *Nat. Photon.*, vol. 6, no. 7, pp. 432–439, 2012.
[5] T. Kruczek *et al.*, "InAs/AlSb widely tunable external cavity quantum cascade laser around 3.2 μm," *Appl. Phys. Lett.*, vol. 102, no. 1, 2013, Art. no. 011 124.
[6] V. Fortin, M. Bernier, S. T. Bah, and R. Valle, "30 W fluoride glass all-fiber laser at 2.94 μm," *Opt. Lett.*, vol. 40, no. 12, pp. 2882–2885, 2015.
[7] S. Tokita, M. Murakami, S. Shimizu, M. Hashida, and S. Sakabe, "12 W q-switched er:zblan fiber laser at 2.8 μm," *Opt. Lett.*, vol. 36, no. 15, pp. 2812–2814, 2012.
[8] S. D. Jackson, "Towards high-power mid-infrared emission from a fibre laser," *Nature Photon.*, vol. 6, no. 7, pp. 423–431, 2012.
[9] V. Fomin, "10 kw single-mode fiber laser," in *Proc. 5th Int. Symp. High-Power Fiber Lasers Appl.*, 2010.
[10] Y. Jeong *et al.*, "Erbium:ytterbium codoped large-core fiber laser with 297-W continuous-wave output power," *IEEE J. Sel. Topics Quantum Electron.*, vol. 13, no. 3, pp. 573–578, May/Jun. 2007.
[11] T. Ehrenreich *et al.*, "1-kW, all-glass Tm:fiber laser," in *Proc. SPIE Photon. West 2010, LASE Fiber Lasers VII, Technol., Syst. Appl.*, 2010.
[12] A. Hemming, S. Bennetts, N. Simakov, J. Haub, and A. Carter, "Development of resonantly cladding-pumped holmium-doped fibre lasers," *Proc. SPIE*, vol. 8237, 2012.
[13] S. Tokita, M. Murakami, S. Shimizu, M. Hashida, and S. Sakabe, "Liquid-cooled 24 W mid-infrared Er^{3+}:zblan fiber laser," *Opt. Lett.*, vol. 34, no. 20, pp. 3062–3064, 2009.
[14] S. Crawford, D. D. Hudson, and S. D. Jackson, "High-power broadly tunable 3-μm fiber laser for the measurement of optical fiber loss," *IEEE Photon. J.*, vol. 7, no. 3, pp. 1–9, Jun. 2015.
[15] J. Li, D. Hudson, and S. Jackson, "High-power diode-pumped fiber laser operating at 3 μm," *Opt. Lett.*, vol. 36, no. 18, pp. 3642–3644, 2011.
[16] C. Carbonnier, H. Többen, and U. B. Unrau, "Room temperature CW fibre laser at 3.22 μm," *Electron. Lett.*, vol. 34, no. 9, pp. 893–894, 1998.
[17] M. R. Majewski and S. D. Jackson, "Highly efficient mid-infrared dysprosium fiber laser," *Opt. Lett.*, vol. 41, no. 10, pp. 2173–2176, 2016.
[18] V. Fortin *et al.*, "Watt-level erbium-doped all-fiber laser at 3.44 μm," *Opt. Lett.*, vol. 41, no. 3, pp. 559–562, Feb. 2016.
[19] O. Henderson-Sapir, S. D. Jackson, and D. J. Ottaway, "Versatile and widely tunable mid-infrared erbium doped ZBLAN fiber laser," *Opt. Lett.*, vol. 41, no. 7, pp. 1676–1679, Apr. 2016.
[20] H. Többen, "Room temperature CW fibre laser at 3.5 μm in Er^{3+}-doped ZBLAN glass," *Electron. Lett.*, vol. 28, no. 14, pp. 1361–1362, 1992.
[21] O. Henderson-Sapir, J. Munch, and D. J. Ottaway, "Mid-infrared fiber lasers at and beyond 3.5 μm using dual-wavelength pumping," *Opt. Lett.*, vol. 39, no. 3, pp. 493–6, Feb. 2014.
[22] J. Schneider, "Fluoride fibre laser operating at 3.9 μm," *Electron. Lett.*, vol. 31, no. 15, pp. 1250–1251, 1995.
[23] S. D. Jackson and D. G. Lancaster, *Fiber Lasers That Bridge the Shortwave to Midwave Regions of the Infrared Spectrum*, O. G. Okhotnikov, Ed. Hoboken, NJ, USA: Wiley, 2012.
[24] O. Henderson-Sapir, J. Munch, and D. J. Ottaway, "New energy-transfer upconversion process in Er^{3+}:ZBLAN mid-infrared fiber lasers," *Opt. Express*, vol. 24, no. 7, pp. 6869–6883, Apr. 2016.
[25] O. Henderson-Sapir, J. Munch, and D. J. Ottaway, "A higher power 3.5 μm fibre laser," in *Advanced Solid State Lasers*. Washington, DC, USA: Optical Society of America, 2014.
[26] O. Henderson-Sapir, "Development of dual-wavelength pumped mid-infrared fibre laser," Ph.D. dissertation, Univ. Adelaide, Adelaide, SA, Australia, 2015.

Appendix B. Modelling Fibre Lasers: Supporting Information

[27] A. Malouf, O. Henderson-Sapir, and D. J. Ottaway, "Numerical modeling of 3.5 μm dual-wavelength pumped erbium doped mid-infrared fiber lasers," *IEEE J. Quantum Electron.*, to be published.

[28] K. Tanimura, M. Shinn, W. Sibley, M. Drexhage, and R. Brown, "Optical transitions of Ho^{3+} ions in fluorozirconate glass," *Phys. Rev. B*, vol. 30, no. 5, 1984, Art. no. 2429.

[29] D. E. McCumber, "Theory of phonon-terminated optical masers," *Phys. Rev.*, vol. 134, no. 2A, pp. A299–A306, 1964.

[30] R. Caspary, "Applied rare earth spectroscopy for fiber laser optimization," Ph.D. dissertation, Tech. Univ. Braunschweig, Braunschweig, Germany, 2001.

[31] V. Fortin, F. Maes, M. Bernier, and R. Vallée, "Erbium-doped all-fiber laser operating at 3.44 μm: Experimental and numerical studies," in *Proc. CLEO, Sci. Innov.*, 2016, Paper STh1O–3.

[32] M. Pollnau, E. Heumann, and G. Huber, "Time-resolved spectra of excited-state absorption in Er^{3+} doped $YAlO_3$," *Appl. Phys. A*, vol. 54, no. 5, pp. 404–410, 1992.

[33] M. Pollnau, C. Ghisler, W. Lüthy, and H. P. Weber, "Cross sections of excited-state absorption at 800 nm in erbium-doped zblan fiber," *Appl. Phys. B*, vol. 67, no. 1, pp. 23–28, 1998.

[34] P. S. Golding, S. D. Jackson, T. A. King, and M. Pollnau, "Energy transfer processes in Er^{3+}-doped and Er^{3+}, Pr^{3+}-codoped ZBLAN glasses," *Phys. Rev. B*, vol. 62, no. 2, 2000, Art. no. 856.

[35] V. K. Bogdanov, "Energy exchange processes in erbium-doped fluoride glasses," Ph.D. dissertation, Vic. Univ. Technol., Newport, VIC, Australia, 1999.

[36] D. E. McCumber, "Einstein relations connecting broadband emission and absorption spectra," *Phys. Rev.*, vol. 136, pp. A954–A957, Nov. 1964.

[37] Y. D. Huang, M. Mortier, and F. Auzel, "Stark level analysis for Er^{3+}-doped ZBLAN glass," *Opt. Mater.*, vol. 17, no. 4, pp. 501–511, 2001.

[38] F. McClung and R. Hellwarth, "Giant optical pulsations from ruby," *J. Appl. Phys.*, vol. 33, no. 3, pp. 828–829, 1962.

[39] H. Riris *et al.*, "Airborne measurements of atmospheric methane column abundance using a pulsed integrated-path differential absorption lidar," *Appl. Opt.*, vol. 51, no. 34, pp. 8296–8305, 2012.

[40] N. Chang *et al.*, "Resonantly diode-pumped continuous-wave and q-switched er: Yag laser at 1645 nm," *Opt. Express*, vol. 18, no. 13, pp. 13673–13678, 2010.

Ori Henderson-Sapir received the B.Sc. degree in physics and mathematics from Hebrew University, Jerusalem, Israel, and the M.Eng. degree from Tel-Aviv University, Tel Aviv, Israel, where he worked on the development of electrically small antennas. He received the Ph.D. degree from the University of Adelaide, Adelaide, SA, Australia with the Lasers and Optics Group. He is currently dividing his time as an Optics and Laser Engineer at Ellex Medical and as a Research Associate at the University of Adelaide. His current research interests include mid-infrared sensing and the development of mid-infrared fiber lasers.

Andrew Malouf received the B.Sc. degree in experimental and theoretical physics from the University of Adelaide, Adelaide, SA, Australia, in 2013 and was awarded first class Honours in 2015. He is currently working toward the Ph.D. degree at the University of Adelaide with the Lasers and Optics Group.

Nathaniel Bawden received the B.Sc. degree in laser physics and technology from the University of Adelaide, Adelaide, SA, Australia, in 2015. He is currently working toward the Honours degree at the University of Adelaide with the Laser and Optics Group.

Jesper Munch received the Ph.D. degree in physics from the University of Chicago, Chicago, IL, USA, in 1975. He then worked for 17 years at TRW, Redondo Beach, CA, USA, in laser development and nonlinear optics. In 1990, he joined the University of Adelaide, Adelaide, SA, Australia, as the Chair of experimental physics and started a lasers and nonlinear optics group concentrating on the physics of lasers and their applications, including sodium guide-star lasers and gravitational wave detection, as well as diffractive and nonlinear optics.

Stuart D. Jackson received the B.Sc.(Hons.) degree from the University of Newcastle, Callaghan, NSW, Australia, in 1989. In 1990, he joined the Centre for Lasers and Applications, Macquarie University to undertake research toward the Ph.D. degree. He is currently an Associate Professor in the Department of Engineering, Macquarie University. In 1995, he joined the Laser Photonics Group, University of Manchester and initiated the research there into high-power fiber lasers. Later in 1999, he returned to Australia and joined the Optical Fiber Technology Centre, University of Sydney, where he became a Senior Research Fellow and the Technical Manager of silicate fiber fabrication. During this time, he received an Australian Research Fellowship from the Australian Research Council (ARC). In 2009, he joined the School of Physics, University of Sydney as a Queen Elizabeth II Fellow (ARC), where became the Leader of the Flagship Project "Mid-infrared photonics" within the ARC Centre of Excellence funded Centre for Ultrahigh-Bandwidth Devices for Optical Systems. In early 2014, he moved to the Department of Engineering, Macquarie University to take up a permanent position in teaching and optical and photonics engineering research.

David J. Ottaway received the Ph.D. degree from the University of Adelaide, Adelaide, SA, Australia, in 1999. His Ph.D. dissertation was on solid-state laser sources for gravitational wave detection. In 2000, he joined the LIGO Laboratory, first as a Postdoctoral Scholar at the LIGO Hanford Observatory, Richland, Washington, and later as a Staff Scientist in the Massachusetts Institute of Technology. During this period, he conducted research on commissioning the initial LIGO detectors and developing optical and mechanical systems for the advanced LIGO detectors. In 2007, he returned to the University of Adelaide, where he continues to develop laser and optical systems for advanced gravitational wave detectors and other forms of extreme remote sensing, including remote trace gas detection and atmospheric temperature studies.

Appendix C
Graphene Properties: Supporting Information

C.1 Graphene lattice

The graphene lattice is illustrated in Figure C.1 in both real space and reciprocal space. Parallel lattice planes in Figure C.1a (real space) are duplicated in Figure C.1b (reciprocal space) to illustrate the relationship between the two lattice representations. The spacing between parallel lattice planes in real space determine the spatial frequency representation of the lattice in reciprocal space. The spacing between parallel planes in the reciprocal space representation is the inverse of those in real space, multiplied by a factor of 2π.

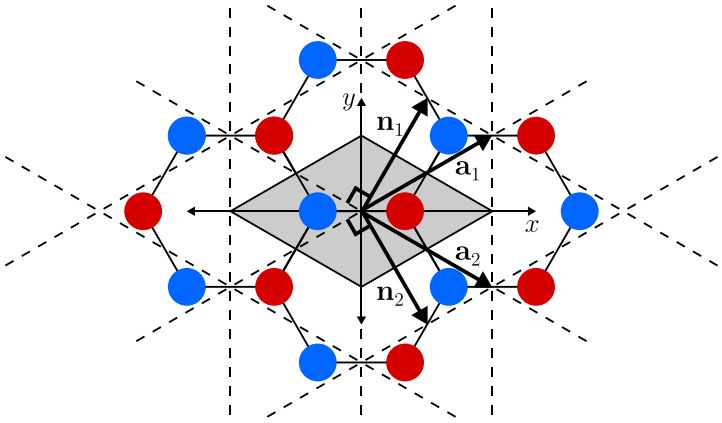

(a) Real lattice spanned by vectors $\mathbf{a}_1$ and $\mathbf{a}_2$. The vectors $\mathbf{n}_1$ and $\mathbf{n}_2$ are normal to vectors $\mathbf{a}_2$ and $\mathbf{a}_1$ respectively. The dashed lines represent parallel lattice planes.

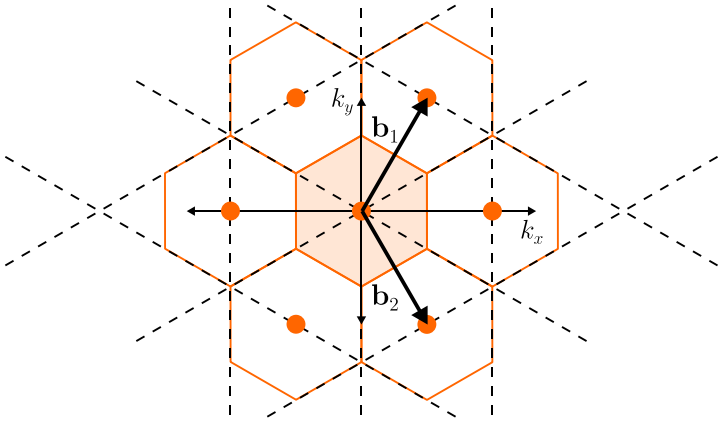

(b) Reciprocal lattice spanned by vectors $\mathbf{b}_1$ and $\mathbf{b}_2$. The lattice points are shown by filled orange circles. Each lattice point corresponds to a spatial frequency defined by a set of parallel lattice planes in real space.

Figure C.1: Graphene lattice in real and reciprocal space. The relation between the two lattice representations is illustrated by relating lattice planes in real space with lattice points in reciprocal space. Vectors $\mathbf{n}_1$ and $\mathbf{n}_2$ point in the same directions as vectors $\mathbf{b}_1$ and $\mathbf{b}_2$ respectively. The magnitudes of vectors $\mathbf{b}_1$ and $\mathbf{b}_2$ are the inverse of the $\mathbf{n}_1$ and $\mathbf{n}_2$ magnitudes respectively, multiplied by a factor of 2π.

C.2 Energy dispersion derivation

This Section presents a derivation of the energy dispersion of graphene given by Equations 4.10, 4.11, and 4.12 and illustrated in Figure 4.4. The expressions are derived using the tight binding approach to a first approximation, which assumes that π electrons may 'hop' between neighbouring atoms only.[196] The derivations presented in this Section were compiled from multiple sources available in literature.[186,192,193,195–199,201]

C.2.1 Mathematical formulation

The wave function $\psi(\mathbf{r})$ for a π electron at position $\mathbf{r}$ is a weighted sum of contributions $\psi_A(\mathbf{r})$ and $\psi_B(\mathbf{r})$ from sublattices A and B respectively. The sublattices contribute weighted sums of atomic wavefunctions $\phi_A(\mathbf{r}-\mathbf{R})$ and $\phi_B(\mathbf{r}-\mathbf{R})$ from the atoms contained in each unit cell located at lattice points $\mathbf{R}$. The lattice has N unit cells ($2N$ atoms) where N is very large.

$$\psi(\mathbf{r}) = c_A\psi_A(\mathbf{r}) + c_B\psi_B(\mathbf{r}) \tag{C.1}$$

$$\psi(\mathbf{r}) = \frac{1}{\sqrt{N}}\left[c_A\sum_{\mathbf{R}} b_A(\mathbf{R})\,\phi_A(\mathbf{r}-\mathbf{R}) + c_B\sum_{\mathbf{R}} b_B(\mathbf{R})\,\phi_B(\mathbf{r}-\mathbf{R})\right] \tag{C.2}$$

where the summations are over all lattice vectors $\mathbf{R}$. The sublattice wavefunctions ψ_A and ψ_B have coefficients c_A and c_B respectively. Each atomic wavefunction ϕ_A and ϕ_B for atoms in each unit cell located at $\mathbf{R}$ has coefficients $b_A(\mathbf{R})$ and $b_B(\mathbf{R})$ respectively.

Applying the Hamiltonian to Equation C.1 gives

$$\hat{H}\psi = E\psi \tag{C.3}$$

$$c_A\hat{H}\psi_A + c_B\hat{H}\psi_B = c_AE\psi_A + c_BE\psi_B \tag{C.4}$$

Equation C.4 may be multiplied by ψ_A^* and ψ_B^* from the left and integrated over all space to obtain the following two equations:[197]

$$c_A\langle\psi_A|\hat{H}|\psi_A\rangle + c_B\langle\psi_A|\hat{H}|\psi_B\rangle = c_AE\langle\psi_A|\psi_A\rangle + c_BE\langle\psi_A|\psi_B\rangle \tag{C.5}$$

$$c_A\langle\psi_B|\hat{H}|\psi_A\rangle + c_B\langle\psi_B|\hat{H}|\psi_B\rangle = c_AE\langle\psi_B|\psi_A\rangle + c_BE\langle\psi_B|\psi_B\rangle \tag{C.6}$$

which can be expressed in terms of a tight binding Hamiltonian matrix $\mathbf{H}$ and overlap matrix $\mathbf{S}$ as

$$\mathbf{Hc} = E\mathbf{Sc} \tag{C.7}$$

where

$$\mathbf{H} = \begin{pmatrix} \langle\psi_A|\hat{H}|\psi_A\rangle & \langle\psi_A|\hat{H}|\psi_B\rangle \\ \langle\psi_B|\hat{H}|\psi_A\rangle & \langle\psi_B|\hat{H}|\psi_B\rangle \end{pmatrix}, \quad \mathbf{c} = \begin{pmatrix} c_A \\ c_B \end{pmatrix}, \quad \mathbf{S} = \begin{pmatrix} \langle\psi_A|\psi_A\rangle & \langle\psi_A|\psi_B\rangle \\ \langle\psi_B|\psi_A\rangle & \langle\psi_B|\psi_B\rangle \end{pmatrix}.$$

This is an eigenvalue problem where the non-trivial solutions can be found by solving the characteristic (secular) equation[196]

$$\det(\mathbf{H} - E\mathbf{S}) = 0 \tag{C.8}$$

The band structure may then be determined by solving $E = E(\mathbf{k})$ for every $\mathbf{k}$.

C.2.2 Matrix elements

The matrix elements $\mathbf{H}_{mn}$ and $\mathbf{S}_{mn}$ in Equation C.8 may be derived from the periodicity of the lattice. According to Bloch's theorem,[201] the wavefunction for an electron in a periodic lattice has the form $\psi(\mathbf{r}) = e^{i\mathbf{k}\cdot\mathbf{r}}u(\mathbf{r})$ where $u(\mathbf{r}) = u(\mathbf{r}+\mathbf{R})$ is a periodic function. A translation by lattice vector $\mathbf{R}$ results in

$$\psi(\mathbf{r}+\mathbf{R}) = e^{i\mathbf{k}\cdot(\mathbf{r}+\mathbf{R})}u(\mathbf{r}+\mathbf{R}) \tag{C.9}$$
$$= e^{i\mathbf{k}\cdot\mathbf{R}}e^{i\mathbf{k}\cdot\mathbf{r}}u(\mathbf{r}) \tag{C.10}$$
$$= e^{i\mathbf{k}\cdot\mathbf{R}}\psi(\mathbf{r}) \tag{C.11}$$

Bloch's theorem can be applied to ψ_A (and similarly for ψ_B) in Equation C.2 with a translation by lattice vector $\mathbf{R}'$ as follows:

$$\psi_A(\mathbf{r}+\mathbf{R}') = e^{i\mathbf{k}\cdot\mathbf{R}'}\psi_A(\mathbf{r}) \tag{C.12}$$
$$\sum_{\mathbf{R}} b_A(\mathbf{R})\,\phi_A(\mathbf{r}-(\mathbf{R}-\mathbf{R}')) = e^{i\mathbf{k}\cdot\mathbf{R}'}\sum_{\mathbf{R}} b_A(\mathbf{R})\,\phi_A(\mathbf{r}-\mathbf{R}) \tag{C.13}$$

Letting $\mathbf{R}'' = \mathbf{R} - \mathbf{R}'$, the left side of the equation is summed over lattice vectors $\mathbf{R}''$.

$$\sum_{\mathbf{R}''} b_A(\mathbf{R}''+\mathbf{R}')\,\phi_A(\mathbf{r}-\mathbf{R}'') = e^{i\mathbf{k}\cdot\mathbf{R}'}\sum_{\mathbf{R}} b_A(\mathbf{R})\,\phi_A(\mathbf{r}-\mathbf{R}) \tag{C.14}$$

The size of the lattice is assumed to be much larger than the magnitude of the translation $\mathbf{R}'$ so that the set of all lattice vectors $\mathbf{R}''$ is equal to the set of all lattice vectors $\mathbf{R}$. Therefore, $\mathbf{R}''$ can be substituted by $\mathbf{R}$ as follows:

$$\sum_{\mathbf{R}} b_A(\mathbf{R}+\mathbf{R}')\,\phi_A(\mathbf{r}-\mathbf{R}) = e^{i\mathbf{k}\cdot\mathbf{R}'}\sum_{\mathbf{R}} b_A(\mathbf{R})\,\phi_A(\mathbf{r}-\mathbf{R}) \tag{C.15}$$
$$b_A(\mathbf{R}+\mathbf{R}') = e^{i\mathbf{k}\cdot\mathbf{R}'}b_A(\mathbf{R}) \tag{C.16}$$

Equation C.16 must be satisfied for all $\mathbf{R}$, including $\mathbf{R} = \mathbf{0}$, and $\mathbf{R} = \mathbf{R}'$. Therefore,

$$b_A(\mathbf{R}') = e^{i\mathbf{k}\cdot\mathbf{R}'}b_A(\mathbf{0}) \tag{C.17}$$
$$b_A(\mathbf{R}) = e^{i\mathbf{k}\cdot\mathbf{R}}b_A(\mathbf{0}) \tag{C.18}$$

Constants $b_A(\mathbf{0})$ and $b_B(\mathbf{0})$ can be absorbed by coefficients c_A and c_B respectively

in Equation C.2 without loss of generality. Then the revised wavefunctions become

$$\psi(\mathbf{r}) = \frac{1}{\sqrt{N}}\left[c_A \sum_{\mathbf{R}} e^{i\mathbf{k}\cdot\mathbf{R}}\phi_A(\mathbf{r}-\mathbf{R}) + c_B \sum_{\mathbf{R}} e^{i\mathbf{k}\cdot\mathbf{R}}\phi_B(\mathbf{r}-\mathbf{R})\right] \tag{C.19}$$

$$\psi_{A(B)}(\mathbf{r}) = \frac{1}{\sqrt{N}} \sum_{\mathbf{R}} e^{i\mathbf{k}\cdot\mathbf{R}}\phi_{A(B)}(\mathbf{r}-\mathbf{R}) \tag{C.20}$$

The Hamiltonian $\hat{H}$ for a π electron of mass m_e is determined by the potential $V(\mathbf{r})$ due to all nuclei and electrons of the lattice. The potential is the same in each unit cell due to the periodicity of the lattice. Therefore,

$$\hat{H} = \frac{-\hbar^2}{2m_\mathrm{e}}\nabla^2 + \sum_{\mathbf{R}} V(\mathbf{r}-\mathbf{R}) \tag{C.21}$$

$$= \frac{-\hbar^2}{2m_\mathrm{e}}\nabla^2 + \sum_{\mathbf{R}} V_0(\mathbf{r}-\mathbf{R}-\mathbf{r}_A) + \sum_{\mathbf{R}} V_0(\mathbf{r}-\mathbf{R}-\mathbf{r}_B) \tag{C.22}$$

$$= \frac{-\hbar^2}{2m_\mathrm{e}}\nabla^2 + V_0(\mathbf{r}-\mathbf{r}_A) + \sum_{\mathbf{R}\neq\mathbf{0}} V_0(\mathbf{r}-\mathbf{R}-\mathbf{r}_A) + \sum_{\mathbf{R}} V_0(\mathbf{r}-\mathbf{R}-\mathbf{r}_B) \tag{C.23}$$

$$= \hat{H}_{\mathrm{atom},A} + \Delta V_A(\mathbf{r}) \tag{C.24}$$

where $\hat{H}_{\mathrm{atom},A}$ is the Hamiltonian for an electron that belongs to a single atom from sublattice A, assumed to be isolated, and $\Delta V_A(\mathbf{r})$ is the perturbed potential due to all other atoms. Potential V_0 is the potential due to a single atom. Vectors $\mathbf{r}_A$ and $\mathbf{r}_B = -\mathbf{r}_A$ are atom locations in the unit cell $\mathbf{R} = \mathbf{0}$.

The matrix elements $\mathbf{H}_{mn}$, where indices 1 and 2 correspond to sublattices A and B respectively, are given by

$$\mathbf{H}_{mn} = \langle\psi_m|\,\hat{H}\,|\psi_n\rangle \tag{C.25}$$

$$= \frac{1}{N}\sum_{\mathbf{R}'}\sum_{\mathbf{R}} e^{i\mathbf{k}\cdot(\mathbf{R}-\mathbf{R}')}\,\langle\phi_m(\mathbf{r}-\mathbf{R}')|\,\hat{H}\,|\phi_n(\mathbf{r}-\mathbf{R})\rangle \tag{C.26}$$

$$= \frac{1}{N}\sum_{\mathbf{R}'}\sum_{\mathbf{R}} e^{i\mathbf{k}\cdot(\mathbf{R}-\mathbf{R}')}\,\langle\phi_m(\mathbf{r})|\,\hat{H}\,|\phi_n(\mathbf{r}-(\mathbf{R}-\mathbf{R}'))\rangle \tag{C.27}$$

The overlap of two functions depends on their *relative* position $\mathbf{R}'' = \mathbf{R}-\mathbf{R}'$. There are N unique relative positions, one for every lattice vector $\mathbf{R}'$ of the outer sum. Therefore, the matrix elements $\mathbf{H}_{mn}$ can be simplified to

$$\mathbf{H}_{mn} = \sum_{\mathbf{R}} e^{i\mathbf{k}\cdot\mathbf{R}}\,\langle\phi_m(\mathbf{r})|\,\hat{H}\,|\phi_n(\mathbf{r}-\mathbf{R})\rangle \tag{C.28}$$

and the Hamiltonian matrix $\mathbf{H}$ may be written as

$$\mathbf{H} = \sum_{\mathbf{R}} e^{i\mathbf{k}\cdot\mathbf{R}} \begin{pmatrix} \langle \phi_A(\mathbf{r})| \hat{H} |\phi_A(\mathbf{r}-\mathbf{R})\rangle & \langle \phi_A(\mathbf{r})| \hat{H} |\phi_B(\mathbf{r}-\mathbf{R})\rangle \\ \langle \phi_B(\mathbf{r})| \hat{H} |\phi_A(\mathbf{r}-\mathbf{R})\rangle & \langle \phi_B(\mathbf{r})| \hat{H} |\phi_B(\mathbf{r}-\mathbf{R})\rangle \end{pmatrix} \tag{C.29}$$

Similarly, the matrix elements $\mathbf{S}_{mn}$ are given by

$$\mathbf{S}_{mn} = \sum_{\mathbf{R}} e^{i\mathbf{k}\cdot\mathbf{R}} \langle \phi_m(\mathbf{r})|\phi_n(\mathbf{r}-\mathbf{R})\rangle \tag{C.30}$$

and the overlap matrix $\mathbf{S}$ may be written as

$$\mathbf{S} = \sum_{\mathbf{R}} e^{i\mathbf{k}\cdot\mathbf{R}} \begin{pmatrix} \langle \phi_A(\mathbf{r})|\phi_A(\mathbf{r}-\mathbf{R})\rangle & \langle \phi_A(\mathbf{r})|\phi_B(\mathbf{r}-\mathbf{R})\rangle \\ \langle \phi_B(\mathbf{r})|\phi_A(\mathbf{r}-\mathbf{R})\rangle & \langle \phi_B(\mathbf{r})|\phi_B(\mathbf{r}-\mathbf{R})\rangle \end{pmatrix} \tag{C.31}$$

C.2.3 Energy dispersion

To a first approximation, the tight binding approach is calculated with nearest neighbour hopping only. Each atom has three nearest neighbours only, each from the alternate sublattice. The overlap of nearest neighbour wavefunctions is assumed to be zero while the overlap of a wavefunction with itself is one.[199] Then the overlap matrix $\mathbf{S}$ is the identity matrix.

$$\mathbf{S} = \begin{pmatrix} 1 & 0 \\ 0 & 1 \end{pmatrix} \tag{C.32}$$

The Hamiltonian matrix elements $\mathbf{H}_{AA} = \mathbf{H}_{BB} = E_0$ are determined for the case $\mathbf{R} = \mathbf{0}$ only. They represent the onsite energy E_0 of the π electron and must be equal due to reflection symmetry of the honeycomb structure. Note that E_0 is not simply the atomic energy of an isolated atom because the Hamiltonian includes a perturbed potential ΔV.

The Hamiltonian matrix elements $\mathbf{H}_{AB}$ and $\mathbf{H}_{BA}$ are determined by the lattice vectors that connect the unit cells of nearest neighbours. From Figure 4.2, the lattice vectors of nearest neighbour unit cells to sublattice A atoms are $\mathbf{0}$, $-\mathbf{a}_1$, and $-\mathbf{a}_2$. Similarly, the lattice vectors of nearest neighbour unit cells to sublattice B atoms are $\mathbf{0}$, $\mathbf{a}_1$, and $\mathbf{a}_2$. The atomic wavefunctions ϕ_A and ϕ_B have reflective symmetry with respect to each other and 120° rotational symmetry. Therefore, the hopping integrals $\gamma = \langle \phi_m(\mathbf{r})| \hat{H} |\phi_n(\mathbf{r}-\mathbf{R})\rangle$ between nearest neighbours ($m \neq n$) must be equal for

matrix elements $\mathbf{H}_{AB}$ and $\mathbf{H}_{BA}$.

$$\mathbf{H} = \begin{pmatrix} E_0 & \gamma\left(1 + e^{-i\mathbf{k}\cdot\mathbf{a}_1} + e^{-i\mathbf{k}\cdot\mathbf{a}_2}\right) \\ \gamma\left(1 + e^{i\mathbf{k}\cdot\mathbf{a}_1} + e^{i\mathbf{k}\cdot\mathbf{a}_2}\right) & E_0 \end{pmatrix} \tag{C.33}$$

The energy dispersion $E(\mathbf{k})$ can now be solved using Equations C.8, C.32, C.33, and the primitive translation vectors of the real lattice given in Equation 4.2.

$$(E_0 - E)^2 = \gamma^2\left(1 + e^{-i\mathbf{k}\cdot\mathbf{a}_1} + e^{-i\mathbf{k}\cdot\mathbf{a}_2}\right)\left(1 + e^{i\mathbf{k}\cdot\mathbf{a}_1} + e^{i\mathbf{k}\cdot\mathbf{a}_2}\right) \tag{C.34}$$

$$= \gamma^2\left[3 + 2\cos\left(\mathbf{k}\cdot\mathbf{a}_1\right) + 2\cos\left(\mathbf{k}\cdot\mathbf{a}_2\right) + 2\cos\left(\mathbf{k}\cdot\left(\mathbf{a}_1 - \mathbf{a}_2\right)\right)\right] \tag{C.35}$$

$$= \gamma^2\left[1 + 4\cos\left(\frac{\sqrt{3}a}{2}k_x\right)\cos\left(\frac{a}{2}k_y\right) + 4\cos^2\left(\frac{a}{2}k_y\right)\right] \tag{C.36}$$

$$E(\mathbf{k}) = E_0 \pm \gamma\sqrt{1 + 4\cos\left(\frac{\sqrt{3}a}{2}k_x\right)\cos\left(\frac{a}{2}k_y\right) + 4\cos^2\left(\frac{a}{2}k_y\right)} \tag{C.37}$$

C.2.4 Low energy dispersion

The low energy dispersion E_K and $E_{K'}$ in the vicinity of the K and K' points can be simplified by expanding Equation C.33 to first order around the K and K' points. This is done be letting $\mathbf{k} = K + \mathbf{q}$ where $|\mathbf{q}| \ll |K| = 4\pi/3a \sim 1/a$ and expanding to first order in $|\mathbf{q}|a \ll 1$ such that $e^{iqa} = 1 + iqa$.

For example, consider the first K point given in Equation 4.8. From Equation C.33, the Hamiltonian $\mathbf{H}$ around the K point may be written as

$$\mathbf{H} = \begin{pmatrix} E_0 & \gamma\left(1 + e^{-i(K+\mathbf{q})\cdot\mathbf{a}_1} + e^{-i(K+\mathbf{q})\cdot\mathbf{a}_2}\right) \\ \gamma\left(1 + e^{i(K+\mathbf{q})\cdot\mathbf{a}_1} + e^{i(K+\mathbf{q})\cdot\mathbf{a}_2}\right) & E_0 \end{pmatrix} \tag{C.38}$$

where dot products of K with the primitive translation vectors are:

$$K\cdot\mathbf{a}_1 = \left(\frac{2\pi}{\sqrt{3}a}, \frac{2\pi}{3a}\right)\cdot\left(\frac{\sqrt{3}a}{2}, \frac{a}{2}\right) = \frac{4\pi}{3} \tag{C.39}$$

$$K\cdot\mathbf{a}_2 = \left(\frac{2\pi}{\sqrt{3}a}, \frac{2\pi}{3a}\right)\cdot\left(\frac{\sqrt{3}a}{2}, -\frac{a}{2}\right) = \frac{2\pi}{3} \tag{C.40}$$

The matrix element $\mathbf{H}_{AB}$ around the K point may be expanded and simplified as

follows:

$$\mathbf{H}_{AB} = \gamma \left[1 + (1 - i\mathbf{q}\cdot\mathbf{a}_1)\, e^{-i\frac{4\pi}{3}} + (1 - i\mathbf{q}\cdot\mathbf{a}_2)\, e^{-i\frac{2\pi}{3}}\right] \tag{C.41}$$

$$= \gamma \left\{1 - \left[1 - i\frac{a}{2}\left(\sqrt{3}q_x + q_y\right)\right]\left(\frac{1}{2} - i\frac{\sqrt{3}}{2}\right) - \left[1 - i\frac{a}{2}\left(\sqrt{3}q_x - q_y\right)\right]\left(\frac{1}{2} + i\frac{\sqrt{3}}{2}\right)\right\} \tag{C.42}$$

$$= \gamma \left(i\frac{\sqrt{3}a}{2}q_x - \frac{\sqrt{3}a}{2}q_y\right) \tag{C.43}$$

$$= \frac{\sqrt{3}a}{2}\gamma\left(iq_x - q_y\right) \tag{C.44}$$

Similarly, the matrix element $\mathbf{H}_{BA}$ around the K point is

$$\mathbf{H}_{BA} = \mathbf{H}^*_{AB} = -\frac{\sqrt{3}a}{2}\gamma\left(iq_x + q_y\right) \tag{C.45}$$

and the Hamiltonian matrix $\mathbf{H}_K$ around the K point is reduced to

$$\mathbf{H}_K = \begin{pmatrix} E_0 & \frac{\sqrt{3}a}{2}\gamma\left(iq_x - q_y\right) \\ -\frac{\sqrt{3}a}{2}\gamma\left(iq_x + q_y\right) & E_0 \end{pmatrix} \tag{C.46}$$

The characteristic Equation C.8 can now be solved for the low energy dispersion E_K near K.

$$\left(E_0 - E_K\right)^2 = -\frac{3a^2}{4}\gamma^2\left(iq_x - q_y\right)\left(iq_x + q_y\right) \tag{C.47}$$

$$= -\frac{3a^2}{4}\gamma^2\left(-q_x^2 - q_y^2\right) \tag{C.48}$$

$$= \frac{3a^2}{4}\gamma^2\left(q_x^2 + q_y^2\right) \tag{C.49}$$

$$E_K - E_0 = \pm\frac{\sqrt{3}a}{2}\gamma\sqrt{q_x^2 + q_y^2} \tag{C.50}$$

$$= \pm\frac{\sqrt{3}a}{2}\gamma\left|\mathbf{q}\right| \tag{C.51}$$

$$= \pm\frac{\sqrt{3}a}{2}\gamma\left|\mathbf{k} - K\right| \tag{C.52}$$

The low energy dispersion $E_{K'}$ in the vicinity of K' is solved using the same approach

taken to solve for E_K and the low energy dispersion may be summarised as follows:

$$E_K - E_0 = \pm\hbar v_\mathrm{F}|\mathbf{k} - K|, \quad |\mathbf{k} - K|a \ll 1 \tag{C.53}$$

$$E_{K'} - E_0 = \pm\hbar v_\mathrm{F}|\mathbf{k} - K'|, \quad |\mathbf{k} - K'|a \ll 1 \tag{C.54}$$

where $v_\mathrm{F} = \sqrt{3}a\gamma/2\hbar \approx 10^6\,\mathrm{m\,s^{-1}} \approx c/300$ is the Fermi velocity.[186]

C.3 Saturable absorption equation

The transmission of light through graphene can be described by the saturable absorption of a two energy level system. Consider radiation with photon energy $E_\mathrm{ph} = h\nu$ propagating through a material that has two energy levels, E_1 and E_2, such that $E_2 - E_1 = h\nu$. The energy levels E_1 and E_2 have population densities N_1 and N_2 respectively. The possible interactions between photons and atoms are:

i. Photon absorption with cross section σ_{12};

ii. Stimulated emission with cross section σ_{21};

iii. Non-radiative decay at a rate determined by the lifetime τ of the excited state level 2.

From the Einstein relations for the absorption and emission cross sections between two levels of equal degeneracies, $\sigma_{12} = \sigma_{21} = \sigma$ (Siegman[169] pp. 208 and 287).

The photon flux Φ at distance z into the material is given by

$$\frac{\mathrm{d}\Phi}{\mathrm{d}z} = -\sigma N_1\Phi + \sigma N_2\Phi \tag{C.55}$$

$$= -\sigma\left(N_1 - N_2\right)\Phi \tag{C.56}$$

$$= -\sigma\Delta N\Phi \tag{C.57}$$

$$\Phi = \Phi_\mathrm{i}\exp\left(-\sigma\Delta N z\right) \tag{C.58}$$

where Φ_i is the incident photon flux and the population densities (N_1, N_2, and $\Delta N = N_1 - N_2$), as well as the photon flux Φ, are dependent on the depth z into the material and time t.

In a 2D material such as graphene, it is meaningless to describe Φ and ΔN as functions of distance z into the material. It is more appropriate to describe population densities in 2D units of $\mathrm{m^{-2}}$ (rather than $\mathrm{m^{-3}}$) and treat distance z as unity to represent a single 2D layer of graphene. The transmitted flux Φ_t through a single layer of

graphene may be written as

$$\Phi_{\mathrm{t}} = \Phi_{\mathrm{i}} \exp\left(-\sigma \Delta N\right) \tag{C.59}$$

and, therefore, the transmission T through single layer graphene may be written as

$$T = \frac{\Phi_{\mathrm{t}}}{\Phi_{\mathrm{i}}} = \exp\left(-\sigma \Delta N\right) \tag{C.60}$$

The rate equations of this two-level system are

$$\frac{\mathrm{d}N_1}{\mathrm{d}t} = -\sigma \Phi N_1 + \sigma \Phi N_2 + \frac{N_2}{\tau} \tag{C.61}$$

$$= -\sigma \Phi \Delta N + \frac{N_2}{\tau} \tag{C.62}$$

$$\frac{\mathrm{d}N_2}{\mathrm{d}t} = \sigma \Phi N_1 - \sigma \Phi N_2 - \frac{N_2}{\tau} \tag{C.63}$$

$$= \sigma \Phi \Delta N - \frac{N_2}{\tau} \tag{C.64}$$

In steady state, $\frac{\mathrm{d}N_1}{\mathrm{d}t} = \frac{\mathrm{d}N_2}{\mathrm{d}t} = 0$ and

$$\sigma \Phi \Delta N = \frac{N_2}{\tau} \tag{C.65}$$

$$= \frac{N - \Delta N}{2\tau} \tag{C.66}$$

$$\Delta N\left(\Phi\right) = \frac{N}{1 + 2\sigma\tau\Phi} \tag{C.67}$$

$$\Delta N\left(I\right) = \frac{N}{1 + \frac{2\sigma\tau I}{h\nu}} \tag{C.68}$$

where $I = h\nu\Phi$ is the radiation intensity (units $\mathrm{W\,m^{-2}}$).

From Equations C.60 and C.68, the intensity dependent transmission $T\left(I\right)$ in steady state is given by

$$T\left(I\right) = \exp\left(-\frac{\sigma N}{1 + \frac{2\sigma\tau I}{h\nu}}\right) \tag{C.69}$$

$$= \exp\left(-\frac{\alpha_0}{1 + \frac{I}{I_{\mathrm{s}}}}\right) \tag{C.70}$$

where $\alpha_0 = \sigma N$ is the modulation depth parameter and $I_{\mathrm{s}} = \frac{h\nu}{2\sigma\tau}$ is the saturation intensity, i.e., the intensity required to reduce the saturable absorption coefficient to half of its unbleached value.

Equation C.70 describes saturable absorption. As intensity I increases to values

well above the saturation intensity I_s, the absorption decreases and the absorption *saturates*. The modulation depth parameter α_0 is the absorption coefficient at low intensity (more precisely, in the limit $I \to 0$) and determines the range in transmission between low and high intensity regimes.

In practice, a saturable absorber will normally have some non-saturable loss α_{ns} also.[222,231] Therefore, the transmission through graphene is more completely described as follows:

$$T = \exp(-\alpha) \tag{C.71}$$

$$= \exp[-(\alpha_s + \alpha_{ns})] \tag{C.72}$$

$$T(I) = \exp\left[-\left(\frac{\alpha_0}{1+\frac{I}{I_s}} + \alpha_{ns}\right)\right] \tag{C.73}$$

where the total loss coefficient $\alpha(I)$ is given by

$$\alpha(I) = \frac{\alpha_0}{1+\frac{I}{I_s}} + \alpha_{ns} \tag{C.74}$$

There are some limitations in the two energy level model presented to describe saturable absorption. The radiation intensity I of a laser is not uniform in the transverse plane and, therefore, Equation C.73 is limited to describing the transmission through some point rather than the entire beam area. Another limitation of the simple derivation arises from the assumption that the system reaches a steady state. In the ultrashort pulse regime, the system may not reach steady state and a pulse may need to be described with a time dependent Gaussian profile. Furthermore, graphene has two (not one) lifetime constants, due to intraband and interband relaxations.

Appendix D
Graphene Experiment: Supporting Information

D.1 OPA components

The components of the OPA femtosecond tunable laser source, described in Section 5.5 and used throughout all z-scan measurements of transmission through graphene, are summarised in Table D.1.

Table D.1: OPA femtosecond laser system components and optical density required for protective eyewear.

Component	Manufacturer	Wavelength	Average power	Pulse duration	Rep rate	Pulse energy	Beam size	OD[1] required
Millennia (pump)	Spectra-Physics	532 nm	10 W	CW	–	–	2.3 mm	3.7
Tsunami (oscillator)	Spectra-Physics	700 nm – 1000 nm	2.1 W @ 800 nm	100 fs	80 MHz	26 nJ	2 mm	3.1
Empower (pump)	Spectra-Physics	527 nm	20 W	20 ns	1 kHz	20 mJ	3 mm	5.6
Spitfire Pro XP	Spectra-Physics	800 nm	4.2 W	100 fs	1 kHz	4.2 mJ	7 mm	5.4
TOPAS-C 800 fs	Light Conversion	280 nm – 10 µm	>250 mW @1350 nm	100 fs	1 kHz	>250 µJ	<8 mm	5.6

[1] Calculated by LAZAN Quick Calc v.1.1, Rockwell Laser Industries, Cincinnati, OH.

D.2 Characterisation of optical filters

D.2.1 Spectrogon neutral density IR filters

This Section presents a brief analysis of a set of neutral density IR filters, manufactured by Spectrogon, designed for the 2 µm – 16 µm spectral region. These filters were considered for use in attenuating the beam because they were designed for the spectral range used for transmission measurements. However, these filters caused the 3.5 µm beam path to deviate and, therefore, were not suitable for use in this experiment. The beam deviation was not measured using other wavelength bands. The beam deviations may have been caused by a slight wedge in each filter. According to manufacturer specifications, the filters were 1.0 ± 0.2 mm thick. FTIR spectra of these filters and 3.5 µm beam deviation measurements are presented in Figure D.1 and Table D.2 respectively for completeness.

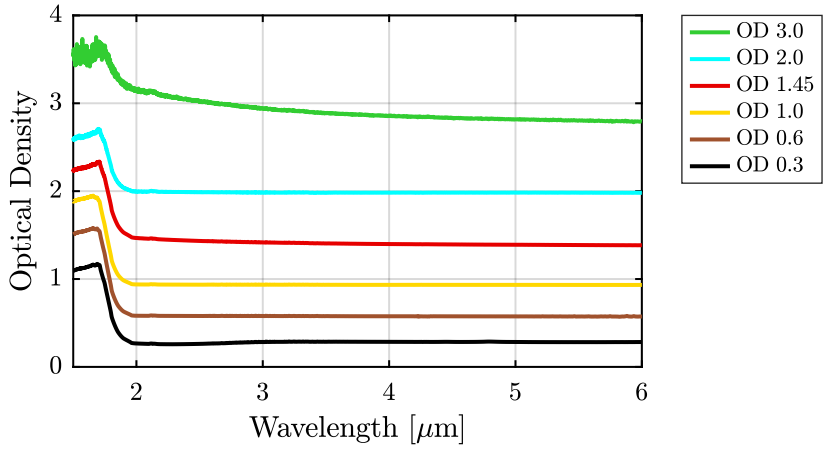

Figure D.1: FTIR spectra of Spectrogon neutral density IR filters.

Optical density spectra presented in Figure D.1 show that these 1 mm thick Ge filters were effective in attenuating the beam, according to the optical densities indicated by the manufacturer, in the spectral range from 2.0 µm to beyond 6.0 µm.

Table D.2 lists the filters and the beam path deviations measured using 3.5 µm light. An iris was mounted on a XY translation stage and aligned to the unfiltered 3.5 µm beam. Each filter was mounted perpendicular to the beam path on a rotation stage placed 1 m before the iris. The filters were rotated about their optical axis and the transmitted light at the iris location was observed to rotate about the iris aperture. The deviation of the beam path was measured by translating the iris to the centre of the beam and measuring the translation. The beam centre location was determined by the position where the maximum power was transmitted through the iris.

Table D.2: Beam path deviation through a set of Spectrogon neutral density IR filters. The angles of deviation were measured using 3.5 µm light emitted by the OPA femtosecond tunable laser source.

OD	Colour code	Deviation [mrad]
3.00	Light Green	1.05
2.00	Cyan	1.55
1.45	Red	1.50
1.00	Yellow	2.20
0.60	Brown	0.00
0.30	Black	2.55

D.2.2 Thorlabs neutral density UV filters

Thorlabs UV fused silica reflective ND filters were used to attenuate the beam throughout all z-scans, even though the specified spectral range of these filters was between 200 nm and 1200 nm. Unlike the Spectrogon ND IR filters, the Thorlabs ND UV filters did not deviate the beam path. The optical density spectra of these mounted filters were measured in the spectral region between 1500 nm and 6000 nm to determine their OD within the spectral region considered for z-scan transmission measurements. The FTIR spectra were measured using a PerkinElmer FT-IR Spectrum Two spectrometer and are presented in Figure D.2. The spectra shows that the filters were suitable for radiation wavelengths between 1500 nm and 4600 nm. However, caution was required in the spectral region between 2600 nm and 2900 nm where all spectra showed a sharp peak in OD.

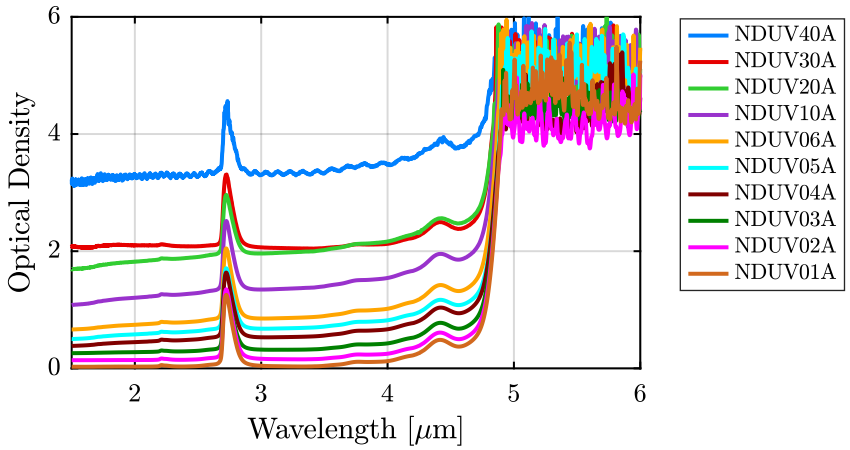

Figure D.2: Absorbance spectra of Thorlabs neutral density UV filters in the spectral region between 1.5 µm and 6.0 µm. The measurements were performed using a PerkinElmer FT-IR Spectrum Two spectrometer. The absorption feature near 2.8 µm was not observed by direct measurement using the OPA femtosecond laser source.

The optical density peak near 2800 nm in the FTIR spectra presented in Figure D.2

did not match observations made in the experimental setup when the OPA femtosecond laser source radiation wavelength was set to 2800 nm. Therefore, the optical density of each filter was measured directly using the OPA femtosecond laser source and the z-scan detection system illustrated in Figure 5.1a in each wavelength band used in z-scan measurements.

D.3 Transmission measurements

The beam intensities for each z-scan transmission measurement through graphene are illustrated in Figure D.3 as functions of sample position z. The beam intensities were calculated using the beam propagation function in Equation 5.2 and beam profile measurements described in Section 5.7. The beam intensities of each z-scan span four orders of magnitude over the z-scan range.

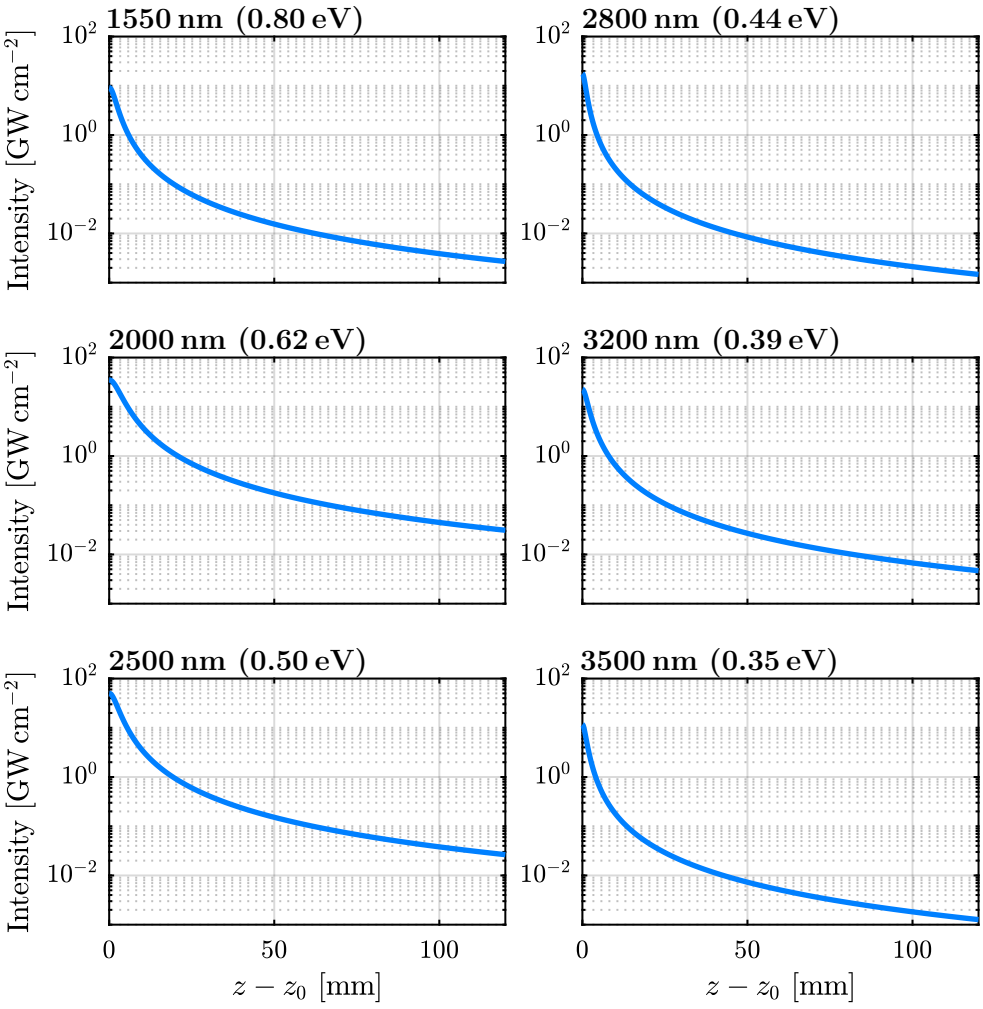

Figure D.3: Beam intensity as function of position z during measurement of transmission through graphene.

D.3.1 Transmission through calcium fluoride only

The transmission through a CaF_2 window (Thorlabs WG51050) was measured in each wavelength band, using the z-scan technique, to rule out any nonlinear effects in the substrate. The measured pulse integrals of the reference and signal beams are illustrated in Figure D.4 while the calculated transmission data are illustrated in Figure D.5. No intensity dependence on transmission was observed.

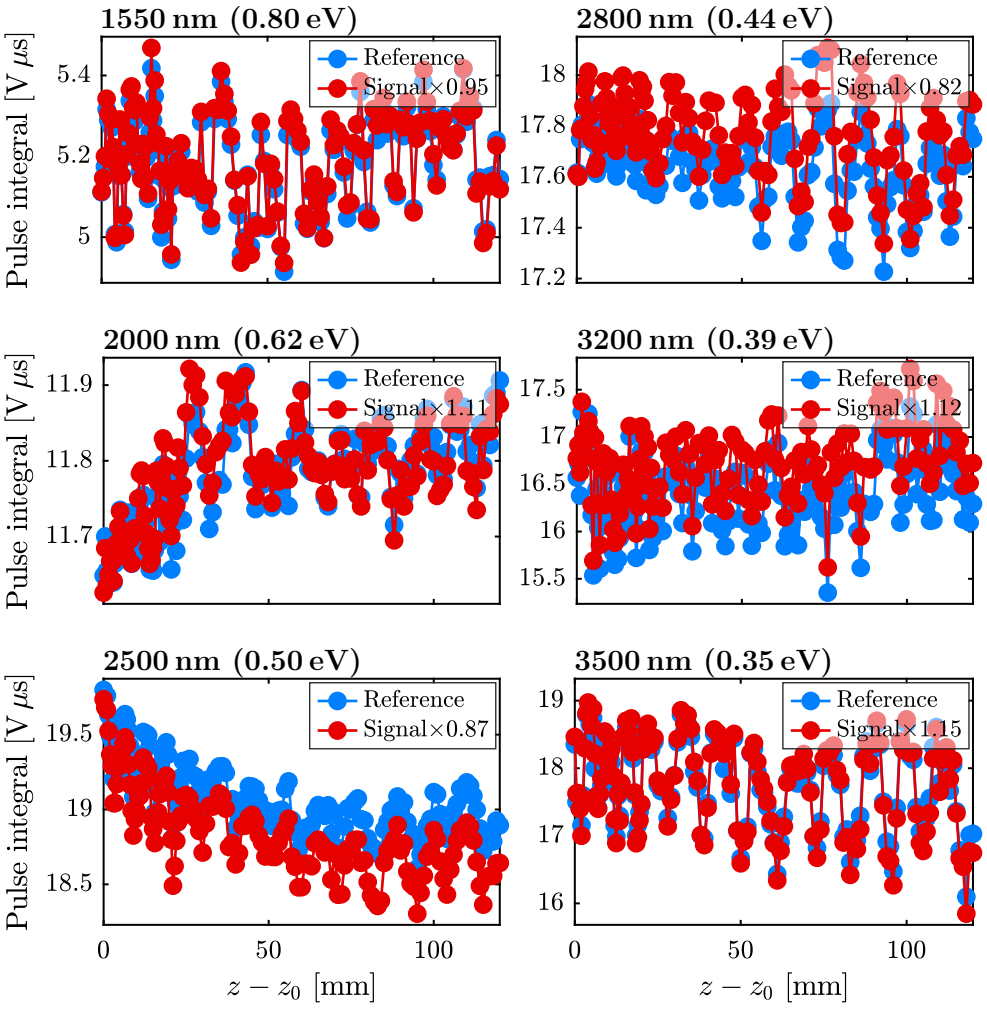

Figure D.4: Pulse integrals for transmission through CaF_2 window. The signal was multiplied by a factor that equates the signal with the reference at $z - z_0 = 0$ for easier comparison between the reference and signal data. The periodic structure in the data matched the cycle of the air conditioner in the laser lab and was an unavoidable noise source.

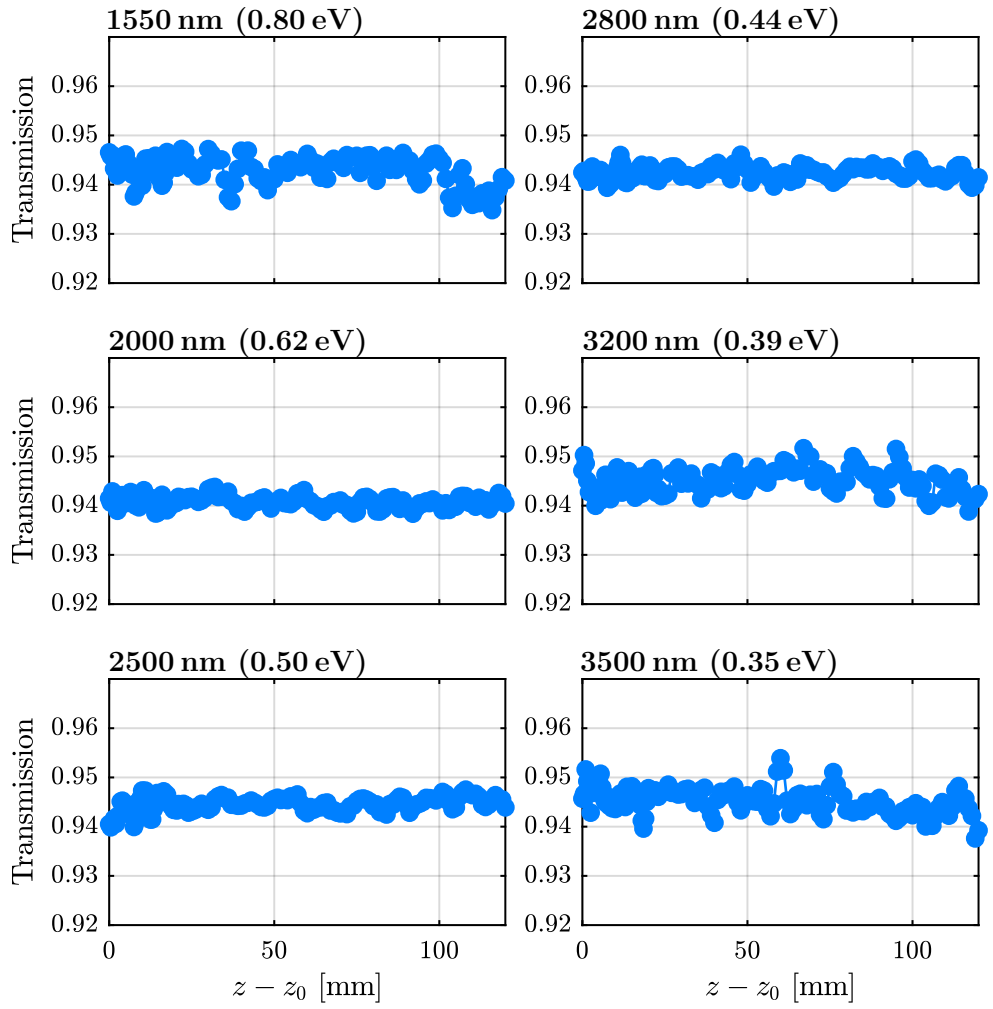

Figure D.5: Z-scan transmission through a CaF_2 window. The transmission was calculated from the integrated pulses illustrated in Figure D.4. No intensity dependence on transmission was observed.

Bibliography

[1] T. H. Maiman. Stimulated optical radiation in ruby. *Nature*, 187:493–494, 1960.

[2] International Organization for Standardization. Optics and photonics - Spectral bands. International standard; ISO 20473, International Organization for Standardization (ISO), Geneva, Switzerland, Apr 2007.

[3] A. Schliesser, N. Picqué, and T. W. Hänsch. Mid-infrared frequency combs. *Nat. Photonics*, 6(7):440–449, 2012. ISSN 1749-4885.

[4] N. Picqué and T. W. Hänsch. Frequency comb spectroscopy. *Nat. Photonics*, 13 (3):146–157, 2019.

[5] C. N. Banwell. *Fundamentals of molecular spectroscopy*. McGraw-Hill, London New York, third edition, 1983. ISBN 007084139X.

[6] S. S. Zumdahl, S. A. Zumdahl, and D. J. DeCoste. *Chemistry*. Cengage, Boston, MA, 2017. ISBN 9781305957404.

[7] Robert S. Mulliken. Report on notation for the spectra of polyatomic molecules. *J. Chem. Phys.*, 23(11):1997–2011, 1955.

[8] D. Jung, S. Bank, M. L. Lee, and D. Wasserman. Next-generation mid-infrared sources. *J. Opt.*, 19(12):123001, 2017.

[9] I. E. Gordon, L. S. Rothman, C. Hill, R. V. Kochanov, Y. Tan, P. F. Bernath, M. Birk, V. Boudon, A. Campargue, K. V. Chance, B. J. Drouin, J.-M. Flaud, R. R. Gamache, J. T. Hodges, D. Jacquemart, V. I. Perevalov, A. Perrin, K. P. Shine, M.-A. H. Smith, J. Tennyson, G. C. Toon, H. Tran, V. G. Tyuterev, A. Barbe, A. G. Császár, V. M. Devi, T. Furtenbacher, J. J. Harrison, J.-M. Hartmann, A. Jolly, T. J. Johnson, T. Karman, I. Kleiner, A. A. Kyuberis, J. Loos, O. M. Lyulin, S. T. Massie, S. N. Mikhailenko, N. Moazzen-Ahmadi, H. S. P. Müller, O. V. Naumenko, A. V. Nikitin, O. L. Polyansky, M. Rey, M. Rotger, S. W. Sharpe, K. Sung, E. Starikova, S. A. Tashkun, J. Vander Auwera, G. Wagner, J. Wilzewski, P. Wcisło, S. Yu, and E. J. Zak. The HITRAN2016 molecular spectroscopic database. *J. Quant. Spectrosc. Radiat. Transfer*, 203:3–69, 2017. ISSN 0022-4073. HITRAN2016 Special Issue.

[10] B. I. Vasil'ev and O. Mannoun. IR differential-absorption lidars for ecological monitoring of the environment. *Quantum Electron.*, 36(9):801–820, 2006.

[11] R. M. Schotland. Errors in the lidar measurement of atmospheric gases by differential absorption. *J. Appl. Meteorol. (1962-1982)*, 13(1):71–77, 1974. ISSN 00218952, 2163534X.

[12] P. F. Ambrico, A. Amodeo, P. Di Girolamo, and N. Spinelli. Sensitivity analysis of differential absorption lidar measurements in the mid-infrared region. *Appl. Opt.*, 39(36):6847–6865, 2000.

[13] S. M. Pershin, A. F. Bunkin, V. A. Lukyanchenko, and R. R. Nigmatullin. Detection of the OH band fine structure in liquid water by means of new treatment procedure based on the statistics of the fractional moments. *Laser Phys. Lett.*, 4 (11):809–813, 2007. ISSN 1612-202X.

[14] V. A. Serebryakov, É. V. Boĭko, N. N. Petrishchev, and A. V. Yan. Medical applications of mid-IR lasers. Problems and prospects. *J. Opt. Technol.*, 77(1): 6–17, 2010.

[15] S. Amini-Nik, D. Kraemer, M. L. Cowan, K. Gunaratne, P. Nadesan, B. A. Alman, and R. J. D. Miller. Ultrafast mid-IR laser scalpel: Protein signals of the fundamental limits to minimally invasive surgery. *PLoS One*, 5(9):1–6, 2010.

[16] L. Ren, W. D. Robertson, R. Reimer, C. Heinze, C. Schneider, D. Eggert, P. Truschow, N.-O. Hansen, P. Kroetz, J. Zou, and R. J. D. Miller. Towards instantaneous cellular level bio diagnosis: laser extraction and imaging of biological entities with conserved integrity and activity. *Nanotechnology*, 26(28):284001, 2015.

[17] R. Gottardi. Towards a minimally invasive sampling tool for high resolution tissue analytical mapping. *Nanotechnology*, 26(37):372501, 2015.

[18] A. B. Seddon. Mid-infrared (IR) – A hot topic: The potential for using mid-IR light for non-invasive early detection of skin cancer *in vivo*. *Phys. Status Solidi B*, 250(5):1020–1027, 2013. ISSN 1521-3951.

[19] K. C. Cossel, E. M. Waxman, I. A. Finneran, G. A. Blake, J. Ye, and N. R. Newbury. Gas-phase broadband spectroscopy using active sources: Progress, status, and applications. *J. Opt. Soc. Am. B*, 34(1):104–129, 2017.

[20] W. Cao and Y. Duan. Current status of methods and techniques for breath analysis. *Crit. Rev. Anal. Chem.*, 37(1):3–13, 2007.

[21] T. Hibbard and A. J. Killard. Breath ammonia analysis: Clinical application and measurement. *Crit. Rev. Anal. Chem.*, 41(1):21–35, 2011.

[22] V. Saasa, T. Malwela, M. Beukes, M. Mokgotho, C.-P. Liu, and B. Mwakikunga. Sensing technologies for detection of acetone in human breath for diabetes diagnosis and monitoring. *Diagnostics*, 8(1), 2018. ISSN 2075-4418.

[23] K. K. Chow, M. Short, and H. Zeng. A comparison of spectroscopic techniques for human breath analysis. *Biomed. Spectrosc. Imaging*, 1(4):339–353, 2012. ISSN 22128794.

[24] A. Sijan. Development of military lasers for optical countermeasures in the mid-IR. In D. H. Titterton and M. A. Richardson, editors, *Technologies for Optical Countermeasures VI*, volume 7483, pages 32–45. International Society for Optics and Photonics, SPIE, 2009.

[25] B. Molocher. Countermeasure laser development. In *European Symposium on Optics and Photonics for Defence and Security*, volume 5989, page 598902. International Society for Optics and Photonics, 2005.

[26] E. Lippert, S. Nicolas, G. Arisholm, K. Stenersen, A. S. Villanger, and G. Rustad. High-power fiber-laser-pumped mid-infrared laser sources. In D. H. Titterton, editor, *Technologies for Optical Countermeasures III*, volume 6397, pages 23–29. International Society for Optics and Photonics, SPIE, 2006.

[27] C. Bauer, A. K. Sharma, U. Willer, J. Burgmeier, B. Braunschweig, W. Schade, S. Blaser, L. Hvozdara, A. Müller, and G. Holl. Potentials and limits of mid-infrared laser spectroscopy for the detection of explosives. *Appl. Phys. B*, 92(3): 327–333, 2008. ISSN 1432-0649.

[28] C. J. Breshike, C. A. Kendziora, R. Furstenberg, V. Nguyen, A. Kusterbeck, and R. A. McGill. Using infrared backscatter imaging spectroscopy to detect trace explosives at standoff distances. In J. A. Guicheteau, A. W. Fountain III, and C. R. Howle, editors, *Chemical, Biological, Radiological, Nuclear, and Explosives (CBRNE) Sensing XIX*, volume 10629, pages 64–70. International Society for Optics and Photonics, SPIE, 2018.

[29] B. M. Walsh, H. R. Lee, and N. P. Barnes. Mid infrared lasers for remote sensing applications. *J. Lumin.*, 169, Part B:400–405, 2016. ISSN 0022-2313. The 17th International Conference on Luminescence and Optical Spectroscopy of Condensed Matter (ICL'14).

[30] L. Isaenko, A. Yelisseyev, A. Tkachuk, and S. Ivanova. New monocrystals with low phonon energy for mid-IR lasers. In M. Ebrahim-Zadeh and I. T. Sorokina, editors, *Mid-Infrared Coherent Sources and Applications*, pages 3–65, Dordrecht, 2008. Springer Netherlands. ISBN 978-1-4020-6463-0.

[31] M. F. S. Ferreira, E. Castro-Camus, D. J. Ottaway, J. M. López-Higuera, X. Feng, W. Jin, Y. Jeong, N. Picqué, L. Tong, B. M. Reinhard, P. M. Pellegrino, A. Méndez, M. Diem, F. Vollmer, and Q. Quan. Roadmap on optical sensors. *J. Opt.*, 19(8):083001, 2017.

[32] J. Faist, F. Capasso, D. L. Sivco, C. Sirtori, A. L. Hutchinson, and A. Y. Cho. Quantum cascade laser. *Science*, 264(5158):553–556, 1994. ISSN 00368075, 10959203.

[33] Y. Yao, A. J. Hoffman, and C. F. Gmachl. Mid-infrared quantum cascade lasers. *Nat. Photonics*, 6(7):432, 2012. ISSN 1749-4885.

[34] C.-H. Lin, R. Q. Yang, D. Zhang, S. J. Murry, S. S. Pei, A. A. Allerman, and S. R. Kurtz. Type-II interband quantum cascade laser at 3.8 µm. *Electron. Lett.*, 33(7):598–599, 1997.

[35] I. Vurgaftman and J. R. Meyer. Analysis of limitations to wallplug efficiency and output power for quantum cascade lasers. *J. Appl. Phys.*, 99(12):123108, 2006.

[36] I. Vurgaftman, W. W. Bewley, C. L. Canedy, C. S. Kim, M. Kim, C. D. Merritt, J. Abell, J. R. Lindle, and J. R. Meyer. Rebalancing of internally generated carriers for mid-infrared interband cascade lasers with very low power consumption. *Nat. Commun.*, 2(1):585, 2011. ISSN 2041-1723.

[37] S. D. Jackson. Towards high-power mid-infrared emission from a fibre laser. *Nat. Photonics*, 6(7):423–431, 2012. ISSN 1749-4885, 1749-4893.

[38] I. Vurgaftman, R. Weih, M. Kamp, J. R. Meyer, C. L. Canedy, C. S. Kim, M. Kim, W. W. Bewley, C. D. Merritt, J. Abell, and S. Höfling. Interband cascade lasers. *J. Phys. D: Appl. Phys.*, 48(12):123001, 2015.

[39] W. W. Bewley, J. R. Lindle, C. S. Kim, M. Kim, C. L. Canedy, I. Vurgaftman, and J. R. Meyer. Lifetimes and Auger coefficients in type-II W interband cascade lasers. *Appl. Phys. Lett.*, 93(4):041118, 2008.

[40] L. D. DeLoach, R. H. Page, G. D. Wilke, S. A. Payne, and W. F. Krupke. Transition metal-doped zinc chalcogenides: Spectroscopy and laser demonstration of a new class of gain media. *IEEE J. Quantum Electron.*, 32(6):885–895, 1996.

[41] S. B. Mirov, V. V. Fedorov, D. Martyshkin, I. S. Moskalev, M. Mirov, and S. Vasilyev. Progress in mid-IR lasers based on Cr and Fe-doped II-VI chalcogenides. *IEEE J. Sel. Topics Quantum Electron.*, 21(1):292–310, 2015.

[42] S. Vasilyev, I. Moskalev, M. Mirov, V. Smolsky, S. Mirov, and V. Gapontsev. Recent breakthroughs in solid-state mid-IR laser technology. *Laser Tech. J.*, 13 (4):24–27, 2016. ISSN 1863-9119.

[43] C. J. Koester and E. Snitzer. Amplification in a fiber laser. *Appl. Opt.*, 3(10): 1182–1186, 1964.

[44] W. Shi, Q. Fang, X. Zhu, R. A. Norwood, and N. Peyghambarian. Fiber lasers and their applications [invited]. *Appl. Opt.*, 53(28):6554–6568, 2014.

[45] X. Zhu and N. Peyghambarian. High-power ZBLAN glass fiber lasers: Review and prospect. *Adv. OptoElectron.*, 2010, 2010.

[46] I. Cozmuta and D. J. Rasky. Exotic optical fibers and glasses: Innovative material processing opportunities in Earth's orbit. *New Space*, 5(3):121–140, 2017.

[47] D. Starodubov, K. McCormick, M. Dellosa, E. Erdelyi, and L. Volfson. Facility for orbital material processing. In *Sensors and Systems for Space Applications XI*, volume 10641 of *Society of Photo-Optical Instrumentation Engineers (SPIE) Conference Series*, 2018.

[48] V. Fomin, M. Abramov, A. Ferin, A. Abramov, D. Mochalov, N. Platonov, and V. Gapontsev. 10 kW single mode fiber laser. In *5th International Symposium on High-Power Fiber Lasers and Their Applications*, page 878, St. Petersburg, Russia, 2010. SPIE.

[49] Y. Jeong, S. Yoo, C. A. Codemard, J. Nilsson, J. K. Sahu, D. N. Payne, R. Horley, P. W. Turner, L. Hickey, A. Harker, M. Lovelady, and A. Piper. Erbium:Ytterbium codoped large-core fiber laser with 297-W continuous-wave output power. *IEEE J. Sel. Topics Quantum Electron.*, 13(3):573–579, 2007.

[50] T. Ehrenreich, R. Leveille, I. Majid, K. Tankala, G. Rines, and P. Moulton. 1-kW, all-glass Tm:fiber laser. *SPIE Photonics West 2010: LASE Fiber Lasers VII: Technology, Systems, and Applications*, 2010.

[51] A. Hemming, S. Bennetts, N. Simakov, J. Haub, and A. Carter. Development of resonantly cladding-pumped holmium-doped fibre lasers. In E. C. Honea and S. T. Hendow, editors, *Fiber Lasers IX: Technology, Systems, and Applications*, volume 8237, pages 286–294. International Society for Optics and Photonics, SPIE, 2012.

[52] S. Tokita, M. Murakami, S. Shimizu, M. Hashida, and S. Sakabe. Liquid-cooled 24 W mid-infrared Er:ZBLAN fiber laser. *Opt. Lett.*, 34(20):3062–3064, 2009.

[53] S. D. Jackson. Single-transverse-mode 2.5-W holmium-doped fluoride fiber laser operating at 2.86 µm. *Opt. Lett.*, 29(4):334–336, 2004.

[54] J. Li, D. D. Hudson, and S. D. Jackson. High-power diode-pumped fiber laser operating at 3 µm. *Opt. Lett.*, 36(18):3642–3644, 2011.

[55] C. Carbonnier, H. Többen, and U. B. Unrau. Room temperature CW fibre laser at 3.22 µm. *Electron. Lett.*, 34(9):893–894, 1998. ISSN 0013-5194.

[56] H. Többen. CW lasing at 3.45 µm in erbium-doped fluorozironate fibres. *FREQUENZ*, 45(9–10):250–252, 1991.

[57] J. Schneider, C. Carbonnier, and U. B. Unrau. Characterization of a Ho^{3+}-doped fluoride fiber laser with a 3.9-µm emission wavelength. *Appl. Opt.*, 36(33):8595–8600, 1997.

[58] S. Crawford, D. D. Hudson, and S. D. Jackson. High-power broadly tunable 3-µm fiber laser for the measurement of optical fiber loss. *IEEE Photon. J.*, 7(3):1–9, 2015. ISSN 1943-0655.

[59] M. R. Majewski and S. D. Jackson. Highly efficient mid-infrared dysprosium fiber laser. *Opt. Lett.*, 41(10):2173–2176, 2016.

[60] V. Fortin, F. Maes, M. Bernier, S. T. Bah, M. D'Auteuil, and R. Vallee. Watt-level erbium-doped all-fiber laser at 3.44 µm. *Opt. Lett.*, 41(3):559–62, 2016. ISSN 1539-4794, 0146-9592.

[61] O. Henderson-Sapir, S. D. Jackson, and D. J. Ottaway. Versatile and widely tunable mid-infrared erbium doped ZBLAN fiber laser. *Opt. Lett.*, 41(7):1676–9, 2016. ISSN 1539-4794, 0146-9592.

[62] O. Henderson-Sapir, J. Munch, and D. J. Ottaway. Mid-infrared fiber lasers at and beyond 3.5 µm using dual-wavelength pumping. *Opt. Lett.*, 39(3):493–6, 2014. ISSN 1539-4794, 0146-9592.

[63] O. Henderson-Sapir, A. Malouf, N. Bawden, J. Munch, S. D. Jackson, and D. J. Ottaway. Recent advances in 3.5 µm erbium-doped mid-infrared fiber lasers. *IEEE J. Sel. Top. Quantum Electron.*, 23(3):6–14, 2017. ISSN 1077-260X.

[64] H. Többen. Room temperature CW fibre laser at 3.5 µm in Er^{3+}-doped ZBLAN glass. *Electron. Lett.*, 28(14):1361–1362, 1992. ISSN 1350-911X.

[65] F. Maes, V. Fortin, M. Bernier, and R. Vallée. 5.6 W monolithic fiber laser at 3.55 µm. *Opt. Lett.*, 42(11):2054–2057, 2017.

[66] F. Maes, V. Fortin, M. Bernier, and R. Vallée. Quenching of 3.4 µm dual-wavelength pumped erbium doped fiber lasers. *IEEE J. Quantum Electron.*, 53 (2):1–8, 2017.

[67] N. Bawden, H. Matsukuma, O. Henderson-Sapir, E. Klantsataya, S. Tokita, and D. J. Ottaway. Actively Q-switched dual-wavelength pumped Er^{3+} ZBLAN fiber laser at 3.47 µm. *Opt. Lett.*, 43(11):2724–2727, 2018.

[68] H. R. Telle, G. Steinmeyer, A. E. Dunlop, J. Stenger, D. H. Sutter, and U. Keller. Carrier-envelope offset phase control: A novel concept for absolute optical frequency measurement and ultrashort pulse generation. *Appl. Phys. B*, 69(4): 327–332, 1999. ISSN 1432-0649.

[69] S. Duval, M. Bernier, V. Fortin, J. Genest, M. Piché, and R. Vallée. Femtosecond fiber lasers reach the mid-infrared. *Optica*, 2(7):623–626, 2015.

[70] G. Zhu, X. Zhu, F. Wang, S. Xu, Y. Li, X. Guo, K. Balakrishnan, R. A. Norwood, and N. Peyghambarian. Graphene mode-locked fiber laser at 2.8 µm. *IEEE Photonics Technol. Lett.*, 28(1):7–10, 2016. ISSN 1041-1135.

[71] O. Henderson-Sapir, N. Bawden, M. R. Majewski, R. I. Woodward, D. J. Ottaway, and S. D. Jackson. Mode-locked and tunable fiber laser at the 3.5 µm band using frequency-shifted feedback, 2019.

[72] J. C. Gauthier, V. Fortin, J. Y. Carrée, S. Poulain, M. Poulain, R. Vallée, and M. Bernier. Mid-IR supercontinuum from 2.4 to 5.4 µm in a low-loss fluoroindate fiber. *Opt. Lett.*, 41(8):1756–9, 2016. ISSN 1539-4794, 0146-9592.

[73] C. R. Petersen, U. Møller, I. Kubat, B. Zhou, S. Dupont, J. Ramsay, T. Benson, S. Sujecki, N. Abdel-Moneim, Z. Tang, D. Furniss, A. Seddon, and O. Bang. Mid-infrared supercontinuum covering the 1.4-13.3 µm molecular fingerprint region using ultra-high NA chalcogenide step-index fibre. *Nat. Photonics*, 8(11), 2014. ISSN 1749-4885.

[74] T. Cheng, K. Nagasaka, T. H. Tuan, X. Xue, M. Matsumoto, H. Tezuka, T. Suzuki, and Y. Ohishi. Mid-infrared supercontinuum generation spanning 2.0 to 15.1 µm in a chalcogenide step-index fiber. *Opt. Lett.*, 41(9):2117–2120, 2016.

[75] D. D. Hudson, S. Antipov, L. Li, I. Alamgir, T. Hu, M. El Amraoui, Y. Messaddeq, M. Rochette, S. D. Jackson, and A. Fuerbach. Toward all-fiber supercontinuum spanning the mid-infrared. *Optica*, 4(10):1163–1166, 2017.

[76] R. R. Gattass, L. B. Shaw, V.Q. Nguyen, P.C. Pureza, I. D. Aggarwal, and J. S. Sanghera. All-fiber chalcogenide-based mid-infrared supercontinuum source. *Opt. Fiber Technol.*, 18(5):345–348, 2012. ISSN 1068-5200.

[77] J. Swiderski and M. Michalska. Mid-infrared supercontinuum generation in a single-mode thulium-doped fiber amplifier. *Laser Phys. Lett.*, 10(3):035105, 2013.

[78] L. Yang, Y. Li, B. Zhang, T. Wu, Y. Zhao, and J. Hou. 30-W supercontinuum generation based on ZBLAN fiber in an all-fiber configuration. *Photon. Res.*, 7 (9):1061–1065, 2019.

[79] S. H. Yun and B. E. Bouma. *Wavelength swept lasers*, chapter 20, pages 619–637. Springer International Publishing, Switzerland, 2015. ISBN 978-3-319-06419-2.

[80] R. I. Woodward, M. R. Majewski, D. D. Hudson, and S. D. Jackson. Swept-wavelength mid-infrared fiber laser for real-time ammonia gas sensing. *APL Photonics*, 4(2):020801, 2019.

[81] W. Koechner and M. Bass. *Solid-state lasers : A graduate text*. Springer, New York, 2003. ISBN 0387955909.

[82] Z. Qin, T. Hai, G. Xie, J. Ma, P. Yuan, L. Qian, L. Li, L. Zhao, and D. Shen. Black phosphorus Q-switched and mode-locked Er:ZBLAN fiber lasers at 3.5 µm. *Opt. Express*, 26(7):8224–8231, 2018.

[83] U. Sharma, C.-S. Kim, and J. U. Kang. Highly stable tunable dual-wavelength Q-switched fiber laser for DIAL applications. *IEEE Photon. Technol. Lett.*, 16 (5):1277–1279, 2004. ISSN 1041-1135.

[84] Z. T. Wang, Y. Chen, C. J. Zhao, H. Zhang, and S. C. Wen. Switchable dual-wavelength synchronously Q-switched erbium-doped fiber laser based on graphene saturable absorber. *IEEE Photon. J.*, 4(3):869–876, 2012. ISSN 1943-0655.

[85] J. Ma, Z. Qin, G. Xie, L. Qian, and D. Tang. Review of mid-infrared mode-locked laser sources in the 2.0 µm – 3.5 µm spectral region. *Applied Physics Reviews*, 6 (2):021317, 2019.

[86] S. Y. Set, H. Yaguchi, Y. Tanaka, and M. Jablonski. Ultrafast fiber pulsed lasers incorporating carbon nanotubes. *IEEE J. Sel. Top. Quantum Electron.*, 10(1): 137–146, 2004. ISSN 1077-260X.

[87] Q. Bao, H. Zhang, Y. Wang, Z. Ni, Y. Yan, Z. X. Shen, K. P. Loh, and D. Y. Tang. Atomic-layer graphene as a saturable absorber for ultrafast pulsed lasers. *Adv. Funct. Mater.*, 19(19):3077–3083, 2009. ISSN 1616-3028.

[88] Z. Sun, T. Hasan, F. Torrisi, D. Popa, G. Privitera, F. Wang, F. Bonaccorso, D. M. Basko, and A. C. Ferrari. Graphene mode-locked ultrafast laser. *ACS Nano*, 4(2):803–810, 2010. ISSN 1936-0851.

[89] A. Martinez, K. Fuse, and S. Yamashita. Mechanical exfoliation of graphene for the passive mode-locking of fiber lasers. *Appl. Phys. Lett.*, 99(12):121107, 2011. ISSN 0003-6951.

[90] W. D. Tan, C. Y. Su, R. J. Knize, G. Q. Xie, L. J. Li, and D. Y. Tang. Mode locking of ceramic Nd:yttrium aluminum garnet with graphene as a saturable absorber. *Appl. Phys. Lett.*, 96(3):031106, 2010.

[91] E. Ugolotti, A. Schmidt, V. Petrov, J. W. Kim, D.-I. Yeom, F. Rotermund, S. Bae, B. H. Hong, A. Agnesi, C. Fiebig, G. Erbert, X. Mateos, M. Aguiló, F. Diaz, and U. Griebner. Graphene mode-locked femtosecond Yb:KLuW laser. *Appl. Phys. Lett.*, 101(16):161112, 2012.

[92] J. Ma, G. Q. Xie, P. Lv, W. L. Gao, P. Yuan, L. J. Qian, H. H. Yu, H. J. Zhang, J. Y. Wang, and D. Y. Tang. Graphene mode-locked femtosecond laser at 2 µm wavelength. *Opt. Lett.*, 37(11):2085–2087, 2012.

[93] A. A. Lagatsky, Z. Sun, T. S. Kulmala, R. S. Sundaram, S. Milana, F. Torrisi, O. L. Antipov, Y. Lee, J. H. Ahn, C. T. A. Brown, W. Sibbett, and A. C. Ferrari. 2 µm solid-state laser mode-locked by single-layer graphene. *Appl. Phys. Lett.*, 102(1):013113, 2013.

[94] M. N. Cizmeciyan, J. W. Kim, S. Bae, B. H. Hong, F. Rotermund, and A. Sennaroglu. Graphene mode-locked femtosecond Cr:ZnSe laser at 2500 nm. *Opt. Lett.*, 38(3):341–343, 2013.

[95] N. Tolstik, E. Sorokin, and . T. Sorokina. Graphene mode-locked Cr:ZnS laser with 41 fs pulse duration. *Opt. Express*, 22(5):5564–5571, 2014.

[96] L. Benbrahim-Tallaa, R. A. Baan, Y. Grosse, B. Lauby-Secretan, F. El Ghissassi, V. Bouvard, N. Guha, D. Loomis, and K. Straif. Carcinogenicity of diesel-engine and gasoline-engine exhausts and some nitroarenes. *Lancet Oncol.*, 13(7):663–664, 2012. ISSN 1470-2045.

[97] İ. A. Reşitoğlu, K. Altinişik, and A. Keskin. The pollutant emissions from diesel-engine vehicles and exhaust aftertreatment systems. *Clean Technol. Environ. Policy*, 17(1):15–27, 2015. ISSN 1618-9558.

[98] United States Environmental Protection Agency. *AP 42, Fifth Edition Compilation of Air Pollutant Emissions Factors, Volume 1: Stationary Point and Area Sources*, volume 1. Office of Air Quality Planning and Standards, fifth edition, 1996.

[99] Department of the Environment, Water, Heritage and the Arts. *Emission Estimation Technique Manual for Combustion Engines*. Commonwealth of Australia, third edition, 2008.

[100] K. Lawrence, K. Zeise, and P. Morgan. Management options for non-road engine emissions in urban areas. Technical report, Department for Environment and Heritage, Canberra, 2005. Consultancy report for Department for Environment and Heritage, Canberra. Prepared by Pacific Air & Environment Pty. Ltd.

[101] S. B. Dalsøren, M. S. Eide, Ø. Endresen, A. Mjelde, G. Gravir, and I. S. A. Isaksen. Update on emissions and environmental impacts from the international fleet of ships: the contribution from major ship types and ports. *Atmos. Chem. Phys.*, 9(6):2171–2194, 2009.

[102] D. P. McArthur and L. Osland. Ships in a city harbour: An economic valuation of atmospheric emissions. *Transport. Res. Part D*, 21:47–52, 2013. ISSN 1361-9209.

[103] J. Ćelić, S. Valčić, and M. Bistrović. Air pollution from cruise ships. In *Proceedings ELMAR-2014*, pages 1–4, Sep 2014.

[104] M. Tichavska, B. Tovar, D. Gritsenko, L. Johansson, and J. P. Jalkanen. Air emissions from ships in port: Does regulation make a difference? *Transport Policy*, 75:128–140, 2019. ISSN 0967-070X.

[105] L. Goldsworthy and B. Goldsworthy. Modelling of ship engine exhaust emissions in ports and extensive coastal waters based on terrestrial AIS data – An Australian case study. *Environ. Model. Softw.*, 63:45–60, 2015. ISSN 1364-8152.

[106] A. Maragkogianni and S. Papaefthimiou. Evaluating the social cost of cruise ships air emissions in major ports of Greece. *Transport. Res. Part D*, 36:10–17, 2015. ISSN 1361-9209.

[107] T. W. P. Smith, J. P. Jalkanen, B. A. Anderson, J. J. Corbett, J. Faber, S. Hanayama, E. O'Keeffe, S. Parker, L. Johansson, L. Aldous, C. Raucci, M. Traut, S. Ettinger, D. Nelissen, D. S. Lee, S. Ng, A. Agrawal, J. J. Winebrake, M. Hoen, S. Chesworth, and A. Pandey. *Third IMO Greenhouse Gas Study 2014*. International Maritime Organization, United Kingdom, 2015.

[108] N. Olmer, B. Comer, B. Roy, X. Mao, and D. Rutherford. Greenhouse gas emissions from global shipping, 2013-2015. *The International Council on Clean Transportation*, pages 1–38, 2017.

[109] S. Kopela. Making ships cleaner: Reducing air pollution from international shipping. *Review of European, Comparative & International Environmental Law*, 26 (3):231–242, 2017.

[110] C. Ris. U.S. EPA health assessment for diesel engine exhaust: A review. *Inhalation Toxicol.*, 19(sup1):229–239, 2007.

[111] S. Peters, R. N. Carey, T. R. Driscoll, D. C. Glass, G. Benke, A. Reid, and L. Fritschi. The Australian work exposures study: Prevalence of occupational exposure to diesel engine exhaust. *Annals of Work Exposures and Health*, 59(5): 600–608, 2015. ISSN 2398-7308.

[112] D. G. Murdock, S. V. Stearns, R. T. Lines, D. Lenz, D. M. Brown, and C. R. Philbrick. Applications of real-world gas detection: Airborne natural gas emission lidar (ANGEL) system. *J. Appl. Remote Sens.*, 2:1–18, 2008.

[113] F. Innocenti, R. Robinson, T. Gardiner, A. Finlayson, and A. Connor. Differential absorption lidar (DIAL) measurements of landfill methane emissions. *Remote Sens.*, 9(9/953), 2017. ISSN 2072-4292.

[114] M. Queißer, M. Burton, and L. Fiorani. Differential absorption lidar for volcanic CO_2 sensing tested in an unstable atmosphere. *Opt. Express*, 23(5):6634–6644, 2015.

[115] C. J. Grund, S. Shald, and S. V. Stearns. Airborne three-line mid-IR DIAL for rapid chemical species plume mapping. In *Laser Radar Technology and Applications IX*, volume 5412, pages 1–10. International Society for Optics and Photonics, 2004.

[116] R. Measures. *Laser remote sensing : Fundamentals and applications*. Krieger Pub. Co, Malabar, Fla, 1992. ISBN 0-89464-619-2.

[117] A. R. Huete. Remote sensing for environmental monitoring. In J. F. Artiola, I. L. Pepper, and M. L. Brusseau, editors, *Environmental Monitoring and Characterization*, chapter 11, pages 183–206. Academic Press, Burlington, 2004. ISBN 978-0-12-064477-3.

[118] X. Ye, X. Wang, Y. Wang, Y. Luo, G. Yang, and R. Sun. *Design features and construction enlightenments of Oasis-class luxury cruise ships*, pages 201–218. Springer Singapore, Singapore, 2019. ISBN 978-981-13-3780-2.

[119] J. Seinfeld and S. Pandis. *Atmospheric chemistry and physics : From air pollution to climate change*. John Wiley & Sons, Hoboken, New Jersey, 2016. ISBN 9781118947401.

[120] A. Tiwary and J. Colls. *Air pollution : Measurement, modelling and mitigation*. Routledge, London and New York, third edition, 2010. ISBN 0203871960.

[121] F. Pasquill. The estimation of the dispersion of windborne material. *Meteorol. Mag.*, 90(1063):33–49, 1961.

[122] S. R. Hanna, G. A. Briggs, and R. P. Jr. Hosker. Handbook on atmospheric diffusion. Technical report, U. S. Department of Energy, 1982.

[123] C. L. Archer and M. Z. Jacobson. Evaluation of global wind power. *J. Geophys. Res.: Atmos.*, 110(D12), 2005.

[124] E. Hinkley. *Laser monitoring of the atmosphere*. Springer-Verlag, Berlin New York, 1976. ISBN 3-540-07743-X.

[125] E.-T. Es-Sebbar, M. Alrefae, and A. Farooq. Infrared cross-sections and integrated band intensities of propylene: Temperature-dependent studies. *J. Quant. Spectrosc. Radiat. Transfer*, 133(C):559–569, 2014. ISSN 0022-4073.

[126] R. F. Kokaly, R. N. Clark, G. A. Swayze, K. E. Livo, T. M. Hoefen, N. C. Pearson, R. A. Wise, W. M. Benzel, H. A. Lowers, R. L. Driscoll, et al. USGS spectral library version 7. Technical report, U. S. Geological Survey, 2017.

[127] L. W. Pinkley and D. Williams. Optical properties of sea water in the infrared*. *J. Opt. Soc. Am.*, 66(6):554–558, 1976.

[128] J. L. Bufton, F. E. Hoge, and R. N. Swift. Airborne measurements of laser backscatter from the ocean surface. *Appl. Opt.*, 22(17):2603–2618, 1983.

[129] R. T. Menzies, D. M. Tratt, and W. H. Hunt. Lidar in-space technology experiment: measurements of sea surface directional reflectance and the link to surface wind speed. *Appl. Opt.*, 37(24):5550–5559, 1998.

[130] D. Barrick. Rough surface scattering based on the specular point theory. *IEEE Trans. Antennas Propag.*, 16(4):449–454, 1968. ISSN 0018-926X.

[131] J. Wu. Sea surface slope and equilibrium wind wave spectra. *Phys. Fluids*, 15 (5):741–747, 1972.

[132] C. Cox and W. Munk. Measurement of the roughness of the sea surface from photographs of the Sun's glitter. *J. Opt. Soc. Am.*, 44(11):838–850, 1954.

[133] W. B. Grant. Effect of differential spectral reflectance on DIAL measurements using topographic targets. *Appl. Opt.*, 21(13):2390–2394, 1982.

[134] J. W. Goodman. Some fundamental properties of speckle*. *J. Opt. Soc. Am.*, 66 (11):1145–1150, 1976.

[135] J. C. Dainty, A. E. Ennos, M. Françon, J. W. Goodman, T. S. McKechnie, and G. Parry. *Laser Speckle and Related Phenomena*. Topics in Applied Physics, 9. Springer-Verlag, Berlin New York, second edition, 1975. ISBN 0-387-07498-8.

[136] B. J. Cooke, B. E. Laubscher, M. M. Cafferty, N. L. Olivas, M. J. Schmitt, K. R. Fuller, R. M. Goeller, D. E. Mietz, J. J. Tiee, R. K. Sander, J. L. Vampola, S. L. Price, and I. Kasai. Analysis and design methodology for the development of optimized direct detection CO_2 DIAL receivers. In *Infrared Spaceborne Remote Sensing V*, volume 3122. SPIE, 1997.

[137] C.A. Gueymard, D. Myers, and K. Emery. Proposed reference irradiance spectra for solar energy systems testing. *Sol. Energy*, 73(6):443–467, 2002. ISSN 0038-092X.

[138] D. Giancoli. *Physics for scientists & engineers with modern physics*. Pearson Prentice Hall, Upper Saddle River, N.J, 2009. ISBN 9780131495081.

[139] S. Tokita, M. Murakami, S. Shimizu, M. Hashida, and S. Sakabe. 12 W Q-switched Er:ZBLAN fiber laser at 2.8 µm. *Opt. Lett.*, 36(15):2812–2814, 2011.

[140] Y. Shen, Y. Wang, K. Luan, H. Chen, M. Tao, and J. Si. High peak power actively Q-switched mid-infrared fiber lasers at 3 µm. *Appl. Phys. B*, 123(4):105, 2017. ISSN 1432-0649.

[141] M. Rößler, A. Velji, C. Janzer, T. Koch, and M. Olzmann. Formation of engine internal NO_2: Measures to control the NO_2/NO_x ratio for enhanced exhaust after treatment. *SAE Int. J. Engines*, 10(2017-01-1017):1880–1893, 2017.

[142] M. Puškár, M. Kopas, D. Puškár, J. Lumnitzer, and E. Faltinová. Method for reduction of the NO_x emissions in marine auxiliary diesel engine using the fuel mixtures containing biodiesel using HCCI combustion. *Mar. Pollut. Bull.*, 127: 752–760, 2018. ISSN 0025-326X.

[143] C. He, J. Li, Z. Ma, J. Tan, and L. Zhao. High NO_2/NO_x emissions downstream of the catalytic diesel particulate filter: An influencing factor study. *J. Environ. Sci.*, 35:55–61, 2015. ISSN 1001-0742.

[144] J. A. Logan. Nitrogen oxides in the troposphere: Global and regional budgets. *J. Geophys. Res.: Oceans*, 88(C15):10785–10807, 1983.

[145] P. Boylan, D. Helmig, and S. Oltmans. Ozone in the Atlantic Ocean marine boundary layer. *Elem. Sci. Anth.*, 3, 2015.

[146] F. Jobin, V. Fortin, F. Maes, M. Bernier, and R. Vallée. Gain-switched fiber laser at 3.55 µm. *Opt. Lett.*, 43(8):1770–1773, 2018.

[147] World Health Organization. *Guidelines for indoor air quality: Selected pollutants*. World Health Organization Regional Office for Europe, Copenhagen, Denmark, 2010. ISBN 9789289002134.

[148] N. B. Jones, K. Riedel, W. Allan, S. Wood, P. I. Palmer, K. Chance, and J. Notholt. Long-term tropospheric formaldehyde concentrations deduced from ground-based fourier transform solar infrared measurements. *Atmos. Chem. Phys.*, 9(18):7131–7142, 2009. ISSN 1680-7316.

[149] X. Li, S. Wang, R. Zhou, and B. Zhou. Urban atmospheric formaldehyde concentrations measured by a differential optical absorption spectroscopy method. *Environ. Sci.: Processes Impacts*, 16:291–297, 2014.

[150] W. Lin, X. Xu, Z. Ma, H. Zhao, X. Liu, and Y. Wang. Characteristics and recent trends of sulfur dioxide at urban, rural, and background sites in North China: Effectiveness of control measures. *J. Environ. Sci.*, 24(1):34–49, 2012. ISSN 1001-0742.

[151] World Health Organization. *Air quality guidelines : Global update 2005 : Particulate matter, ozone, nitrogen dioxide, and sulfur dioxide*. World Health Organization Regional Office for Europe, Copenhagen, Denmark, 2006. ISBN 9289021926.

[152] G. D. Nielsen, S. T. Larsen, and P. Wolkoff. Re-evaluation of the WHO (2010) formaldehyde indoor air quality guideline for cancer risk assessment. *Arch. Toxicol.*, 91(1):35–61, 2017. ISSN 1432-0738.

[153] United States Code of Federal Regulations. *Title 40 - Protection of Environment: Part 50 - National Primary and Secondary Ambient Air Quality Standards*, volume 2. United States Code of Federal Regulations, Jul 2018.

[154] S. D. Jackson, T. A. King, and M. Pollnau. Modelling of high-power diode-pumped erbium 3 µm fibre lasers. *J. Mod. Opt.*, 47(11):1987–1994, 2000. ISSN 0950-0340.

[155] X. Zhu and R. Jain. Numerical analysis and experimental results of high-power Er/Pr:ZBLAN 2.7 µm fiber lasers with different pumping designs. *Appl. Opt.*, 45 (27):7118–7125, 2006.

[156] J. Li and S. D. Jackson. Numerical modeling and optimization of diode pumped heavily-erbium-doped fluoride fiber lasers. *IEEE J. Quantum Electron.*, 48(4): 454–464, 2012. ISSN 0018-9197.

[157] J. Li, H. Luo, Y. Liu, L. Zhang, and S. D. Jackson. Modeling and optimization of cascaded erbium and holmium doped fluoride fiber lasers. *IEEE J. Sel. Top. Quantum Electron.*, 20(5):15–28, 2014.

[158] G. Zhu, X. Zhu, R. A. Norwood, and N. Peyghambarian. Experimental and numerical investigations on Q-switched laser-seeded fiber MOPA at 2.8 µm. *J. Lightwave Technol.*, 32(23):4553–4557, 2014. ISSN 0733-8724.

[159] M. Gorjan, M. Marinček, and M. Čopič. Role of interionic processes in the efficiency and operation of erbium-doped fluoride fiber lasers. *IEEE J. Quantum Electron.*, 47(2):262–273, 2011. ISSN 0018-9197.

[160] A. Malouf. Optimisation of 3.5 µm dual-wavelength pumped fibre laser. Honours thesis, The University of Adelaide, 2015.

[161] O. Henderson-Sapir. *Development of dual-wavelength pumped mid-infrared fibre laser*. PhD thesis, The University of Adelaide, 2015.

[162] S. S. Kim, C. Young, B. Vidakovic, S. G. A. Gabram-Mendola, C. W. Bayer, and B. Mizaikoff. Potential and challenges for mid-infrared sensors in breath diagnostics. *IEEE Sensors J.*, 10(1):145–158, 2010. ISSN 1530-437X.

[163] M. Vainio and L. Halonen. Mid-infrared optical parametric oscillators and frequency combs for molecular spectroscopy. *Phys. Chem. Chem. Phys.*, 18(6): 4266–4294, 2016.

[164] O. Henderson-Sapir, J. Munch, and D. J. Ottaway. New energy-transfer upconversion process in Er^{3+}:ZBLAN mid-infrared fiber lasers. *Opt. Express*, 24(7): 6869–83, 2016. ISSN 1094-4087, 1094-4087.

[165] MATLAB. *version 8.1.0.604 (R2013a)*. The MathWorks Inc., Natick, Massachusetts, 2013.

[166] P. S. Golding, S. D. Jackson, T. A. King, and M. Pollnau. Energy transfer processes in Er^{3+}-doped and Er^{3+}, Pr^{3+}-codoped ZBLAN glasses. *Phys. Rev. B*, 62(2):856, 2000.

[167] Y. D. Huang, M. Mortier, and F. Auzel. Stark level analysis for Er^{3+}-doped ZBLAN glass. *Opt. Mater.*, 17(4):501–511, 2001.

[168] P. M. Becker, A. A. Olsson, and J. R. Simpson. *Erbium-doped fiber amplifiers: Fundamentals and technology*. Academic press, 1999. ISBN 0080505848.

[169] A. E. Siegman. *Lasers*. University Science Books, Mill Valley, Calif, 1986. ISBN 0935702113.

[170] D. E. McCumber. Einstein relations connecting broadband emission and absorption spectra. *Phys. Rev.*, 136:A954–A957, 1964.

[171] D. Marcuse. Loss analysis of single-mode fiber splices. *Bell Syst. Tech. J.*, 56(5): 703–718, 1977. ISSN 1538-7305.

[172] R. Caspary. *Applied Rare Earth Spectroscopy for Fiber Laser Optimization*. Shaker, 2001. ISBN 383220315X.

[173] R. S. Quimby, W. J. Miniscalco, and B. A. Thompson. Excited-state absorption at 980 nm in erbium-doped glass. In *Fiber Laser Sources and Amplifiers III*, pages 72–79. International Society for Optics and Photonics, 1991.

[174] V. K. Bogdanov. *Energy exchange processes in erbium-doped fluoride glasses*. Phd thesis, School of Communications and Informatics, Victoria University, 1999.

[175] F. Gan. Optical properties of fluoride glasses: A review. *J. Non-Cryst. Solids*, 184:9–20, 1995. ISSN 0022-3093.

[176] B. Wang, L. Cheng, H. Zhong, J. Sun, Y. Tian, X. Zhang, and B. Chen. Excited state absorption cross sections of $^4I_{13/2}$ of Er^{3+} in ZBLAN. *Opt. Mater.*, 31(11): 1658–1662, 2009. ISSN 0925-3467.

[177] M. A. Couto dos Santos, E. Antic-Fidancev, J. Y. Gesland, J. C. Krupa, M. Lemaître-Blaise, and P. Porcher. Absorption and fluorescence of Er^{3+}-doped $LiYF_4$: measurements and simulation. *J. Alloys Compd.*, 275–277:435–441, 1998. ISSN 0925-8388.

[178] M. Pollnau and S. D. Jackson. Energy recycling versus lifetime quenching in erbium-doped 3-µm fiber lasers. *IEEE J. Quantum Electron.*, 38(2):162–169, 2002. ISSN 0018-9197.

[179] B. Srinivasan, R. K. Jain, and G. Monnom. Indirect measurement of the magnitude of ion clustering at high doping densities in Er:ZBLAN fibers. *J. Opt. Soc. Am. B*, 17(2):178–181, 2000.

[180] O. Henderson-Sapir, J. Munch, and D. J. Ottaway. A higher power 3.5 µm fibre laser. In *Advanced Solid State Lasers*, page ATu1A.3. Optical Society of America, 2014.

[181] A. Malouf, O. Henderson-Sapir, M. Gorjan, and D. J. Ottaway. Numerical modeling of 3.5 µm dual-wavelength pumped erbium-doped mid-infrared fiber lasers. *IEEE J. Quantum Electron.*, 52(11):1–12, 2016. ISSN 0018-9197.

[182] S. Sujecki. Simple and efficient method of lines based algorithm for modeling of erbium doped Q-switched fluoride fiber lasers. *J. Opt. Soc. Am. B*, 33(11): 2288–2295, 2016.

[183] F. Bonaccorso, Z. Sun, T. Hasan, and A. C. Ferrari. Graphene photonics and optoelectronics. *Nat. Photonics*, 4(9):611, 2010.

[184] G. Sobon, J. Sotor, I. Pasternak, A. Krajewska, W. Strupinski, and K. M. Abramski. Multilayer graphene-based saturable absorbers with scalable modulation depth for mode-locked Er- and Tm-doped fiber lasers. *Opt. Mater. Express*, 5 (12):2884–2894, 2015.

[185] F. Zhang, S. Han, Y. Liu, Z. Wang, and X. Xu. Dependence of the saturable absorption of graphene upon excitation photon energy. *Appl. Phys. Lett.*, 106(9): 091102, 2015.

[186] A. H. Castro Neto, F. Guinea, N. M. R. Peres, K. S. Novoselov, and A. K. Geim. The electronic properties of graphene. *Rev. Mod. Phys.*, 81(1):109–162, 2009. ISSN 0034-6861, 1539-0756.

[187] A. K. Geim. Graphene: Status and prospects. *Science*, 324(5934):1530–1534, 2009. ISSN 0036-8075.

[188] K. S. Novoselov, A. K. Geim, S. V. Morozov, D. Jiang, Y. Zhang, S. V. Dubonos, I. V. Grigorieva, and A. A. Firsov. Electric field effect in atomically thin carbon films. *Science*, 306(5696):666–669, 2004. ISSN 0036-8075.

[189] H. Tetlow, J. Posthuma de Boer, I. J. Ford, D. D. Vvedensky, J. Coraux, and L. Kantorovich. Growth of epitaxial graphene: Theory and experiment. *Phys. Rep.*, 542(3):195–295, 2014. ISSN 0370-1573.

[190] A. N. Obraztsov. Chemical vapour deposition: Making graphene on a large scale. *Nat. Nanotechnol.*, 4(4):212, 2009.

[191] X. Liang, B. A. Sperling, I. Calizo, G. Cheng, C. A. Hacker, Q. Zhang, Y. Obeng, K. Yan, H. Peng, Q. Li, X. Zhu, H. Yuan, A. R. Hight Walker, Z. Liu, L. Peng, and C. A. Richter. Toward clean and crackless transfer of graphene. *ACS Nano*, 5(11):9144–9153, 2011.

[192] M. I. Katsnelson. *Graphene : Carbon in two dimensions*. Cambridge University Press, Cambridge New York, 2012. ISBN 9780521195409.

[193] J. Warner. *Graphene : Fundamentals and emergent applications*. Elsevier, Amsterdam, 2013. ISBN 978-0-12-394593-8.

[194] D. G. Papageorgiou, I. A. Kinloch, and R. J. Young. Mechanical properties of graphene and graphene-based nanocomposites. *Prog. Mater Sci.*, 90:75–127, 2017. ISSN 0079-6425.

[195] D. R. Cooper, B. D'Anjou, N. Ghattamaneni, B. Harack, M. Hilke, A. Horth, N. Majlis, M. Massicotte, L. Vandsburger, E. Whiteway, et al. Experimental review of graphene. *ISRN Condens. Matter Phys.*, 2012, 2012.

[196] P. R. Wallace. The band theory of graphite. *Phys. Rev.*, 71:622–634, 1947.

[197] R. Saito, G. Dresselhaus, and M. S. Dresselhaus. *Physical properties of carbon nanotubes*. Imperial College Press, London, 1998. ISBN 1-86094-093-5.

[198] S. Reich, J. Maultzsch, C. Thomsen, and P. Ordejón. Tight-binding description of graphene. *Phys. Rev. B*, 66:035412, 2002.

[199] J.-C. Charlier, X. Blase, and S. Roche. Electronic and transport properties of nanotubes. *Rev. Mod. Phys.*, 79:677–732, 2007.

[200] R. R. Haering. Band structure of rhombohedral graphite. *Can. J. Phys.*, 36(3): 352–362, 1958.

[201] N. W. Ashcroft and N. D. Mermin. *Solid state physics*. Holt, Rinehart and Winston, New York, 1976. ISBN 0030839939.

[202] K. S. Novoselov, A. K. Geim, S. V. Morozov, D. Jiang, M. I. Katsnelson, I. V. Grigorieva, S. V. Dubonos, and A. A. Firsov. Two-dimensional gas of massless Dirac fermions in graphene. *Nature*, 438(7065):197–200, 2005. ISSN 0028-0836.

[203] F. Guinea. Charge distribution and screening in layered graphene systems. *Phys. Rev. B*, 75:235433, 2007.

[204] S. Yamashita. A tutorial on nonlinear photonic applications of carbon nanotube and graphene. *J. Lightwave Technol.*, 30(4):427–447, 2012.

[205] K. F. Mak, M. Y. Sfeir, J. A. Misewich, and T. F. Heinz. The evolution of electronic structure in few-layer graphene revealed by optical spectroscopy. *Proc. Natl. Acad. Sci. U. S. A.*, 107(34):14999–15004, 2010. ISSN 0027-8424.

[206] M. S. Dresselhaus and G. Dresselhaus. Intercalation compounds of graphite, graphene. *Adv. Phys.*, 51(1):1–186, 2002.

[207] M. Koshino and T. Ando. Orbital diamagnetism in multilayer graphenes: Systematic study with the effective mass approximation. *Phys. Rev. B*, 76:085425, 2007.

[208] R. R. Nair, P. Blake, A. N. Grigorenko, K. S. Novoselov, T. J. Booth, T. Stauber, N. M. R. Peres, and A. K. Geim. Fine structure constant defines visual transparency of graphene. *Science*, 320(5881):1308–1308, 2008. ISSN 0036-8075.

[209] F. T. Vasko. Saturation of interband absorption in graphene. *Phys. Rev. B*, 82: 245422, 2010.

[210] A. Marini, J. D. Cox, and F. J. García de Abajo. Theory of graphene saturable absorption. *Phys. Rev. B*, 95:125408, 2017.

[211] H. Yang, X. Feng, Q. Wang, H. Huang, W. Chen, A. T. S. Wee, and W. Ji. Giant two-photon absorption in bilayer graphene. *Nano Lett.*, 11(7):2622–2627, 2011.

[212] W. Chen, Y. Wang, and W. Ji. Two-photon absorption in graphene enhanced by the excitonic fano resonance. *J. Phys. Chem. C*, 119(29):16954–16961, 2015.

[213] G. Demetriou, H. T. Bookey, F. Biancalana, E. Abraham, Y. Wang, W. Ji, and A. K. Kar. Nonlinear optical properties of multilayer graphene in the infrared. *Opt. Express*, 24(12):13033–13043, 2016.

[214] A. Roberts, D. Cormode, C. Reynolds, T. Newhouse-Illige, B. J. LeRoy, and A. S. Sandhu. Response of graphene to femtosecond high-intensity laser irradiation. *Appl. Phys. Lett.*, 99(5):051912, 2011.

[215] M. Currie, J. D. Caldwell, F. J. Bezares, J. Robinson, T. Anderson, H. Chun, and M. Tadjer. Quantifying pulsed laser induced damage to graphene. *Appl. Phys. Lett.*, 99(21):211909, 2011. ISSN 0003-6951.

[216] C.-C. Lee, J. M. Miller, and T. R. Schibli. Doping-induced changes in the saturable absorption of monolayer graphene. *Appl. Phys. B*, 108(1):129–135, 2012. ISSN 1432-0649.

[217] G. Xing, H. Guo, X. Zhang, T. C. Sum, and C. H. A. Huan. The physics of ultrafast saturable absorption in graphene. *Opt. Express*, 18(5):4564–4573, 2010.

[218] S. Yamashita, A. Martinez, and B. Xu. Short pulse fiber lasers mode-locked by carbon nanotubes and graphene. *Opt. Fiber Technol.*, 20(6):702–713, 2014. ISSN 1068-5200.

[219] S. Kumar, M. Anija, N. Kamaraju, K. S. Vasu, K. S. Subrahmanyam, A. K. Sood, and C. N. R. Rao. Femtosecond carrier dynamics and saturable absorption in graphene suspensions. *Appl. Phys. Lett.*, 95(19):191911, 2009.

[220] J. M. Dawlaty, S. Shivaraman, M. Chandrashekhar, F. Rana, and M. G. Spencer. Measurement of ultrafast carrier dynamics in epitaxial graphene. *Appl. Phys. Lett.*, 92(4):042116, 2008.

[221] J. Shang, S. Yan, C. Cong, H.-S. Tan, T. Yu, and G. G. Gurzadyan. Probing near dirac point electron-phonon interaction in graphene. *Opt. Mater. Express*, 2(12):1713–1722, 2012.

[222] U. Keller, K. J. Weingarten, F. X. Kartner, D. Kopf, B. Braun, I. D. Jung, R. Fluck, C. Honninger, N. Matuschek, and J. Aus der Au. Semiconductor saturable absorber mirrors (SESAM's) for femtosecond to nanosecond pulse generation in solid-state lasers. *IEEE J. Sel. Top. Quantum Electron.*, 2(3):435–453, 1996. ISSN 1077-260X.

[223] H. Yang. *Saturable Absorption and Two-Photon Absorption in Graphene*. PhD thesis, National University of Singapore, 2012.

[224] M. Sheik-Bahae, A. A. Said, T. H. Wei, D. J. Hagan, and E. W. Van Stryland. Sensitive measurement of optical nonlinearities using a single beam. *IEEE J. Quantum Electron.*, 26(4):760–769, 1990. ISSN 0018-9197.

[225] P. B. Chapple, J. Staromlynska, J. A. Hermann, T. J. Mckay, and R. G. Mcduff. Single-beam z-scan: Measurement techniques and analysis. *J. Nonlinear Opt. Phys. Mater.*, 06(03):251–293, 1997.

[226] K. F. Mak, M. Y. Sfeir, Y. Wu, C. H. Lui, J. A. Misewich, and T. F. Heinz. Measurement of the optical conductivity of graphene. *Phys. Rev. Lett.*, 101(19): 196405, 2008.

[227] D. Wright, P. Greve, J. Fleischer, and L. Austin. Laser beam width, divergence and beam propagation factor – an international standardization approach. *Opt. Quantum. Electron.*, 24(9):S993–S1000, 1992. ISSN 1572-817X.

[228] A. E. Siegman. Defining, measuring, and optimizing laser beam quality. In A. Bhowmik, editor, *Laser Resonators and Coherent Optics: Modeling, Technology, and Applications*, volume 1868, pages 2–12. International Society for Optics and Photonics, SPIE, 1993.

[229] R. Grange, M. Haiml, R. Paschotta, G. J. Spühler, L. Krainer, M. Golling, O. Ostinelli, and U. Keller. New regime of inverse saturable absorption for self-stabilizing passively mode-locked lasers. *Appl. Phys. B: Lasers Opt.*, 80(2):151–158, 2005. ISSN 1432-0649.

[230] J. Yang, H. Zhong, S. Zhang, Y. Tang, and D. Fan. Cascade-gain-switching for generating 3.5-µm nanosecond pulses from monolithic fiber lasers. *IEEE Photonics J.*, 10(5):1–12, 2018. ISSN 1943-0655.

[231] R. Boyd. *Nonlinear Optics*. Academic Press, Amsterdam Boston, 2008. ISBN 9780123694706.

[232] L. M. Malard, M. A. Pimenta, G. Dresselhaus, and M. S. Dresselhaus. Raman spectroscopy in graphene. *Phys. Rep.*, 473(5):51–87, 2009. ISSN 0370-1573.

[233] A. J. Pollard, B. Brennan, H. Stec, B. J. Tyler, M. P. Seah, I. S. Gilmore, and D. Roy. Quantitative characterization of defect size in graphene using Raman spectroscopy. *Appl. Phys. Lett.*, 105(25):253107, 2014.

[234] K. Kim, S. Coh, L. Z. Tan, W. Regan, J. M. Yuk, E. Chatterjee, M. F. Crommie, M. L. Cohen, S. G. Louie, and A. Zettl. Raman spectroscopy study of rotated double-layer graphene: Misorientation-angle dependence of electronic structure. *Phys. Rev. Lett.*, 108:246103, 2012.

[235] H. Hu, B. Liao, X. Guo, D. Hu, X. Qiao, N. Liu, R. Liu, K. Chen, B. Bai, X. Yang, and Q. Dai. Large-scale suspended graphene used as a transparent substrate for infrared spectroscopy. *Small*, 13(25):1603812, 2017.

[236] X. Jiang, S. Gross, M. J. Withford, H. Zhang, D.-I. Yeom, F. Rotermund, and A. Fuerbach. Low-dimensional nanomaterial saturable absorbers for ultrashort-pulsed waveguide lasers. *Opt. Mater. Express*, 8(10):3055–3071, 2018.

[237] P. J. Linstrom and W. G. Mallard, editors. *NIST Chemistry WebBook, NIST Standard Reference Database Number 69*. National Institute of Standards and Technology, Gaithersburg MD, 20899, Oct 2018.